Patterns in Network Dynamics

by

Moyi Tian

B.Sc., Dickinson College; Carlisle, PA, 2019

M.Sc., Brown University; Providence, RI, 2021

A dissertation submitted in partial fulfillment of the

requirements for the degree of Doctor of Philosophy

in The Division of Applied Mathematics at Brown University

PROVIDENCE, RHODE ISLAND

May 2024

This dissertation by Moyi Tian is accepted in its present form
by The Division of Applied Mathematics as satisfying the
dissertation requirement for the degree of Doctor of Philosophy.

Date______________ ____________________________

Björn Sandstede, Ph.D., Advisor

Recommended to the Graduate Council

Date______________ ____________________________

Matthew T. Harrison, Ph.D., Reader

Date______________ ____________________________

Jason J. Bramburger, Ph.D., Reader

Approved by the Graduate Council

Date______________ ____________________________

Thomas A. Lewis, Dean of the Graduate School

Vita

Education

Brown University, Providence, RI *May 2024*
Ph.D. in Applied Mathematics
Advisor: Dr. Björn Sandstede
Brown University, Providence, RI *May 2021*
Masters of Science in Applied Mathematics
Dickinson College, Carlisle, PA *May 2019*
Bachelor of Science in Mathematics & Physics
Phi Beta Kappa Honors, Honors in Mathematics, *Summa Cum Laude*

Research

Brown University *June 2020 - May 2024*
Topic on Bifurcation of Localized Patterns on Rings
Advised by Dr. Björn Sandstede, Division of Applied Mathematics
Analyzed localized patterns arising in lattice dynamical systems using numerical and analytical techniques

Los Alamos National Laboratory *September 2023 - November 2023*
Applied Mathematics Graduate Student
Supervised by Dr. Andrey Lokhov, Applied Mathematics and Plasma Physics group
Investigated algorithm for learning many-body interaction systems from time-series data using graphical models

AMS Mathematics Research Communities *June 2023*
Topic on Complex Social Systems
Collaborative group project led by Dr. Heather Z. Brooks and Dr. Philip S. Chodrow
Developed likelihood-based methods to infer interaction structure in opinion dynamics

Oak Ridge National Laboratory *June 2022 - August 2022*
NSF Mathematical Sciences Graduate Internship
Supervised by Dr. Pablo Moriano, Computer Science and Mathematics Division
Studied the robustness of network community structure under addition of edges using data science

Dickinson College *September 2018 - May 2019*
Honors project in mathematics
Advised by Dr. David Richeson, Department of Mathematics & Computer Science
Used various algebraic descriptions of the annular braid group to analyze maypole dancing

Physics senior research
Advised by Dr. Lars Q. English, Department of Physics & Astronomy
Investigated symmetry breaking in coupled logistic maps through experimental realization on electronic circuit

Experience

SAS Institute *May 2023 - August 2023 & January 2024 - May 2024*
Investigated Functional Principal Component Analysis (FPCA) methods and its applications in IoT

Publications

M Tian and P Moriano, *Robustness of Community Structure under Edge Addition*, Physical Review E **108** (2023), 054302

M Tian, JJ Bramburger, and B Sandstede, *Snaking Bifurcations of Localized Patterns on Ring Lattices*, IMA Journal of Applied Mathematics (2021), hxab023

H Mhiri, **M Tian**, E Wynne, S Jones, A Mareno, and LQ English, *An Experimental Survey of Chaos and Symmetry Breaking in Coupled and Driven Logistic Maps*, European Journal of Physics **40** (2019), no. 6, 065802

Teaching Experience

Spring 2021 **Applied Ordinary Differential Equations**, Teaching Assistant, Brown University
Led interactive recitation sessions, held office hours, and graded homework and exams

Fall 2020 **Operations Research: Deterministic Models**, Teaching Assistant, Brown University
Held tutorial sessions and office hours for the class, prepared solutions, and graded homework and exams

Fall 2020 **Sheridan Center Certificate I: Reflective Teaching**, Brown University
Introductory seminar in a cross-disciplinary setting that helps develop and refine fundamental, evidence-based teaching skills and strategies

2017 - 2019 **Quantitative Reasoning Center**, Dickinson College
Tutored college entry-level math, physics and economics students and classes

2016 - 2019 **Math Help Room**, Dickinson College
Tutored walk-in students from college entry-level mathematics classes

Fall 2017 **Introduction to Calculus**, Teaching Assistant, Dickinson College
Facilitated students' questions during lab sessions for the class, graded homework, and helped prepare practice problems for review

Fall 2016 & Fall 2018 **Single Variable Calculus**, Teaching Assistant, Dickinson College
Facilitated students' questions during lab sessions for classes, and graded homework

Honors and Awards

2023 **SIAM Student Travel Awards**
Support students to attend and present at SIAM conferences

2019 **James Fowler Rusling Prize**
Presented to a member of the senior class whose scholarly achievements have been judged most superior by the All-College Committee on Academic Program and Standards

The Lance E. Kohlhaas Memorial Prize in Mathematics
Awarded to a graduating mathematics major who has demonstrated excellence in that field and shows promise in an actuarial or mathematics career

2018 **The Caroline Hatton Clark Mathematics Scholarship**
Awarded for outstanding achievement in mathematics

2017 **The Henry P. Cannon Memorial Prize**
Awarded to a member of the sophomore class who excels in mathematics

The Junior Class Sophister Prize
Awarded to the junior with the highest academic ranking at the start of the academic year

2016 **The John Patton Memorial Prize**
Awarded to a rising sophomore for high scholastic standing

Professional Organizations

American Mathematical Society
Society for Industrial and Applied Mathematics
Phi Beta Kappa Honor Society
Pi Mu Epsilon National Honorary Mathematics Society
Sigma Pi Sigma National Physics Honor Society
Alpha Lambda Delta Honor Society

Presentations

Talks

2024 **2024 Joint Mathematics Meetings (JMM 2024)**
Inferring Interaction Kernels for Stochastic Agent-Based Opinion Dynamics, San Francisco, CA, January, 2024

2023 **SIAM Conference on Applications of Dynamical Systems (DS23)**
Localized Patterns on Graphs, Portland, OR, May, 2023

2022 **SIAM Workshop on Network Science (NS22)** (virtual) - Lightning Talk
How Robust are Communities in Temporal Networks? A Comparative Analysis Using Community Detection Algorithms, September, 2022

2022 **Jane Street's Symposium** (virtual)
Localized Patterns on Ring Lattices, January, 2022

2021 **Graduate Seminar**
Localized Patterns on Symmetric Coupled Rings - The Influence of Interaction Length on Pattern Formation, Brown University, Providence, RI, December, 2021

2021 **Brown / BU / UMass Dynamics & PDE Seminar**
Snaking Bifurcations of Localized Patterns, University of Massachusetts Amherst, Amherst, MA, November, 2021

2019 **Mathematics Honors Presentation**
Maypole Braids: An Analysis Using the Annular Braid Group, Dickinson College, Carlisle, PA, April, 2019

2019 **Physics Senior Research Talks**
Bifurcation, Symmetry Breaking, and Synchronization in a Coupled-Logistic Map Circuit, Dickinson College, Carlisle, PA, April, 2019

Posters

2024 **2024 Dynamics Days US**
Efficient Learning of Models for Temporal Networks, Davis, CA, January, 2024

2023 **Mathematical Opportunities in Digital Twins (MATH-DT) Workshop**
Community Robustness under Edge Addition in Synthetic and Empirical Temporal Networks, George Mason University, Fairfax, VA, January, 2023

2023 **Dynamics Days US 2023** (virtual)
Community Robustness in Temporal Networks under Edge Addition, January, 2023

2021 **SIAM Conference on Applications of Dynamical Systems (DS21)** (virtual)
Snaking Bifurcations of Localized Patterns on Ring Lattices, May, 2021

2019 **34th Annual All Science Symposium**
1. *Maypole Braids: An Analysis Using the Annular Braid Group*
2. *Using LabView to Explore Symmetry Breaking in a Coupled Logistic Map Circuit*, Dickinson College, Carlisle, PA, April, 2019

2019 **American Physical Society March Meeting 2019**
Using an Arduino in a Coupled Logistic Map Circuit to Explore Basins of Attraction for Symmetry-Broken States, Boston, MA, March, 2019

Workshops and Summer Schools Attended

2023 American Mathematical Society Mathematics Research Communities 2023 on Complex Social Systems, Java Center, NY, June 18 - June 24, 2023

2023 Women in Network Science Collabathon, group project on topic modeling, Northeastern University, May 1 - May 5, 2023

2022 Fall 2022 Data Science Boot Camp, group project on English language proficiency evaluation model, the Erdős Institute, September - December, 2022 (virtual)

2022 OLCF Summer Hands-On High Performance Computing Course, Certificate of Completion, Oak Ridge National Laboratory, July 2022 (virtual)

2022 May 2022 Data Science Boot Camp, group project on predicting chocolate ratings with feature engineering, the Erdős Institute, May 9 - June 4, 2022 (virtual)

2021 ICERM Workshop: Geometric and Topological Methods in Data Science, Brown University, December 16 - 17, 2021

2020 IMSD Module: Introduction to Statistical Analysis of Data 2020, Brown University, November 5, 12 and 19, 2020 (virtual)

2020 IMSD Module: Scientific Presentations, Brown University, June 4, 5 and 11, 2020 (virtual)

2018 Budapest Semesters in Mathematics Program, completed with honors, Budapest, Hungary, Summer 2018

Outreach and Service

2021 - 2023 **APMA Diversity, Equity, and Inclusion Committee**, Brown University
Attended bi-weekly meetings and developed plans and projects to improve climate and increase diversity and inclusion in the Division of Applied Mathematics

2021 - 2023 **Brown SIAM Student Chapter Executive Board**, Brown University
Kept record for organizational plans and helped facilitate on-campus events

2021 - 2023 **Sheridan Center Departmental Graduate Student Liaison**, Brown University
Maintained communications and forwarded events information between the Sheridan Center for Teaching and Learning and the Division of Applied Mathematics

Fall 2021 **Brown Division of Applied Mathematics - Directed Reading Program**, Brown University
Mentored an undergraduate student on mathematical optimal control theory and applications

Summer 2020 **5-week Undergraduate Program in Experimental Math**, Brown University
Supervised a team of 3 undergraduate students on studying the dynamics and patterns of graphing fleas

2019 - 2020 **Brown Applied Math Undergraduate/Graduate Mentoring Program**
Mentored an undergraduate student with regards to study plans and academic/career goals

2016 - 2019 **Math & CS Major's Committee**, Dickinson College
Gave feedback on personnel reviews and provided a student voice in departmental issues

Graduate Coursework

Real Function Theory
Theory of Probability
Nonlinear Dynamical Systems: Theory and Applications
Numerical Solution of Partial Differential Equations
Deep Learning
Partial Differential Equations
Topology
Recent Applications of Probability and Statistics
Graphs and Networks
Advanced Probabilistic Methods in Computer Science
Language Processing in Humans and Machines

Skills

Programming and Lab: Python, Julia, MATLAB, R, SAS (Certified Specialist), Maple, Mathematica, Igor Pro, Logger Pro and LabView
Tools: High performance computing, parallel computing, Git, Google Colab, Jupyter, LaTeX, numpy, pandas, scikit-learn, PyTorch, TensorFlow, BERT, NLTK, word2vec
Languages: Mandarin(native), Japanese(fluent; Japanese Language Proficiency Test N1 Certificate) and German (elementary)

Dedication

To my Mom, Fengqin Yu, and Dad, Ye Tian, for inspiring and supporting me from childhood to develop interests and pursue my passions in life.

Acknowledgments

I would like to extend my deepest gratitude to my thesis advisor, Dr. Björn Sandstede, for his guidance and support throughout my graduate studies. His academic conduct, advising style, and teaching standards have served as my role model for being a respectful researcher, mentor, and teacher. I am immensely thankful for the invaluable advice and encouragement he has provided, which have been pivotal in my research and professional development during my time in graduate school.

I would also like to express gratitude to Dr. Jason Bramburger for our fruitful collaboration and his consistent support over the years. My sincere thanks go to Dr. Matthew Harrison as well, for his insightful consultations and for his role on my committee.

Furthermore, I wish to thank my collaborators and mentors, Dr. Pablo Moriano, Dr. Heather Zinn Brooks, Dr. Phil Chodrow, Dr. Andrey Lokhov, and Dr. Abhijith Jayakumar, for the enriching research experience and career advice. I am equally grateful to my research project teammates and my peers in the AMS MRC cohort.

Last but not least, I am grateful to have shared my graduate school experience with an exceptional cohort of students in the Division of Applied Mathematics and the remarkable peers in the Sandstede research group. I am also thankful to my family and friends for their unwavering support.

Contents

List of Tables

List of Figures

Chapter One

Introduction

1 Patterns in Network Dynamics

Real-world systems, such as those in social, physical, and biological domains, often manifest as networks characterized by dynamic processes. These involve interactions among entities and the evolution of the networks over time. For instance, in a social context, diseases, opinions, or beliefs propagate through human contact networks Keeling and Eames (2005), Noorazar et al. (2020); in magnetism, the interplay among spins follows an underlying graph structure, and such models, along with the corresponding physical laws, elucidate the dynamics of spin configurations over time Glauber (1963); in cellular biology, gene expression levels are governed by molecular interactions within regulatory networks, leading to models that capture system behaviors and aid experiments Bressloff (2021). In the study of these complex systems, mathematical analysis of network dynamics has played an important role in uncovering the fundamental mechanisms and correlations due to the structures and functions, enhancing our ability to more accurately model, predict, and control systems in these applications.

One important aspect in the field of network dynamics is the study of *patterns*, which appear in natural, physical, and social network systems in diverse ways. In different problem settings, these patterns can refer to distinct mathematical objects, depending on the objectives of interest. This thesis explores the impact of graph structures on emergent patterns in network dynamics from two distinct perspectives: the dynamical systems analysis of stationary patterned states and the computational analysis of the robustness of communities discovered from data. These two viewpoints on the pattern analysis problem highlight the differences between model-driven and data-driven approaches, respectively. Here, we provide a brief introduction to each of these two projects and discuss them in full detail in Chapters 2 through 4.

2 Bifurcation of Patterns on Networks

Localized patterns have been observed in various applications, including ferrofluid experiments Richer and Barashenkov (2005), vegetation models Meron (2018), and urban crime spots SHORT et al. (2008). Figure 1.1 showcases some of these instances. These patterns are characterized by two distinct coexisting states and are present in systems governed by reaction-diffusion equations with bistable nonlinearity.

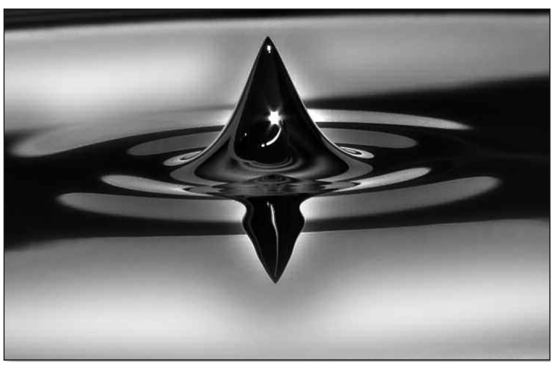

Ferrosoliton in ferrofluids. Source: Richter, Reinhard (2011)

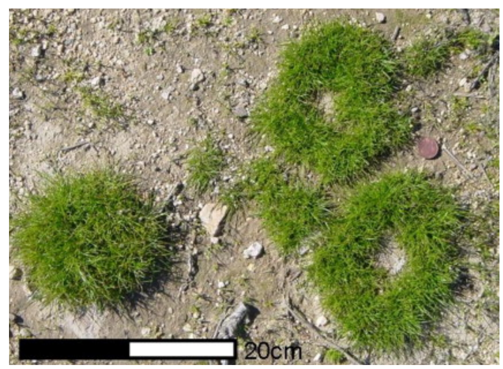

Ring patterned grass. Source: Sheffer et al. (2007)

Figure 1.1: Example of patterns in experiments and in nature.

Observations of snaking bifurcations of patterns, from both experiments and models Groves et al. (2017), Chong et al. (2009), have inspired decades of research into snaking. Previous research in the field spans from spatially extended systems modeled by partial differential equations (PDEs) to those on regular, spatially discrete spaces Lloyd et al. (2008), Bramburger (2020), Bramburger and Sandstede (2020a). However, the behavior of localized patterns within less regular graph structures remains less explored. Motivated by the findings of McCullen and Wagenknecht (2016), where snaking was observed in computational models on random networks, we aim to analytically investigate how graph structures influence the bifurcation of localized patterns.

2.1 Snaking Bifurcation of Localized Patterns on Rings

In this initial investigation into how graph structures influence the existence curves of localized patterns with varying system parameters using dynamical systems analysis, we concentrate on a simple graph with a controllable interaction length. We study a reaction-diffusion system with bistable nonlinearity, imposed on symmetrically coupled rings. Here, the number of nearest neighbors connected to each node is controlled by a specific parameter. By altering this interaction length parameter, we explore various coupling regimes and analyze the connections of patterned states in these different scenarios.

We present analytical findings for sparse coupling scenarios, specifically nearest-neighbor and next-nearest-neighbor couplings, as well as for all-to-all coupling. We prove that in the case of sparse coupling, the bifurcation diagram of stationary solutions forms a snaking curve where the number of folds increases with the number of elements on the graph, while for all-to-all coupling, the bifurcation is always a closed curve with six nodes, which begins and ends at two symmetry-breaking bifurcations from the homogeneous solution branch, near the two opposite extremities of the system's bifurcation parameter domain.

2.2 Bifurcation from Homogeneous States on Rings

One remaining question from our work on the snaking bifurcation of localized patterns in symmetrically coupled ring systems concerns the ending points of the snaking curve: it is unclear whether these ends simply terminate or if they are connected to other solution branches and bifurcate from them. The study of symmetry-breaking bifurcation from homogeneous solutions has long been a classical theme in the field of dynamical systems, with commonly used standardized techniques. Interested readers may find references in Golubitsky et al. (1988), Pismen (2023), Hoyle (2006). This motivates our investigation into the homogeneous solution branch and the bifurcations from it. By doing so, we can then verify whether these branches of solutions, which bifurcate from the homogeneous solutions, match with the snaking curve, thus providing a way to address our question.

In particular, for our approaches, we utilize the fact that our ring system exhibits dihedral symmetry and employ equivariant bifurcation theory to analyze bifurcations from the homogeneous branch. We show that branches of patterned states emerge from these homogeneous branches and that they connect with the snaking branch of patterned states numerically. Interestingly, we also find that the criticality of these branches transitions from supercritical to subcritical at a specific value of the degree of coupling for any given number of elements in the ring, N. Additionally, we consider the limiting case as N goes to infinity and provide analytical computations that predict the changing point in bifurcation criticality in relation to the ratio of coupling degree over N for this case.

3 Community Robustness

In many cases, we possess data from empirical complex network systems – such as measurements from critical infrastructures, recordings from biological networks, and survey results from social groups. These datasets exhibit network structures, but usually the underlying dynamics are unknown. In such scenarios, model-driven analysis becomes less feasible. Computational methods, on the other hand, can uncover important characteristics of the system's structure and functionality more adeptly, specific to the observed system. One key network property that is identifiable from data is known as *communities*, which represent patterns that carry essential functional information, showing the groupings where nodes within the same group tend to be more densely connected to each other than to nodes in different groups Fortunato (2010).

Since real networks change dynamically, it is reasonable to anticipate that the underlying community structures also evolve over time. Consequently, the concept of community *robustness* captures the interest of researchers and gains importance in the field Karrer et al. (2008). Specifically, community robustness pertains to the resilience of a community structure to network perturbations. So far, research on community robustness has predominantly concentrated on perturbations such as the rewiring of edges or the removal of nodes or edges Wang and Liu (2019), Albert et al. (2000). The impact of network densification on community robustness, however, remains underexplored, despite being identified as a significant characteristic of many social network systems Leskovec et al. (2005). Moreover, considering the addition of edges is crucial for simulating and analyzing errors, especially for the case when false edges erroneously appear in data, which is a common type of measurement error in social datasets Wang et al. (2012).

Our work focuses on understanding how the community robustness is affected by edge-addition perturbation to the networks. We propose different edge-addition strategies and analyze their effects in both synthetic and empirical temporal networks through computational experiments. These experiments utilize community detection algorithms and community similarity metrics. We find that the robustness of communities depends strongly on the choice of community detection method.

4 Outline and Overview

Chapters 2 and 4 are largely adapted, with minor edits and additions, from the papers cited at the beginning of each chapter Tian et al. (2021), Tian and Moriano (2023).

In Chapter 2, we analyze the existence curves of localized patterns in symmetrically coupled ring systems across different coupling regimes. Specially, we prove that for sparse coupling, the localized patterns are connected through a snaking curve, whereas for all-to-all coupling, the bifurcation forms a closed curve. This work was conducted in collaboration with Dr. Björn Sandstede and Dr. Jason Bramburger. Chapter 3 then delves into the ending points of snaking bifurcation curves, further exploring an open question introduced in Chapter 2. We show that the snaking curves bifurcate from the homogeneous solution branch and analyze the criticality of such bifurcations. This second part was a collaborative work with Dr. Björn Sandstede.

Chapter 4 introduces a computational methodology to study the robustness of community structures in networks under different edge-addition perturbations, using synthetic and empirical data. We highlight our primary finding that the choice of community detection method significantly influences community robustness. This research was in collaboration with Dr. Pablo Moriano.

Chapter Two

Snaking Bifurcations of Localized Patterns on Ring Lattices

This chapter is based on work presented in Tian et al. (2021).

1 Introduction

We study the structure of stationary patterns in bistable lattice systems. More precisely, we take a ring of $N \geq 3$ identical nodes and consider the lattice dynamical system

$$\dot{u}_n = d(\Delta_m U)_n + f(u_n, \mu), \quad 1 \leq n \leq N, \quad U = (u_1, u_2 \ldots, u_N) \in \mathbb{R}^N \tag{2.1}$$

on this ring for small coupling strength $0 < d \ll 1$, where $f(u, \mu)$ is a bistable nonlinearity, and the coupling operator Δ_m denotes the symmetric m-nearest-neighbour connections on the ring that we describe in more detail below. We refer to Figure 2.1 for an illustration of typical nonlinearities and the coupling structures we consider in this chapter. Throughout this chapter, we will use the notation $U = (u_1, u_2 \ldots, u_N) \in \mathbb{R}^N$ and will always take all indices in the set $\{1, \ldots, N\}$ modulo N so that, for instance, $u_{N+1} = u_1$ and $u_{-1} = u_N$. With these conventions, the coupling operator in the case $m = 1$ is the usual discrete diffusive (nearest-neighbour) operator

$$(\Delta_1 U)_n = u_{n+1} + u_{n-1} - 2u_n,$$

the case $m = 2$ results in the next-nearest-neighbour coupling

$$(\Delta_2 U)_n = u_{n+2} + u_{n+1} + u_{n-1} + u_{n-2} - 4u_n,$$

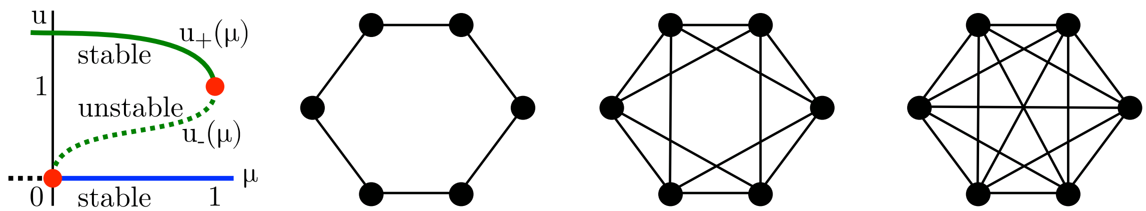

Figure 2.1: The left panel illustrates the zero set $\{(u,\mu) : f(u,\mu) = 0\}$ of a typical bistable nonlinearity $f(u,\mu)$ with two stable states at $u = 0$ and $u = u_+(\mu)$ and an unstable state at $u = u_-(\mu)$. The three rightmost panels contain graphs that consist of $N = 6$ identical nodes with (from left to right) nearest neighbour, next-nearest neighbour, and all-to-all coupling, respectively.

and the general case is given by

$$(\Delta_m U)_n = \begin{cases} -(2m+1)u_n + \sum_{j=-m}^{m} u_{n+j}, & 1 \le m < \lfloor \frac{N}{2} \rfloor \\ -N u_n + \sum_{j=1}^{N} u_j, & m = \lfloor \frac{N}{2} \rfloor. \end{cases}$$

We refer to the case $m = \lfloor \frac{N}{2} \rfloor$ as all-to-all coupling as each element on the ring is connected to all other elements.

Our goal is to understand how the arrangement of stationary patterns in the (u,μ) configuration space depends on the interaction length m of the coupling on the ring. Steady states of (2.1) correspond to solutions to the system

$$\mathcal{F}(U,\mu,d) = 0 \tag{2.2}$$

where

$$\mathcal{F} : \mathbb{R}^N \times \mathbb{R} \times \mathbb{R} \longrightarrow \mathbb{R}^N, \quad (U,\mu,d) \longmapsto \mathcal{F}(U,\mu,d), \quad \mathcal{F}(U,\mu,d)_n = d(\Delta_m U)_n + f(u_n,\mu).$$

We focus on the case $0 < d \ll 1$, which allows us to exploit the anti-continuum limit $d = 0$ when the system (2.2) is uncoupled. Setting $d = 0$ and choosing $\mu \in (0,1)$, we select the solution of (2.2) for which u_1 lies on the upper stable branch $u = u_+(\mu)$

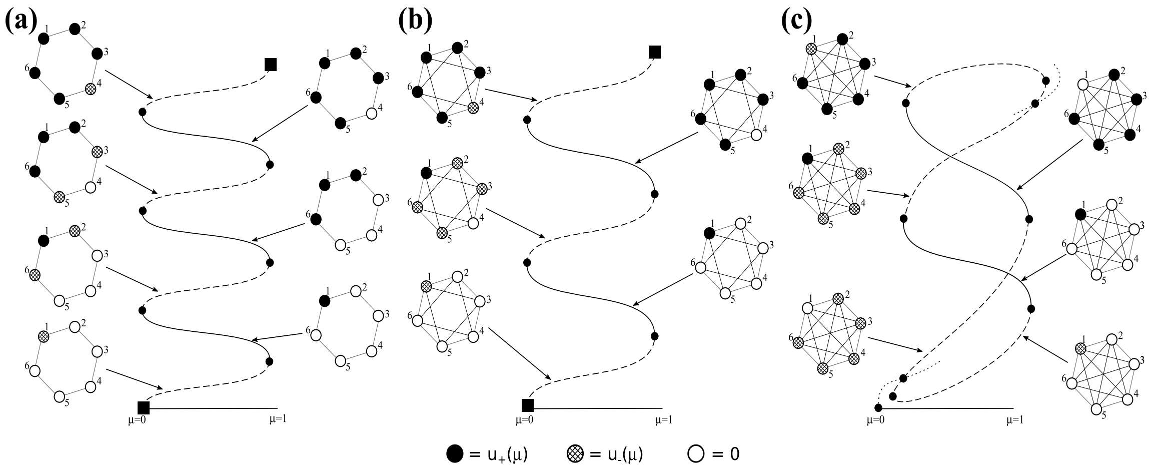

Figure 2.2: Different bifurcation curves depending on the number of symmetric connections over a six element ring. (a) Nearest-neighbour connections lead to a typical snaking bifurcation diagram, as is proven in Theorem 1, (b) Next-nearest-neighbour connections on a six element ring introduce a further symmetry for which the elements indexed by 2,3,5,6 bifurcate together near $\mu = 0$, as proven in Theorem 2. (c) In the case of all-to-all coupling, the system is invariant with respect to any permutation of the nodes on the ring and so the bifurcation curves form a small closed curve that bifurcates from the homogeneous state (dotted curve) near the origin, as proven in Theorem 4. Squares marking the end of the curves in panels (a) and (b) represent the set of exceptional bifurcations which are not proven in this chapter.

and the remaining nodes u_j with $j \neq 1$ lie on the lower stable branch $u = 0$ of the zero set of $f(u, \mu)$; see Figure 2.1 for an illustration of the zero set of $f(u, \mu)$. We are then interested in describing the connected component of the solution set $\{(U, \mu, d) : \mathcal{F}(U, \mu, d) = 0\}$ that this solution belongs to and understand how this connected component changes as the interaction range m varies.

For $m = 1$ and each fixed value of $0 < d \ll 1$, we will show that solutions are arranged in a "snaking" pattern (see Figure 2.2(a)): starting with a configuration where one node is set to $u_+(\mu)$ and all other nodes are set to zero, we show that the solution branch exhibits fold bifurcations at which the number of nodes that are close to $u_+(\mu)$ increases until all nodes are equal to $u_+(\mu)$. Snaking has first been conjectured in Pomeau (1986) for spatially extended systems modelled by partial differential equations (PDEs) on the real line and was first investigated rigorously in the seminal work Woods and Champneys (1999); see also (Coullet et al., 2000) for related work. Since then, snaking for PDEs in one and two space dimensions has been analyzed extensively, and we refer, for instance, to (Avitabile et al., 2010, Beck et al., 2009, Burke and Knobloch, 2006, 2007, Chapman and Kozyreff, 2009, Kozyreff and Chapman, 2006, Lloyd et al., 2008) and the reviews (Dawes, 2010, Knobloch, 2015). Many of these investigations were motivated by the observation of snaking patterns in experiments and models, including in ferrofluids Groves et al. (2017), Lloyd et al. (2015), Richer and Barashenkov (2005), optical systems Chong et al. (2009), Gomila et al. (2007), Firth et al. (2007), and vegetation models Meron (2018), to name but a few. Similarly complex bifurcation structures of localized solutions have also been observed in spatially discrete systems posed on integer lattices in Chong et al. (2009), Chong and Pelinovsky (2011), Kusdiantara and Susanto (2019), McCullen and Wagenknecht (2016), Papangelo et al. (2017), Kusdiantara and Susanto (2017), Taylor and Dawes (2010), Yulin and Champneys (2010, 2011) and were explained in part by Bramburger (2020), Bramburger and Sandstede (2020a,b). While the latter works have explained the bifurcation structure of localized solutions on "regular" graphs, such as the integer lattices, little is known about how graph structure and connection topology influence the connections of localized solutions in parameter space.

Motivated by these previous investigations, we explore here the role of different finite interaction lengths and the effect of boundaries on snaking patterns in lattice systems. Focusing on ring lattices allows us to address these questions together. We will provide analytical results for two distinct coupling regimes, namely sparse coupling (with nearest-neighbour and next-nearest-neighbour coupling) and all-to-all coupling. We will prove that the resulting bifurcation curves differ significantly as illustrated in Figure 2.2: sparse coupling leads to snaking curves with many fold bifurcations (the number will increase as the number of nodes, N, increases), while all-to-all coupling will always result in a curve with six saddle nodes and two symmetry-breaking bifurcations near $\mu = 0$ and $\mu = 1$ from the branch of equilibria at which all nodes are equal to the unstable state $u_-(\mu)$. We also provide illustrative examples in the case of almost all-to-all coupling where additional symmetries in the system result in entirely unique bifurcation curves that would be difficult to predict. We conjecture that sparse coupling will lead to snaking curves that exhibit $\lfloor \frac{N}{2} \rfloor$ saddle nodes for each m with $1 \leq m \leq \lfloor \frac{N}{2} \rfloor - 2$ (thus excluding almost all-to-all coupling).

2 Main results

Recall that we are interested in the solution structure of the system

$$\dot{u}_n = d(\Delta_m U)_n + f(u_n, \mu), \quad 1 \leq n \leq N. \tag{2.3}$$

First, note that system (2.3) is equivariant with respect to the dihedral symmetry group D_N, generated by the actions

$$\begin{aligned} \zeta(u_1, u_2, \ldots, u_N) &= (u_2, \ldots, u_N, u_1) \\ \kappa(u_1, u_2, u_3, \ldots, u_{N-1}, u_N) &= (u_1, u_N, u_{N-1}, \ldots, u_3, u_2) \end{aligned} \tag{2.4}$$

which define rotations and flips of the ring, respectively. Clearly $\zeta^N = 1$ and $\kappa^2 = 1$, where we use 1 to denote the identity element that acts trivially on vectors in $\mathbb{R}^N$. Our interest in what follows will lie in solutions of (2.3) that are invariant with respect to the action of κ. Notice that the action of κ on rings with N even leaves exactly two elements fixed, while when N is odd only the element at index 1 is fixed. We

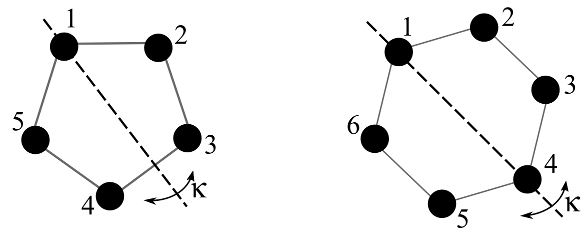

Figure 2.3: Action of the flip κ on odd and even element rings. On the left is a ring of $N = 5$ elements, for which the flip leaves only the element at index 1 fixed, while the right presents a ring of $N = 6$ elements, for which the flip leaves the elements at index 1 and 4 fixed.

refer the reader to Figure 2.3 for a demonstration of these two cases with $N = 5, 6$. Finally, in the case of all-to-all coupling, system (2.3) is equivariant with respect to the symmetric group S_N of permutations on N elements, which is a strictly larger class of symmetries than those for all other classes of coupling functions considered in this chapter.

Here the function f is assumed to be bistable, satisfying the same properties as in Bramburger and Sandstede (2020b). We summarize these properties in the following hypothesis; see also Figure 2.1.

Hypothesis 1. *The function $f : \mathbb{R} \times \mathbb{R} \to \mathbb{R}$ is smooth and satisfies the following:*

(i) The function f is odd in u so that $f(-u, \mu) = -f(u, \mu)$ for all (u, μ).

(ii) The set of roots of $f(u, \mu)$ is as shown in the left panel of Figure 2.1. In particular, for each $\mu \in (0, 1)$, the function $f(u, \mu)$ has exactly three nonnegative zeros, namely $u = 0$ and $u = u_\pm(\mu)$ with $0 < u_-(\mu) < u_+(\mu)$, and these satisfy $f_u(0, \mu), f_u(u_+(\mu), \mu) < 0 < f_u(u_-(\mu), \mu)$.

(iii) At $\mu = 0$, the zeros $u = 0$ and $u = \pm u_-(\mu)$ collide in a generic subcritical pitchfork bifurcation.

(iv) At $\mu = 1$, the zeros $u = u_\pm(\mu)$ collide in a generic saddle-node bifurcation at $u = 1$.

Our assumption (iv) that the saddle-node bifurcation at $\mu = 1$ occurs at $u = 1$ is for convenience only as this can always be achieved through an appropriate change of variables. We also note that all of our analysis can be applied to bistable functions for which the bifurcation at $\mu = 0$ or $\mu = 1$ is instead a transcritical bifurcation, as was shown to be true in Bramburger and Sandstede (2020b). To precisely state our results we instead focus on functions satisfying Hypothesis 1 with the prototypical example being the cubic-quintic nonlinearity

$$f(u, \mu) = -\mu u + 2u^3 - u^5. \tag{2.5}$$

This type of nonlinearity appears naturally from the study of optical solitons in cubic-quintic nonlinear Schrödinger lattices Chong et al. (2009), Chong and Pelinovsky (2011) and it serves as a simple solid example for analysis that gives rise to snaking localized patterns. Throughout this chapter, we detail our results on localized pattern formation in the lattice system (2.3) with functions f satisfying Hypothesis 1 based on the value of m. In the statement of our proofs we will adopt the notation $\mathcal{B}_\delta(X)$ to denote an open set of all points within distance $\delta > 0$ from the set X. All proofs will be left to Section 3.

2.1 Sparse coupling

We begin with the case of "sparse" coupling, i.e. $m \ll \lfloor N/2 \rfloor$. In particular, we will focus on the cases of $m = 1, 2$ to show that localized solutions grow around the ring in the form of a snaking bifurcation curve with the region of activation growing symmetrically around the ring as one ascends the diagram, as is illustrated in panel (a) of Figure 2.2. Since we are interested in solutions which are invariant with respect to the action of κ, we can restrict our attention to the index set

$$I = \left\{1 \leq n \leq \left\lfloor \frac{N}{2} \right\rfloor + 1\right\} \tag{2.6}$$

for any fixed $N \geq 2$. Indeed, an element $U \in \mathbb{R}^N$ satisfying $\kappa U = U$ is uniquely identified by elements with indices belonging to I. The reader is referred to Figure 2.3, where we see that when $N = 5$ we have $I = \{1, 2, 3\}$ and the elements at indices $4, 5$ are identical to those at $3, 2$, respectively. Similarly, from Figure 2.3, when $N = 6$ we have $I = \{1, 2, 3, 4\}$ and the elements at indices $5, 6$ are identical to those at $3, 2$, respectively.

Hypothesis 1 implies that any nonnegative solution of (2.2) with $d = 0$ must have $u_n \in \{0, u_\pm(\mu)\}$ when $\mu \in [0, 1]$. We use k to specify nodes that are activated at $u_+(\mu)$. Then, for each $0 \leq \mu \leq 1$ and $k \in I$ we define the elements $\bar{U}^{(k)}(\mu) = \{\bar{u}_n^{(k)}(\mu)\}_{n\in I}$ and $\bar{V}^{(k)}(\mu) = \{\bar{v}_n^{(k)}(\mu)\}_{n\in I}$ by

$$\bar{u}_n^{(k)}(\mu) = \begin{cases} u_+(\mu) & 1 \leq n \leq k \\ 0 & n > k \end{cases} \tag{2.7}$$

and

$$\bar{v}_n^{(k)}(\mu) = \begin{cases} u_+(\mu) & 1 \leq n < k \\ u_-(\mu) & n = k \\ 0 & n > k \end{cases} \tag{2.8}$$

for all $n \in I$ and $\mu \in [0, 1]$. Notice that when $k = \lfloor N/2 \rfloor + 1$ we have that $\bar{U}^{(k)}$ is a uniform state with all entries given by $u_+(\mu)$. From the discussion above, we have that these elements can be extended to κ-invariant solutions of (2.2) by having u_n for $n \notin I$ be defined by the relation $\kappa U = U$.

The elements (2.7) and (2.8) are pairwise distinct when $\mu \in (0,1)$, but Hypothesis 1 gives that $\lim_{\mu\to 0^+} u_-(\mu) = 0$ and $\lim_{\mu\to 1_-} u_-(\mu) = u_+(1)$, and so the patterns (2.7) and (2.8) satisfy

$$\begin{aligned} \bar{U}^{(k-1)}(0) &= \bar{V}^{(k)}(0), \quad k = 2, \dots, \left\lfloor \frac{N}{2} \right\rfloor + 1 \\ \bar{U}^{(k)}(1) &= \bar{V}^{(k)}(1), \quad k = 1, \dots, \left\lfloor \frac{N}{2} \right\rfloor \end{aligned} \tag{2.9}$$

at the parameter boundaries $\mu = 0, 1$. We can therefore define the connected set

$$\Gamma_{\text{sparse}} := \bigcup_{k\in I} \bigcup_{0\le\mu\le 1} \{(\bar{U}^{(k)}(\mu), \mu), (\bar{V}^{(k)}(\mu), \mu)\} \subset \mathbb{R}^N \times [0,1], \tag{2.10}$$

which represents the union of the curves traced out for $\mu \in [0,1]$ by the patterns (2.7) and (2.8) of (2.2) when $d = 0$. We will also define the exceptional set $\mathcal{E}$, given by

$$\mathcal{E} := \{\bar{V}^{(1)}(0)\} \cup \{\bar{V}^{(\lfloor \frac{N}{2} \rfloor + 1)}(1)\}, \tag{2.11}$$

representing the endpoints of the curve Γ_{sparse}. We present the following theorem, for which Figure 2.2(a) provides an illustration of the results for $(N, m) = (6, 1)$. The proofs for $m = 1$ are left to Section 3.1 and $m = 2$ are left to Section 3.2.

Theorem 1. *Assume that f satisfies Hypothesis 1. If $N \ge 4$ and $m = 1$ or $N \ge 7$ and $m = 2$, then for each $\delta_* > 0$ there exists $d_* > 0$ such that for each $0 < d < d_*$ the set $\mathcal{B}_{\delta_*}(\Gamma_{\text{sparse}}) \setminus \mathcal{B}_{2\delta_*}(\mathcal{E})$ contains a unique, nonempty, continuous branch of κ-symmetric solutions of the steady-state system (2.2). Furthermore, this branch is smooth and C^1-close to Γ_{sparse} for each d, depends smoothly on d, and its limit as $d \to 0^+$ is contained in Γ_{sparse}.*

2.2 Almost all-to-all coupling

Notice that in the statement of Theorem 1 we were required to take $N \geq 7$ when $m = 2$ to obtain the snaking bifurcation curves of localized solutions similar to those with $m = 1$. This is because when N is even and $m = \lfloor \frac{N}{2} \rfloor - 1$, new symmetries are introduced into the model. This has the effect that the resulting bifurcation diagram is markedly different than the usual snaking diagram for sparse coupling, while also being distinct from the fully symmetric case of all-to-all coupling covered in the following subsection. It appears that many of these bifurcations curves must be understood on a case-by-case basis for varying N, and so instead of attempting to exhaustively document all of these cases, we opt to illustrate with two specific examples. The cases detailed here will take $N = 6, 8$, representing the smallest ring sizes where these atypical bifurcation diagrams can be observed.

Let us begin with $N = 6$. Much of the bifurcation structure in the case when $(N, m) = (6, 2)$ is similar to that of the case when $N \geq 7$ and $m = 2$, with the following exception: the connection from the continued solutions of $\bar{U}^{(1)}(\mu)$ to $\bar{V}^{(2)}(\mu)$, defined in (2.7) and (2.8), respectively, near $(d, \mu) = (0, 0)$ is not present. This connection is replaced by a connection from the continued solutions of $\bar{U}^{(1)}(\mu)$ to the branch continued from the solution $\bar{W}^{(23)}(\mu)$, given by

$$\bar{w}_n^{(23)} = \begin{cases} u_+(\mu) & n = 1 \\ u_-(\mu) & n = 2, 3 \\ 0 & n = 4 \end{cases} \tag{2.12}$$

for each $\mu \in [0,1]$. Since the solution $\bar{W}^{(23)}(\mu)$ satisfies

$$\lim_{\mu\to 0^+} \bar{W}^{(23)}(\mu) = \bar{U}^{(1)}(0) \quad \text{and} \quad \lim_{\mu\to 1^-} \bar{W}^{(23)}(\mu) = \bar{U}^{(3)}(1),$$

we may define the connected set

$$\Gamma_{6,2} := \bigcup_{0\le\mu\le 1} \{(\bar{V}^{(1)},\mu),(\bar{U}^{(1)},\mu),(\bar{W}^{(23)},\mu),(\bar{U}^{(3)},\mu),(\bar{V}^{(4)},\mu)\} \subset \mathbb{R}^6 \times [0,1]. \quad (2.13)$$

Using again $\mathcal{E}$ defined in (2.11), this leads to the following theorem whose results are presented visually in Figure 2.2(b). The proof is left to Section 3.3.

Theorem 2. *Assume that f satisfies Hypothesis 1 and that $(N,m) = (6,2)$. Then for each $\delta_* > 0$ there exists $d_* > 0$ such that for each $0 < d < d_*$ the set $\mathcal{B}_{\delta_*}(\Gamma_{6,2})\backslash\mathcal{B}_{2\delta_*}(\mathcal{E})$ contains a nonempty, continuous branch of κ-symmetric solutions of the steady-state system (2.2). Furthermore, this branch is smooth and C^1-close to $\Gamma_{6,2}$ for each d, depends smoothly on d, and its limit as $d \to 0^+$ is contained in $\Gamma_{6,2}$.*

Turning now to the case $(N,m) = (8,3)$, we are required to define two more patterns which correspond to κ-invariant solutions of (2.2) with $d = 0$. Consider the elements $\bar{W}^{(24)}_{\pm}(\mu)$ and $W^{(3)}_{-}(\mu)$, given by

$$\bar{w}^{(24)}_{\pm,n}(\mu) = \begin{cases} u_+(\mu) & n = 1 \\ u_\pm(\mu) & n = 2,4 \\ 0 & n = 3,5 \end{cases} \quad (2.14)$$

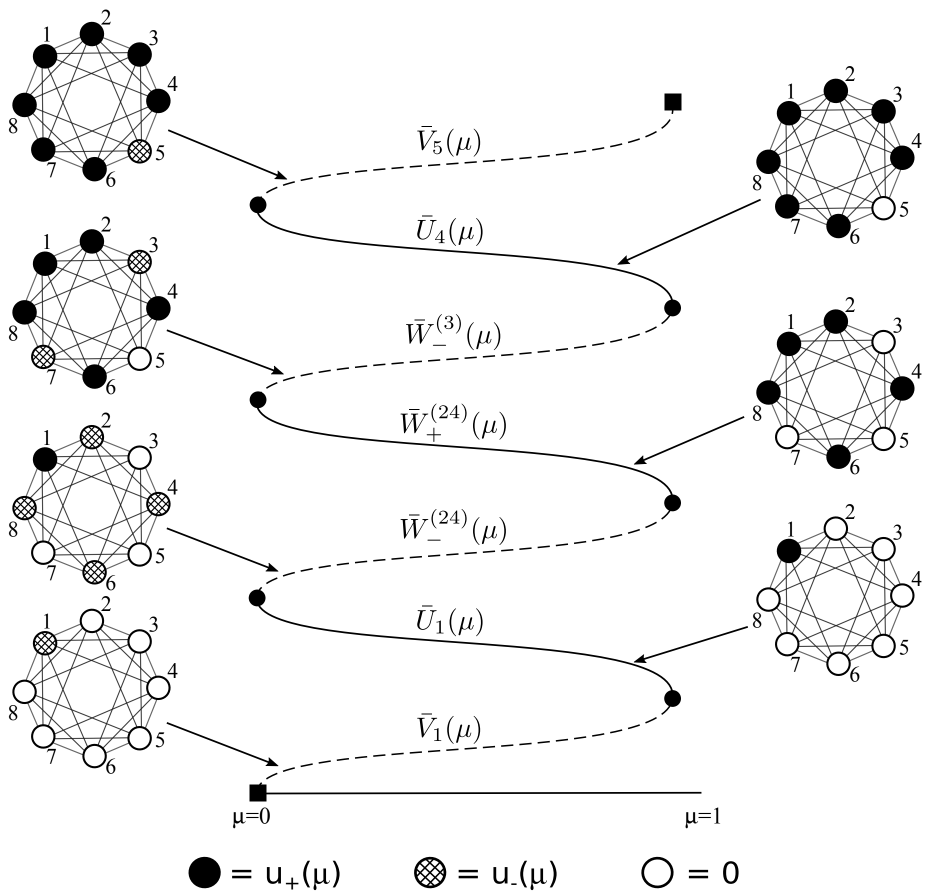

Figure 2.4: The bifurcation diagram on a ring with $(N, m) = (8, 3)$ for small $d > 0$. The number of neighbour connections induces an added symmetry, thus leading to the above bifurcation diagram which bears little resemblance to that of the case $(N, m) = (8, 1), (8, 2)$ featured in Theorem 1. Squares marking the end of the curve represent the set of exceptional bifurcations, continued from $\mathcal{E}$, which are not proven in this chapter.

and

$$\bar{w}^{(3)}_{-,n}(\mu) = \begin{cases} u_+(\mu) & n = 1,2,4 \\ u_-(\mu) & n = 3 \\ 0 & n = 5 \end{cases} \tag{2.15}$$

respectively, for each $\mu \in [0,1]$. Here the values in the superscript detail which terms are at $u_-(\mu)$ when the subscript is $-$, while the element $\bar{W}^{(24)}_+(\mu)$ connects the two elements with $-$ subscripts. We refer the reader to panels (b) and (c) of Figure 2.6 below for visual depictions of these elements extended by κ symmetry to the entire ring. Notice that we have the following connections:

$$\begin{aligned} \lim_{\mu\to 0^+} \bar{W}^{(24)}_-(\mu) &= \lim_{\mu\to 0^+} \bar{U}^{(1)}(\mu) \\ \lim_{\mu\to 1^-} \bar{W}^{(24)}_+(\mu) &= \lim_{\mu\to 1^-} \bar{W}^{(24)}_-(\mu) \\ \lim_{\mu\to 0^+} \bar{W}^{(3)}_-(\mu) &= \lim_{\mu\to 0^+} \bar{W}^{(24)}_+(\mu) \\ \lim_{\mu\to 1^-} \bar{W}^{(3)}_-(\mu) &= \lim_{\mu\to 1^-} \bar{U}^{(4)}(\mu). \end{aligned} \tag{2.16}$$

These connections allow one to define the connected set

$$\Gamma_{8,3} := \bigcup_{0\le\mu\le 1} \{(\bar{V}^{(1)},\mu),(\bar{U}^{(1)},\mu),(\bar{W}^{(24)}_-,\mu),(\bar{W}^{(24)}_+,\mu),(\bar{W}^{(3)}_-,\mu),(\bar{U}^{(4)},\mu),(\bar{V}^{(5)},\mu)\} \subset \mathbb{R}^8\times[0,1]. \tag{2.17}$$

This leads to the following theorem whose results are represented visually in Figure 2.4. The proof is again left to Section 3.3.

Theorem 3. *Assume that f satisfies Hypothesis 1 and that $(N,m) = (8,3)$. Then for each $\delta_* > 0$ there exists $d_* > 0$ such that for each $0 < d < d_*$ the set $\mathcal{B}_{\delta_*}(\Gamma_{8,3})\backslash\mathcal{B}_{2\delta_*}(\mathcal{E})$ contains a nonempty, continuous branch of κ-symmetric solutions of the steady-state system (2.2). Furthermore, this branch is smooth and C^1-close to $\Gamma_{8,3}$ for each d, depends smoothly on d, and its limit as $d\to 0^+$ is contained in $\Gamma_{8,3}$.*

2.3 All-to-all coupling

Let us now consider the case of all-to-all coupling, i.e. $m = \lfloor \frac{N}{2} \rfloor$. In this case (2.2) becomes

$$d \sum_{j=1}^{N} (u_j - u_n) + f(u_n, \mu) = 0, \tag{2.18}$$

so that every element is coupled to every other element, thus representing a complete graph with N vertices. The symmetry group associated with (2.18) is therefore given by the group S_N of all permutations of the vectors $U = (u_1, u_2, \ldots, u_N) \in \mathbb{R}^N$, which is larger than the dihedral group D_N. For each $k = 1, \ldots, \lfloor N/2 \rfloor$, we will construct solutions whose first k elements are identical and whose last $N - k$ elements are identical: such solutions admit the isotropy group $S_k \times S_{N-k}$, defined by the set of all permutations of the first k elements of a vector in $\mathbb{R}^N$ together with all permutations of the last $N - k$ elements of the vector. Note that the fixed point space of $S_k \times S_{N-k}$ in $\mathbb{R}^N$ is the two-dimensional space of all vectors whose first k elements are identical and whose last $N - k$ elements are identical.

Generic symmetry-breaking bifurcations from homogeneous equilibria with isotropy group S_N to equilibria with isotropy $S_k \times S_{N-k}$ were investigated in Elmhirst (2004), Dias and Rodrigues (2006) in the context of sympathic speciation (see, for instance, Stewart et al. (2003), Golubitsky and Stewart (2015) for further background). Genericity requires in particular that the linearization at a homogeneous equilibrium at the bifurcation point has a zero eigenvalue in precisely one of the two complementary S_N-invariant subspaces given by $\{U \in \mathbb{R}^N : u_1 = \ldots = u_N\}$ and $\{U \in \mathbb{R}^N : u_1 + \ldots + u_N = 0\}$ but not in both simultaneously; see (Elmhirst, 2004, §2). Unfortunately, the bifurcations occurring in (2.18) at $(d, \mu) = (0, 0)$ and $(d, \mu) = (0, 1)$ are not generic as the zero eigenvalue has multiplicity N, and we therefore need to analyse the resulting bifurcations occurring in (2.18) here.

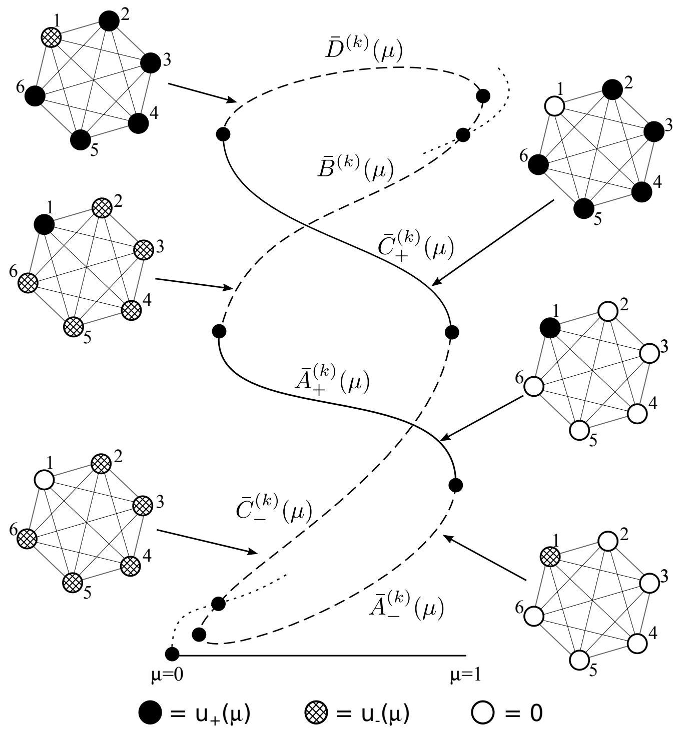

Figure 2.5: We illustrate the solution branch for symmetric all-to-all coupling and the different patterns along the branch. The dotted curve corresponds to the branch of S_N-symmetric equilibria at which all nodes are equal to the unstable state $u_{-}(\mu)$.

For each $k = 1, \ldots, \lfloor N/2 \rfloor$ and each $0 \leq \mu \leq 1$, we define the $S_k \times S_{N-k}$-invariant vectors $\bar{A}_{\pm}^{(k)}(\mu) = \{\bar{a}_{\pm,n}^{(k)}(\mu)\}$, $\bar{B}^{(k)}(\mu) = \{\bar{b}_n^{(k)}(\mu)\}$, $\bar{C}_{\pm}^{(k)}(\mu) = \{\bar{c}_{\pm,n}^{(k)}(\mu)\}$, and $\bar{D}^{(k)}(\mu) = \{\bar{d}_n^{(k)}(\mu)\}$ by

$$\bar{a}_{\pm,n}^{(k)}(\mu) = \begin{cases} u_{\pm}(\mu) & 1 \leq n \leq k \\ 0 & n > k \end{cases} \tag{2.19}$$

$$\bar{b}_n^{(k)}(\mu) = \begin{cases} u_{+}(\mu) & 1 \leq n \leq k \\ u_{-}(\mu) & n > k \end{cases} \tag{2.20}$$

$$\bar{c}_{\pm,n}^{(k)}(\mu) = \begin{cases} 0 & 1 \leq n \leq k \\ u_{\pm}(\mu) & n > k \end{cases} \tag{2.21}$$

and

$$\bar{d}_n^{(k)}(\mu) = \begin{cases} u_-(\mu) & 1 \leq n \leq k \\ u_+(\mu) & n > k; \end{cases} \tag{2.22}$$

see Figure 2.5 for an illustration. From Hypothesis 1 we have that for any k the vectors (2.19)–(2.22) are $S_k \times S_{N-k}$-invariant solutions of (2.2) when $d = 0$. Furthermore, we have the following connections:

$$\begin{aligned}
\lim_{\mu\to 0^+} \bar{A}_-^{(k)}(\mu) &= \lim_{\mu\to 0^+} \bar{C}_-^{(k)}(\mu) \\
\lim_{\mu\to 1^-} \bar{A}_-^{(k)}(\mu) &= \lim_{\mu\to 1^-} \bar{A}_+^{(k)}(\mu) \\
\lim_{\mu\to 0^+} \bar{A}_+^{(k)}(\mu) &= \lim_{\mu\to 0^+} \bar{B}^{(k)}(\mu) \\
\lim_{\mu\to 1^-} \bar{B}^{(k)}(\mu) &= \lim_{\mu\to 1^-} \bar{D}^{(k)}(\mu) \\
\lim_{\mu\to 0^+} \bar{C}_+^{(k)}(\mu) &= \lim_{\mu\to 0^+} \bar{D}^{(k)}(\mu) \\
\lim_{\mu\to 1^-} \bar{C}_-^{(k)}(\mu) &= \lim_{\mu\to 1^-} \bar{C}_+^{(k)}(\mu)
\end{aligned} \tag{2.23}$$

for each k. We therefore introduce the connected curve

$$\Gamma_{\text{all}}^k := \bigcup_{0\leq\mu\leq 1} \{(\bar{A}_\pm^{(k)}(\mu),\mu), (\bar{B}^{(k)}(\mu),\mu), (\bar{C}_\pm^{(k)}(\mu),\mu), (\bar{D}^{(k)}(\mu),\mu)\} \subset \mathbb{R}^N \times [0,1], \tag{2.24}$$

for each $k = 1, \dots, \lfloor N/2 \rfloor$. We present the following result, whose proof is left to Section 3.4.

Theorem 4. *Assume that f satisfies Hypothesis 1. For each $k = 1, \dots, \lfloor N/2 \rfloor$ and $\delta_* > 0$, there exists $d_* > 0$ such that for each $0 < d < d_*$ the set $\mathcal{B}_{\delta_*}(\Gamma_{\text{all}}^k)$ contains two unique, distinct, nonempty, and continuous branches of $S_k \times S_{N-k}$-symmetric solutions of the steady-state system (2.18), which emerge from and terminate at the homogeneous branch of solutions to (2.2) given by $u_n = u_-(\mu)$ for $n = 1, \dots, N$ at $\mu = \frac{Nd}{2} + \mathcal{O}(d^2)$ and $\mu = 1 - (\frac{Nd}{2})^2 + \mathcal{O}(d^3)$, respectively. Furthermore, these branches* *are smooth and C^1-close to Γ^k_{all} for each d, depends smoothly on d, and its limit as $d \to 0^+$ is contained in Γ^k_{all}.*

We note that the results of Theorem 4 do not include an exceptional set, meaning that the theorem completely characterizes the entire bifurcation curve of localized solutions in the presence of all-to-all coupling. We refer to Figure 2.5 for an illustration of the result with a ring of $N = 6$ elements. Interestingly, we see that this curve of solutions does not originate at the origin $(U, \mu) = (0, 0)$ in $\mathbb{R}^N \times [0, 1]$ when $0 < d \ll 1$, but instead bifurcates from the homogeneous branch of solutions at a positive value of μ. For more details on this bifurcation from the homogeneous branch, we refer the reader to Lemma 14 below.

3 Proofs

In this section we will prove the various theorems from the previous section detailing the existence and bifurcation structure of steady-state solutions to (2.3). As discussed in the introduction, we can define the function

$$\mathcal{F} :\ \mathbb{R}^N \times \mathbb{R} \times \mathbb{R} \longrightarrow \mathbb{R}^N,\ (U, \mu, d) \longmapsto \mathcal{F}(U, \mu, d),\ \mathcal{F}(U, \mu, d)_n := d(\Delta_m U)_n + f(u_n, \mu), \tag{2.25}$$

to see that the steady-state system

$$d(\Delta_m U)_n + f(u_n, \mu) = 0 \tag{2.26}$$

corresponding to (2.3) is given by $\mathcal{F}(U, \mu, d) = 0$. Note that $\mathcal{F}$ is smooth in its arguments, and upon taking $d = 0$, solving $\mathcal{F}(U, \mu, 0) = 0$ with $\mu \in (0, 1)$ reduces to taking $u_n \in \{0, \pm u_\pm(\mu)\}$ for each $n = 1, \ldots N$ per Hypothesis 1.

From the assumption on the non-degeneracy of the roots of f, it follows that for μ belonging to any compact interval of $(0,1)$ these solutions may be continued regularly into $d > 0$ using the implicit function theorem. The challenge is therefore to understand the cases where μ is close to zero or one. In these cases, the Jacobian of $\mathcal{F}$ at $d = 0$ will have a null space of dimension at least one, and Lyapunov–Schmidt reduction allows us to reduce the equation $\mathcal{F}(U, \mu, d) = 0$ to a reduced equation $\mathcal{F}^{\mathrm{c}}(U^{\mathrm{c}}, \mu, d) = 0$ defined on the null space. As we will see below, the reduced equation $\mathcal{F}^{\mathrm{c}}(U^{\mathrm{c}}, \mu, d) = 0$ is, to leading order, quasihomogeneous, and we now explain what this means and how it helps us in our analysis. Given exponents $a_1, a_2, a_3 \geq 1$, and focusing for ease of notation on the case where μ is close to zero, we introduce the coordinate transformation $(U^{\mathrm{c}}, \mu, d) = (\nu^{a_1}\tilde{U}^{\mathrm{c}}, \nu^{a_2}\tilde{\mu}, \nu^{a_3}\tilde{d})$, where $0 \leq \nu \ll 1$ and $(\tilde{U}^{\mathrm{c}}, \tilde{\mu}, \tilde{d})$ now lies on the unit sphere. This change of coordinates is invertible away from the origin $(U^{\mathrm{c}}, \mu, d) = 0$ or, alternatively, for $\nu > 0$. The key is that for an appropriate choice of a_1, a_2, a_3 there is a constant $b \geq 1$ so that

$$\mathcal{F}^{\mathrm{c}}(\nu^{a_1}\tilde{U}^{\mathrm{c}}, \nu^{a_2}\tilde{\mu}, \nu^{a_3}\tilde{d}) = \nu^b \left(\mathcal{F}^{\mathrm{c}}(\tilde{U}^{\mathrm{c}}, \tilde{\mu}, \tilde{d}) + \mathcal{O}(\nu) \right), \quad |(\tilde{U}^{\mathrm{c}}, \tilde{\mu}, \tilde{d})| = 1.$$

Hence, all zeros of $\mathcal{F}^{\mathrm{c}}(U^{\mathrm{c}}, \mu, d)$ must lie near zeros of $\mathcal{F}^{\mathrm{c}}(\tilde{U}^{\mathrm{c}}, \tilde{\mu}, \tilde{d})$, and we can therefore focus on the desingularized equation $\mathcal{F}^{\mathrm{c}}(\tilde{U}^{\mathrm{c}}, \tilde{\mu}, \tilde{d}) = 0$ with arguments on the unit sphere: if the set of zeros of the desingularized equation consists entirely of regular zeros and generically unfolded bifurcations, then it persists robustly for $0 < \nu \ll 1$, and no additional roots can appear for $\nu > 0$. In practice, we will use a directional blowup in our proofs below by setting $\tilde{d} = 1$ or $\tilde{\mu} = 1$ and will not consider the other directional blowups that together parametrize the entire sphere as they do not contribute additional solutions. We refer to (Kuehn, 2015, §7) for references and additional details on geometric blowup.

Throughout the proofs we will make use of the following. Through two independent μ-dependent coordinate transformations of the u variable near $(u, \mu) = (0, 0)$ and $(u_+(0), 0)$, respectively, we can bring the Taylor expansion of $f(u, \mu)$ at $(0, 0)$ into the form

$$f(u, \mu) = -\mu u + u^3 + \mathcal{O}(\mu^2 u + \mu u^3 + u^5) \tag{2.27}$$

and achieve that $u_+(0) = 1$. Using a similar change of coordinates near $(u, \mu) = (1, 1)$, we can bring the Taylor expansion of $f(u, \mu)$ at $(1, 1)$ into the form

$$f(u, \mu) = f(1 + \check{u}, 1 - \check{\mu}) = \check{\mu} - \check{u}^2 - b\check{\mu}\check{u} + \mathcal{O}(\check{\mu}^2 + \check{\mu}\check{u}^2 + \check{u}^3), \tag{2.28}$$

for some constant b. These changes of coordinates will greatly simplify the analysis in what follows.

3.1 Nearest-neighbour coupling

Throughout this subsection we will consider $N \geq 4$ and take $m = 1$, representing nearest-neighbour connections in the system (2.1). Here we prove Theorem 1 with $m = 1$, while the case of $m = 2$ is left to the following subsection. Per the discussion at the beginning of this section, we need only continue the connections in $\Gamma_{\text{sparse}} \setminus \mathcal{E}$ near $\mu = 0, 1$. We begin with the following lemma which continues the patterns near $\mu = 0$.

Lemma 1. *Fix $m = 1$ and $2 \leq k \leq \lfloor \frac{N}{2} \rfloor + 1$, then the following is true for (2.26). There are constants $d_1, \mu_1 > 0$ and a smooth function $\mu_l : [0, d_1] \to [0, \mu_1]$ such that for each $d \in (0, d_1]$, there is a pair of κ-symmetric solutions $U_l(\mu, d)$ and $V_l(\mu, d)$ of (2.26) that bifurcate at a fold bifurcation at $\mu = \mu_l(d)$ and exist for all $\mu \in [\mu_l(d), \mu_1]$. These solutions are smooth in (μ, d), and for each fixed μ, we* *have* $U_l(\mu,d) \to \bar{U}^{(k-1)}(\mu)$ *and* $V_l(\mu,d) \to \bar{V}^{(k)}(\mu)$ *as* $d \to 0^+$. *The function* $\mu_l(d)$ *satisfies* $\mu_l(d) = \frac{3}{\sqrt[3]{2}} d^{\frac{2}{3}} + \mathcal{O}(d)$.

Proof. We will fix $k \in \{2, \ldots, \lfloor \frac{N}{2} \rfloor + 1\}$ and construct symmetric solutions of (2.26) near the pattern

$$\bar{U}^{(k)}(0) = \bar{V}^{(k)}(0) = \begin{cases} 1 & n < k \\ 0 & \text{otherwise} \end{cases}$$

for (μ, d) near zero. We reduce patterns to the index set I, defined in (2.6), using the aforementioned κ symmetry. To solve $\mathcal{F}(U,\mu,d) = 0$, we note that $\mathcal{F}(\bar{U}^{(k)}(0), 0, 0) = 0$ and that the linearization of $\mathcal{F}$ is given by

$$(\mathcal{F}_U(\bar{U}^{(k)}(0), 0, 0)v)_n = \begin{cases} f_u(1,0)v_n & n < k \\ 0 & n \geq k. \end{cases}$$

Writing $U^+ := U|_{n<k}$ and $U^c := U|_{n\geq k}$, and using that $f_u(1,0) \neq 0$, we can apply the implicit function theorem to conclude that $\mathcal{F}(U,\mu,d) = 0$ restricted to the index set $1 \leq n < k$ has a unique solution $U^+(u^c, \mu, d) \in \mathbb{R}^{k-1}$ for each $U^c \in \mathbb{R}^{\lfloor \frac{N}{2} \rfloor - k + 1}$ and (μ, d) near zero. Furthermore, this solution depends smoothly on its arguments, and so we have

$$U^+(U^c, \mu, d) = 1 + \mathcal{O}(|\mu| + |d| \|U^c\|). \tag{2.29}$$

To solve (2.26) for the indices $n \geq k$, we introduce the scaling

$$\mu = \nu^2, \qquad d = \nu^3 \tilde{d}, \qquad u_n = \nu^{n-k+1} \tilde{u}_n, \tag{2.30}$$

for $n \geq k$ with $|\nu| \ll 1$. Substituting these expressions into (2.26) for each $n \geq k$, we see that (2.26) restricted to the index set $I \setminus I_+$ becomes

$$\begin{aligned} n = k: &\qquad 0 = \nu^3(\tilde{d} - \tilde{u}_k + \tilde{u}_k^3) + \mathcal{O}(\nu^4) \\ n > k: &\qquad 0 = \nu^{n-k+3}(\tilde{d}\tilde{u}_{n-1} - \tilde{u}_n) + \mathcal{O}(\nu^{n-k+4}), \end{aligned}$$

where we recall that we have introduced a change of variable to bring the system to the normal form (2.27). Upon dividing by the leading factors in ν, we arrive at the system

$$\begin{aligned} n = k: &\qquad 0 = \tilde{d} - \tilde{u}_k + \tilde{u}_k^3 + \mathcal{O}(\nu) \\ n > k: &\qquad 0 = \tilde{d}\tilde{u}_{n-1} - \tilde{u}_n + \mathcal{O}(\nu) \end{aligned} \tag{2.31}$$

for which we can see that at the index $n = k$ a fold bifurcation takes place at $(\tilde{u}_k, \tilde{d}, \nu) = (\frac{1}{\sqrt{3}}, \frac{2}{3\sqrt{3}}, 0)$. Extending this fold bifurcation to the full system for the indices $n \geq k$ into $\nu > 0$ now follows as in the proof of (Bramburger and Sandstede, 2020b, Lemma 3.2). As this method underpins many of the proofs that follow, we will include the details to complete this proof.

First, by setting $\nu = 0$ we can parametrize the fold bifurcation at index $n = k$ by

$$(\tilde{u}_k, \tilde{d})(s) = (s, s(1 - s^2)), \quad s \in [0, 1].$$

Notice that this parametrization connects $(0, 0)$ to $(1, 0)$ as s increases through the interval $[0, 1]$. Furthermore, the fold bifurcation takes place when $s = \frac{1}{\sqrt{3}}$, giving $\tilde{d}_{\rm sn} = \frac{2}{3\sqrt{3}}$. Continuing with $\nu = 0$, the remaining $n > k$ indices in (2.31) can be written as the matrix equation

$$(-\mathbb{I} + \tilde{d}(s)Z)\tilde{U}_{n>k} = \tilde{d}(s)\tilde{u}_k(s)\hat{e}_1$$

where $\mathbb{I}$ denotes the identity matrix, Z is a matrix with ones along the diagonal above the main diagonal and zeros elsewhere, $\tilde{U}_{n>k}$ is the vector of $\tilde{u}_n$ with $n > k$, and $\hat{e}_1$ is the vector with 1 in its first entry and zeros elsewhere. Since $\|Z\| \leq 1$ and $\tilde{d}(s) \in [0, \frac{2}{3\sqrt{3}}]$ for all $s \in [0,1]$, it follows that the matrix $(-1 + \tilde{d}(s)Z)$ is invertible for all $s \in [0,1]$. Therefore, for each $s \in [0,1]$ we can uniquely solve for $\tilde{U}_{n>k}$ in terms of $(\tilde{u}_k, \tilde{d})(s)$ which parametrize the fold bifurcation. This extends the fold bifurcation into the indices $n > k$ for $\nu = 0$.

The persistence of the fold bifurcation at $\nu = 0$ into $0 < \nu \ll 1$ can first be obtained by writing the right-hand-side of (2.31) compactly as $G(\tilde{U}^c, \tilde{d}, \nu)$. Note that the branch constructed above, denoted $(\tilde{U}^c, \tilde{d})(s)$ satisfies $G(\tilde{U}^c(s), \tilde{d}(s), 0) = 0$ and the derivative $G_{(\tilde{U}^c, \tilde{d})}(\tilde{U}^c(s), \tilde{d}(s), 0)$ has full rank for all $s \in [0,1]$. We can therefore apply the implicit function theorem and use persistence results for fold bifurcations to conclude that the branch persists for sufficiently small $\nu > 0$. Moreover, the unique fold bifurcation takes place at $\tilde{d} = \tilde{d}_{\mathrm{sn}}(\nu)$ with $\tilde{d}_{\mathrm{sn}}(0) = \frac{2}{3\sqrt{3}}$. This completes the proof of the lemma. $\square$

We now turn to the continuation when $\mu = 1$. Recall that from (2.28) we have that upon changing coordinates we can bring the Taylor expansion of $f(u,\mu)$ about $(1,1)$ into the form

$$f(u,\mu) = f(1+\check{u}, 1-\check{\mu}) = \check{\mu} - \check{u}^2 - b\check{\mu}\check{u} + \mathcal{O}(\check{\mu}^2 + \check{\mu}\check{u}^2 + \check{u}^4).$$

This leads to the following result which continues the connections in Γ near $\mu = 1$ and completes the proof of Theorem 1 when $m = 1$.

Lemma 2. *Fix $m = 1$ and $1 \leq k \leq \lfloor \frac{N}{2} \rfloor$, then the following is true for (2.26). There exist constants $d_2, \mu_2 > 0$ and a smooth function $\mu_r : [0, d_2] \to [\mu_2, 1]$ such that for each fixed $d \in (0, d_2]$, there is a pair of κ-symmetric solutions $U_r(\mu, d)$ and $V_r(\mu, d)$ of (2.26) that bifurcate at a fold bifurcation at $\mu = \mu_r(d)$ and exist for all*

$\mu \in [\mu_2, \mu_r(d)]$. These solutions are smooth in (μ, d), and for each fixed μ, we have $U_r(\mu, d) \to \bar{U}^{(k)}(\mu)$ and $V_r(\mu, d) \to \bar{V}^{(k)}(\mu)$ as $d \to 0^+$. The function $\mu_r(d)$ is given by $\mu_r(d) = 1 - d + \mathcal{O}(d^{\frac{3}{2}})$.

Proof. We again restrict to the index set I and extend the solutions by symmetry to $n \geq \lfloor N/2 \rfloor + 2$. As the branch passes near $\mu = 1$, the cell u_k changes from $u_-(\mu)$ to $u_+(\mu)$, while the remaining cells stay near 0 or $u_+(\mu)$. We have that $\mathcal{F}(\bar{U}^{(k)}(1), 1, 0) = 0$ and that the linearization of $\mathcal{F}$ about this solution is given by

$$(\mathcal{F}_U(\bar{U}^{(k)}(1), 1, 0)v)_n = \begin{cases} f_u(0,1)v_n & n > k \\ 0 & n \leq k. \end{cases}$$

Writing $U^0 := U|_{n>k}$ and $U^c := U|_{n\leq k}$, and using that $f_u(0,1) \neq 0$, we can apply the implicit function theorem to find that $\mathcal{F}(U, \mu, d) = 0$ restricted to the index set $n > k$ has a unique solution $U^0(U^c, \mu, d) \in \ell^\infty(I|_{n>k})$ for each $U^c \in \mathbb{R}^k$ and (μ, d) near $(1, 0)$. This solution depends smoothly on its arguments, and in particular, has the expansion

$$U^0(U^c, \mu, d) = \mathcal{O}(|\mu - 1| + |d||U^c|). \tag{2.32}$$

To solve (2.26) on the index set $n \leq k$, we introduce the scaling

$$\mu = 1 - \nu^2, \quad d = \nu^2 \tilde{d}, \quad u_n = 1 + \nu \tilde{u}_n,$$

where $1 \leq n \leq k$ and $|\nu| \ll 1$. Expanding $\mathcal{F}(U, \mu, d) = 0$ restricted to the index set $n \in \{1, \ldots, k\}$ in powers of ν and dividing by the leading factor in ν, we arrive at the finite system

$$\begin{aligned} n = k: &\qquad 0 = -\tilde{d} + 1 - \tilde{u}_k^2 + \mathcal{O}(\nu) \\ n < k: &\qquad 0 = 1 - \tilde{u}_n^2 + \mathcal{O}(\nu) \end{aligned} \tag{2.33}$$

where we used (2.32) to simplify the equation with $n = k$ using the connection to the element at index $n = k+1$. We now see that at the index $n = k$, a fold bifurcation takes place at $(\tilde{u}_k, \tilde{d}, \nu) = (0, 1, 0)$. Extending this fold bifurcation to the full system on the indices $n \geq k$ and into $\nu > 0$ follows as in the previous lemma and is omitted. This completes the proof of the lemma. □

3.2 Next-nearest-neighbour coupling

In this subsection we provide analogous results to the nearest-neighbour bifurcation branches, but with $m = 2$, representing next-nearest-neighbour connections. The results of this subsection therefore complete the proof of Theorem 1 with $m = 2$. We will consider $N \geq 7$, since $N = 4, 5$ and $m = 2$ represent all-to-all connections, and $N = 6$ with $m = 2$ has an extra symmetry that can be exploited, as presented in Theorem 2. We present the following result, analogous to Lemma 1 above.

Lemma 3. *Fix $m = 2$ and $3 \leq k \leq \lfloor \frac{N}{2} \rfloor + 1$, then the following is true for (2.26). There are constants $d_1, \mu_1 > 0$ and a smooth function $\mu_l : [0, d_1] \to [0, \mu_1]$ such that for each $d \in (0, d_1]$, there is a pair of κ-symmetric solutions $U_l(\mu, d)$ and $V_l(\mu, d)$ of (2.26) that bifurcate at a fold bifurcation at $\mu = \mu_l(d)$ and exist for all $\mu \in [\mu_l(d), \mu_1]$. These solutions are smooth in (μ, d), and for each fixed μ, we have $U_l(\mu, d) \to \bar{U}^{(k-1)}(\mu)$ and $V_l(\mu, d) \to \bar{V}^{(k)}(\mu)$ as $d \to 0^+$. The function $\mu_l(d)$ satisfies $\mu_l(d) = 3d^{\frac{2}{3}} + \mathcal{O}(d)$.*

Proof. Fix $m = 2$ and $3 \leq k \leq \lfloor \frac{N}{2} \rfloor + 1$. Then, following as in Lemma 1 to continue the elements with $n < k$ into $d > 0$ near $\mu = 0$ using the implicit function theorem. We again get the asymptotic expansion (2.29), and for the indices with $n \geq k$ we introduce the scaling

$$\mu = \nu^2, \qquad d = \nu^3 \tilde{d}, \qquad u_n = \nu^{\lfloor \frac{n-k}{2} \rfloor + 1} \tilde{u}_n. \tag{2.34}$$

That is, $u_k = \nu \tilde{u}_k$, $u_{k+1} = \nu \tilde{u}_{k+1}$, $u_{k+2} = \nu^2 \tilde{u}_{k+2}$, $u_{k+3} = \nu^2 \tilde{u}_{k+3}$, and so on. Putting these rescaled variables into (2.26), expanding in powers of ν, and dividing off the leading power in ν brings us to the equations, analogous to (2.31),

$$\begin{aligned} n = k: &\qquad 0 = 2\tilde{d} - \tilde{u}_k + \tilde{u}_k^3 + \mathcal{O}(\nu) \\ n = k+1: &\qquad 0 = \tilde{d} - \tilde{u}_{k+1} + \tilde{u}_{k+1}^3 + \mathcal{O}(\nu) \\ n \geq k+2: &\qquad 0 = \tilde{d}\tilde{u}_{n-2} + \tilde{d}\tilde{u}_{n-1} - \tilde{u}_n + \mathcal{O}(\nu) \end{aligned} \tag{2.35}$$

where we have used the fact that at index $n = k$ we are connected to the elements at index $k-1, k-2$, both of which are equal to 1 at $(\mu, d) = (0, 0)$. Similarly, since $m = 2$, the element at index $n = k+1$ is only connected to one element (at $n = k-1$) that is equal to 1 at $(\mu, d) = (0, 0)$. The proof is now the same as that of Lemma 1. □

Let us now finish the case of bifurcations near $\mu = 0$ by considering the case $k = 2$. We present the following result.

Lemma 4. *Fix $m = k = 2$, then the following is true for (2.26). There are constants $d_1, \mu_1 > 0$ and a smooth function $\mu_l : [0, d_1] \to [0, \mu_1]$ such that for each $d \in (0, d_1]$, there is a pair of κ-symmetric solutions $U_l(\mu, d)$ and $V_l(\mu, d)$ of (2.26) that bifurcate at a fold bifurcation at $\mu = \mu_l(d)$ and exist for all $\mu \in [\mu_l(d), \mu_1]$. These solutions are smooth in (μ, d), and for each fixed μ, we have $U_l(\mu, d) \to \bar{U}^{(1)}(\mu)$ and $V_l(\mu, d) \to \bar{V}^{(2)}(\mu)$ as $d \to 0^+$. The function $\mu_l(d)$ satisfies $\mu_l(d) = \frac{3}{\sqrt[3]{2}} d^{\frac{2}{3}} + \mathcal{O}(d)$.*

Proof. Following as in the proof of Lemma 3 up to (2.35), we now arrive at the equations

$$
\begin{aligned}
n = 2: \qquad & 0 = \tilde{d} - \tilde{u}_2 + \tilde{u}_2^3 + \nu(\tilde{u}_3 - 3\tilde{u}_2) + \mathcal{O}(\nu^2) \\
n = 3: \qquad & 0 = \tilde{d} - \tilde{u}_3 + \tilde{u}_3^3 + \nu(\tilde{u}_2 - 4\tilde{u}_3) + \mathcal{O}(\nu^2) \\
n \geq 4: \qquad & 0 = \tilde{d}\tilde{u}_{n-2} + \tilde{d}\tilde{u}_{n-1} - \tilde{u}_n + \mathcal{O}(\nu)
\end{aligned}
\tag{2.36}
$$

where now, since $m = 2$, we have that the elements at indices $n = 2, 3$ are both connected to the single element at $n = 1$ that equals 1 at $(\mu, d) = (0, 0)$. Note that the equations at indices $n = 2, 3$ agree at the lowest order in ν, but differ at $\mathcal{O}(\nu)$. This comes from the symmetry imposed by our assumption that the solution is invariant with respect to the action of κ, which enforces that $u_N = u_2$ and thus eliminating one of the connections at $n = 2$. In contrast, we have exactly four self-interactions at index $n = 3$ in (2.36) at order ν since the element at index $n = 3$ has no neighbours that have a symmetric restriction imposed on them. From here the proof now follows as in (Bramburger and Sandstede, 2020b, Lemma 3.3), but we include the details to keep this manuscript self-contained.

Let us introduce the new variables (d_0, v_2, v_3), given by

$$
\tilde{d} = \frac{2}{3\sqrt{3}} + \nu d_0, \quad \tilde{u}_2 = \frac{1}{\sqrt{3}} + \nu^{\frac{1}{2}} v_2, \qquad \tilde{u}_3 = \frac{1}{\sqrt{3}} + \nu^{\frac{1}{2}} v_3
$$

so that (2.36) becomes

$$
\begin{aligned}
n = 2: \qquad & 0 = d_0 + \sqrt{3} v_2^2 - \tfrac{4}{27} + \mathcal{O}(\nu^{\frac{1}{2}}) \\
n = 3: \qquad & 0 = d_0 + \sqrt{3} v_3^2 - \tfrac{2}{9} + \mathcal{O}(\nu^{\frac{1}{2}}) \\
n = 4: \qquad & 0 = \tfrac{4}{9} - \tilde{u}_4 + \mathcal{O}(\nu^{\frac{1}{2}}) \\
n = 5: \qquad & 0 = \tfrac{2}{9} + \tfrac{2}{3\sqrt{3}}\tilde{u}_4 - \tilde{u}_5 + \mathcal{O}(\nu^{\frac{1}{2}}) \\
n \geq 6: \qquad & 0 = \tfrac{2}{3\sqrt{3}}\tilde{u}_{n-2} + \tfrac{2}{3\sqrt{3}}\tilde{u}_{n-1} - \tilde{u}_n + \mathcal{O}(\nu)
\end{aligned}
$$

after dividing off the leading factor of ν in the equations for $n = 2, 3$. The equations for indices $n \geq 4$ can be solved uniquely for all bounded (d_0, v_2, v_3) and sufficiently small $\nu > 0$, and therefore we focus exclusively on the equations for the indices $n = 2, 3$. Setting $\nu = 0$ we find that a fold bifurcation takes place in the equation at index $n = 2$ at $(d_0, v_2) = (\frac{4}{27}, 0)$. Furthermore, we can solve the equation at $n = 3$ uniquely for v_3 for (d_0, v_2, ν) in a neighbourhood of this fold bifurcation, leaving only the equation at $n = 2$. Then, as in the proof of Lemma 1, the fold bifurcation at $n = 2$ with $\nu = 0$ can be shown to persist into $0 < \nu \ll 1$, thus concluding the proof of the lemma. □

We now turn to the continuation when $\mu = 1$, which will similarly follow the proof of Lemma 2.

Lemma 5. *Fix $m = 2$ and $1 \leq k \leq \lfloor \frac{N}{2} \rfloor$, then the following is true for (2.26). There exist constants $d_2, \mu_2 > 0$ and a smooth function $\mu_r : [0, d_2] \to [\mu_2, 1]$ such that each fixed $d \in (0, d_2]$, there is a pair of κ-symmetric solutions $U_r(\mu, d)$ and $V_r(\mu, d)$ of (2.26) that bifurcate at a fold bifurcation at $\mu = \mu_r(d)$ and exist for all $\mu \in [\mu_2, \mu_r(d)]$. These solutions are smooth in (μ, d), and for each fixed μ, we have $U_r(\mu, d) \to \bar{U}^{(k)}(\mu)$ and $V_r(\mu, d) \to \bar{V}^{(k)}(\mu)$ as $d \to 0^+$. The function $\mu_r(d)$ is given by $\mu_r(d) = 1 - 2d + \mathcal{O}(d^{\frac{3}{2}})$.*

Proof. This proof is almost the same as that of Lemma 2 with (2.33) replaced by

$$\begin{aligned} n = k: &\qquad 0 = -2\tilde{d} + 1 - \tilde{u}_k^2 + \mathcal{O}(\nu) \\ n = k-1: &\qquad 0 = -\tilde{d} + 1 - \tilde{u}_{k-1}^2 + \mathcal{O}(\nu) \\ n \leq k-2: &\qquad 0 = 1 - \tilde{u}_n^2 + \mathcal{O}(\nu). \end{aligned} \tag{2.37}$$

The subsequent analysis proceeds in the same way as Lemma 2. □

3.3 Almost all-to-all coupling

Let us begin with the proof of Theorem 2, which features $(N, m) = (6, 2)$. With the exception of the connections involving curves continued from $\bar{W}^{(23)}(\mu)$, the analysis is the same as in the proof of Theorem 1. Hence, we will focus exclusively on the connections involving $\bar{W}^{(23)}(\mu)$. There is only one such connection near $\mu = 0$, which is illustrated for small $d > 0$ in Figure 2.6(a). We prove this with the following lemma.

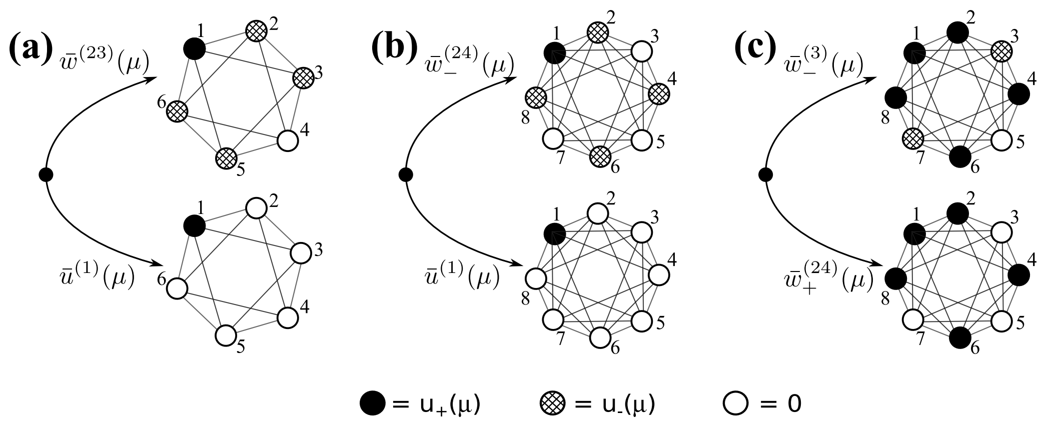

Figure 2.6: Atypical bifurcations near $\mu = 0$ for $N = 6, 8$ and $m = \lfloor N/2 \rfloor - 1$. Panel (a) contains an illustration of the proof of Lemma 6. Panels (b) and (c) illustrate the bifurcations near $\mu = 0$ when $N = 8$, as presented in Lemmas 8 and 10. In all images black circles represent elements continued from $u_+(\mu)$ into $d > 0$, shaded grey circles are continued from $u_-(\mu)$, and white circles are continued from 0. Connections are represented by lines connecting the circles.

Lemma 6. *Fix* $(N, m) = (6, 2)$*, then the following is true for* (2.26)*. There are constants* $d_1, \mu_1 > 0$ *and a smooth function* $\mu_l : [0, d_1] \to [0, \mu_1]$ *such that for each* $d \in (0, d_1]$*, there is a pair of* κ*-symmetric solutions* $U_l(\mu, d)$ *and* $V_l(\mu, d)$ *of* (2.26) *that bifurcate at a fold bifurcation at* $\mu = \mu_l(d)$ *and exist for all* $\mu \in [\mu_l(d), \mu_1]$*. These solutions are smooth in* (μ, d)*, and for each fixed* μ*, we have* $U_l(\mu, d) \to \bar{U}^{(1)}(\mu)$ *and* $V_l(\mu, d) \to \bar{W}^{(23)}(\mu)$ *as* $d \to 0^+$*. The function* $\mu_l(d)$ *satisfies* $\mu_l(d) = \frac{3}{\sqrt[3]{2}} d^{\frac{2}{3}} + \mathcal{O}(d)$*.*

Proof. This proof is handled in exactly the same way as the other proofs for bifurcations near $\mu = 0$, and so we will only seek to highlight why we have a different connection when $N = 6$ and $m = 2$. Using the implicit function theorem, we can solve (2.26) at the index $n = 1$ in a neighbourhood of $(d, \mu) = (0, 0)$ to get

$$u_1 = u_1(U^c, \mu, d) = 1 + \mathcal{O}(|\mu| + |d||U^c|),$$

where $U^c = (u_2, u_3, u_4)$ since we have imposed $u_5 = u_3$ and $u_6 = u_2$ by symmetry. It then remains to solve (2.26) for the indices associated with U^c, i.e. $n = 2, 3, 4$. Specifically, we are required to solve

$$\begin{aligned} d(u_1 + u_3 + u_4 - 3u_2) + f(u_2, \mu) &= 0, \\ d(u_1 + u_2 + u_4 - 3u_3) + f(u_3, \mu) &= 0, \\ 2d(u_2 + u_3 - 2u_4) + f(u_4, \mu) &= 0, \end{aligned} \tag{2.38}$$

where we have simplified the equations using the symmetric restrictions $u_5 = u_3$ and $u_6 = u_2$. One can see that the resulting equations are invariant with respect to the action $(u_2, u_3) \mapsto (u_3, u_2)$, and therefore we may restrict ourselves to the symmetric subspace that has $u_2 = u_3$. Upon imposing this restriction we may then proceed as in the previous proofs to obtain the desired result. □

Near $\mu = 1$ we find that the branch continued from $\bar{W}^{(23)}(\mu)$ connects to $\bar{U}^{(3)}(\mu)$, summarized in the following lemma and illustrated in Figure 2.7(a). The lemma is stated without proof since it is identical to the previous lemmas.

Lemma 7. *Fix $(N, m) = (6, 2)$, then the following is true for (2.26). There exist constants $d_2, \mu_2 > 0$ and a smooth function $\mu_r : [0, d_2] \to [\mu_2, 1]$ such that for each fixed $d \in (0, d_2]$, there is a pair of κ-symmetric solutions $U_r(\mu, d)$ and $V_r(\mu, d)$ of (2.26) that bifurcate at a fold bifurcation at $\mu = \mu_r(d)$ and exist for all $\mu \in [\mu_2, \mu_r(d)]$.*

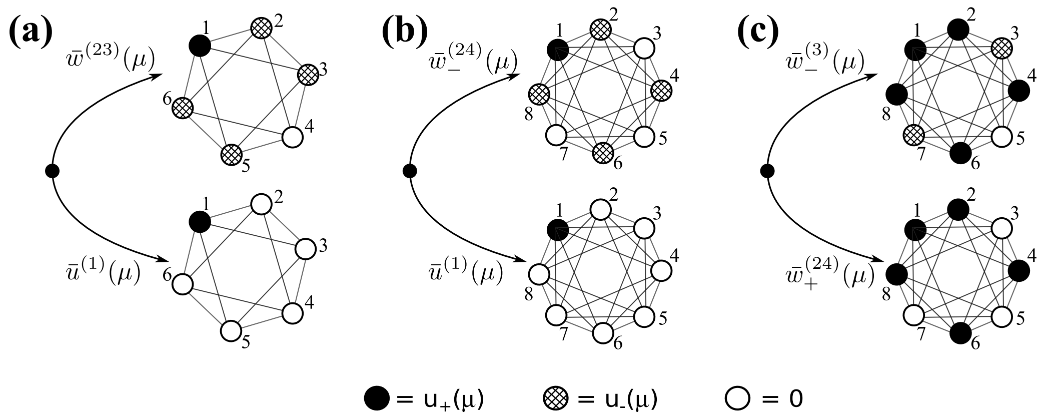

Figure 2.7: Atypical bifurcations near $\mu = 1$ for $N = 6, 8$ and $m = \lfloor N/2 \rfloor - 1$. Panel (a) contains an illustration of the proof of Lemma 7. Panels (b) and (c) illustrate the bifurcations near $\mu = 1$ when $N = 8$, as presented in Lemmas 9 and 11. Shading and connections are the same as in Figure 2.6.

These solutions are smooth in (μ, d), and for each fixed μ, we have $U_r(\mu, d) \to \bar{U}^{(3)}(\mu)$ and $V_r(\mu, d) \to \bar{W}^{(23)}(\mu)$ as $d \to 0^+$. The function $\mu_r(d)$ is given by $\mu_r(d) = 1 - 2d + \mathcal{O}(d^{\frac{3}{2}})$.

Turning now to the case of $(N, m) = (8, 3)$, we remark that much of the analysis is similar. Recall that the set $\Gamma_{8,3}$ is characterized by following along solution branches at $d = 0$ given by the following sequence:

$$\bar{V}^{(1)}(\mu) \to \bar{U}^{(1)}(\mu) \to \bar{W}_-^{(24)}(\mu) \to \bar{W}_+^{(24)}(\mu) \to \bar{W}_-^{(3)}(\mu) \to \bar{U}^{(4)}(\mu) \to \bar{V}^{(4)}(\mu).$$

The connections between $\bar{U}$ and $\bar{V}$ elements are handled as in the proof of Theorem 1, while the connections between any of the $\bar{W}$ elements are summarized in the following lemmas. We refer the reader to Figure 2.6 for illustrations of the connections near $\mu = 0$ and to Figure 2.7 for illustrations near $\mu = 1$. The lemmas are listed according to the order of the sequence above, while the proofs are omitted since they are similar to much of the work performed in this section. Together these results complete the proof of Theorem 3.

Lemma 8. *Fix* $(N, m) = (8, 3)$*, then the following is true for* (2.26)*. There are constants* $d_1, \mu_1 > 0$ *and a smooth function* $\mu_l : [0, d_1] \to [0, \mu_1]$ *such that for each* $d \in (0, d_1]$*, there is a pair of* κ*-symmetric solutions* $U_l(\mu, d)$ *and* $V_l(\mu, d)$ *of* (2.26) *that bifurcate at a fold bifurcation at* $\mu = \mu_l(d)$ *and exist for all* $\mu \in [\mu_l(d), \mu_1]$*. These solutions are smooth in* (μ, d)*, and for each fixed* μ*, we have* $U_l(\mu, d) \to \bar{U}^{(1)}(\mu)$ *and* $V_l(\mu, d) \to \bar{W}_-^{(24)}(\mu)$ *as* $d \to 0^+$*. The function* $\mu_l(d)$ *satisfies* $\mu_l(d) = \frac{3}{\sqrt[3]{2}} d^{\frac{2}{3}} + \mathcal{O}(d)$*.*

Lemma 9. *Fix* $(N, m) = (8, 3)$*, then the following is true for* (2.26)*. There exist constants* $d_2, \mu_2 > 0$ *and a smooth function* $\mu_r : [0, d_2] \to [\mu_2, 1]$ *such that for each fixed* $d \in (0, d_2]$*, there is a pair of* κ*-symmetric solutions* $U_r(\mu, d)$ *and* $V_r(\mu, d)$ *of* (2.26) *that bifurcate at a fold bifurcation at* $\mu = \mu_r(d)$ *and exist for all* $\mu \in [\mu_2, \mu_r(d)]$*. These solutions are smooth in* (μ, d)*, and for each fixed* μ*, we have* $U_r(\mu, d) \to \bar{W}_-^{(24)}(\mu)$ *and* $V_r(\mu, d) \to \bar{W}_+^{(24)}(\mu)$ *as* $d \to 0^+$*. The function* $\mu_r(d)$ *is given by* $\mu_r(d) = 1 - 2d + \mathcal{O}(d^{\frac{3}{2}})$*.*

Lemma 10. *Fix* $(N, m) = (8, 3)$*, then the following is true for* (2.26)*. There are constants* $d_1, \mu_1 > 0$ *and a smooth function* $\mu_l : [0, d_1] \to [0, \mu_1]$ *such that for each* $d \in (0, d_1]$*, there is a pair of* κ*-symmetric solutions* $U_l(\mu, d)$ *and* $V_l(\mu, d)$ *of* (2.26) *that bifurcate at a fold bifurcation at* $\mu = \mu_l(d)$ *and exist for all* $\mu \in [\mu_l(d), \mu_1]$*. These solutions are smooth in* (μ, d)*, and for each fixed* μ*, we have* $U_l(\mu, d) \to \bar{W}_+^{(23)}(\mu)$ *and* $V_l(\mu, d) \to \bar{W}_-^{(3)}(\mu)$ *as* $d \to 0^+$*. The function* $\mu_l(d)$ *satisfies* $\mu_l(d) = \frac{3}{\sqrt[3]{2}} d^{\frac{2}{3}} + \mathcal{O}(d)$*.*

Lemma 11. *Fix* $(N, m) = (8, 3)$*, then the following is true for* (2.26)*. There exist constants* $d_2, \mu_2 > 0$ *and a smooth function* $\mu_r : [0, d_2] \to [\mu_2, 1]$ *such that for each fixed* $d \in (0, d_2]$*, there is a pair of* κ*-symmetric solutions* $U_r(\mu, d)$ *and* $V_r(\mu, d)$ *of* (2.26) *that bifurcate at a fold bifurcation at* $\mu = \mu_r(d)$ *and exist for all* $\mu \in [\mu_2, \mu_r(d)]$*. These solutions are smooth in* (μ, d)*, and for each fixed* μ*, we have* $U_r(\mu, d) \to \bar{W}_-^{(3)}(\mu)$ *and* $V_r(\mu, d) \to \bar{U}^{(4)}(\mu)$ *as* $d \to 0^+$*. The function* $\mu_r(d)$ *is given by* $\mu_r(d) = 1 - 2d + \mathcal{O}(d^{\frac{3}{2}})$*.*

3.4 All-to-all coupling

Let us now consider the case of all-to-all coupling. That is, $m = \lfloor \frac{N}{2} \rfloor$, and so every element is connected to all other elements. Then, our interest in $S_k \times S_{N-k}$-invariant solutions means that the system (2.18) reduces to solving the two equations

$$\begin{cases} d(N-k)(v_2 - v_1) + f(v_1, \mu) = 0, & \text{(2.39a)} \\ dk(v_1 - v_2) + f(v_2, \mu) = 0 & \text{(2.39b)} \end{cases}$$

where v_1 denotes the values of the vector in $\mathbb{R}^N$ at the first k indices and v_2 the values of the last $N-k$. As stated at the beginning of this section, we clearly have that for μ belonging to any compact interval of $[0,1]$ we can continue a solution of (2.25) at $d = 0$ with $u_n \in \{0, u_\pm(\mu)\}$ for all $n = 2, \dots, N$ regularly into $d > 0$ with the implicit function theorem. Moreover, from the form of (2.39), we may restrict $\mathcal{F}$ to a $S_k \times S_{N-k}$-invariant subspace to guarantee that solutions which are $S_k \times S_{N-k}$-invariant at $d = 0$ persist into $d > 0$ with the same symmetry. Hence, to prove Theorem 4 we again need only check continuation into $d > 0$ of the connections between the elements $\bar{A}^{(k)}_\pm(\mu)$, $\bar{B}^{(k)}(\mu)$, $\bar{C}^{(k)}_\pm(\mu)$, and $\bar{D}^{(k)}(\mu)$ near $\mu = 0, 1$ (see Figure 2.5 for visual demonstration).

We begin with the following lemma which details the continuation into $d > 0$ of the connections between $\bar{A}^{(k)}_+(\mu)$ and $\bar{B}^{(k)}(\mu)$, and $\bar{C}^{(k)}_+(\mu)$ and $\bar{D}^{(k)}(\mu)$, near $\mu = 0$.

Lemma 12. *For any $N \geq 2$ and $k = 1, \dots, \lfloor N/2 \rfloor$, the following is true for (2.26).*

1) *There are constants $d_{ab}, \mu_{ab} > 0$ and a smooth function $\mu_l : [0, d_{ab}] \to [0, \mu_{ab}]$ such that for each $d \in (0, d_{ab}]$, there is a pair of $S_k \times S_{N-k}$-symmetric solutions $U_{ab}(\mu, d)$ and $V_{ab}(\mu, d)$ of (2.26) that bifurcate at a fold bifurcation at $\mu = \mu_l(d)$ and exist for all $\mu \in [\mu_l(d), \mu_{ab}]$. These solutions are smooth in (μ, d), and for*

each fixed μ*, we have* $U_{ab}(\mu, d) \to \bar{A}_{+}^{(k)}(\mu)$ *and* $V_{ab}(\mu, d) \to \bar{B}^{(k)}(\mu)$ *as* $d \to 0^{+}$*. The function* $\mu_l(d)$ *satisfies* $\mu_l(d) = 3\sqrt[3]{\frac{k^2}{4}}d^{\frac{2}{3}} + \mathcal{O}(d)$*.*

2) *There are constants* $d_{cd}, \mu_{cd} > 0$ *and a smooth function* $\mu_l : [0, d_{cd}] \to [0, \mu_{cd}]$ *such that for each* $d \in (0, d_{cd}]$*, there is a pair of* $S_k \times S_{N-k}$*-symmetric solutions* $U_{cd}(\mu, d)$ *and* $V_{cd}(\mu, d)$ *of* (2.26) *that bifurcate at a fold bifurcation at* $\mu = \mu_l(d)$ *and exist for all* $\mu \in [\mu_l(d), \mu_{cd}]$*. These solutions are smooth in* (μ, d)*, and for each fixed* μ*, we have* $U_{cd}(\mu, d) \to \bar{C}_{+}^{(k)}(\mu)$ *and* $V_{cd}(\mu, d) \to \bar{D}^{(k)}(\mu)$ *as* $d \to 0^{+}$*. The function* $\mu_l(d)$ *satisfies* $\mu_l(d) = 3\sqrt[3]{\frac{(N-k)^2}{4}}d^{\frac{2}{3}} + \mathcal{O}(d)$*.*

Proof. We will only prove the first case in the lemma since the second can simply be obtained by exchanging v_1 and v_2 in (2.39) in what follows. In this notation, the functions $\bar{A}_{\pm}^{(k)}(\mu)$ and $\bar{B}^{(k)}(\mu)$ correspond to solutions of (2.39) with $d = 0$ as well as $(v_1, v_2) = (u_{\pm}(\mu), 0)$ and $(u_{+}(\mu), u_{-}(\mu))$, respectively, for all $\mu \in [0, 1]$. For convenience, we will denote

$$\begin{aligned} \mathcal{F}_1(v_1, v_2, \mu, d) &= d(N-k)(v_2 - v_1) + f(v_1, \mu) \\ \mathcal{F}_2(v_1, v_2, \mu, d) &= dk(v_1 - v_2) + f(v_2, \mu) \end{aligned} \tag{2.40}$$

to emphasize the connection of the system (2.39) with the function $\mathcal{F}$ that we defined in (2.25). Importantly, solutions of $\mathcal{F}_1 = \mathcal{F}_2 = 0$ represent $S_k \times S_{N-k}$-invariant steady-state solutions of (2.25).

In the present scenario, we recall that $u_{+}(0) = 1$ and restrict ourselves to a neighbourhood of the solution $(v_1, v_2, \mu, d) = (1, 0, 0, 0)$ to (2.39). From the previous discussion, this represents a $S_k \times S_{N-k}$-invariant neighbourhood of the solution $(U, \mu, d) = (\bar{A}_{+}^{(k)}(0), 0, 0)$ to $\mathcal{F}$ in (2.25). Then, since

$$\frac{\partial \mathcal{F}_1}{\partial v_1}(1, 0, 0, 0) = f_u(1, 0) \neq 0, \tag{2.41}$$

the implicit function theorem guarantees the existence of a unique smooth function $v_1^*(v_2,\mu,d)$ satisfying $v_1^*(0,0,0) = 1$ and $\mathcal{F}_1(v_1^*(v_2,\mu,d),v_2,\mu,d) = 0$ for all (v_2,μ,d) in a neighbourhood of $(0,0,0)$. Hence, the Taylor series of $v_1^*(v_2,\mu,d)$ about $(v_2,\mu,d) = (0,0,0)$ is given by

$$v_1^*(v_2,\mu,d) = 1 + \mathcal{O}(|\mu| + |d| + |v_2||d|). \tag{2.42}$$

The analysis now reduces to solving $\mathcal{F}_2(v_1,v_2,\mu,d) = 0$ with $v_1 = v_1^*(v_2,\mu,d)$ in a neighbourhood of $(v_2,\mu,d) = (0,0,0)$.

As in the previous lemmas of this section, let us introduce the re-scaled variables

$$\mu = \nu^2, \qquad d = \nu^3\tilde{d}, \qquad v_2 = \nu\tilde{v}_2, \tag{2.43}$$

for $|\nu| \ll 1$, so that (2.42) becomes

$$v_1^*(v_2,\mu,d) = 1 + \mathcal{O}(\nu^2). \tag{2.44}$$

Then, putting $v_1 = v_1^*(v_2,\mu,d)$ into $\mathcal{F}_2$ and expanding using (2.42) and (2.27) gives

$$\mathcal{F}_2(v_1^*(v_2,\mu,d),v_2,\mu,d) = \nu^3(k\tilde{d} - \tilde{v}_2 + \tilde{v}_2^3) + \mathcal{O}(\nu^4). \tag{2.45}$$

Hence, solving $\mathcal{F}_2(v_1^*(v_2,\mu,d),v_2,\mu,d) = 0$ is equivalent to solving

$$0 = k\tilde{d} - \tilde{v}_2 + \tilde{v}_2^3 + \mathcal{O}(\nu) \tag{2.46}$$

after dividing off ν^3. It is therefore clear that the above expression experiences a fold bifurcation at

$$(\tilde{v}_2,\tilde{d},\nu) = \left(\sqrt[3]{\frac{k}{2}}, \frac{2}{3\sqrt{3}k}, 0\right), \tag{2.47}$$

for which we may follow as in the proofs of the previous lemmas to demonstrate the persistence of this fold into sufficiently small $\nu > 0$. This completes the proof. $\square$

Let us now turn to the bifurcation near $\mu = 1$. The following lemma details the persistence of the connections between $\bar{A}_-^{(k)}(\mu)$ and $\bar{A}_+^{(k)}(\mu)$, and $\bar{C}_-^{(k)}(\mu)$ and $\bar{C}_+^{(k)}(\mu)$ into $d > 0$.

Lemma 13. *For any $N \geq 2$ and $k = 1, \ldots, \lfloor N/2 \rfloor$, the following is true for (2.26).*

1) *There exist constants $d_{aa}, \mu_{aa} > 0$ and a smooth function $\mu_r : [0, d_{aa}] \to [\mu_{aa}, 1]$ such that for each fixed $d \in (0, d_{aa}]$, there is a pair of $S_k \times S_{N-k}$-symmetric solutions $U_{aa}(\mu, d)$ and $V_{aa}(\mu, d)$ of (2.26) that bifurcate at a fold bifurcation at $\mu = \mu_r(d)$ and exist for all $\mu \in [\mu_{aa}, \mu_r(d)]$. These solutions are smooth in (μ, d), and for each fixed μ, we have $U_{aa}(\mu, d) \to \bar{A}_-^{(k)}(\mu)$ and $V_{aa}(\mu, d) \to \bar{A}_+^{(k)}(\mu)$ as $d \to 0^+$. The function $\mu_r(d)$ satisfies $\mu_r(d) = 1 - (N-k)d + \mathcal{O}(d^{\frac{3}{2}})$.*
2) *There exist constants $d_{cc}, \mu_{cc} > 0$ and a smooth function $\mu_r : [0, d_{cc}] \to [\mu_{cc}, 1]$ such that for each fixed $d \in (0, d_{cc}]$, there is a pair of $S_k \times S_{N-k}$-symmetric solutions $U_{cc}(\mu, d)$ and $V_{cc}(\mu, d)$ of (2.26) that bifurcate at a fold bifurcation at $\mu = \mu_r(d)$ and exist for all $\mu \in [\mu_{cc}, \mu_r(d)]$. These solutions are smooth in (μ, d), and for each fixed μ, we have $U_{cc}(\mu, d) \to \bar{C}_-^{(k)}(\mu)$ and $V_{cc}(\mu, d) \to \bar{C}_+^{(k)}(\mu)$ as $d \to 0^+$. The function $\mu_r(d)$ satisfies $\mu_r(d) = 1 - kd + \mathcal{O}(d^{\frac{3}{2}})$.*

Proof. Since we are interested in $S_k \times S_{N-k}$-invariant solutions of (2.26), we may again proceed as in the proof of Lemma 12 and reduce to solving the equations (2.39). As in Lemma 12, we will only prove the first statement since the second follows from simply interchanging v_1 and v_2 in what follows. The difference is that now we focus a neighbourhood of the solution $(v_1, v_2, \mu, d) = (1, 0, 1, 0)$, corresponding to a $S_k \times S_{N-k}$-invariant neighbourhood of the solution $(U, \mu, d) = (\bar{A}_\pm^{(k)}(1), 1, 0)$ of

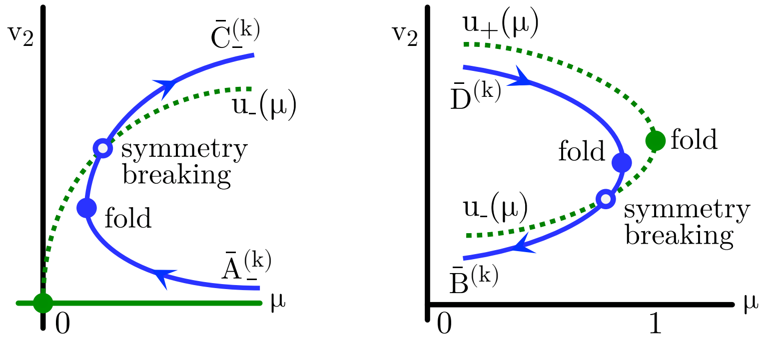

Figure 2.8: We illustrate the bifurcation diagrams of $S_k \times S_{N-k}$-symmetric solutions for all-to-all coupling for fixed $0 < d \ll 1$ and $1 \leq k \leq \lfloor N/2 \rfloor$ outlined in Lemma 14 for μ near zero (left panel) and in Lemma 15 for μ near one (right panel). The dotted curve corresponds to the family of S_N-symmetric equilibria (where $v_1 = v_2$), and the solid curve reflects the branch of $S_k \times S_{N-k}$-symmetric solutions (with $v_1 \neq v_2$), which bifurcates from the branch of S_N-symmetric solutions in a symmetry-breaking bifurcation and also undergoes a fold bifurcation; arrows indicate the direction of increasing ϕ (left) and s (right) that parametrize these branches.

(2.26). Since we have

$$\frac{\partial \mathcal{F}_2}{\partial v_2}(1,0,1,0) = f_u(0,1) \neq 0, \tag{2.48}$$

we may apply the implicit function theorem to obtain a smooth function $v_2^*(v_1, \mu, d)$ defined in a neighbourhood of $(v_1, \mu, d) = (1,1,0)$ satisfying $v_2^*(1,1,0) = 0$ and $\mathcal{F}_2(v_1, v_2^*(v_1,\mu,d), \mu, d) = 0$. Solving

$$\mathcal{F}_1(v_1, v_2^*(v_1,\mu,d), \mu, d) = 0 \tag{2.49}$$

in a neighbourhood of $(v_1, \mu, d) = (1,1,0)$ then proceeds as in the lemmas of the previous subsections and is therefore omitted. $\square$

Next, we investigate the patterns $\bar{A}_-^{(k)}(\mu)$ and $\bar{C}_-^{(k)}(\mu)$ near $\mu = 0$ for $0 < d \ll 1$ and prove that they disappear through a collision with the branch of S_N-symmetric equilibria at which $v_1 = v_2 = u_-(\mu)$. We state this lemma for the system (2.39) and refer to the left panel in Figure 2.8 for an illustration of the bifurcation diagram.

Lemma 14. *For each $N \geq 2$, $k = 1, \ldots, \lfloor N/2 \rfloor$, and $\epsilon > 0$, there is a constant $\delta > 0$ with the following property. There is a unique branch of positive $S_k \times S_{N-k}$-symmetric equilibria of (2.26) near $(u, \mu) = (0, 0)$, and this branch is smooth and given by*

$$(v_1, v_2, d, \mu)(\phi, s) = \Bigg(s\cos\phi, s\sin\phi, \frac{(\cos\phi + \sin\phi)\cos\phi\sin\phi}{k\cos\phi + (N-k)\sin\phi} s^2 + \mathcal{O}(s^4), \\ \frac{k\cos^3\phi + (N-k)\sin^3\phi}{k\cos\phi + (N-k)\sin\phi} s^2 + \mathcal{O}(s^4) \Bigg)$$

for $\epsilon < \phi < \frac{\pi}{2} - \epsilon$ and $0 \leq s < \delta$. Furthermore, the branch can also be parametrized smoothly by (d, ϕ) via

$$s = \frac{k\cos\phi + (N-k)\sin\phi}{(\cos\phi + \sin\phi)\cos\phi\sin\phi} d + \mathcal{O}(d^2).$$

It bifurcates at $\mu = \mu_{\mathrm{sb}}(d) = \frac{Nd}{2} + \mathcal{O}(d^2)$ from the S_N-symmetric branch $v_1 = v_2 = u_-(\mu)$ (this bifurcation point is the same for each k), and it undergoes a unique fold bifurcation at $\mu = \mu_{\mathrm{fd}}(d)$ for some $0 < \phi \leq \frac{\pi}{4}$ with $0 < \mu_{\mathrm{fd}}(d) \leq \mu_{\mathrm{sb}}(d)$. As $\phi \to 0$ and $\phi \to \frac{\pi}{2}$, the parameter d approaches zero, and the equilibria (v_1, v_2) approach $\bar{A}_-^{(k)}(\mu(0, s))$ and $\bar{C}_-^{(k)}(\mu(\frac{\pi}{2}, s))$, respectively.

Proof. Recall that we need to solve the system (2.39) given by

$$\begin{cases} d(N-k)(v_2 - v_1) + f(v_1, \mu) = 0, & \text{(2.50a)} \\ dk(v_1 - v_2) + f(v_2, \mu) = 0 & \text{(2.50b)} \end{cases}$$

where v_1 denotes the values of the vector in $\mathbb{R}^N$ at the first k indices and v_2 the values of the last $N - k$ indices. Recall also that

$$f(u, \mu) = -\mu u + u^3 + \mathcal{O}(\mu^2 u + \mu u^3 + u^5)$$

First, when $u = v_1 = v_2$, equation (2.50) reduces to $f(u, \mu) = 0$ which admits the solution branch $(u, \mu) = (u_-(s), \mu_\mathrm{h}(s))$ for $0 \leq s \ll 1$ with $u_-(0) = \mu_\mathrm{h}(0) = 0$ and $\mu_\mathrm{h}(s) > 0$ for $s > 0$. Next, we subtract the two equations in (2.50) to obtain

$$dN(v_2 - v_1) + f(v_1, \mu) - f(v_2, \mu) = 0. \tag{2.51}$$

Defining $v = (v_1, v_2)$ and

$$g(v_1, v_2, \mu) := \int_0^1 f_u(v_2 + \tau(v_1 - v_2), \mu) d\tau = -\mu + v_1^2 + v_1 v_2 + v_2^2 + \mathcal{O}(\mu^2 + |v|^4),$$

we can write (2.51) as

$$dN(v_2 - v_1) + f(v_1, \mu) - f(v_2, \mu) = dN(v_2 - v_1) + (v_1 - v_2) g(v_1, v_2, \mu) = 0.$$

Since we already analysed the case $v_1 = v_2$, we can divide by $v_1 - v_2$ to arrive at

$$-dN + g(v_1, v_2, \mu) = -dN - \mu + v_1^2 + v_1 v_2 + v_2^2 + \mathcal{O}(\mu^2 + |v|^4) = 0,$$

which we can solve for μ as a function $\mu(v_1, v_2, d)$ near $(v_1, v_2, d) = (0, 0, 0)$ where

$$\mu(v_1, v_2, d) = v_1^2 + v_1 v_2 + v_2^2 - dN + \mathcal{O}(d^2 + |v|^4).$$

It therefore suffices to solve (2.50b) which becomes

$$\begin{aligned}
0 &= dk(v_1 - v_2) + f(v_2, \mu) \\
&= dk(v_1 - v_2) - \mu(v_1, v_2, d) v_2 + v_2^3 + v_2 \mathcal{O}(\mu(v_1, v_2, d)^2 + \mu(v_1, v_2, d) v_2^2 + v_2^4) \\
&= dk(v_1 - v_2) + v_2(dN - v_1^2 - v_1 v_2 + \mathcal{O}(d^2 + |v|^4))
\end{aligned}$$

and finally arrives at

$$dkv_1 + d(N-k)v_2 - v_1v_2(v_1+v_2) + v_2\mathcal{O}(d^2+|v|^4) = 0. \tag{2.52}$$

To solve (2.52), we set $v = (v_1, v_2) = s(\cos\phi, \sin\phi)$ with $0 \le s \ll 1$ and $0 < \phi < \pi/2$ so that (2.52) becomes

$$d(k\cos\phi + (N-k)\sin\phi) - s^2\cos\phi\sin\phi(\cos\phi+\sin\phi) + \mathcal{O}(d^2+s^4) = 0 \tag{2.53}$$

after dividing by s. Using the implicit function theorem, we can now solve this equation for d as a function of (ϕ, s) with $|s| < \delta$ for some $\delta > 0$ uniformly in $0 \le \phi \le \pi/2$ and obtain

$$d(\phi, s) = \frac{(\cos\phi+\sin\phi)\cos\phi\sin\phi}{k\cos\phi+(N-k)\sin\phi}s^2 + \mathcal{O}(s^4).$$

Substituting the expressions for (v_1, v_2, d) as functions of (ϕ, s) into the formula for $\mu(v_1, v_2, d)$ gives

$$\mu(\phi, s) = \frac{k\cos^3\phi+(N-k)\sin^3\phi}{k\cos\phi+(N-k)\sin\phi}s^2 + \mathcal{O}(s^4),$$

which proves the first part of the lemma. Inspecting the limits $\phi \to 0$ and $\phi \to \frac{\pi}{2}$ for each fixed $0 < s < \delta$, we see that d converges to zero, μ approaches $s^2 + \mathcal{O}(s^4)$, and (v_1, v_2) approach $\bar{A}_-^{(k)}(\mu(0,s))$ and $\bar{C}_-^{(k)}(\mu(\frac{\pi}{2}, s))$, respectively, as claimed. Similarly, substituting $\phi = \pi/4$ into the expressions for (v_1, v_2, d, μ) shows that the branch we constructed bifurcates from the branch of S_N-symmetric equilibria at $(\mu, d) = (\frac{1}{2}, \frac{1}{N})s^2 + (\mathcal{O}(s^4), \mathcal{O}(s^4))$.

Fixing $\epsilon > 0$, we now restrict ourselves to values of ϕ with $\epsilon < \phi < \frac{\pi}{2} - \epsilon$. For such values, we can solve for s as a function of (d, ϕ) where

$$s^2 = s(d,\phi)^2 = \frac{k\cos\phi + (N-k)\sin\phi}{(\cos\phi + \sin\phi)\cos\phi\sin\phi} d + \mathcal{O}(d^2)$$

so that μ can be written as a smooth function of (d, ϕ) via

$$\mu(d,\phi) = \left(\frac{k\cos^3\phi + (N-k)\sin^3\phi}{(\cos\phi + \sin\phi)\cos\phi\sin\phi} + \mathcal{O}(d)\right) d =: (\tilde{\mu}(\phi) + \mathcal{O}(d))d.$$

It remains to prove that the branch has a unique fold for each fixed d, and it suffices to prove this for $\tilde{\mu}(\phi)$ since its folds are generic and therefore persist upon adding the remainder term in d. We now outline the strategy for proving that $\tilde{\mu}(\phi)$ has a unique generic fold. Note that $\tilde{\mu}(\phi) \to \infty$ for $\phi \to 0$ and $\phi \to \frac{\pi}{2}$, and it therefore suffices to show that $\tilde{\mu}'(\phi)$ increases strictly, which holds when $\tilde{\mu}''(\phi) > 0$. The second derivative $\tilde{\mu}''(\phi)$ is a fraction of trigonometric polynomials, and we can then show that this derivative is indeed positive (we omit the tedious details). The fold bifurcation occurs in the region $0 < \phi \leq \frac{\pi}{4}$ since $\tilde{\mu}'(\frac{\pi}{4}) = \frac{3}{2}(N-2k) \geq 0$ (recall that $1 \leq k \leq \lfloor N/2 \rfloor$). □

Finally, we describe the continuation into $0 < d \ll 1$ of the connection between $\bar{B}^{(k)}(\mu)$ and $\bar{D}^{(k)}(\mu)$ near $\mu = 1$. We comment that this lemma covers the connection in the top-right corner of Figure 2.2(c) and that the results are also illustrated in the right panel in Figure 2.8.

Lemma 15. *For each $N \geq 2$ and $k = 1, \ldots, \lfloor N/2 \rfloor$, there is a constant $\delta > 0$ with the following property. There is a unique branch of $S_k \times S_{N-k}$-symmetric equilibria of (2.26) near $(u, \mu) = (1, 1)$, and this branch is smooth and given by*

$$(v_1, v_2, \mu)(s,d) = (1+s, 1-s-Nd+\mathcal{O}(s^2+d^2), 1-s^2-(N-k)(2s+Nd)d+\mathcal{O}(ds^2+s^3+d^3))$$

for $|s| < \delta$ and $0 \le d < \delta$. Furthermore, this branch bifurcates at $\mu = 1 - \frac{N^2 d}{4} + \mathcal{O}(d^3)$ when $s = -\frac{Nd}{2} + \mathcal{O}(d^2)$ from the S_N-symmetric branch at which $v_1 = v_2 = u_-(\mu)$ (this bifurcation point is the same for each k) and undergoes a unique fold bifurcation at $\mu = 1 - k(N-k)d^2 + \mathcal{O}(d^3)$ when $s = -(N-k)d + \mathcal{O}(d^2)$. As $d \to 0^+$, the solution (v_1, v_2) converges to $\bar{B}^{(k)}(\mu(s,0))$ for fixed $s > 0$ and to $\bar{D}^{(k)}(\mu(s,0))$ for $s < 0$.

Proof. We consider the neighbourhood of the solution $(v_1, v_2, \mu, d) = (1, 1, 1, 0)$ to (2.39). For simplicity, denote $\mu = 1 - \tilde{\mu}$, $v_1 = 1 + \tilde{v}_1$, and $v_2 = 1 + \tilde{v}_2$. Using the expansion (2.28) these new variables transform (2.39) to

$$\begin{cases} \tilde{\mathcal{F}}_1(\tilde{v}_1, \tilde{v}_2, \tilde{\mu}, d) = d(N-k)(\tilde{v}_2 - \tilde{v}_1) + \tilde{\mu} - \tilde{v}_1^2 - b\tilde{\mu}\tilde{v}_1 + \mathcal{O}(\tilde{\mu}^2 + \tilde{\mu}|\tilde{v}_1|^2 + |\tilde{v}_1|^3) = 0, & \text{(2.54a)} \\ \tilde{\mathcal{F}}_2(\tilde{v}_1, \tilde{v}_2, \tilde{\mu}, d) = dk(\tilde{v}_1 - \tilde{v}_2) + \tilde{\mu} - \tilde{v}_2^2 - b\tilde{\mu}\tilde{v}_2 + \mathcal{O}(\tilde{\mu}^2 + \tilde{\mu}|\tilde{v}_2|^2 + |\tilde{v}_2|^3) = 0. & \text{(2.54b)} \end{cases}$$

We can apply the implicit function theorem to equation (2.54a) and find a unique smooth function $\tilde{\mu}^*(\tilde{v}_1, \tilde{v}_2, d)$, defined in a neighbourhood of $(\tilde{v}_1, \tilde{v}_2, d) = (0, 0, 0)$, satisfying $\tilde{\mu}^*(0, 0, 0) = 0$ and $\tilde{\mathcal{F}}_1(\tilde{v}_1, \tilde{v}_2, \tilde{\mu}^*(\tilde{v}_1, \tilde{v}_2, d), d) = 0$, in the neighbourhood of $(0, 0, 0, 0)$. Moreover, we have the expansion

$$\tilde{\mu}^*(\tilde{v}_1, \tilde{v}_2, d) = -d(N-k)(\tilde{v}_2 - \tilde{v}_1) + \tilde{v}_1^2 + \mathcal{O}(|d||\tilde{v}|^2 + |\tilde{v}|^3), \tag{2.55}$$

where $\tilde{v} = (\tilde{v}_1, \tilde{v}_2)$. Next, we subtract the two equations in (2.39) to obtain

$$Nd(v_2 - v_1) + f(v_1, \mu) - f(v_2, \mu) = 0. \tag{2.56}$$

Defining

$$g(\tilde{v}_1, \tilde{v}_2, \tilde{\mu}) := \int_0^1 f_u(v_2 + \tau(v_1 - v_2), \mu) d\tau = -\tilde{v}_1 - \tilde{v}_2 + \mathcal{O}(|\tilde{\mu}| + |\tilde{\mu}||\tilde{v}_1| + |\tilde{\mu}||\tilde{v}_2| + |\tilde{v}|^2),$$

we can write (2.56) in new variables as

$$Nd(\tilde{v}_2-\tilde{v}_1)+f(1+\tilde{v}_1,1-\tilde{\mu})-f(1+\tilde{v}_2,1-\tilde{\mu}) = Nd(\tilde{v}_2-\tilde{v}_1)+g(\tilde{v}_1,\tilde{v}_2,\tilde{\mu})(\tilde{v}_1-\tilde{v}_2) = 0.$$

Assuming $\tilde{v}_1 \neq \tilde{v}_2$, we can divide by $\tilde{v}_2 - \tilde{v}_1$ to arrive at

$$Nd - g(\tilde{v}_1,\tilde{v}_2,\tilde{\mu}) = Nd + \tilde{v}_1 + \tilde{v}_2 + \mathcal{O}(|\tilde{\mu}| + |\tilde{\mu}||\tilde{v}_1| + |\tilde{\mu}||\tilde{v}_2| + |\tilde{v}|^2) = 0.$$

We can further substitute the expression (2.55) for $\tilde{\mu}$ and find

$$Nd + \tilde{v}_1 + \tilde{v}_2 + \mathcal{O}(d|\tilde{v}| + |\tilde{v}|^2) = 0.$$

Using the implicit function theorem to solve for $\tilde{v}_2$ as a function of $(\tilde{v}_1, d)$ in a neighbourhood of $(0,0)$ gives

$$\tilde{v}_2^*(\tilde{v}_1, d) = -Nd - \tilde{v}_1 + \mathcal{O}(d|\tilde{v}_1| + |\tilde{v}_1|^2), \tag{2.57}$$

and substituting this expression into (2.55) we finally find

$$\tilde{\mu}^*(\tilde{v}_1, d) = \tilde{v}_1^2 + (N-k)d(2\tilde{v}_1 + Nd) + \mathcal{O}(d\tilde{v}_1^2 + |\tilde{v}_1|^3 + d^3). \tag{2.58}$$

Hence, a fold bifurcation takes place at $\tilde{v}_1 = \tilde{v}_1^*(d) = -(N-k)d + \mathcal{O}(d^2)$ when d is near 0, and substituting $\tilde{v}_1^*(d)$ into $\tilde{\mu}^*(\tilde{v}_1, d)$ gives the claimed expansion. Solving the equation $\tilde{v}_1 = \tilde{v}_2$ for d near zero using the implicit function theorem provides the existence and expansion of the symmetry-breaking bifurcation from the family of homogeneous equilibria. This completes the proof. $\square$

4 Discussion

In this chapter, we characterized the branches of localized steady states of lattice dynamical systems on a ring with N nodes with symmetric sparse, almost all-to-all, and all-to-all coupling. We found snaking branches with $\lfloor \frac{N}{2} \rfloor$ saddle-node bifurcations on each side for sparse coupling with interaction range $m = 1, 2$ and figure-eight type branches that start and end at homogeneous patterns for all-to-all coupling. The case of almost all-to-all coupling for even N is more complicated due to additional symmetries, and we provided a detailed analysis only for $N \in \{6, 8\}$.

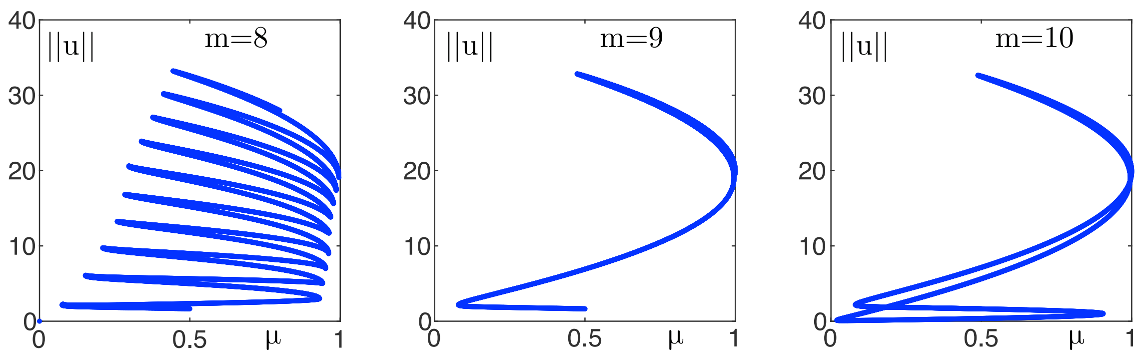

Figure 2.9: Shown are the results of numerical continuation for $d = 0.005$ and $N = 20$ nodes with (from left to right) sparse coupling for $m = 8$, almost all-to-all coupling $m = 9$, and all-to-all coupling $m = 10$. Each branch starts at $\mu = 0.5$ with a single node at the upper stable branch of the zero set of $f(u, \mu) = -\mu u + 2u^3 - u^5$ and the remaining nodes at zero.

There are many questions we did not address in this chapter, and we now outline a few of these. First, for sparse coupling, we do not know whether solution branches terminate at a branch of homogeneous equilibria or pass near those branches. Numerical continuation turns out to be complicated for small coupling strengths since the Jacobian has N eigenvalues close to zero near the homogeneous branches for $0 < d \ll 1$, which makes continuation difficult and allows for the possibility that numerical solutions may jump onto different branches.

Next, we will comment on different forms of coupling. Note first that, near the anti-continuum limit, the precise form of coupling matters only near the pitchfork at $\mu = 0$ and the fold at $\mu = 1$: the branches for $0 < \mu < 1$ can always be continued into $0 < d \ll 1$ regardless of the coupling function, so the key task is to track these branches near $\mu = 0, 1$. We believe that our results for symmetric nearest-neighbour and next-nearest-neighbour coupling can be extended to other values of m: we conjecture that we will always find snaking curves that exhibit $\lfloor \frac{N}{2} \rfloor$ saddle nodes as long as the interaction range m is strictly less than $\lfloor \frac{N}{2} \rfloor - 1$, and we expect that the methods we utilized here can be used to study this more general case. Figure 2.9 indicates that the case of almost all-to-all coupling (when $m = \lfloor \frac{N}{2} \rfloor - 1$) is more complicated. The case of asymmetric or distance-dependent coupling coefficients is also unclear. In the case of asymmetric coupling, our methods should be applicable, though we expect that the specific details will be different. Distance-dependent coupling is likely more complicated: for instance, the case of all-to-all coupling will be different since the S_N symmetry is no longer present in this case.

Finally, we briefly discuss possible extensions to more complicated finite lattices. Surprisingly, snaking was observed also on finite random graphs; see McCullen and Wagenknecht (2016). The formal analysis in Kusdiantara and Susanto (2019) and the complementary rigorous results in Bramburger and Sandstede (2020b) show that the shape of branches near folds seems to be determined by a small number of motifs where only a few nodes interact, whilst the states of all other nodes are essentially irrelevant. It might be this underlying generic structure that leads to the universality of snaking observed on random graphs in McCullen and Wagenknecht (2016). Using computations to obtain summary statistics of snaking on random graphs would be a feasible first step towards a more general description of snaking and branch structures on general finite graphs.

Chapter Three

Bifurcation from Homogeneous Branches on Ring Lattices

1 Introduction

Recall from Chapter 2 that our ring system follows

$$\dot{u}_n = d(\Delta_m U)_n + f(u_n, \mu), \quad 1 \le n \le N, \quad U = (u_1, u_2 \ldots, u_N) \in \mathbb{R}^N \tag{3.1}$$

where

$$(\Delta_m U)_n = \begin{cases} -(2m+1)u_n + \sum_{j=-m}^{m} u_{n+j}, & 1 \le m < \lfloor \frac{N}{2} \rfloor \\ -Nu_n + \sum_{j=1}^{N} u_j, & m = \lfloor \frac{N}{2} \rfloor. \end{cases}$$

Specifically, we use the cubic-quintic nonlinearity $f(u_n, \mu) = -\mu u_n + 2u_n^3 - u_n^5$ where $0 \le \mu \le 1$ and focus on nonnegative solutions where each $u_n \ge 0$ at the anti-continuum limit $d \ll 1$. We denote the two positive roots in u_n of $f(u_n, \mu)$ as $u_+(\mu) = \sqrt{1 + \sqrt{1-\mu}}$ and $u_-(\mu) = \sqrt{1 - \sqrt{1-\mu}}$.

For convenience, we re-show the main bifurcation results from Chapter 2 in Figure 3.1. In this chapter, we build on the results from the previous chapter and focus on investigating the connections of solution patterns near the lower-left and upper-right regions, which are marked by squares in Figure 3.1. Specifically, we want to understand whether the snaking curve terminates or bifurcates from other branches in these regions. To do this, we utilize the fact that our lattice system respects the symmetries of the dihedral group D_N.

Recall that the actions of our lattice group are ζ and κ, which define rotations and reflections respectively. Notice that when N is odd, the action of κ flips the ring with respect an axis joining a vertex of the N-gon to the midpoint of the opposite edge, leaving one node to be fixed; while when N is even, κ reflects the ring with

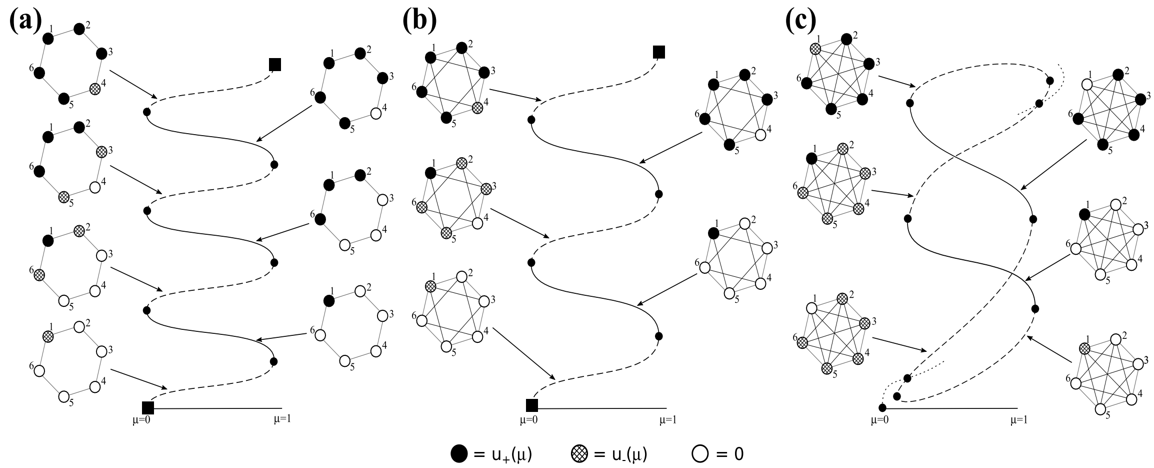

Figure 3.1: Different bifurcation curves depending on the number of symmetric connections over a six element ring. (a) Nearest-neighbour connections lead to a typical snaking bifurcation diagram. (b) Next-nearest-neighbour connections on a six element ring introduce a further symmetry for which the elements indexed by 2,3,5,6 bifurcate together near $\mu = 0$. (c) In the case of all-to-all coupling, the system is invariant with respect to any permutation of the nodes on the ring and so the bifurcation curves form a small closed curve that bifurcates from the homogeneous state (dotted curve) near the origin. Squares marking the end of the curves in panels (a) and (b) represent the set of exceptional bifurcations which are not proven in the previous chapter. This figure is reproduced from Figure 2.2 for ease of reference.

respect to an axis joining two opposite vertices, leaving two nodes to be fixed. The action of ζ does not depend on whether N is odd or even, and it always rotates the ring in the counter-clockwise direction by a radian of $\frac{2\pi}{N}$. Figure 3.2 illustrates examples of group actions on rings for these different cases.

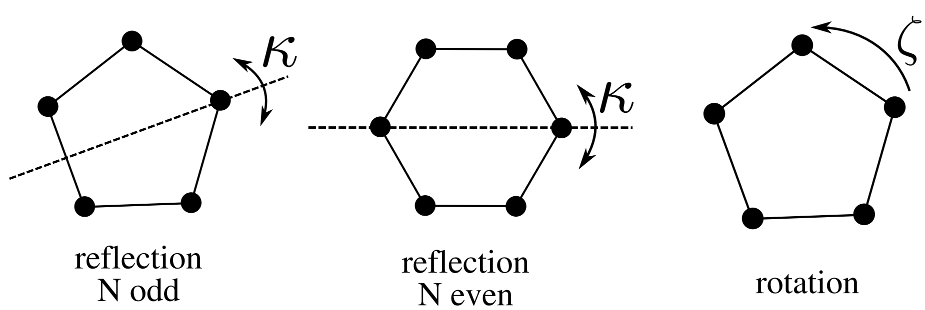

Figure 3.2: Examples of group actions on rings with D_N symmetry. Diagram on the left shows the action of reflection when N is odd, and the middle shows reflection when N is even. The diagram on the right depicts a typical action of rotation, which is independent of whether N is odd or even.

We study the bifurcation problem of system (3.1) with $N \geq 5$. Note that the cases $N = 3$ and $N = 4$ are excluded from our subsequent discussion since the bifurcation results for the dihedral group are exceptional in these cases. Our work examines the steady-state solutions

$$\mathbf{F}(U, \mu, d) = 0 \tag{3.2}$$

where $\mathbf{F}(U, \mu, d)_n \coloneqq d(\Delta_m U)_n - \mu u_n + 2u_n^3 - u_n^5$. We define $\mathbf{L}(U, \mu, d) \coloneqq D_U \mathbf{F}(U, \mu, d)$, which is the Jacobian of $\mathbf{F}(U, \mu, d)$ with respect to U.

We now apply the analysis from bifurcation theory to systems with symmetry. For a summary introduction to this area, we refer readers to Chapter 4 in Hoyle (2006). A representation of D_N, over some field F, is defined as a homomorphism from D_N to the group of matrices $GL_n(F)$, where n represents the dimension of the representation. We consider the group of spatial symmetries, D_N, with a linear matrix representation. Note that equation $\dot{U} = \mathbf{F}(U, \mu, d)$ is equivariant under D_N, which means we have the following equivariance condition on $\mathbf{F}(U, \mu, d)$

$$\gamma \mathbf{F}(U, \mu, d) = \mathbf{F}(\gamma U, \mu, d), \quad \forall \gamma \in D_N.$$

In particular, U is a solution if and only if γU is a solution to the system for every $\gamma \in D_N$. This implies that if U is an equilibrium solution satisfying equation (3.2), then so is γU for all symmetries $\gamma \in D_N$. We define the orbit of the action of D_N on U to be $D_N U = \{\gamma U : \gamma \in D_N\}$. The equivariance condition further implies that fixed-point solutions on the same orbit of D_N have the same stability and existence properties. In our subsequent discussion, all illustrations and results can be applied to all other solutions that lie in the same group orbit.

The isotropy subgroup associated with a stationary solution U to system (3.2) is defined as

$$\Sigma_U = \{\gamma \in D_N : \gamma U = U\} \subset D_N,$$

which is a subgroup comprising group elements that fix U and thus specify the symmetry of U.

In this chapter, we analyze bifurcations from the homogeneous branch using equivariant bifurcation theory for dihedral symmetry group and prove that branches of patterned states emerge from the homogeneous branches. Additionally, we prove the interesting fact that the criticality of the branches of patterns bifurcating from the homogeneous branch changes from supercritical to subcritical at a specific N-dependent value of m, which indicates a relation to the degree of coupling. In the limiting case as $N \to \infty$, we find that the change happens when $m/N \approx 0.39$ for the lower-left and $m/N \approx 0.41$ for the upper-right region.

Our main results for the bifurcation problem in the lower-left and the upper-right regions are summarized as follows. For convenience, let $\mathbb{e} = (1, 1, \ldots, 1) \in \mathbb{R}^N$. We first present results for the lower-left region.

There exist different bifurcation points on the homogeneous solution branch, $u_-(\mu)\mathbb{e}$. The following Theorem 5 (i) states the locations of these bifurcation points, indexed by j, for each given N and m. Figure 3.3 (a) presents a demonstration of these bifurcation points on the bifurcation diagram.

Theorem 5. *We assume $N \geq 5$. Consider the equilibrium solutions in configuration space (u_n, μ, d) where $0 < u_n \ll 1$ for $1 \leq n \leq N$, $0 < \mu \ll 1$ and $0 < d \ll 1$. Let $1 \leq m \leq \left\lfloor \frac{N}{2} \right\rfloor - 1$.*

(i) *The bifurcation points along the homogeneous solution branch* $u_-(\mu)\mathbb{e}$ *are* $\left(U_*^{(j)}, \mu_*^{(j)}\right)$ *with*

$$U_*^{(j)}(d) = \sqrt{d}\left(\sqrt{m - \sum_{p=1}^{m} \cos\left(\frac{2\pi jp}{N}\right)} + \mathcal{O}(d)\right)\mathbb{e}$$

and

$$\mu_*^{(j)}(d) = d\left(m - \sum_{p=1}^{m} \cos\left(\frac{2\pi jp}{N}\right) + \mathcal{O}(d)\right)$$

where $j \in \left\{0, 1, 2, \ldots, \lfloor \frac{N}{2} \rfloor\right\}$.

(ii) *We set* $j = 1$ *and assume that the null space of* $\mathbf{L}\left(U_*^{(1)}, \mu_*^{(1)}, d\right)$ *is 2-dimensional. Then, there are two branches bifurcating from the homogeneous solution branch at* $\left(U_*^{(1)}, \mu_*^{(1)}, d\right)$. *For odd* N, *the patterns along the two distinct branches have isotropy subgroup* $\mathbb{Z}_2(\kappa)$. *For even* N, *the patterns along the two distinct branches have isotropy subgroup* $\mathbb{Z}_2(\kappa)$ *and* $\mathbb{Z}_2(\kappa\zeta)$.

We define

$$\begin{aligned} X^{(j)} &= \left(\cos\left(\frac{2\pi j}{N}\right), \cos\left(2 \cdot \frac{2\pi j}{N}\right), \ldots, \cos\left(N \cdot \frac{2\pi j}{N}\right)\right) \\ \text{and} \quad Y^{(j)} &= \left(\sin\left(\frac{2\pi j}{N}\right), \sin\left(2 \cdot \frac{2\pi j}{N}\right), \ldots, \sin\left(N \cdot \frac{2\pi j}{N}\right)\right). \end{aligned} \tag{3.3}$$

At the bifurcation point $\left(U_*^{(j)}(d), \mu_*^{(j)}(d), d\right)$, we have the following lemma.

Lemma 16. *Let* $N \geq 5$, $1 \leq m \leq \left\lfloor \frac{N}{2} \right\rfloor - 1$, $0 < d \ll 1$, *and* $j \in \left\{1, 2, \ldots, \lfloor \frac{N}{2} \rfloor\right\}$. *Then* $\dim\left(\ker\left(\mathbf{L}(U_*^{(j)}, \mu_*^{(j)}, d)\right)\right) \geq 2$. *If* $\dim\left(\ker\left(\mathbf{L}(U_*^{(j)}, \mu_*^{(j)}, d)\right)\right) = 2$, *then*

$$\ker\left(\mathbf{L}\left(U_*^{(j)}, \mu_*^{(j)}, d\right)\right) = \operatorname{span}\left(X^{(j)}, Y^{(j)}\right).$$

Note that $j = 0$ is a special case where $\ker\left(\mathbf{L}\left(U_*^{(j)}, \mu_*^{(j)}, d\right)\right)$ has only one basis,

$\mathbb{e}$. Figure 3.3 (b) shows examples of the bases $X^{(j)}$ and $Y^{(j)}$ for $j = 1$ and $j = 2$.

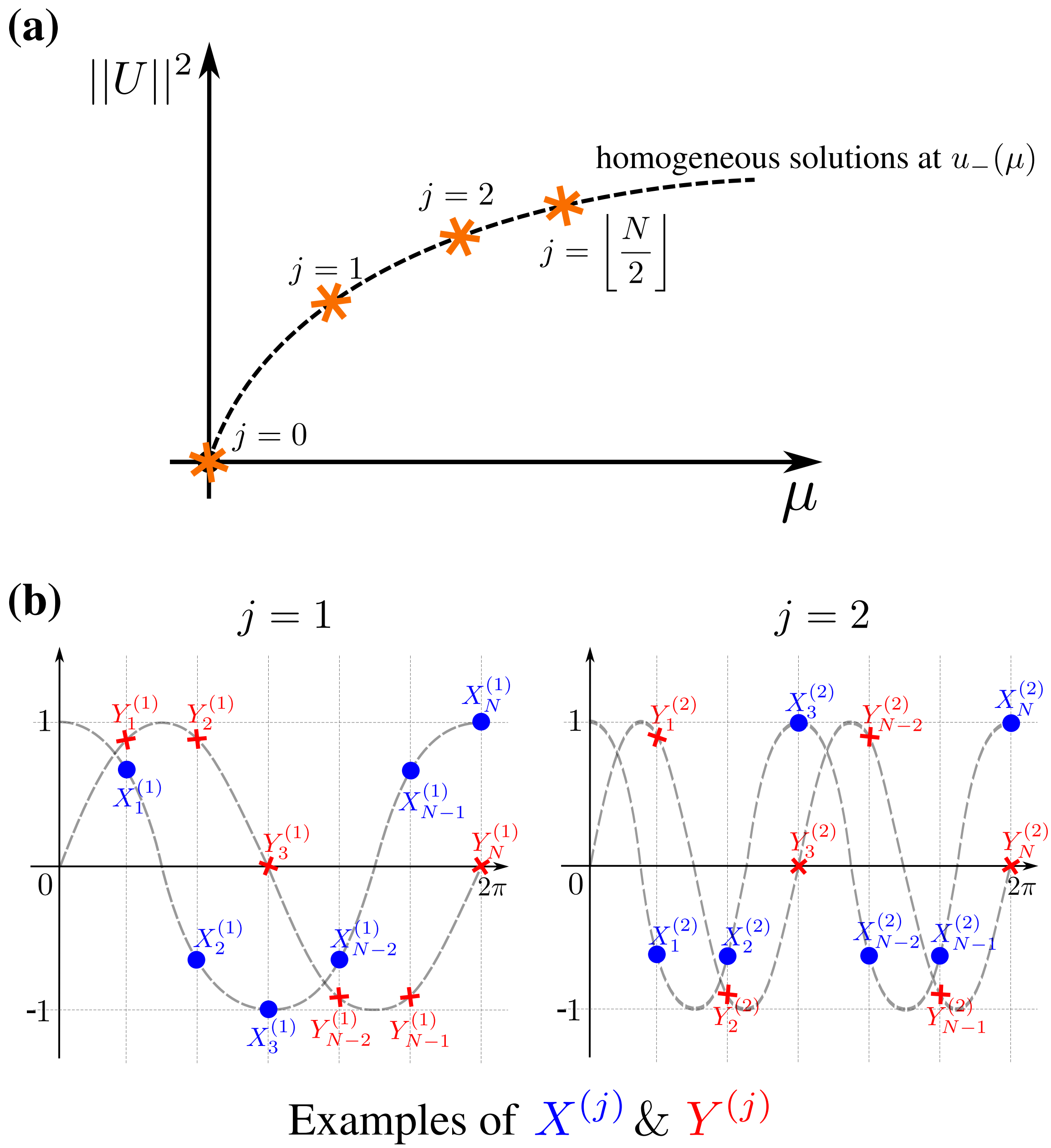

Figure 3.3: Example illustrations of bifurcation points indexed by j along the homogeneous solution branch, $u_-(\mu)\mathbb{e}$, and their corresponding bases. (a) Bifurcation points for $j = 0, 1, \ldots, \left\lfloor \frac{N}{2} \right\rfloor$ along the homogeneous branch, as stated in Theorem 5 (i). (b) Diagrams of the $X^{(j)}$ and $Y^{(j)}$ bases for $\ker\left(\mathbf{L}\left(U_*^{(j)}, \mu_*^{(j)}, d\right)\right)$, defined in equation (3.3), showcasing examples for $j = 1$ and $j = 2$.

We illustrate how the symmetry axes corresponding to the different isotropy subgroups of solutions appear differently for cases when N is odd or even in Figure 3.4. We emphasize that when N is odd, there is only one $\mathbb{Z}_2(\kappa)$ isotropy subgroup, but there are two distinct disjoint branches of solutions with this same group. Figure 3.4 does not distinguish between these different branches but only shows which symmetry axis the solutions correspond to. Details regarding the distinction between the different solution branches for N odd are discussed later.

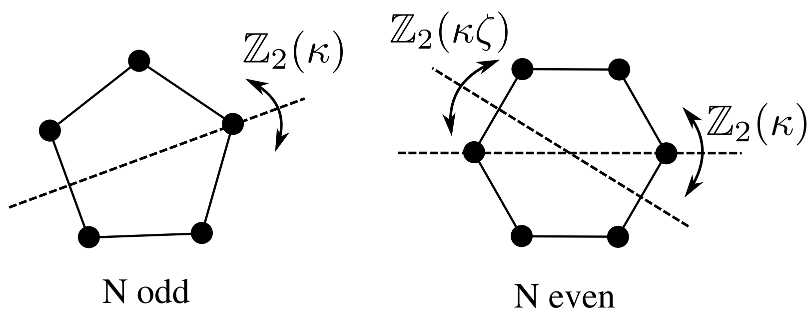

Figure 3.4: Difference in symmetry axes corresponding to the isotropy subgroups of solutions, depending on whether N is odd or even.

We focus on the solution to the bifurcation problem corresponding to $j = 1$ at $\left(U_*^{(1)}, \mu_*^{(1)}\right)$. We are particularly interested in this case since it aligns with observations in numerical simulation. However, we expect our analytical techniques to be generally applicable to the other values of j as well. For convenience, we denote $X^{(1)}$ by X and $Y^{(1)}$ by Y.

In the subsequent sections, our analysis will use the representation of our lattice group on $\mathbb{R}^N$ where actions are defined as

$$\zeta(u_1, u_2, \ldots, u_{N-1}, u_N) = (u_N, u_1, \ldots, u_{N-1})$$

$$\kappa(u_1, u_2, \ldots, u_{N-2}, u_{N-1}, u_N) = (u_{N-1}, u_{N-2}, \ldots, u_2, u_1, u_N)$$

where ζ refers to rotations and κ refers to flips of the ring. When N is even, the action of κ on rings leaves exactly two nodes, $u_{\frac{N}{2}}$ and u_N, fixed. When N is odd, only the node u_N is fixed. The correspondence between our lattice group representation and the canonical D_N group representation on $\mathbb{C}$ is discussed in Section 2.1.

We present the following lemma for specific values of m at the bifurcation point $\left(U_*^{(1)}(d), \mu_*^{(1)}(d), d\right)$.

Lemma 17. *Let* $0 < d \ll 1$. $\dim\left(\ker\left(\mathbf{L}(U_*^{(1)}, \mu_*^{(1)}, d)\right)\right) = 2$ *for* $m = 1$ *when* $N \geq 5$ *and for* $m = 2$ *when* $N \geq 7$.

Assuming the existence of solutions near $\left(U_*^{(1)}, \mu_*^{(1)}, d\right)$, we have the following lemma, which tells us what form the solutions should take.

Lemma 18. *Let* $N \geq 5$ *and* $1 \leq m \leq \left\lfloor \frac{N}{2} \right\rfloor - 1$. *In the space where* $0 < u_n \ll 1$ *for* $1 \leq n \leq N$, $0 < \mu \ll 1$ *and* $0 < d \ll 1$, *assume there exist solutions to system* (3.2) *in the* ϵ*-neiborhood of the homogeneous solution* $\left(U_*^{(1)}(d), \mu_*^{(1)}(d), d\right)$, *denoted by* $\mathcal{B}_\epsilon\left(U_*^{(1)}(d), \mu_*^{(1)}(d), d\right)$. *Then the solution takes the following form*

$$U^*(a(\mu, d)) = U_*^{(1)}(d) + aX + \mathcal{O}(a^2)$$

where $a \in \mathbb{R}$.

We now demonstrate some examples of solution patterns to illustrate their appearance in the case of odd N in Figure 3.5. The figure shows that the two $\mathbb{Z}_2(\kappa)$ solution branches, which bifurcate from the homogeneous branch as mentioned in Theorem 5 (ii), are distinguished by the sign of a ($a > 0$ or $a < 0$). Therefore, Figure 3.5 showcases typical solution patterns and explains how their appearance differs on these distinct branches when N is odd.

We present Figure 3.6 for the case of odd N and Figure 3.7 for the case of even N to demonstrate the bifurcation diagrams of the branching from the homogeneous

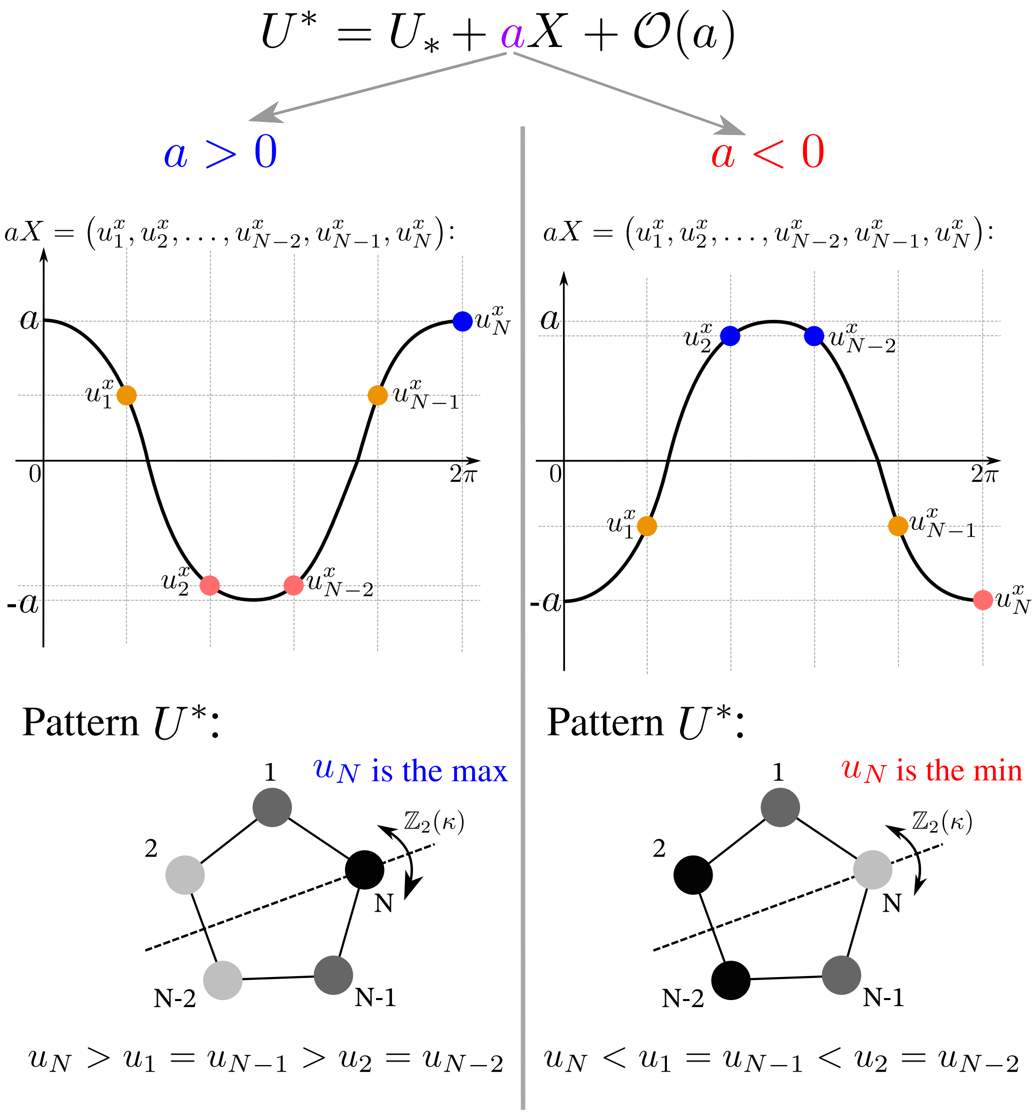

Figure 3.5: Examples of solution patterns in the neighborhood of the bifurcation from the homogeneous solution corresponding to $j = 1$ when N is odd. The solution falls into two cases, depending on the sign of coefficient a. When $a > 0$, u_N on the reflection axis represents the maximum among all node values, and the solution values associated with the nodes decrease symmetrically as one moves farther away from u_N. Conversely, when $a < 0$, u_N on the reflection axis is the minimum, and the values increase symmetrically as one moves away from u_N.

solutions in these different scenarios and detail how patterns appear in the corresponding isotropy subgroups of solutions stated in Theorem 5 (ii).

We prove the following results on the bifurcation criticality at the lower-left corner.

Theorem 6. *Consider $N \geq 5$, $1 \leq m \leq \left\lfloor \frac{N-1}{2} \right\rfloor - 1$ and $0 < d \ll 1$.*

(i) Assume that the null space of $\mathbf{L}\left(U_*^{(1)}, \mu_*^{(1)}, d\right)$ is 2-dimensional. Then the criticality of the bifurcation at $\left(U_*^{(1)}, \mu_*^{(1)}\right)$ is dependent on N, m. Let

$$A(N,m,d) = -\frac{15}{4} - \frac{9}{2}\frac{B(N,m)}{C(N,m)} + \mathcal{O}(d)$$

where

$$B(N,m) = m + \frac{1}{2} - \frac{\sin\left(\frac{(2m+1)\pi}{N}\right)}{2\sin\left(\frac{\pi}{N}\right)}$$
$$C(N,m) = \frac{-\sin\left(\frac{2\pi(m+1)}{N}\right) + \sin\left(\frac{\pi(4m+2)}{N}\right) - \sin\left(\frac{2\pi m}{N}\right)}{\sin\left(\frac{2\pi}{N}\right)}$$

When $A(N,m,d) < 0$, the bifurcation is supercritical; when $A(N,m,d) > 0$, the bifurcation is subcritical.

(ii) Let $N \to \infty$. Denote the ratio $\frac{m}{N}$ by r. Recall that $1 \leq m \leq \left\lfloor \frac{N-1}{2} \right\rfloor - 1$, so $0 < r < \frac{1}{2}$. Assume that the null space of $\mathbf{L}\left(U_*^{(1)}, \mu_*^{(1)}, d\right)$ is 2-dimensional. Then the criticality of bifurcation at $\left(U_*^{(1)}, \mu_*^{(1)}\right)$ changes from supercritical to subcritical when $r \approx 0.39$.

We then present results for the upper-right region.

Theorem 7. *We assume $N \geq 5$. Consider configuration space (u_n, μ, d) where $0 \leq 1-u_n \ll 1$ for $1 \leq n \leq N$, $0 < 1-\mu \ll 1$ and $0 < d \ll 1$. Let $1 \leq m \leq \left\lfloor \frac{N}{2} \right\rfloor - 1$.*

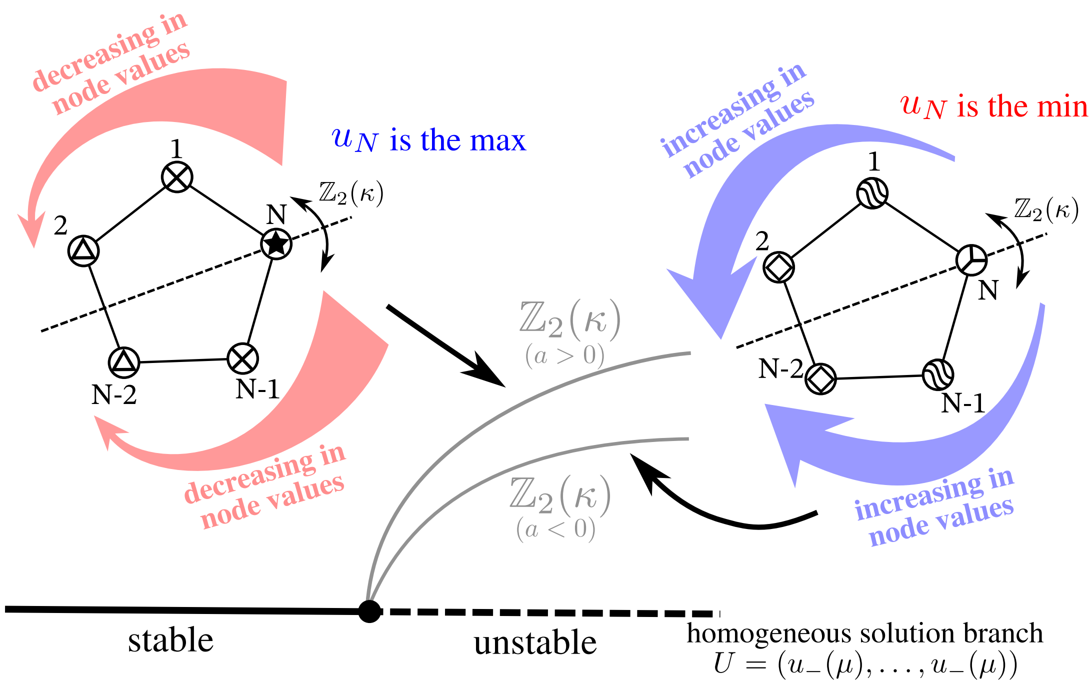

(a) supercritical

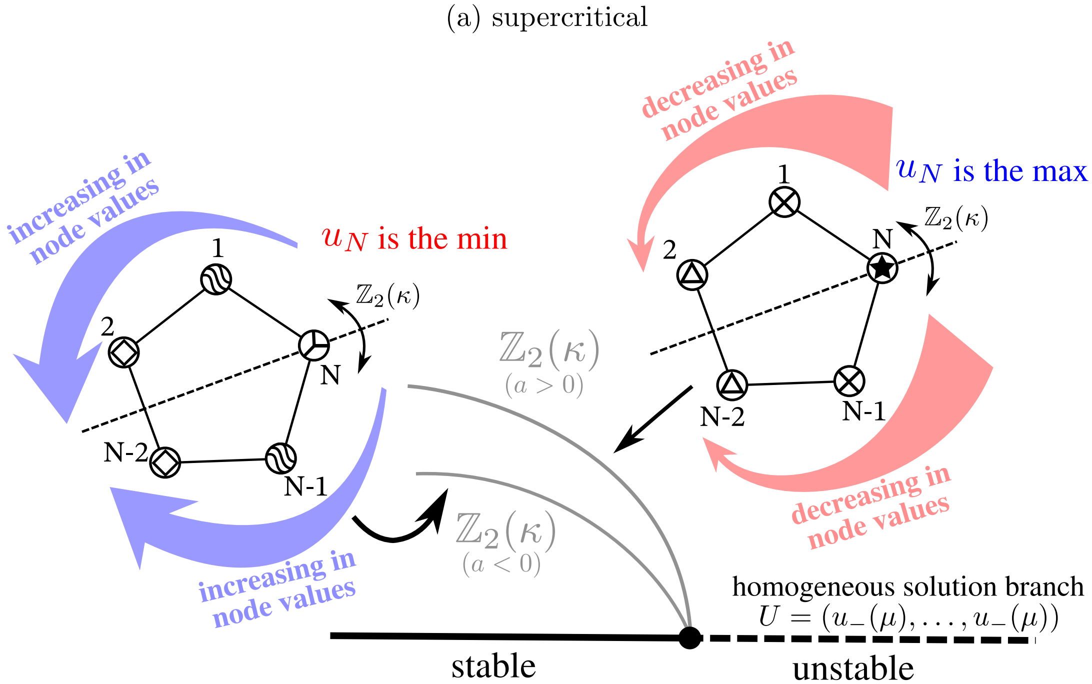

(b) subcritical

Figure 3.6: Example patterns in the isotropy subgroup that bifurcate from the homogeneous solutions, demonstrating Theorem 5 (ii) for the case of odd N. (a) The top depicts a supercritical bifurcation, while (b) the bottom depicts a subcritical bifurcation. The axis of the reflection symmetry goes through the node N. The difference between the two $\mathbb{Z}_2(\kappa)$ branches is that for the first branch, u_N is positive and assumes the maximum value among all nodes, with node values decreasing as one moves away from it. For the second branch, u_N is negative, assuming the minimum value, with node values increasing as one moves away from it. Patterns in the group orbit of the isotropy subgroup are also solutions on the same branch.

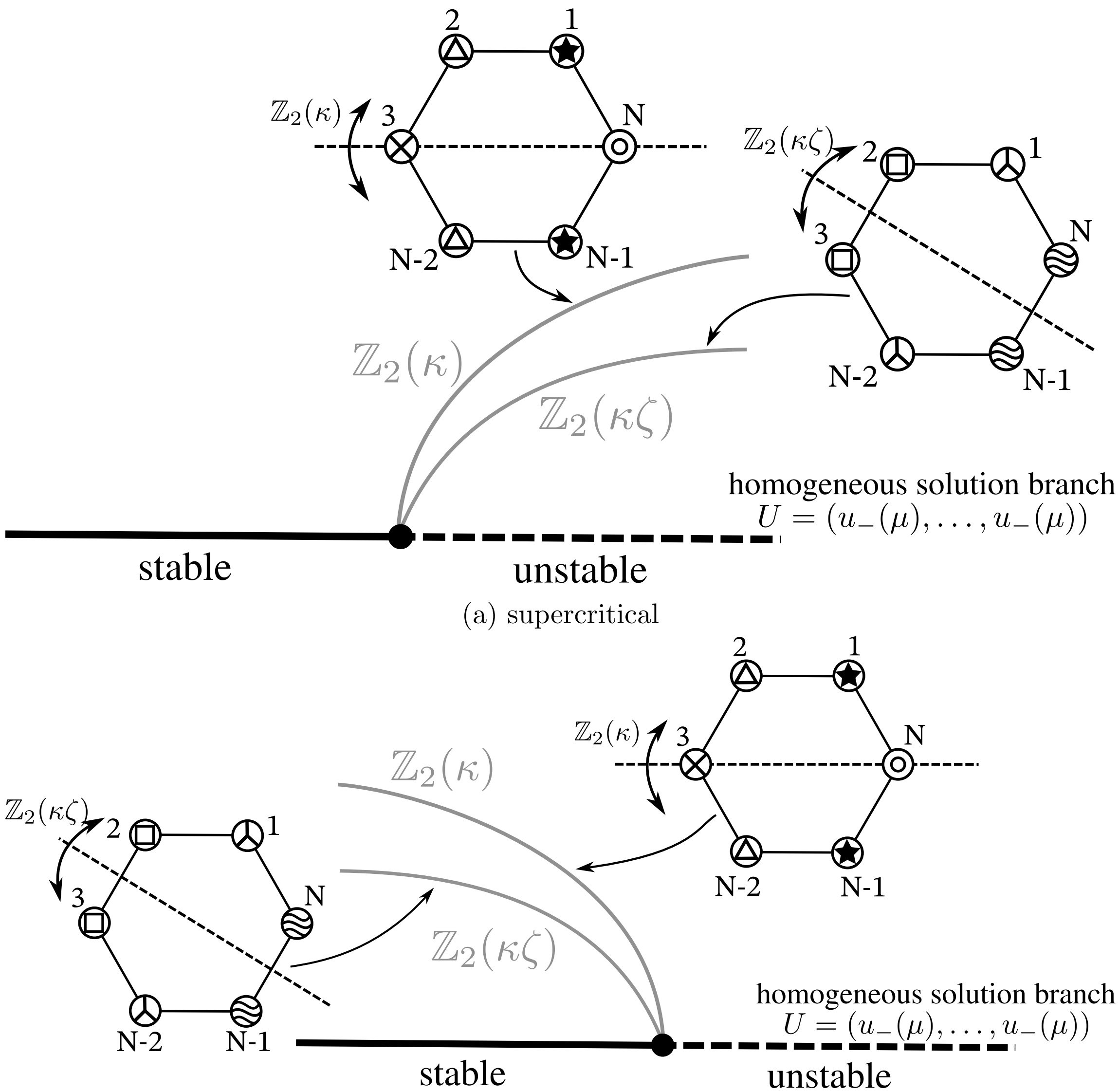

(a) supercritical

(b) subcritical

Figure 3.7: Example patterns in the isotropy subgroup that bifurcate from the homogeneous solutions, demonstrating Theorem 5 (ii) for the case of even N. (a) The top depicts a supercritical bifurcation, while (b) the bottom depicts a subcritical bifurcation. Patterns in the group orbit of the isotropy subgroup are also solutions on the same branch.

(i) The bifurcation points along the homogeneous solution branch $u_-(\mu)\mathbb{e}$ *are* $\left(U_*^{(j)}, \mu_*^{(j)}\right)$ *with*

$$U_*^{(j)}(d) = \left(1 - d\left[m - \sum_{p=1}^{m} \cos\left(\frac{2\pi jp}{N}\right) + \mathcal{O}(d)\right]\right)\mathbb{e}$$

and

$$\mu_*^{(j)}(d) = 1 - d^2\left(\left[m - \sum_{p=1}^{m} \cos\left(\frac{2\pi jp}{N}\right)\right]^2 + \mathcal{O}(d)\right)$$

where $j \in \left\{0, 1, 2, \ldots, \left\lfloor \frac{N}{2} \right\rfloor\right\}$.

(ii) We set $j = 1$ *and assume that the null space of* $\mathbf{L}\left(U_*^{(1)}, \mu_*^{(1)}, d\right)$ *is* 2*-dimensional. Then, there are two branches bifurcating from the homogeneous solution branch at* $\left(U_*^{(1)}, \mu_*^{(1)}, d\right)$. *For odd* N*, the patterns along the two distinct branches have isotropy subgroup* $\mathbb{Z}_2(\kappa)$. *For even* N*, the patterns along the two distinct branches have isotropy subgroup* $\mathbb{Z}_2(\kappa)$ *and* $\mathbb{Z}_2(\kappa\zeta)$.

Specifically focusing on the bifurcation point $\left(U_*^{(1)}(d), \mu_*^{(1)}(d), d\right)$, we have the following lemma and theorem.

Lemma 19. *Let* $N \geq 5$ *and* $1 \leq m \leq \left\lfloor \dfrac{N}{2} \right\rfloor - 1$. *In the space where* $0 \leq 1 - u_n \ll 1$ *for* $1 \leq n \leq N$, $0 < 1 - \mu \ll 1$ *and* $0 < d \ll 1$, *assume there exist solutions to system* (3.2) *in* $\mathcal{B}_\epsilon\left(U_*^{(1)}(d), \mu_*^{(1)}(d), d\right)$. *Then the solution takes the following form*

$$U^*(a(\mu, d)) = U_*^{(1)}(d) + aX + \mathcal{O}(a^2)$$

where $a \in \mathbb{R}$.

Theorem 8. *Consider* $N \geq 5$, $1 \leq m \leq \left\lfloor \dfrac{N-1}{2} \right\rfloor - 1$ *and* $0 < d \ll 1$.

(i) Assume that the null space of $\mathbf{L}\left(U_*^{(1)}, \mu_*^{(1)}, d\right)$ *is* 2*-dimensional. Then the crit-*

icality of the bifurcation at $\left(U_*^{(1)}, \mu_*^{(1)}\right)$ *is dependent on* N, m*. Let*

$$A(N,m,d) = \frac{1}{B(N,m)} + \frac{1}{2C(N,m)} + \mathcal{O}(d)$$

where

$$B(N,m) = -2m - 1 + \frac{\sin\left(\frac{(2m+1)\pi}{N}\right)}{\sin\left(\frac{\pi}{N}\right)}$$
$$C(N,m) = \frac{\sin\left(\frac{2\pi(m+1)}{N}\right) - \sin\left(\frac{\pi(4m+2)}{N}\right) + \sin\left(\frac{2\pi m}{N}\right)}{\sin\left(\frac{2\pi}{N}\right)}$$

When $A(N,m,d) < 0$*, the bifurcation is supercritical; when* $A(N,m,d) > 0$*, the bifurcation is subcritical.*

(ii) Let $N \to \infty$*. Denote the ratio* $\frac{m}{N}$ *by* r*. Recall that* $1 \leq m \leq \left\lfloor \frac{N-1}{2} \right\rfloor - 1$*, so* $0 < r < \frac{1}{2}$*. Assume that the null space of* $\mathbf{L}\left(U_*^{(1)}, \mu_*^{(1)}, d\right)$ *is* 2*-dimensional. Then the criticality of bifurcation at* $\left(U_*^{(1)}, \mu_*^{(1)}\right)$ *changes from supercritical to subcritical when* $r \approx 0.41$*.*

We prove Lemma 16 in Section 2.1, Theorem 5 in Section 3.1, Lemmas 17 and 18 and Theorem 6 in Section 3.2, Theorem 7 in Section 4.1, and Lemma 19 and Theorem 8 in Section 4.2.

Figures 3.8 and 3.9 demonstrate numerically that patterned states emerge from homogeneous branch near the lower-left region. Figure 3.8 shows an example where the bifurcation is supercritical, while Figure 3.9 shows subcritical bifurcation occurs at higher coupling degree. We verify numerically that these emergent patterned states connect with the snaking branches of patterns in Figure 2.2. Details are provided in Sections 3.3 and 4.3.

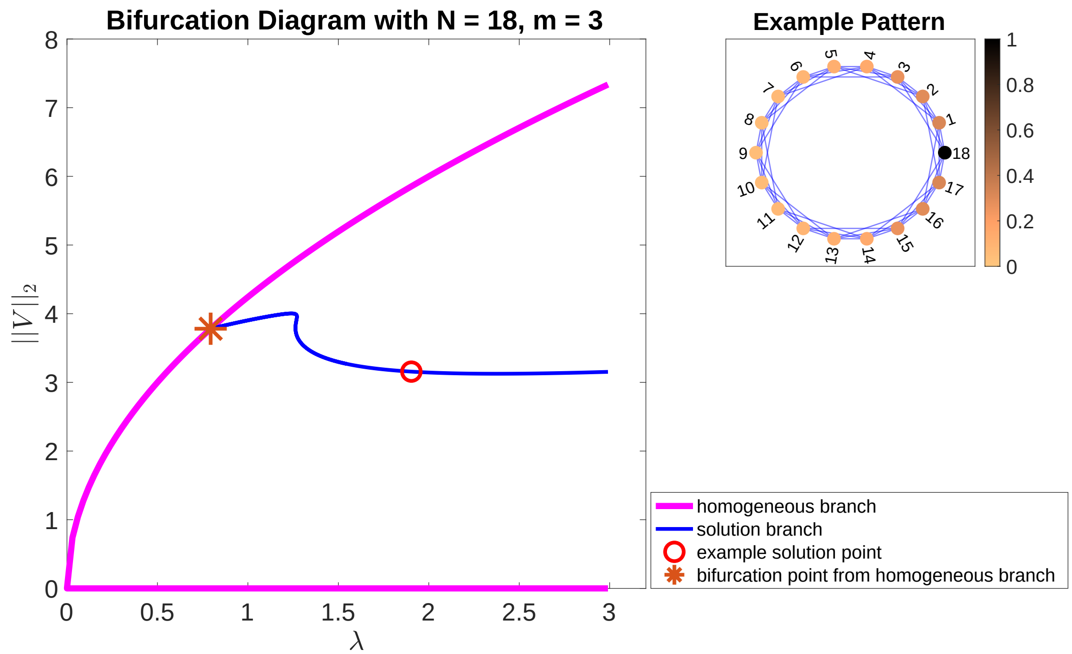

Figure 3.8: Numerical simulation on the rescaled system for $N = 18, m = 3$ near the lower-left region. $V = (v_1, v_2 \ldots, v_N) \in \mathbb{R}^N$ is the rescaled variable with $u_n = \epsilon v_n$, and λ is the bifurcation parameter with $\mu = \lambda\epsilon^2$, where $0 < \epsilon \ll 1$. The numerical solution branch corresponds to the $\mathbb{Z}_2(\kappa)$ branch depicted in Figure 3.7a. The asterisk shows the bifurcation point computed from the analytical result with $j = 1$. An example of the patterns on the solution branch, where node values have been normalized, is illustrated in the right panel, corresponding to the solution point marked by the red circle. Any patterns in the same $\mathbb{Z}_2(\kappa)$ group orbit are also solutions on the same branch, and these patterned solutions are equivariant under D_N group symmetries. Numerically, we confirm that along the homogeneous solution branch, 2 eigenvalues transition from negative to positive upon crossing the bifurcation point in the positive direction of λ. This aligns with the analytical prediction that the bifurcation is supercritical.

An additional interesting point is that during the calculation of eigenvalues along the homogeneous branch, we observe repeated eigenvalues leading to bifurcation with a higher-dimensional null space of $\mathbf{L}\left(U_*^{(j)}(d), \mu_*^{(j)}(d), d\right)$ for specific values of N and m at certain j. In exploring the effect coming from the D_N symmetry group in the Laplace operator, we briefly discuss in Section 2.2 the irreducible representation of dihedral group and use it to verify that the redundant eigenvalues comes from the Laplace operator instead of the graph symmetries.

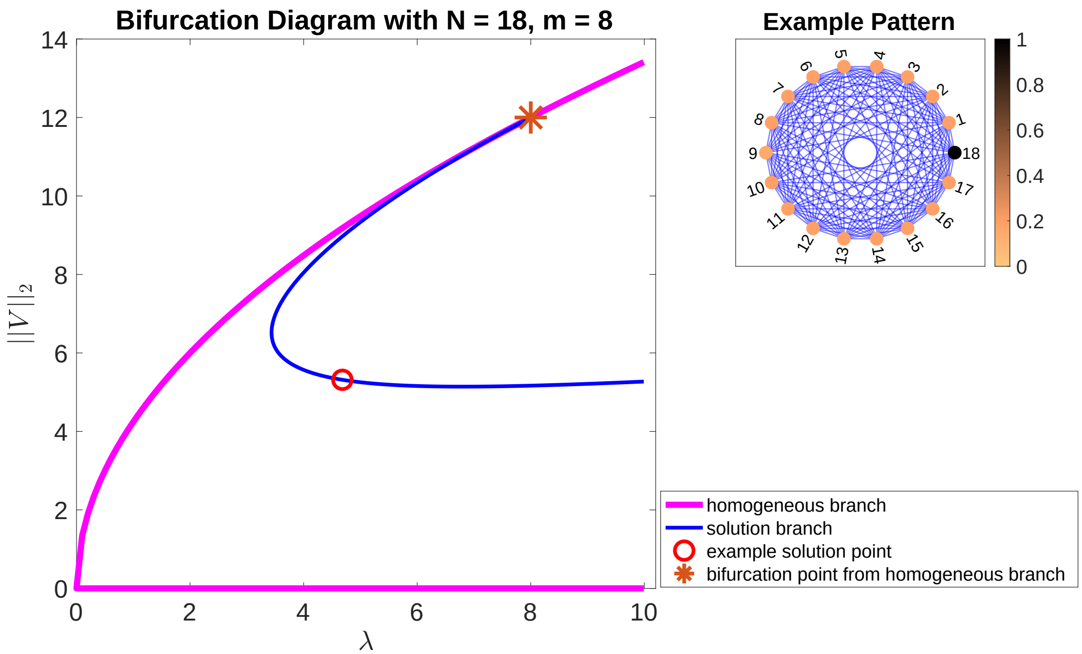

Figure 3.9: Numerical simulation on the rescaled system for $N = 18, m = 8$ near the lower-left region. Details are similarly explained in the previous Figure 3.8. $V = (v_1, v_2 \ldots, v_N) \in \mathbb{R}^N$ is the rescaled variable with $u_n = \epsilon v_n$, and λ is the bifurcation parameter with $\mu = \lambda\epsilon^2$, where $0 < \epsilon \ll 1$. The numerical solution branch corresponds to the $\mathbb{Z}_2(\kappa)$ branch depicted in Figure 3.7b. The numerical continuation aligns with the analytical prediction that the bifurcation is subcritical.

2 Group and Operator Analysis

In this section, we present preliminary results on the group and operator of the lattice systems. In particular, we will show how we can translate the group representation of our lattice systems to the canonical representation of the dihedral group on $\mathbb{C}$. In addition, we observe higher dimensional null space of $\mathbf{L}(U, \mu, d)$ along the homogeneous solutions at bifurcation points resulted from the Laplace operator in the system. These results set the stage for the analysis of the bifurcation at the lower-left and upper-right corners of the original system, which will be discussed in details in Sections 3 and 4.

2.1 Group Representation

Our symmetrically coupled ring system on N nodes respects symmetries of D_N. We are interested in the bifurcation along the homogeneous solutions branch. In the following, we will show how the group representation of the ring system at these points relates to the canonical representation of D_N on $\mathbb{C}$. As for canonical representation, we specifically consider the standard action of D_N on $\mathbb{C}$ as described on page 97 (5.1) in Golubitsky et al. (1988)

$$\begin{aligned} \rho z &= e^{\frac{2\pi i}{N}} z \\ R z &= \bar{z}. \end{aligned} \tag{3.4}$$

The corresponding canonical representation is

$$D_N = \langle \rho, R \mid \rho^n = R^2 = e, R\rho R^{-1} = \rho^{-1} \rangle. \tag{3.5}$$

Before delving into specific group representations, we first calculate the location of the bifurcation along the homogeneous branch. By the end of the calculation, we will obtain the results presented in Lemma 16.

Bifurcation along Homogeneous Solutions Branch

We focus on system (3.1) with the nonlinearity $f(u_n, \mu) = -\mu u_n + 2u_n^3 - u_n^5$. Finding out where solution branches bifurcate from the homogeneous solutions is essentially calculating μ values at which the eigenvalue of the Jacobian corresponding to the homogeneous solutions is zero. Given N, consider $1 \leq m < \lfloor \frac{N}{2} \rfloor$, the Jacobian at homogeneous branch is $\mathbf{L}(\mu) = d\Delta_m + f'(u_-(\mu), \mu) I_N$ where I_N is the identity matrix. We then want to find the eigenvalues of $\mathbf{L}(\mu)$. In order to do so, we need to know the eigenvalues, denoted by λ, of Δ_m. In other words, we want to find $\lambda \in \mathbb{R}$ such that

$$\Delta_m \vec{v} = \lambda \vec{v} \quad \text{where} \quad \vec{v} \in \mathbb{R}^N. \tag{3.6}$$

Discrete Fourier ansatz are

$$v_{k,j} = e^{i\omega_j k}, \quad \text{where } \omega_j = \frac{2\pi j}{N}, \quad k = 1, \dots, N, \quad j = 0, 1, \dots, N-1$$

Plugging in the Fourier ansatz into equation (3.6), we get

$$\begin{aligned} -2me^{i\omega_j k} + \sum_{p=-m}^{m} e^{i\omega_j (k+p)} &= \lambda_j e^{i\omega_j k} \\ \Longrightarrow -2m + \sum_{p=-1}^{m} (e^{i\omega_j p} + e^{-i\omega_j p}) &= \lambda_j \end{aligned}$$

Notice that $e^{i\omega_j p} + e^{-i\omega_j p} = 2\cos(\omega_j p)$ by trigonometric identity, so we can rewrite λ_j as

$$\lambda_j = 2\left(-m + \sum_{p=1}^{m} \cos(\omega_j p)\right) = 2\left(-m + \sum_{p=1}^{m} \cos\left(\frac{2\pi jp}{N}\right)\right).$$

So then we can calculate the eigenvalues of $\mathbf{L}(\mu)$, which are

$$d\lambda_j + f'(u_-(\mu), \mu) = 2d\left(-m + \sum_{p=1}^{m} \cos\left(\frac{2\pi jp}{N}\right)\right) + 4\left(\mu - 1 + \sqrt{1-\mu}\right)$$

since $f'(u, \mu) = -\mu + 6u^2 - 5u^4$ and $u_\pm(\mu) = \sqrt{1 \pm \sqrt{1-\mu}}$.

To find the bifurcation points, we need to determine the values of μ at which the corresponding eigenvalues of $\mathbf{L}(\mu)$ become 0. This is equivalent to solving

$$d\lambda_j + f'(u_-(\mu), \mu) = 0,$$

which is

$$2d\left(-m+\sum_{p=1}^{m}\cos\left(\frac{2\pi jp}{N}\right)\right)+4\left(\mu-1+\sqrt{1-\mu}\right)=0.$$

Then, by solving for μ, we identify the values of μ at the bifurcation points for $j=0,1,\ldots,N-1$, which are

$$\mu_*^{(j)}=1-\frac{1}{2}\left(c_j+1\pm\sqrt{2c_j+1}\right)\ \text{ where } c_j=d\left(-m+\sum_{p=1}^{m}\cos\left(\frac{2\pi jp}{N}\right)\right).$$

We define the corresponding homogeneous solution in U, taking on the value $u_-(\mu)$, as $U_*^{(j)}=u_-\left(\mu_*^{(j)}\right)\mathbb{e}$.

As a sidenote, we briefly mention the general gradient system for the Laplacian Δ_m. Recall that

$$(\Delta_m U)_n=\begin{cases}-(2m+1)u_n+\sum_{j=-m}^{m}u_{n+j}, & 1\le m<\lfloor\frac{N}{2}\rfloor\\ -Nu_n+\sum_{j=1}^{N}u_j, & m=\lfloor\frac{N}{2}\rfloor.\end{cases}$$

The real-valued function $F_m(U)=\displaystyle\sum_{i=1}^{N}\left(-mU_i^2+U_i\sum_{j=1}^{m}U_{i+j}\right)$ satisfies $U'=(\Delta_m U)_n=-\nabla F_m(U)$. We note this as a brief comment about Δ_m but will not use this fact in our subsequent analysis.

Now, we can prove Lemma 16. For convenience, we restate the lemma with slight rewording for ease of reference.

Lemma 20 (Restated)**.** *We here restate Lemma 16.*

Let $N\ge 5$, $1\le m\le\left\lfloor\dfrac{N}{2}\right\rfloor-1$, $0<d\ll 1$, *and* $j\in\left\{1,2,\ldots,\lfloor\frac{N}{2}\rfloor\right\}$. *Then* $\dim\left(\ker\left(\mathbf{L}(U_*^{(j)},\mu_*^{(j)},d)\right)\right)\ge 2$. *If* $\dim\left(\ker\left(\mathbf{L}(U_*^{(j)}(d),\mu_*^{(j)}(d),d)\right)\right)=2$, *then*

$$\ker\left(\mathbf{L}\left(U_*^{(j)}(d),\mu_*^{(j)}(d),d\right)\right)=\operatorname{span}\left(X^{(j)},Y^{(j)}\right)$$

where

$$
\begin{aligned}
X^{(j)} &= \left(\cos\left(\frac{2\pi j}{N}\right), \cos\left(2\cdot\frac{2\pi j}{N}\right), \ldots, \cos\left(N\cdot\frac{2\pi j}{N}\right)\right)\\
Y^{(j)} &= \left(\sin\left(\frac{2\pi j}{N}\right), \sin\left(2\cdot\frac{2\pi j}{N}\right), \ldots, \sin\left(N\cdot\frac{2\pi j}{N}\right)\right).
\end{aligned} \tag{3.7}
$$

Proof. Given N, m and d, first notice that for any $j \in \{1, \ldots, N-1\}$, $c_j = c_{N-j}$ because $\cos\left(\frac{2\pi jp}{N}\right) = \cos\left(\frac{2\pi(N-j)p}{N}\right)$ for any $p \in \{1, \ldots, m\}$. It follows that $\mu_*^{(j)} = \mu_*^{(N-j)}$ for any $j \in \{1, \ldots, N-1\}$. Hence, $\left(U_*^{(j)}(d), \mu_*^{(j)}(d), d\right)$ and $\left(U_*^{(N-j)}(d), \mu_*^{(N-j)}(d), d\right)$ correspond to the same bifurcation point. Also, note that the basis

$$
\begin{aligned}
\left(e^{i\frac{2\pi j}{N}k}\right)_{k=1,\ldots,N} &= \left(\cos\left(\frac{2\pi j}{N}k\right) + i\sin\left(\frac{2\pi j}{N}k\right)\right)_{k=1,\ldots,N}\\
&= \left(\cos\left(\frac{2\pi(N-j)}{N}k\right) - i\sin\left(\frac{2\pi(N-j)}{N}k\right)\right)_{k=1,\ldots,N}
\end{aligned}
$$

so it spans the same space as the basis $\left(e^{i\frac{2\pi(N-j)}{N}k}\right)_{k=1,\ldots,N}$. Thus, we can limit the index j to $j \in \left\{1, 2, \ldots, \frac{N-1}{2}\right\}$ if N is odd, and to $j \in \left\{1, 2, \ldots, \frac{N}{2}\right\}$ if N is even.

Observe that after converting the complex basis into the real vectors in $\mathbb{R}^N$, we find that the corresponding null space of $\mathbf{L}\left(u_-\left(\mu_*^{(j)}\right)\mathbb{e}, \mu_*^{(j)}, d\right)$ has the following two bases in $\mathbb{R}^N$

$$
\begin{aligned}
\operatorname{Re}\left(e^{i\frac{2\pi j}{N}k}\right)_{k=1,2,\ldots,N} &= \left(\cos\left(\frac{2\pi j}{N}\right), \cos\left(2\cdot\frac{2\pi j}{N}\right), \ldots, \cos\left(N\cdot\frac{2\pi j}{N}\right)\right)\\
\operatorname{Im}\left(e^{i\frac{2\pi j}{N}k}\right)_{k=1,2,\ldots,N} &= \left(\sin\left(\frac{2\pi j}{N}\right), \sin\left(2\cdot\frac{2\pi j}{N}\right), \ldots, \sin\left(N\cdot\frac{2\pi j}{N}\right)\right).
\end{aligned}
$$

which are the $X^{(j)}$ and $Y^{(j)}$ in Lemma 16, respectively. Thus, we know that $\ker\left(\mathbf{L}(U_*^{(j)}, \mu_*^{(j)}, d)\right)$ is a space with at least two bases, $X^{(j)}$ and $Y^{(j)}$, and so it is at least 2-dimensional.

Note that when $N \geq 5$, $\dim\left(\operatorname{span}\left(X^{(j)}, Y^{(j)}\right)\right) = 2$. We can see this by showing $X^{(j)} \notin \operatorname{span}\left(Y^{(j)}\right)$. It suffices to only look at the last coordinate of $X^{(j)}$ and $Y^{(j)}$, which are $\cos\left(N \cdot \frac{2\pi j}{N}\right)$ and $\sin\left(N \cdot \frac{2\pi j}{N}\right)$. Note that $\cos\left(N \cdot \frac{2\pi j}{N}\right) = 1$ and $\sin\left(N \cdot \frac{2\pi j}{N}\right) = 0$ always, so there exists no $a \in R$ such that $\cos\left(N \cdot \frac{2\pi j}{N}\right) = a \sin\left(N \cdot \frac{2\pi j}{N}\right)$. Therefore, $X^{(j)} \notin \operatorname{span}\left(Y^{(j)}\right)$ and so $\operatorname{span}\left(X^{(j)}, Y^{(j)}\right) = 2$.

Hence, if we know that $\dim\left(\ker\left(\mathbf{L}\left(u_-\left(\mu_*^{(j)}\right)\mathbb{e}, \mu_*^{(j)}, d\right)\right)\right) = 2$, then

$$\ker\left(\mathbf{L}\left(u_-\left(\mu_*^{(j)}\right)\mathbb{e}, \mu_*^{(j)}, d\right)\right) = \operatorname{span}\left(X^{(j)}, Y^{(j)}\right).$$

This proves Lemma 16. $\square$

In the following discussion, we will specifically focus on the case $j = 1$ since solutions with such an index align with the bifurcation observed in the numerical simulations.

Group Representation at Bifurcation with respect to $j = 1$

At the bifurcation from the homogeneous solutions corresponding to $j = 1$, we define actions on the group of our lattice system living in $\mathbb{R}^N$ in the following way:

$$\begin{aligned} \zeta(u_1, u_2, \ldots, u_{N-1}, u_N) &= (u_N, u_1, \ldots, u_{N-1}) \\ \kappa(u_1, u_2, \ldots, u_{N-2}, u_{N-1}, u_N) &= (u_{N-1}, u_{N-2}, \ldots, u_2, u_1, u_N) \end{aligned} \tag{3.8}$$

where ζ refers to rotations and κ refers to flips of the ring. Clearly $\zeta^N = 1$ and $\kappa^2 = 1$, where we use 1 to denote the identity element that acts trivially on vectors in $\mathbb{R}^N$. Notice that the action of κ on rings with N even leaves exactly two elements, $u_{\frac{N}{2}}$ and u_N, fixed, while when N is odd only the element u_N is fixed.

Recall that the $j = 1$ eigenvector of $\mathbf{L}(\mu) = d\Delta_m + f'(u, \mu)I_N$ is $\left(e^{i\frac{2\pi}{N}k}\right)_{k=1,\ldots,N}$. We specifically choose this Fourier ansatz indexed by $j = 1$ because in the numerical simulations, we observe that the point where the solution branch bifurcates from the homogeneous solutions aligns with the bifurcation point predicted at this index. In later section, Section 3.2, we will discuss the dimensionality of the null space of $\mathbf{L}\left(U_*^{(1)}(d), \mu_*^{(1)}(d), d\right)$ for several specific coupling degrees m as examples. In Sections 3.1 and 4.1, we will present further details on the analysis of the homogeneous solution branch and its bifurcation points, specifically in the lower-left and upper-right corner regimes, respectively. Note that in $\mathbb{R}^N$, the elements that the group acts on, corresponding to the $j = 1$ case, are linear combinations of the bases presented in (3.7) with $j = 1$.

A general element in our lattice system at the $j = 1$ bifurcation can be represented as $aX + bY$ for $a, b \in \mathbb{R}$. We now show that there is a natural isomorphism between the group representation of our lattice system and the canonical representation of D_N in the following Lemma 21.

Lemma 21. *Consider the group representation of the lattice system as defined in* (3.8)*. Then this representation is isomorphic to the canonical representation of* D_N *as defined in* (3.4)*. The isomorphism* $\theta : \mathbb{R}^N \to \mathbb{C}$ *is defined by* $\theta(aX + bY) = a + bi$ *for* $a, b \in \mathbb{R}$*.*

Proof. First, we check ζ agrees with ρ, which is the rotation. Let $a, b \in \mathbb{R}$ be arbitrary. Consider a general element $aX + bY$ in the lattice group. Applying action

ζ to this element gives

$$\begin{aligned}\zeta(aX+bY)=&\zeta\Bigg(a\cos\left(\frac{2\pi}{N}\right)+b\sin\left(\frac{2\pi}{N}\right), a\cos\left(2\cdot\frac{2\pi}{N}\right)+b\sin\left(2\cdot\frac{2\pi}{N}\right),\ldots,\\ &a\cos\left(N\cdot\frac{2\pi}{N}\right)+b\sin\left(N\cdot\frac{2\pi}{N}\right)\Bigg)\\ =&\Bigg(a\cos\left(N\cdot\frac{2\pi}{N}\right)+b\sin\left(N\cdot\frac{2\pi}{N}\right), a\cos\left(\frac{2\pi}{N}\right)+b\sin\left(\frac{2\pi}{N}\right),\\ &a\cos\left(2\cdot\frac{2\pi}{N}\right)+b\sin\left(2\cdot\frac{2\pi}{N}\right),\ldots,\\ &a\cos\left((N-1)\cdot\frac{2\pi}{N}\right)+b\sin\left((N-1)\cdot\frac{2\pi}{N}\right)\Bigg)\end{aligned}$$

Note that for each $k\in\{1,2,\ldots,N\}$,

$$\begin{aligned}&a\cos\left((k-1)\frac{2\pi}{N}\right)+b\sin\left((k-1)\frac{2\pi}{N}\right)\\ =\;& a\left(\cos\left(k\frac{2\pi}{N}\right)\cos\left(\frac{2\pi}{N}\right)+\sin\left(k\frac{2\pi}{N}\right)\sin\left(\frac{2\pi}{N}\right)\right)\\ &+b\left(\sin\left(k\frac{2\pi}{N}\right)\cos\left(\frac{2\pi}{N}\right)-\cos\left(k\frac{2\pi}{N}\right)\sin\left(\frac{2\pi}{N}\right)\right)\\ =\;&\left(a\cos\left(\frac{2\pi}{N}\right)-b\sin\left(\frac{2\pi}{N}\right)\right)\cos\left(k\frac{2\pi}{N}\right)\\ &+\left(b\cos\left(\frac{2\pi}{N}\right)+a\sin\left(\frac{2\pi}{N}\right)\right)\sin\left(k\frac{2\pi}{N}\right).\end{aligned}$$

Hence, $\zeta(aX+bY)=\left(a\cos\left(\frac{2\pi}{N}\right)-b\sin\left(\frac{2\pi}{N}\right)\right)X+\left(b\cos\left(\frac{2\pi}{N}\right)+a\sin\left(\frac{2\pi}{N}\right)\right)Y$. Then, we consider ρ acting on a general element $a+bi$ in the canonical D_N group. Notice that

$$\begin{aligned}\rho(a+bi)&=e^{\frac{2\pi i}{N}}(a+bi)\\ &=\left[\cos\left(\frac{2\pi}{N}\right)+i\sin\left(\frac{2\pi}{N}\right)\right](a+bi)\\ &=\left[a\cos\left(\frac{2\pi}{N}\right)-b\sin\left(\frac{2\pi}{N}\right)\right]+\left[a\sin\left(\frac{2\pi}{N}\right)+b\cos\left(\frac{2\pi}{N}\right)\right]i\end{aligned}$$

Therefore, we find that the coefficients, $a\cos\left(\frac{2\pi}{N}\right)-b\sin\left(\frac{2\pi}{N}\right)$ and $a\sin\left(\frac{2\pi}{N}\right)+$

$b\cos\left(\frac{2\pi}{N}\right)$, for the two bases are in agreement between the actions ζ and ρ.

Second, we do the same to actions κ and R, which are the reflections in the two group representations, and check that they agree. For a general element $aX + bY$ in our lattice group,

$$\begin{aligned}
\kappa(aX+bY) =& \kappa\Bigg(a\cos\left(\frac{2\pi}{N}\right)+b\sin\left(\frac{2\pi}{N}\right), a\cos\left(2\cdot\frac{2\pi}{N}\right)+b\sin\left(2\cdot\frac{2\pi}{N}\right), \ldots, \\
& a\cos\left(N\cdot\frac{2\pi}{N}\right)+b\sin\left(N\cdot\frac{2\pi}{N}\right)\Bigg) \\
=& \Bigg(a\cos\left((N-1)\cdot\frac{2\pi}{N}\right)+b\sin\left((N-1)\cdot\frac{2\pi}{N}\right), \\
& a\cos\left((N-2)\cdot\frac{2\pi}{N}\right)+b\sin\left((N-2)\cdot\frac{2\pi}{N}\right), \ldots \\
& a\cos\left(2\cdot\frac{2\pi}{N}\right)+b\sin\left(2\cdot\frac{2\pi}{N}\right), a\cos\left(\frac{2\pi}{N}\right)+b\sin\left(\frac{2\pi}{N}\right), \\
& a\cos\left(N\cdot\frac{2\pi}{N}\right)+b\sin\left(N\cdot\frac{2\pi}{N}\right)\Bigg)
\end{aligned}$$

Note that last coordinate $a\cos\left(N\cdot\frac{2\pi}{N}\right)+b\sin\left(N\cdot\frac{2\pi}{N}\right)=a$. Additionally, when N is even, we can also compute the value at the $\frac{N}{2}^{th}$ coordinate and find that

$$a\cos\left(\left(N-\frac{N}{2}\right)\cdot\frac{2\pi}{N}\right)+b\sin\left(\left(N-\frac{N}{2}\right)\cdot\frac{2\pi}{N}\right)=a\cos(\pi)+b\sin(\pi)=-a.$$

So these are fixed under reflection and are independent of b. Then observe that for any $k\in\{1,2,\ldots,N-1\}$,

$$\begin{aligned}
& a\cos\left((N-k)\cdot\frac{2\pi}{N}\right)+b\sin\left((N-k)\cdot\frac{2\pi}{N}\right) \\
=& a\cos\left(2\pi-\frac{2\pi k}{N}\right)+b\sin\left(2\pi-\frac{2\pi k}{N}\right) \\
=& a\cos\left(\frac{2\pi k}{N}\right)-b\sin\left(\frac{2\pi k}{N}\right)
\end{aligned}$$

On the other hand, in the canonical representation of D_N group, R acting on a general element $a + bi$ gives

$$R(a + bi) = a - bi.$$

Therefore, we find that the coefficients, a and $-b$, for the two bases are in agreement between the actions κ and R.

In conclusion, the representation of the lattice system is isomorphic to the canonical representation of D_N and $\theta(aX + bY) = a + bi$ is an isomorphism. $\square$

To this point, we see that the bijective map $\theta(aX + bY) = a + bi$ presents a linear isomorphism between the group representation of our lattice system and the canonical group representation of the dihedral group D_N on $\mathbb{C}$. This shows how we can linearly transform our group representation into the canonical D_N group representation through a change of basis in the vector space. This translation will come in handy when we apply bifurcation theory to understand our system in the following Sections 3 and 4.

2.2 Repeated Eigenvalues and Irreducible Representations

In later Sections 3 and 4, we will specifically focus on the bifurcation from the homogeneous solution branch with respect to $j = 1$ at the lower-left and upper-right corner regimes. Before doing so, in this subsection, we will take a slight detour and provide discussions related to the bifurcation with general j.

Specifically, we present a preliminary investigation into the dimensionality of the null space of $\mathbf{L}(U, \mu, d)$ about the homogeneous solutions at bifurcation points with generality, extending our analysis beyond the specific case of $j = 1$. Note that our previous analysis indicates that it suffices to concentrate on understanding the eigenspace of the Laplace operator. This is because the nonlinearity affects only the eigenvalues, altering them by a constant, without changing the eigenspace itself. Hence, for now, our discussion focuses on Δ_m.

In examining Δ_1 and Δ_2, we observe the following. When $m = 1$, the eigenvectors of Δ_m are

$$v_{k,j} = e^{i\omega_j k}, \quad \text{where } \omega_j = \frac{2\pi j}{N}, \quad k = 1, \ldots, N, \quad j = 0, 1, \ldots, N-1$$

and the corresponding eigenvalues are

$$\lambda_j = -2 + 2\cos\left(\frac{2\pi j}{N}\right).$$

Note that $\cos\left(\frac{2\pi j}{N}\right) = \cos\left(\frac{2\pi(N-j)}{N}\right)$. So when N is odd, $\lambda_j = \lambda_{N-j}$ for $j = 1, \ldots, \frac{N-1}{2}$. There is one 1-dimensional eigenspace and $\frac{N-1}{2}$ 2-dimensional eigenspaces. When N is even, $\lambda_j = \lambda_{N-j}$ for $j = 1, \ldots, \frac{N}{2} - 1$. There are two 1-dimensional eigenspaces and $\frac{N}{2} - 1$ 2-dimensional eigenspaces.

When $m = 2$, using symbolic calculation in MATLAB, we observe that eigenspaces higher than 2-dimensional arise for some N. When N is odd, we find that a 4-dimensional eigenspace exists when N is an odd multiple of 5 with $j = \frac{N}{5}, \frac{2N}{5}, \frac{3N}{5}, \frac{4N}{5}$. When N is even, we have not found a regular pattern. For example, for $N = 12$, there is a 3-dimensional eigenspace with $j = 2, 6, 10$ and a 4-dimensional eigenspace with $j = 3, 4, 8, 9$; for $N = 18$, there is a 3-dimensional eigenspace with $j = 3, 9, 15$.

These higher dimensional eigenspaces occur when eigenvalues are repeated among more than two distinct eigenvectors of the system. To determine whether they arise due to the underlying symmetric structure, we analyze them from the perspective of irreducible representations.

An irreducible representation is defined as follows. Consider a representation θ of D_N over a field F, which is n-dimensional and maps the actions to a vector space $V = F^n$. A subspace W of V is said to be D_N-invariant under the representation θ if

$$\theta(\gamma)\mathbf{w} \in W, \quad \forall \gamma \in D_N, \forall \mathbf{w} \in W.$$

The representation, θ, is irreducible if the only D_N-invariant subspaces are the origin, $\{\mathbf{0}\}$, and the whole space V.

For now, let us consider the canonical representation of the dihedral group D_N over $\mathbb{C}$, as given in (3.5). In this case, the matrix representation belongs to the general linear group $GL_1(\mathbb{C})$. Since our lattice group respects symmetries of D_N, the results from the widely studied dihedral group can be naturally applied to our system. Specifically, we consider the projection of the eigenspace onto irreducible representations. This leads to a unique canonical decomposition of a representation into irreducible representations.

Notice that D_N is an ambivalent group with order $2N$, with actions ρ^k and $R\rho^k$ for $0 \leq k \leq N-1$. We first prove the following lemma.

Lemma 22. *All irreducible representations of D_N are 1 or 2 dimensional.*

Proof. D_N has a normal abelian subgroup, $H = \langle \rho \rangle$ (the cyclic group), of index 2. According to Theorem 16 and its proof in Serre (1977), any irreducible representation of D_N is induced by a representation of dimension 1 of this subgroup. We denote such 1-dimensional representation of H as (π, V). So then we may consider any irreducible representation of D_N as acting on the space $\oplus_i V_i$ where each $V_i = g_i V$ is a 1-dimensional vector space with g_i's to be a full set of representatives in D_N of the left cosets of H. Recall that the left cosets of H in D_N are defined as $gH = \{gh : h \in H\}$, and the right cosets of H in D_N are $Hg = \{hg : h \in H\}$ for each $g \in D_N$. Note that for our chosen H, the left cosets always agree with the right cosets. The action of the full group is determined by the action of a representative of the nontrivial coset, RH, indexed 2. So for any 1-dimensional space V, the representative either sends V to itself or to another 1-dimensional space, denoted by W. Hence, either V or $V \oplus W$ is invariant under the full group. Therefore, any irreducible representation of D_N is 1 or 2 dimensional. $\square$

The character, $\chi(M)$, of a square matrix M is defined as its trace. According to Section 5.3 in Serre (1977), when $N \geq 2$ is even, D_N has 4 1-dimensional irreducible representations and their characters are

1. $\chi(\rho^k) = 1, \chi(R\rho^k) = 1$
2. $\chi(\rho^k) = 1, \chi(R\rho^k) = -1$
3. $\chi(\rho^k) = (-1)^k, \chi(R\rho^k) = (-1)^k$
4. $\chi(\rho^k) = (-1)^k, \chi(R\rho^k) = (-1)^{k+1}$

In addition, there are $\frac{N}{2} - 1$ 2-dimensional irreducible representations and we index them by $1 \leq h \leq \frac{N}{2} - 1$. The corresponding characters are

$$\chi_h(\rho^k) = 2\cos\left(\frac{2\pi hk}{N}\right), \text{ and } \chi_h(R\rho^k) = 0 \text{ where } 0 \leq k \leq N-1.$$

When N is odd, there are 2 1-dimensional irreducible representations with characters

$$\text{(1)} \quad \chi(\rho^k) = 1, \chi(R\rho^k) = 1$$

$$\text{(2)} \quad \chi(\rho^k) = 1, \chi(R\rho^k) = -1$$

and $\frac{N-1}{2}$ 2-dimensional irreducible representations whose characters can be calculated by the same formula as for the even case.

According to Theorem 8 of Chapter 2.6 in Serre (1977), suppose V is a linear representation, then we have a unique canonical decomposition of V into direct sum of irreducible representations, $V = V_1 \oplus \ldots \oplus V_h$, and the associated projection p_i of V onto V_i can be calculated by

$$p_i = \frac{n_i}{2N} \sum_{\gamma \in D_N} \chi_i(\gamma)^* \Psi_\gamma \tag{3.9}$$

where n_i is the degree of irreducible representation, χ_i is the character of the irreducible representation and Ψ_γ is the matrix representation of action $\gamma \in D_N$.

Using MATLAB, we have checked values of N up to 120 and observed that none of the irreducible representations appear more than once. We include our code and its detailed explanations in Section 5. This result suggests that for our lattice system with these values of N, the redundant eigenvalues do not arise from the symmetry of the D_N group but from other underlying structures of the Laplace operator. This insight opens up future directions, including proving this result for general N, analyzing which irreducible representations appear in our matrix representation for the Laplace operator in the lattice system, and ultimately figuring out why high-dimensional eigenspaces of Δ_m, which are also the null spaces of $\mathbf{L}(U, \mu, d)$, occur for certain values of N, m and j.

3 Bifurcation Analysis for the Lower-Left Corner

In this section, we present analysis of the main results on bifurcation at the lower-left corner of the original system when (u_n, μ, d) near $(0, 0, 0)$. Analysis for the upper-right corner follows the same idea and will be presented in details in Section 4. Results in this section illustrate that the patterned equilibrium states bifurcate from the homogeneous solutions at the lower-left corner, and the criticality changes from supercritical to subcritical while increasing m for each N. Specifically, proofs for Theorem 5 and 6 as well as Lemmas 18 and 17 are presented.

3.1 Bifurcation from Homogeneous Solutions

Recall that the ring system is

$$\dot{u}_n = d(\Delta_m U)_n + f(u_n, \mu), \quad 1 \leq n \leq N, \quad U = (u_1, u_2 \ldots, u_N) \in \mathbb{R}^N$$

where

$$(\Delta_m U)_n = \begin{cases} -(2m+1)u_n + \sum_{j=-m}^{m} u_{n+j}, & 1 \leq m < \lfloor \frac{N}{2} \rfloor \\ -Nu_n + \sum_{j=1}^{N} u_j, & m = \lfloor \frac{N}{2} \rfloor. \end{cases}$$

In the region of lower-left corner when (u_n, μ, d) near $(0, 0, 0)$, the nonlinearity

$$f(u_n, \mu) = -\mu u_n + u_n^3 + \mathcal{O}(u_n^5).$$

Denote $\mathscr{F}(U, \mu, d) = d(\Delta_m U)_n - \mu u_n + u_n^3 + \mathcal{O}(u_n^5)$.

Now, we show where bifurcation occurs along the homogeneous solution branch at the lower-left corner, which proves Theorem 5 (i). To do this, we analyze the rescaled system.

Rescaled Systems

In this parameter regime, we can rescale as $u_n = \epsilon v_n, \mu = \lambda\epsilon^2, d = \epsilon^2$. Then let $V = (v_1, v_2 \ldots, v_N) \in \mathbb{R}^N$, we have

$$\mathbb{F}(V, \lambda) \coloneqq \dot{v}_n = \epsilon^3(\Delta_m V)_n - \epsilon^3\lambda v_n + \epsilon^3 v_n^3 + \mathcal{O}(\epsilon^5).$$

Since we are interested in studying the stationary solutions, we can set $\dot{v}_n = 0$:

$$\mathbb{F}(V, \lambda) = 0 \quad \Rightarrow \quad (\Delta_m V)_n - \lambda v_n + v_n^3 + \mathcal{O}(\epsilon^2) = 0. \tag{3.10}$$

To find spatially homogeneous equilibria, we can further rescale equation (3.10) by $v_n = \sqrt{\lambda} w_n$

$$\begin{aligned} & \sqrt{\lambda}\,(\Delta_m W)_n - \left(\sqrt{\lambda}\right)^3 w_n + \left(\sqrt{\lambda}\right)^3 w_n^3 + \mathcal{O}(\epsilon^2) = 0 \\ \Longrightarrow \quad & \frac{1}{\lambda}\,(\Delta_m W)_n - w_n + w_n^3 + \mathcal{O}(\epsilon^2) = 0 \end{aligned}$$

Let $\lambda \to \infty$. Then we get roots $w_n \in \{-1 + \mathcal{O}(\epsilon^2), \mathcal{O}(\epsilon^2), 1 + \mathcal{O}(\epsilon^2)\}$ for the decoupled system. Denote $w_- = 1 + \mathcal{O}(\epsilon^2)$ and $v_-(\lambda) = \sqrt{\lambda} w_-$.

In numerical simulation, we choose $\epsilon = 0$. When computing the solution branch, we solve $(\Delta_m V)_n - \lambda v_n + v_n^3 = 0$ for V and continue in the parameter λ. For the initial step, we pick a sufficiently large λ, put in the corresponding initial guess of the solution in V as $(0, 0, \ldots, \sqrt{\lambda})$, and then converge the initial guess to a real solution close-by using `fsolve` in MATLAB.

Bifurcation Points along Homogeneous Solutions Branch at Lower-Left Corner

Next, we can find out all bifurcating points from the homogeneous solution branch. This essentially involves finding the corresponding λ values for which the eigenvalue of the Jacobian matrix of $\mathbb{F}(V, \lambda)$ along the homogeneous solutions is zero.

Given N, consider $1 \leq m < \lfloor \frac{N}{2} \rfloor$, we define the Jacobian of $\mathbb{F}(V, \lambda)$ with respect to V at homogeneous branch solutions $V = v_-(\lambda)\mathbb{e}$ as

$$\mathbb{L}(\lambda) \coloneqq D_V \mathbb{F}\left(v_-(\lambda)\mathbb{e}, \lambda\right) = \Delta_m + \left(2\lambda + \mathcal{O}(\epsilon^2)\right) I_N$$

where I_N is the identity matrix. We are interested in finding the eigenvalues of $\mathbb{L}(\mu)$.

Recall from Section 2.1, we have shown that the eigenvectors of Δ_m are

$$v_{k,j} = e^{i\omega_j k}, \quad \text{where } \omega_j = \frac{2\pi j}{N}, \quad k = 1, \ldots, N, \quad j = 0, 1, \ldots, \left\lfloor \frac{N}{2} \right\rfloor$$

with the corresponding eigenvalues to be

$$\lambda_j = 2\left(-m + \sum_{p=1}^{m} \cos\left(\frac{2\pi j p}{N}\right)\right).$$

So we can calculate the eigenvalues of $\mathbb{L}(\lambda)$, which are

$$\lambda_j + \left(2\lambda + \mathcal{O}(\epsilon^2)\right) = 2\left(-m + \sum_{p=1}^{m} \cos\left(\frac{2\pi j p}{N}\right)\right) + 2\lambda + \mathcal{O}(\epsilon^2).$$

When eigenvalue is 0, $\lambda^{(j)} = m - \sum_{p=1}^{m} \cos\left(\frac{2\pi jp}{N}\right) + \mathcal{O}(\epsilon^2)$. These are the λ values at the bifurcating points from the homogeneous solution branch.

Since the ring system is equivariant with respect to the dihedral group, we can use equivariant bifurcation theory for D_N symmetry to understand the bifurcation from the homogeneous solutions. Our analysis is based on the following results on D_N group from Chapter 5 in Golubitsky's book Golubitsky et al. (1988).

Theorem 9. *Consider the ODE system with the form*

$$\frac{dz}{dt} + g(z, \delta) = 0.$$

where map $g : \mathbb{C} \times \mathbb{R} \to \mathbb{C}$ commutes with D_N. Then the normal form is

$$g(z, \delta) = p(\alpha, \beta, \delta)z + q(\alpha, \beta, \delta)\bar{z}^{N-1}$$

where $z = x + iy \in \mathbb{C}$, $\alpha = z\bar{z}$ and $\beta = z^{N-1} + \bar{z}^{N-1}$. Consider $N \geq 5$ and assume

$$p(0, 0, 0) = 0 \quad \text{and} \quad p_\delta(0, 0, 0) \neq 0.$$

Then, from the trivial solution branch $z = 0$, the following bifurcation branch exists, with the equation

$$\delta = -\frac{p_\alpha(0, 0, 0)}{p_\delta(0, 0, 0)}x^2 + \cdots . \tag{3.11}$$

Additionally, assume that $p_\alpha(0, 0, 0) \neq 0$. Then, the directions of branching from $z = 0$ in the bifurcation diagram for $g(z, \delta) = 0$ are as illustrated in Figure 3.10 for odd N and Figure 3.11 for even N.

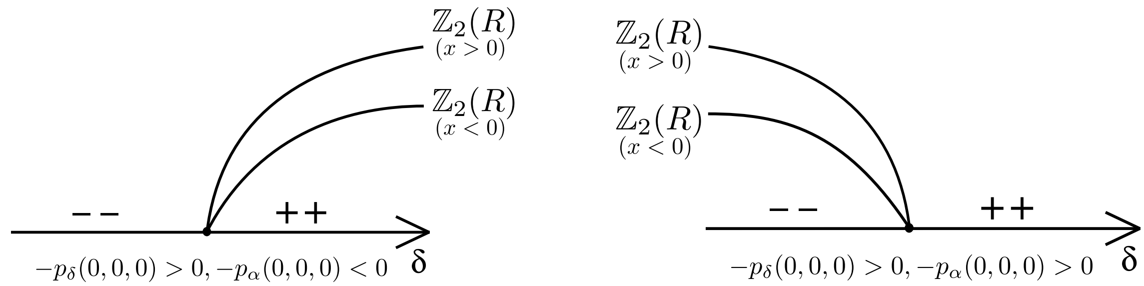

(a) $-p_\alpha(0,0,0) < 0$, supercritical (b) $-p_\alpha(0,0,0) > 0$, subcritical

Figure 3.10: Illustrations of the criticality of bifurcation from the homogeneous solution branch, $z = 0$, with D_N symmetry when $-p_\delta(0,0,0) > 0$, for $N \geq 5$ being an odd number. There are two distinct bifurcation branches, $\mathbb{Z}_2(R)$ with $x > 0$ and $\mathbb{Z}_2(R)$ with $x < 0$. The branching directions are dependent on the sign of $-p_\alpha(0,0,0)$. $-$ means stable eigenvalues and $+$ means unstable eigenvalues.

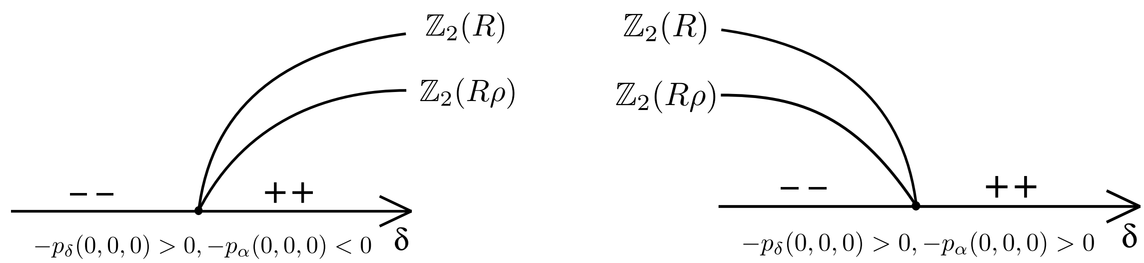

(a) $-p_\alpha(0,0,0) < 0$, supercritical (b) $-p_\alpha(0,0,0) > 0$, subcritical

Figure 3.11: Illustrations of the criticality of bifurcation from the homogeneous solution branch, $z = 0$, with D_N symmetry when $-p_\delta(0,0,0) > 0$, for $N \geq 5$ being an even number. There are two distinct bifurcation branches, $\mathbb{Z}_2(R)$ and $\mathbb{Z}_2(R\rho)$. The branching directions are dependent on the sign of $-p_\alpha(0,0,0)$. $-$ means stable eigenvalues and $+$ means unstable eigenvalues.

Specifically, there are two branches of solutions in isotropy subgroups that bifurcate from the branch $z = 0$. When N is odd, the two branches are $\mathbb{Z}_2(R)$ with $x > 0$ and $\mathbb{Z}_2(R)$ with $x < 0$. When N is even, the two branches are $\mathbb{Z}_2(R)$ and $\mathbb{Z}_2(R\rho)$.

Note that in Theorem 9, the condition $p(0,0,0) = 0$ ensures that it is a bifurcation problem for $g(a, \delta)$. The condition $p_\delta(0,0,0) \neq 0$ corresponds to the genericity hypothesis of the equivariant branching lemma, allowing the equivariant branching lemma to be applied. In addition, $p_\alpha(0,0,0) \neq 0$ is assumed so that the branching direction can be determined.

We then briefly comment on the role of q. If we assume that $q(0,0,0) \neq 0$, then the only local solution branches to the system $g(z,\delta) = 0$ that bifurcate from $z = 0$ are those shown in Figs. 3.10 and 3.11. The stability of the bifurcation branch is determined by whether $q(0,0,0) > 0$ or $q(0,0,0) < 0$. If we do not know whether $q(0,0,0) \neq 0$, then the existence results in Theorem 9 still hold, but there might exist other bifurcation branches not described in the theorem.

3.2 Verification of Genericity Hypotheses

In Section 2.1, we have shown how the group representation of our ring lattice can be mapped to the canonical representation of D_N. This fact allows us to apply the results from Theorem 9 to our ring system. In this subsection, we show how we can understand the criticality of bifurcation in the lower-left corner using the theory. Specifically, we present proofs for Theorem 6. In the process, we also prove Lemmas 18 and 17.

Note that in order to apply Theorem 9 to the bifurcation problem in our system, we require the conditions that $p_\delta(0,0,0) \neq 0$, $p_\alpha(0,0,0) \neq 0$, and also that the null space of $\mathbb{L}\left(\lambda^{(1)}\right)$ about the homogeneous solution at the bifurcation point is 2-dimensional. This subsection will first provide a discussion on the dimensionality of the null space of $\mathbb{L}\left(\lambda^{(1)}\right)$ for certain values of m, and show that we can obtain the 2-dimensional condition in Theorem 9 when $\dim\left(\ker\left(\mathbb{L}\left(\lambda^{(1)}\right)\right)\right) = 2$. Then, we will verify the conditions $p_\alpha(0,0,0) \neq 0$ and $p_\delta(0,0,0) \neq 0$ in the theorem by presenting explicit calculations.

Recall that in Section 2.1, we have proved the isomorphism between the group representation of our lattice system, (3.8), and the canonical group representation of D_N, (3.5). Hence, if we assume that the null space of $\mathbb{L}\left(\lambda^{(1)}\right)$ is 2-dimensional, after performing the following verifications, we can then obtain the results for Theorems 5 (ii) and 6 according to Theorem 9.

Dimension of $\ker\left(\mathbb{L}\left(\lambda^{(1)}\right)\right)$ for Certain m Values

As mentioned in the previous Section 2.1, we specifically focus on the bifurcation corresponding to $j = 1$ because our numerical simulation coincides with it. Here, we want to verify under what conditions of N and m the null space of $\mathbb{L}\left(\lambda^{(1)}\right)$ is 2-dimensional. Notice that according to the previous calculation, for a general $N \geq 5$ and $1 \leq m \leq \lfloor \frac{N}{2} \rfloor$, the eigenvectors of the eigenproblem with respect to $j = 0, 1, \ldots, N-1$ at the bifurcation are

$$\left(\cos\left(\frac{2\pi j}{N}k\right)\right)_{k=1,\ldots,N} \quad \text{and} \quad \left(\sin\left(\frac{2\pi j}{N}k\right)\right)_{k=1,\ldots,N},$$

which are obtained by converting the complex ansatz $\left(e^{i\frac{2\pi j}{N}k}\right)_{k=1,2,\ldots,N}$ into real vectors. The corresponding eigenvalues are $\lambda^{(j)} = m - \sum_{p=1}^{m} \cos\left(\frac{2\pi jp}{N}\right) + \mathcal{O}(\epsilon^2)$.

Note that, as discussed in the proof of Lemma 16 presented in Section 2.1, we can restrict the index j to be within the set $\left\{0, 1, 2, \ldots, \lfloor \frac{N}{2} \rfloor\right\}$ since j and $N-j$ for $j = 1, \ldots, N-1$ provide redundant solutions with the same eigenspace. However, for convenience in our subsequent discussions, we continue to use $j = 0, 1, \ldots, N-1$. Any argument that holds for $j \in \{0, 1, \ldots, N-1\}$ will automatically be valid for $j \in \left\{0, 1, \ldots, \lfloor \frac{N}{2} \rfloor\right\}$.

In order to check the dimensionality of null space of $\mathbb{L}\left(\lambda^{(1)}\right)$, we need to find out if there are $\lambda^{(j)} = \lambda^{(1)}$ with $j \neq 1$. Notice that when $j = 0$, $\lambda^{(0)} = m - \sum_{p=1}^{m} 1 + \mathcal{O}(\epsilon^2) = \mathcal{O}(\epsilon^2)$, which is independent of N and m. For any fixed N and m, $\lambda^{(1)} = m - \sum_{p=1}^{m} \cos\left(\frac{2\pi p}{N}\right) + \mathcal{O}(\epsilon^2) > \mathcal{O}(\epsilon^2) = \lambda^{(0)}$ since $0 < \frac{2\pi}{N} \leq \frac{2\pi p}{N} \leq \pi$, which implies that $\cos\left(\frac{2\pi p}{N}\right) < 1$. Hence, $\lambda^{(1)} \neq \lambda^{(0)}$, so we can omit the case $j = 0$ in the following discussion.

Given N and m, we define a difference function between the eigenvalue with $j = 1$ and the eigenvalue with the general j as

$$
\begin{aligned}
\mathcal{D}(j) \coloneqq \lambda^{(1)} - \lambda^{(j)} &= \sum_{p=1}^{m} \cos\left(\frac{2\pi jp}{N}\right) - \sum_{p=1}^{m} \cos\left(\frac{2\pi p}{N}\right) \\
&= \frac{\sin\left(\frac{\pi j(2m+1)}{N}\right)}{2\sin\left(\frac{\pi j}{N}\right)} - \frac{\sin\left(\frac{\pi(2m+1)}{N}\right)}{2\sin\left(\frac{\pi}{N}\right)} \\
&= \frac{\sin\left(\frac{\pi j(2m+1)}{N}\right)\sin\left(\frac{\pi}{N}\right) - \sin\left(\frac{\pi(2m+1)}{N}\right)\sin\left(\frac{\pi j}{N}\right)}{2\sin\left(\frac{\pi j}{N}\right)\sin\left(\frac{\pi}{N}\right)}.
\end{aligned}
$$

Note that for $1 \leq j \leq N-1$, $0 < \frac{\pi}{N} \leq \frac{\pi j}{N} < \pi$. So the denominator $2\sin\left(\frac{\pi j}{N}\right)\sin\left(\frac{\pi}{N}\right) \neq 0$. When finding out whether a specific $\lambda^{(j)} = \lambda^{(1)}$, we only need to check whether the numerator $\mathcal{D}^A(j)$ of $\mathcal{D}(j)$ is zero.

When $j = N-1$, $\mathcal{D}^A(N-1) = 0$, which confirms our previous observation that $\lambda^{(N-1)} = \lambda^{(1)}$. Recall that, as shown in Section 2.1, although the bifurcation point corresponding to $j = N-1$ collides with that of $j = 1$, the direct sum of their eigenspaces remains 2-dimensional. So for now, it suffices to verify whether there exists $\lambda^{(j)} = \lambda^{(1)}$ for $j = 2, 3, \ldots, N-2$, and if so, then we check the dimensionality of the space spanned by their eigenvectors.

We first discuss the all-to-all and almost all-to-all cases and demonstrate that $\dim\left(\ker\left(\mathbb{L}\left(\lambda^{(1)}\right)\right)\right) > 2$ for these two scenarios.

Consider $j \in \{2, 3, \ldots, N-2\}$.

(a) All-to-all case

Recall that the all-to-all case refers to when $m = \left\lfloor \frac{N}{2} \right\rfloor$ for any given N. When N is odd, $m = \frac{N-1}{2}$ and we have

$$\mathcal{D}^A(j) = \sin(\pi j)\sin\left(\frac{\pi}{N}\right) - \sin(\pi)\sin\left(\frac{\pi j}{N}\right) = 0$$

for $j = 2, 3, \ldots, N-2$.

When N is even, $m = \frac{N}{2}$ and

$$\begin{aligned}\mathcal{D}^A(j) &= \sin\left(\frac{(N+1)\pi j}{N}\right)\sin\left(\frac{\pi}{N}\right) - \sin\left(\frac{(N+1)\pi}{N}\right)\sin\left(\frac{\pi j}{N}\right)\\ &= \cos(\pi j)\sin\left(\frac{\pi j}{N}\right)\sin\left(\frac{\pi}{N}\right) + \sin\left(\frac{\pi}{N}\right)\sin\left(\frac{\pi j}{N}\right)\\ &= (1+\cos(\pi j))\sin\left(\frac{\pi j}{N}\right)\sin\left(\frac{\pi}{N}\right).\end{aligned}$$

Again, $\sin\left(\frac{\pi}{N}\right) \neq 0$ and $\sin\left(\frac{\pi j}{N}\right) \neq 0$ since $0 < j < N$. So $\mathcal{D}^A(j) = 0$ only if $\cos(\pi j) = -1$, which is when $j = 3, 5, \ldots, N-3$.

Therefore, in the case of all-to-all coupling, when N is odd, $\lambda^{(j)} = \lambda^{(1)}$ for integer $j = 2, 3, \ldots, N-2$. When N is even, $\lambda^{(j)} = \lambda^{(1)}$ for odd integer $j = 3, 5, \ldots, N-3$.

(b) Almost all-to-all case

The almost all-to-all case refers to when $N \geq 6$ is even and $m = \frac{N}{2} - 1$, i.e., every node is connected to every other node except for the one at the furthest opposite end.

In this case,

$$\begin{aligned}\mathcal{D}^A(j) &= \sin\left(\frac{(N-1)\pi j}{N}\right)\sin\left(\frac{\pi}{N}\right) - \sin\left(\frac{(N-1)\pi}{N}\right)\sin\left(\frac{\pi j}{N}\right)\\ &= -\cos(\pi j)\sin\left(\frac{\pi j}{N}\right)\sin\left(\frac{\pi}{N}\right) - \sin\left(\frac{\pi}{N}\right)\sin\left(\frac{\pi j}{N}\right)\\ &= (-1-\cos(\pi j))\sin\left(\frac{\pi j}{N}\right)\sin\left(\frac{\pi}{N}\right).\end{aligned}$$

Similarly as before, $\mathcal{D}^A(j) = 0$ only if $-1-\cos(\pi j) = 0$, and this is when j is an odd integer. Hence, in the case of almost all-to-all coupling, $\lambda^{(j)} = \lambda^{(1)}$ for odd integer $j = 3, 5, \ldots, N-3$.

In order to conclude that, for both all-to-all and almost all-to-all cases, the null space of $\mathbb{L}\left(\lambda^{(1)}\right)$ is more than 2-dimensional – regardless of N is even or odd – we only need to show that the space spanned by the eigenvectors is at least 3-dimensional. It suffices to focus on the case where $j = 3$. Note that one of the eigenvectors corresponding to this case is

$$\left(\cos\left(\frac{6\pi}{N}k\right)\right)_{k=1,\ldots,N}$$

and for any $N \geq 5$, this vector cannot be represented as a linear combination of the two eigenvectors with respect to $j = 1$, which are

$$\left(\cos\left(\frac{2\pi}{N}k\right)\right)_{k=1,\ldots,N} \quad \text{and} \quad \left(\sin\left(\frac{2\pi}{N}k\right)\right)_{k=1,\ldots,N}.$$

To quickly see this, we can use a proof by contradiction. Assume that for any $N \geq 5$, there exist $c_1, c_2 \in \mathbb{R}$ such that $\cos\left(\frac{6\pi}{N}k\right) = c_1\cos\left(\frac{2\pi}{N}k\right) + c_2\sin\left(\frac{2\pi}{N}k\right)$, where $k = 1, 2, \ldots, N$. Notice that when $k = N$, we have $\cos\left(\frac{6\pi}{N}k\right) = \cos\left(\frac{2\pi}{N}k\right) = 1$ and $\sin\left(\frac{2\pi}{N}k\right) = 0$, implying that $c_1 = 1$ and $c_2 = 0$. Therefore, we should have $\cos\left(\frac{6\pi}{N}k\right) = \cos\left(\frac{2\pi}{N}k\right)$ for all k.

However, considering $k = 1$, we find that for $N \geq 6$, $\cos\left(\frac{6\pi}{N}k\right) < \cos\left(\frac{2\pi}{N}k\right)$ because the cosine function strictly decreases in the domain $(0, \pi]$. For the remaining case where $N = 5$, we can explicitly show that $\cos\left(\frac{6\pi}{N}k\right) < 0 < \cos\left(\frac{2\pi}{N}k\right)$. Thus, for any $N \geq 5$, $\cos\left(\frac{6\pi}{N}k\right) \neq \cos\left(\frac{2\pi}{N}k\right)$ when $k = 1$, which results in a contradiction. In conclusion, for all $N \geq 5$, there are no $c_1, c_2 \in \mathbb{R}$ such that $\cos\left(\frac{6\pi}{N}k\right) = c_1 \cos\left(\frac{2\pi}{N}k\right) + c_2 \sin\left(\frac{2\pi}{N}k\right)$ for all $k = 1, 2, \ldots, N$, which is what we aimed to prove.

Hence, the null space of $\mathbb{L}\left(\lambda^{(1)}\right)$ is more than 2-dimensional, and so we cannot apply Theorem 9 for all-to-all and almost all-to-all coupling cases. Consequently, we exclude these two cases from the subsequent analysis on the criticality of bifurcation.

We then focus on the following cases where $m = 1$ and 2 and prove Lemma 17. For ease of reference, we restate the content of Lemma 17 here.

Lemma 23 (Restated)**.** *We restate Lemma 17.*

Let $0 < d \ll 1$. $\dim\left(\ker\left(\mathbf{L}(U_*^{(1)}, \mu_*^{(1)}, d)\right)\right) = 2$ *for* $m = 1$ *when* $N \geq 5$ *and for* $m = 2$ *when* $N \geq 7$.

Proof. (a) $N \geq 5, m = 1$

When $m = 1$, for any given $N \geq 5$, $\lambda^{(j)} = 1 - \cos\left(\frac{2\pi j}{N}\right) + \mathcal{O}(\epsilon^2)$ for integer j. Consider continuous function $\mathbf{f}(x) = \cos\left(\frac{2\pi}{N}x\right)$ on bounded domain $[1, N-1]$. Note that

$$\mathbf{f}(N-1) = \cos\left(\frac{2\pi(N-1)}{N}\right) = \cos\left(\frac{2\pi}{N}\right) = \mathbf{f}(1).$$

The derivative

$$\mathbf{f}'(x) = -\frac{2\pi}{N}\sin\left(\frac{2\pi}{N}x\right).$$

Since $\sin\left(\frac{2\pi}{N}x\right) > 0$ when $x \in \left(1, \frac{N}{2}\right)$ and $\sin\left(\frac{2\pi}{N}x\right) < 0$ when $x \in \left(\frac{N}{2}, N-1\right)$, $\mathbf{f}'(x) < 0$, which means $\mathbf{f}(x)$ decreases monotonically, on $\left(1, \frac{N}{2}\right)$, and $\mathbf{f}'(x) > 0$, which means $\mathbf{f}(x)$ increases monotonically, on $\left(\frac{N}{2}, N-1\right)$. Hence, for any $x \in (1, N-1)$, $\mathbf{f}(x) \neq \mathbf{f}(1)$, which implies that there is no $j \in \{2, 3, \ldots, N-2\}$ such that $\lambda^{(j)} = \lambda^{(1)}$.

Therefore, the null space of $\mathbb{L}\left(\lambda^{(1)}\right)$ is strictly 2-dimensional when $m = 1$.

(b) $N \geq 7, m = 2$

When $m = 2$, for any given $N \geq 7$,

$$\begin{aligned}
\lambda^{(j)} &= 2 - \cos\left(\frac{2\pi j}{N}\right) - \cos\left(\frac{4\pi j}{N}\right) + \mathcal{O}(\epsilon^2) \\
&= 3 - \cos\left(\frac{2\pi j}{N}\right) - 2\cos^2\left(\frac{2\pi j}{N}\right) + \mathcal{O}(\epsilon^2)
\end{aligned}$$

according to the double-angle identity $2\cos^2\left(\frac{\theta}{2}\right) = 1 + \cos(\theta)$.

Again, we consider the difference function between the eigenvalue for $j = 1$ and those for other general j, this time specifically for $m = 2$. We have

$$\mathcal{D}_2(j) \coloneqq \lambda^{(1)} - \lambda^{(j)} = \cos\left(\frac{2\pi j}{N}\right) + 2\cos^2\left(\frac{2\pi j}{N}\right) - \cos\left(\frac{2\pi}{N}\right) - 2\cos^2\left(\frac{2\pi}{N}\right).$$

Since we know $\lambda^{(N-1)} = \lambda^{(1)}$, $\mathcal{D}_2(1) = \mathcal{D}_2(N-1) = 0$. Consider $1 < j < N-1$, the derivative of $\mathcal{D}_2(j)$ with respect to j is

$$\mathcal{D}_2'(j) = -\frac{2\pi \sin\left(\frac{2\pi j}{N}\right)\left(1 + 4\cos\left(\frac{2\pi j}{N}\right)\right)}{N}.$$

The sign of $\mathcal{D}_2'(j)$ is determined by the signs of the multipliers in its numerator. When $1 < j < \frac{N}{2}$, $\sin\left(\frac{2\pi j}{N}\right) > 0$; when $\frac{N}{2} < j < N-1$, $\sin\left(\frac{2\pi j}{N}\right) < 0$. To simplify the notation, let $a_1 = \frac{\cos^{-1}\left(-\frac{1}{4}\right)}{2\pi}N$ and $a_2 = \left(1 - \frac{\cos^{-1}\left(-\frac{1}{4}\right)}{2\pi}\right)N$. When $1 < j < a_1$,

$1+4\cos\left(\frac{2\pi j}{N}\right) > 0$; when $a_1 < j < a_2$, $1+4\cos\left(\frac{2\pi j}{N}\right) < 0$; when $a_2 < j < N-1$, $1+4\cos\left(\frac{2\pi j}{N}\right) > 0$. Hence, $\mathcal{D}_2'(j) < 0$ on $(1, a_1)$ and $\left(\frac{N}{2}, a_2\right)$, and $\mathcal{D}_2'(j) > 0$ on $\left(a_1, \frac{N}{2}\right)$ and $(a_2, N-1)$. So function $\mathcal{D}_2(j)$ has a local maximum at $\frac{N}{2}$. Note that

$$\begin{aligned}\mathcal{D}_2\left(\frac{N}{2}\right) &= \cos(\pi) + 2\cos^2(\pi) - \cos\left(\frac{2\pi}{N}\right) - 2\cos^2\left(\frac{2\pi}{N}\right) \\ &= 1 - \cos\left(\frac{2\pi}{N}\right) - 2\cos^2\left(\frac{2\pi}{N}\right).\end{aligned}$$

For $N \geq 7$, $\cos\left(\frac{2\pi}{N}\right) \geq \cos\left(\frac{2}{7}\pi\right) > \cos\left(\frac{1}{3}\pi\right) = \frac{1}{2}$, so

$$\mathcal{D}_2\left(\frac{N}{2}\right) \leq 1 - \cos\left(\frac{2}{7}\pi\right) - 2\cos^2\left(\frac{2}{7}\pi\right) < 0.$$

Therefore, on $(1, N-1)$, $\mathcal{D}_2(j)$ first monotonically decreases on $(1, a_1)$ and then monotonically increases on $\left(a_1, \frac{N}{2}\right)$. After reaching a local maximum $\mathcal{D}_2\left(\frac{N}{2}\right) < 0$, it then again monotonically decreases on $\left(\frac{N}{2}, a_2\right)$ and finally monotonically increases on $(a_2, N-1)$. Thus there exists no $j \in \{2, 3, \ldots, N-2\}$ such that $\lambda^{(j)} = \lambda^{(1)}$.

In conclusion, the null space of $\mathbb{L}\left(\lambda^{(1)}\right)$ is strictly 2-dimensional when $m = 2$. $\square$

To prepare for the upcoming calculation, recall that if $\dim\left(\ker\left(\mathbb{L}\left(\lambda^{(1)}\right)\right)\right) = 2$, then the space $\ker\left(\mathbb{L}\left(\lambda^{(1)}\right)\right)$ is spanned by bases

$$\begin{aligned}X &= \left(\cos\left(\frac{2\pi}{N}\right), \cos\left(2\cdot\frac{2\pi}{N}\right), \ldots, \cos\left(N\cdot\frac{2\pi}{N}\right)\right) \\ Y &= \left(\sin\left(\frac{2\pi}{N}\right), \sin\left(2\cdot\frac{2\pi}{N}\right), \ldots, \sin\left(N\cdot\frac{2\pi}{N}\right)\right).\end{aligned}$$

We denote the bifurcation point from the homogeneous branch solution corresponding to $j = 1$ as (λ_*, v_*) where $\lambda_* = \bar{\lambda} + \mathcal{O}(\epsilon^2)$ for $\bar{\lambda} = m - \sum_{p=1}^{m} \cos\left(\frac{2\pi p}{N}\right)$ and $v_* = \left(\sqrt{\bar{\lambda}} + \mathcal{O}(\epsilon^2)\right)\mathbb{e}$ where $\mathbb{e} = (1, 1, \ldots, 1) \in \mathbb{R}^N$.

Proof of Theorem 6 (i)

We now present proofs for Theorem 6 (i). This process also verifies the conditions $p_\alpha(0,0,0) \neq 0$ and $p_\delta(0,0,0) \neq 0$, which are required by Theorem 9. Therefore, by the end, we will be able to directly use the branching results from the theorem. To begin, we make the assumption that the null space of $\mathbb{L}(\lambda_*)$ is 2-dimensional.

We first prove for the result in Lemma 18. In our current context, the restatement of the lemma is as follows.

Lemma 24 (Restated)**.** *We here restate Lemma 18.*

Let $N \geq 5$ *and* $1 \leq m \leq \left\lfloor \dfrac{N}{2} \right\rfloor - 1$. *Assuming there exist solutions to system* (3.10) *in* $\mathcal{B}_\epsilon(v_*, \lambda_*)$. *Then the solution takes the following form*

$$U^*(a(\lambda_*, \epsilon)) = v_*(\epsilon) + aX + \mathcal{O}(a^2)$$

where $a \in \mathbb{R}$.

Proof. In order to apply the results of Theorem 9 to determine the criticality of bifurcation, we need to find the normal form for our system. To do so, we first simplify the notation. Let $\tilde{w} = w - v_*$, and $\eta = \lambda - \lambda_*$. Then, applying the Center Manifold Theorem on our system, we have that for fixed $k \geq 1$, there exists $h \in C^k$ such that

$$W^c_{loc}(\eta) = \left\{ v_* + \tilde{w} + \tilde{h}(\tilde{w}, \eta) : \tilde{w} \in \mathcal{B}_\xi(0) \subset E^C \right\}$$

where $\tilde{h}(0,0) = 0$, $\tilde{h}_{\tilde{w}}(0,0) = 0$ and $0 < \eta \ll 1$. Note that $\tilde{w} \in \mathrm{span}(X, Y)$ so we can write $\tilde{w} = aX + bY$ for $a, b \in \mathbb{R}$.

Let $\mathcal{F}(V, \eta) = \mathbb{F}(V, \lambda)$. Apply spectral projection onto the center manifold, so then

$$\frac{d\tilde{w}}{dt} = P^c \mathcal{F}\left(v_* + aX + bY + \tilde{h}(aX + bY, \eta), \eta\right),$$

which is the normal form of our system near the branching point along the homogeneous branch at the lower-left corner.

Notice that $aX + bY = \tilde{w} \cong z = x + iy$. We consider the case when $b = y = 0$ and denote $h(a + b, \eta) = \tilde{h}(aX + bY, \eta)$, so then we have

$$P^c \mathcal{F}\left(v_* + aX + h(a, \eta), \eta\right) = -p(a^2, a^{N-1}, \eta)a - q(a^2, a^{N-1}, \eta)a^{N-1} \tag{3.12}$$

where $h : E^c \times (-\eta_0, \eta_0) \to E^h$ with $h(0, 0) = h_a(0, 0) = 0$ and $h(a, \eta) = \mathcal{O}\left(|a|^2 + |\eta|\right)$. $P^c h(a, \eta) = 0$ for all a, η.

We have thus far obtained results presented in Lemma 18. □

To use the branching results from Theorem 9, we want to compute $-p_\eta(0, 0, 0)$ and $-p_\alpha(0, 0, 0)$. Note that in the following computations, we restrict to $N \geq 5$.

Lemma 25. *For $N \geq 5$, it follows from equation (3.12) that $-p_\eta(0, 0, 0) = 2 + \mathcal{O}(\epsilon^2)$.*

Proof. Note that

$$\begin{aligned}
-p(0, 0, \eta) &= P^c D_a \left(\mathcal{F}(v_* + aX + h(a, \eta), \eta)\right)|_{a=0} \\
&= P^c \left(\mathcal{F}_V(v_* + aX + h(a, \eta), \eta)(X + h_a(a, \eta))\right)|_{a=0} \\
&= P^c \left(\mathcal{F}_V(v_* + h(0, \eta), \eta)(X + h_a(0, \eta))\right) \\
&= P^c \mathcal{F}_V(v_* + h(0, \eta), \eta)X \quad \text{ since } P^c h_a(0, \eta) = 0 \quad \forall \eta
\end{aligned}$$

So

$$-p_\eta(0,0,0) = D_\eta P^c \mathcal{F}_V(v_* + h(0,\eta),\eta)X|_{\eta=0}$$
$$= P^c\left(\mathcal{F}_{VV}(v_*,0)[X,h_\eta(0,0)] + \mathcal{F}_{V\eta}(v_*,0)\right)$$

To compute $-p_\eta(0,0,0)$, we first need to compute $h_\eta(0,0)$.

Note that $\mathcal{F}(V,\eta) = \mathbb{F}(V,\lambda_* + \eta) = 0$ when $V = v^*(\eta) = \left(\sqrt{\lambda+\eta} + \mathcal{O}(\epsilon^2)\right)\mathbb{e}$ and $v_* = v^*(0) = \left(\sqrt{\lambda} + \mathcal{O}(\epsilon^2)\right)\mathbb{e}$. According to the Center Manifold Theorem, $v^*(\eta) \in W^c_{loc}(v_*,\eta)$ for all η. Hence, there exists a unique $a = a^*(\eta)$ with

$$v^*(\eta) = v_* + a^*(\eta)X + h(a^*(\eta),\eta).$$

Further notice that $P^c v^*(\eta) = 0$ for all η. Thus, $a^*(\eta) = 0$ for all η. We then have $v^*(\eta) = v_* + h(0,\eta)$. Therefore, $h(0,\eta) = \left(\sqrt{\lambda+\eta} - \sqrt{\lambda} + \mathcal{O}(\epsilon^2)\right)\mathbb{e}$, and so

$$h_\eta(0,0) = \left(\frac{1}{2\sqrt{\lambda}} + \mathcal{O}(\epsilon^2)\right)\mathbb{e}.$$

We then can compute $P^c\mathcal{F}_{VV}(v_*,0)[X,h_\eta(0,0)]$.

Since $\mathcal{F}_{VV}$ has no dependency on η, we may consider function $\mathcal{F}_j : \mathbb{R}^N \to \mathbb{R}$ where $\mathcal{F}_j(V) = v_j^3 + \mathcal{O}(\epsilon^2)$. For $A, B \in \mathbb{R}^N$, we can calculate that

$$D_V\mathcal{F}_j(V)A = 3v_j^2 A_j + \mathcal{O}(\epsilon^2)$$

and

$$D_V^2\mathcal{F}_j(V)[A,B] = 6v_jA_jB_j + \mathcal{O}(\epsilon^2). \tag{3.13}$$

Using this information, we can compute

$$\begin{aligned}\mathcal{F}_{VV}(v_*,0)[X,h_\eta(0,0)] &= \left(6\left(\sqrt{\bar\lambda}+\mathcal{O}(\epsilon^2)\right)\mathbb{e}_j X_j\left(\frac{1}{2\sqrt{\bar\lambda}}+\mathcal{O}(\epsilon^2)\right)\mathbb{e}_j\right)_{j=1,\ldots,N}\\ &= 3X+\mathcal{O}(\epsilon^2).\end{aligned}$$

So

$$P^c\mathcal{F}_{VV}(v_*,0)[X,h_\eta(0,0)] = P^c\left(3X+\mathcal{O}(\epsilon^2)\right) = 3+\mathcal{O}(\epsilon^2).$$

We are left to compute $P^c\mathcal{F}_{V\eta}(v_*,0)$, which can be calculated directed:

$$P^c\mathcal{F}_{V\eta}(v_*,0) = P^c D_V D_\eta(-\eta V) = -1+\mathcal{O}(\epsilon^2).$$

Therefore,

$$-p_\eta(0,0,0) = P^c\left(\mathcal{F}_{VV}(v_*,0)[X,h_\eta(0,0)]+\mathcal{F}_{V\eta}(v_*,0)\right) = 2+\mathcal{O}(\epsilon^2).$$

□

Lemma 26. *For $N \geq 5$, it follows from equation (3.12) that*

$$-p_\alpha(0,0,0) = -\frac{15}{4}-\frac{9}{2}\frac{\bar\lambda}{\lambda_2+2\bar\lambda}+\mathcal{O}(\epsilon^2)$$

where

$$\bar\lambda = m+\frac{1}{2}-\frac{\sin(2\pi m+\pi)}{2\sin\left(\frac{\pi}{N}\right)}$$

and

$$\lambda_2+2\bar\lambda = \frac{-\sin\left(\frac{2\pi(m+1)}{N}\right)+\sin\left(\frac{\pi(4m+2)}{N}\right)-\sin\left(\frac{2\pi m}{N}\right)}{\sin\left(\frac{2\pi}{N}\right)}.$$

Proof. Notice that

$$\begin{aligned} p(a^2, a^{N-1}, 0) &= p(0,0,0) + a^2 p_\alpha(0,0,0) + \mathcal{O}(|a|^4 + |a|^{N-1}) \\ &= a^2 p_\alpha(0,0,0) + \mathcal{O}(|a|^3) \end{aligned}$$

So $g(a,0) = a^3 p_\alpha(0,0,0) + \mathcal{O}(|a|^4)$. We then have

$$-p_\alpha(0,0,0) = -\frac{1}{6} g_{aaa}(0,0) = \frac{1}{6} P^c D_a^3 \mathcal{F}(v_* + aX + h(a,0), 0)|_{a=0}$$

To find $-p_\alpha(0,0,0)$, we then need to compute $D_a^3 \mathcal{F}(v_* + aX + h(a,0),0)|_{a=0}$:

$$\begin{aligned} & D_a \mathcal{F}(v_* + aX + h(a,0), 0) = \mathcal{F}_V(v_* + aX + h(a,0),0)[X + h_a(a,0)] \\ \implies & D_a^2 \mathcal{F}(v_* + aX + h(a,0), 0) = \mathcal{F}_{VV}(v_* + aX + h(a,0),0)[X + h_a(a,0)]^2 \\ & \qquad + \mathcal{F}_V(v_* + aX + h(a,0),0) h_{aa}(a,0) \\ \implies & D_a^3 \mathcal{F}(v_* + aX + h(a,0), 0)|_{a=0} = \mathcal{F}_{VVV}(v_*,0)[X + h_a(0,0)]^3 \\ & \qquad + 2\mathcal{F}_{VV}(v_*,0)[X + h_a(0,0), h_{aa}(0,0)] \\ & \qquad + \mathcal{F}_{VV}(v_*,0)[X + h_a(0,0), h_{aa}(0,0)] \\ & \qquad + \mathcal{F}_V(v_*,0) h_{aaa}(0,0) \end{aligned}$$

Since $h_a(0,0) = 0$ and $P^c h_{aaa}(0,0) = 0$,

$$\begin{aligned} & P^c \left(D_a^3 \mathcal{F}(v_* + aX + h(a,0),0)|_{a=0} \right) \\ = \; & P^c \mathcal{F}_{VVV}(v_*,0)[X]^3 + 3 P^c \mathcal{F}_{VV}(v_*,0)[X, h_{aa}(0,0)] \\ = \; & \left(6 \sum_{j=1}^N X_j^4 + 3 \left\langle X, \left(6 \left(\sqrt{\lambda} + \mathcal{O}(\epsilon^2) \right) X_j D_a^2 h_j(0,0) \right)_{j=1,\ldots,N} \right\rangle + \mathcal{O}(\epsilon^2) \right) \frac{1}{|X|^2} \\ = \; & \left(6 \sum_{j=1}^N X_j^4 + 18\sqrt{\lambda} \sum_{j=1}^N X_j^2 D_a^2 h_j(0,0) \right) \frac{1}{|X|^2} + \mathcal{O}(\epsilon^2) \end{aligned}$$

using $P^c = \langle X, \cdot \rangle \frac{1}{|X|^2}$ and equation (3.13). It follows that

$$-p_\alpha(0,0,0) = \left(\sum_{j=1}^{N} X_j^4 + 3\sqrt{\bar{\lambda}} \sum_{j=1}^{N} X_j^2 D_a^2 h_j(0,0) \right) \frac{1}{|X|^2} + \mathcal{O}(\epsilon^2). \tag{3.14}$$

So to compute $-p_\alpha(0,0,0)$, we need to first find out $h_{aa}(0,0)$. To simplify the notation, let $H \coloneqq h_{aa}(0,0)$. Then

$$h(a,0) = \frac{a^2}{2} h_{aa}(0,0) + \mathcal{O}(|a|^3) = \frac{a^2}{2} H + \mathcal{O}(|a|^3).$$

Note that when $\eta = 0$, one trajectory of solutions is

$$V(t) = v_* + a(t)X + h(a(t), 0)$$

which then gives

$$\frac{d}{dt} V = \dot{a}X + \dot{a}aH + \dot{a}\mathcal{O}(a^2).$$

but also

$$\begin{aligned} \frac{d}{dt} V &= \mathcal{F}(v_* + aX + h(a,0), 0) \\ &= \mathcal{F}_V(v_*, 0) \left(aX + \frac{a^2}{2} H \right) + \frac{a^2}{2} \mathcal{F}_{VV}(v_*, 0)[X]^2 + \mathcal{O}(a^3). \end{aligned}$$

Hence

$$\dot{a}X + \dot{a}aH + \dot{a}\mathcal{O}(a^2) = \mathcal{F}_V(v_*, 0) \left(aX + \frac{a^2}{2} H \right) + \frac{a^2}{2} \mathcal{F}_{VV}(v_*, 0)[X]^2 + \mathcal{O}(a^3).$$

Because $\dot{a} = \mathcal{O}(a^2)$ when $\eta = 0$, applying P^h, the spectral projection onto the stable and unstable manifolds, gives

$$\mathcal{O}(a^3) = P^h \left(\mathcal{F}_V(v_*, 0) \frac{a^2}{2} H \right) + P^h \left(\frac{a^2}{2} \mathcal{F}_{VV}(v_*, 0)[X]^2 \right) + \mathcal{O}(a^3).$$

Therefore,

$$P^h \mathcal{F}_V(v_*, 0) H = -P^h \mathcal{F}_{VV}(v_*, 0)[X]^2. \tag{3.15}$$

Notice that

$$\begin{aligned}
\mathcal{F}_V(v_*, 0) &= \Delta_m + \left(-\lambda_* + 3v_*^2\right) I_N + \mathcal{O}(\epsilon^2) \\
&= \Delta_m + \left(-\bar{\lambda} + 3\left(\sqrt{\bar{\lambda}} + \mathcal{O}(\epsilon^2)\right)^2\right) I_N + \mathcal{O}(\epsilon^2) \\
&= \Delta_m + 2\bar{\lambda} I_N + \mathcal{O}(\epsilon^2)
\end{aligned}$$

where $\bar{\lambda} = m - \sum_{p=1}^{m} \cos\left(\frac{2\pi p}{N}\right)$. Note that P^h commutes with F_V and $H \notin \text{span}(X, Y)$, the center space, so

$$P^h \mathcal{F}_V(v_*, 0) H = \Delta_m H + 2\bar{\lambda} H + \mathcal{O}(\epsilon^2). \tag{3.16}$$

According to equation (3.13), we have

$$\mathcal{F}_{VV}(v_*, 0)[X]^2 = \left(6\sqrt{\bar{\lambda}} \cdot X_j^2\right)_{j=1,\ldots,N} + \mathcal{O}(\epsilon^2).$$

where $X_j = \cos\left(\frac{2\pi j}{N}\right)$ for $j = 1, \ldots, N$. To simplify further, we use the trigonometric identity $1 + \cos(2\phi) = 2\cos^2(\phi)$, which gives $1 + \cos\left(2\frac{2\pi j}{N}\right) = 2\cos^2\left(\frac{2\pi j}{N}\right) = 2X_j^2$. So

$$\left(6\sqrt{\bar{\lambda}} \cdot X_j^2\right)_{j=1,\ldots,N} = 3\sqrt{\bar{\lambda}}\left(\mathbb{e} + X^{(2)}\right)$$

where $X^{(2)} = \left(\cos\left(\frac{4\pi j}{N}\right)\right)_{j=1,\ldots,N}$ is the eigenvector of Δ_m corresponding to the eigenvalue $\lambda_2 = 2\left(-m + \sum_{p=1}^{m} \cos\left(\frac{4\pi p}{N}\right)\right)$. Notice that P^h commutes with F_{VV} and neither $\mathbb{e}$ nor $X^{(2)}$ is in span(X, Y), the center space, so

$$P^h \mathcal{F}_{VV}(v_*, 0)[X]^2 = 3\sqrt{\bar{\lambda}}\left(\mathbb{e} + X^{(2)}\right) + \mathcal{O}(\epsilon^2). \tag{3.17}$$

Plugging equations (3.16) and (3.17) into equation (3.15), we get

$$\Delta_m H + 2\bar{\lambda} H + \mathcal{O}(\epsilon^2) = -3\sqrt{\bar{\lambda}}\left(\mathbb{e} + X^{(2)}\right) + \mathcal{O}(\epsilon^2). \tag{3.18}$$

We can consider $H = c_0\mathbb{e} + c_2 X^{(2)}$ for some $c_0, c_2 \in \mathbb{R}$ and plug this expression of H into equation (3.18):

$$2\bar{\lambda} c_0 \mathbb{e} + \left(\lambda_2 + 2\bar{\lambda}\right) c_2 X^{(2)} = -3\sqrt{\bar{\lambda}}\mathbb{e} - 3\sqrt{\bar{\lambda}} X^{(2)}. \tag{3.19}$$

Solving (3.19) for c_0 and c_2, we can find that

$$h_{aa}(0,0) = H = -\frac{3}{2\sqrt{\bar{\lambda}}}\mathbb{e} - \frac{3\bar{\lambda}}{\lambda_2 + 2\bar{\lambda}} X^{(2)}.$$

Plugging $h_{aa}(0,0)$ back into equation (3.14), we yield

$$-p_\alpha(0,0,0) = \left(\sum_{j=1}^{N} X_j^4 - \frac{9}{2}\sum_{j=1}^{N} X_j^2\left(\mathbb{e}_j + \frac{2\bar{\lambda}}{\lambda_2 + 2\bar{\lambda}} X_j^{(2)}\right)\right)\frac{1}{|X|^2} + \mathcal{O}(\epsilon^2). \tag{3.20}$$

We utilize the following identities

$$\sum_{j=1}^{N} X_j^4 = \sum_{j=1}^{N} \cos^4\left(\frac{2\pi j}{N}\right) = \frac{3}{8}N,$$
$$\sum_{j=1}^{N} X_j^2 = \sum_{j=1}^{N} \cos^2\left(\frac{2\pi j}{N}\right) = \frac{N}{2},$$

$$
\begin{aligned}
\sum_{j=1}^{N} X_j^2 X_j^{(2)} &= \sum_{j=1}^{N} \cos^2\left(\frac{2\pi j}{N}\right)\cos\left(\frac{4\pi j}{N}\right) = \frac{N}{4}, \\
\frac{1}{|X|^2} &= \frac{1}{\sum_{j=1}^{N}\cos^2\left(\frac{2\pi j}{N}\right)} = \frac{2}{N},
\end{aligned}
$$

so equation (3.20) can be simplified as

$$
-p_\alpha(0,0,0) = -\frac{15}{4} - \frac{9}{2}\frac{\bar{\lambda}}{\lambda_2 + 2\bar{\lambda}} + \mathcal{O}(\epsilon^2)
$$

where

$$
\begin{aligned}
\bar{\lambda} &= m - \sum_{k=1}^{m}\cos\left(\frac{2\pi k}{N}\right) \\
&= m + \frac{1}{2} - \frac{\sin\left(\frac{(2m+1)\pi}{N}\right)}{2\sin\left(\frac{\pi}{N}\right)} \\
\text{and} \quad \lambda_2 + 2\bar{\lambda} &= 2\left(-m + \sum_{k=1}^{m}\cos\left(\frac{4\pi k}{N}\right)\right) + 2\left(m - \sum_{k=1}^{m}\cos\left(\frac{2\pi k}{N}\right)\right) \\
&= \frac{-\sin\left(\frac{2\pi(m+1)}{N}\right) + \sin\left(\frac{\pi(4m+2)}{N}\right) - \sin\left(\frac{2\pi m}{N}\right)}{\sin\left(\frac{2\pi}{N}\right)}.
\end{aligned}
$$

□

Hence, by Lemma 25 and Lemma 26, applying Theorem 9, we obtain results in Theorem 6 (i).

Additionally, we also know that the branching directions from the homogeneous solutions at the lower-left corner fall into the following cases in Figure 3.12 for odd N and Figure 3.13 for even N. Specifically, Theorem 9 tells us there are two branches of isotropy subgroups of solutions bifurcating from the homogeneous solution branch. When N is odd, there are two $\mathbb{Z}_2(\kappa)$ branches, and when N is even, there are one $\mathbb{Z}_2(\kappa)$ and one $\mathbb{Z}_2(\kappa\zeta)$ branches.

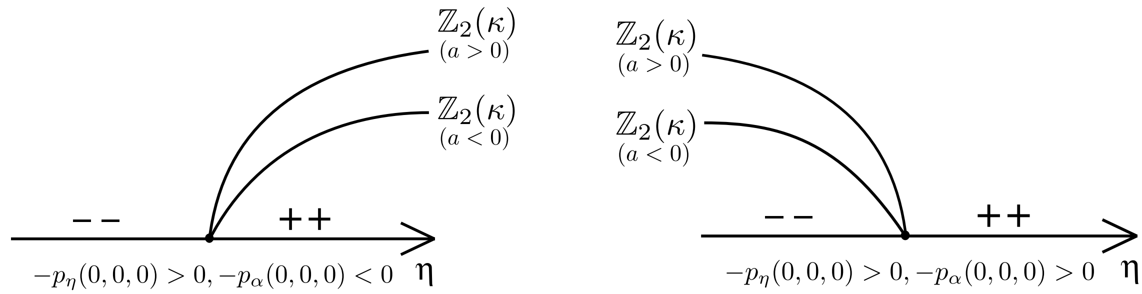

(a) $-p_\alpha(0,0,0)<0$, supercritical

(b) $-p_\alpha(0,0,0)>0$, subcritical

Figure 3.12: Illustrations of the criticality of bifurcation from the homogeneous solution branch for the lattice system at the lower-left corner with $N \geq 5$ being an odd number. There are two distinct bifurcation branches, $\mathbb{Z}_2(\kappa)$ with $a>0$ and $\mathbb{Z}_2(\kappa)$ with $a<0$. The branching directions are dependent on the sign of $-p_\alpha(0,0,0)$. $-$ means stable eigenvalues and $+$ means unstable eigenvalues.

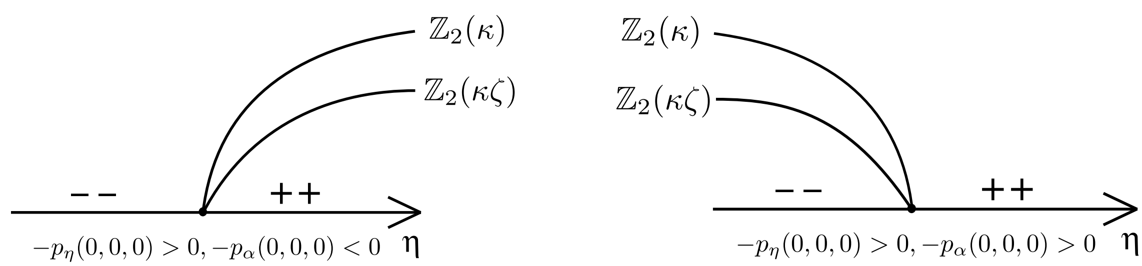

(a) $-p_\alpha(0,0,0)<0$, supercritical

(b) $-p_\alpha(0,0,0)>0$, subcritical

Figure 3.13: Illustrations of the criticality of bifurcation from the homogeneous solution branch for the lattice system at the lower-left corner with $N \geq 5$ being an even number. There are two distinct bifurcation branches, $\mathbb{Z}_2(\kappa)$ and $\mathbb{Z}_2(\kappa\zeta)$. The branching directions are dependent on the sign of $-p_\alpha(0,0,0)$. $-$ means stable eigenvalues and $+$ means unstable eigenvalues.

In short, the branching direction depends on the sign of $-p_\alpha(0,0,0)$. For simplicity, we set $\epsilon = 0$ and explicitly compute when $N = 16, 17, 18, 19$ for $1 \leq m \leq \left\lfloor \frac{N-1}{2} \right\rfloor - 1$ (all cases except for almost all-to-all and all-to-all couplings). The prediction shows that as m increases, $-p_\alpha(0,0,0)$ transitions from negative to positive, indicating a shift in the branching direction. For odd N, the change is from the scenario depicted in Figure 3.12a to that in Figure 3.12b; for even N, the shift is from Figure 3.13a to Figure 3.13b. We checked numerically and confirmed that the numerical observations align with the analytical predictions.

Specifically, we find that the smallest m when $-p_\alpha(0,0,0)$ becomes positive for each N is $(N,m) = (16,6),(17,7),(18,7),(19,7)$.

Criticality in Limiting Case $N \to \infty$

We assume that the null space of $\mathbb{L}\left(\lambda_*\right)$ is 2-dimensional and then study the limiting case as $N \to \infty$. For $m = 1, 2$, we can compute that $\lim\limits_{N\to\infty} \dfrac{\bar{\lambda}}{\lambda_2 + 2\bar{\lambda}} = -\dfrac{1}{6}$, so $\lim\limits_{N\to\infty} -p_\alpha(0,0,0) = -3 + \mathcal{O}(\epsilon^2)$.

When $m = \left\lfloor \dfrac{N-1}{2} \right\rfloor - 1$, $\lim\limits_{N\to\infty} \dfrac{\bar{\lambda}}{\lambda_2 + 2\bar{\lambda}} = \infty$ and so $\lim\limits_{N\to\infty} -p_\alpha(0,0,0) = \infty$.

After these initial observations, we proceed to provide proofs for Theorem 6 (ii).

Let $r = \dfrac{m}{N}$. We focus on $1 \le m \le \left\lfloor \dfrac{N-1}{2} \right\rfloor - 1$ so $0 \le r \le \frac{1}{2}$. An interesting question to ask is as $N \to \infty$, at which ratio r the branching direction switches, i.e., $-p_\alpha(0,0,0)$ changes sign. Note that when $m = 1$, $\lim\limits_{N\to\infty} r = 0$ and when $m = \left\lfloor \dfrac{N-1}{2} \right\rfloor - 1$, $\lim\limits_{N\to\infty} r = \dfrac{1}{2}$, so we already know as $N \to \infty$, $-p_\alpha(0,0,0)$ is negative at $r = 0$ and positive at $r = \frac{1}{2}$. To see when the direction changes, we are left to find out when $\lim\limits_{N\to\infty} -p_\alpha(0,0,0)$ crosses zero. To do so, we rewrite $-p_\alpha(0,0,0)$ in terms of r and get

$$-p_\alpha(0,0,0) = -\frac{15}{4} - \frac{9}{2}\frac{\bar{\lambda}}{\lambda_2 + 2\bar{\lambda}} + \mathcal{O}(\epsilon^2)$$

where

$$\bar{\lambda} = \frac{2rN\sin\left(\frac{\pi}{N}\right) - \sin\left(2\pi r + \frac{\pi}{N}\right) + \sin\left(\frac{\pi}{N}\right)}{2\sin\left(\frac{\pi}{N}\right)}$$

$$\lambda_2 + 2\bar{\lambda} = \frac{-\sin\left(2\pi r + \frac{2\pi}{N}\right) + \sin\left(4\pi r + \frac{2\pi}{N}\right) - \sin\left(2\pi r\right)}{\sin\left(\frac{2\pi}{N}\right)}$$

so

$$\lim_{N\to\infty} -p_\alpha(0,0,0) = -\frac{15}{4} - \frac{9}{2}\frac{2\pi r - \sin\left(2\pi r\right)}{\sin\left(4\pi r\right) - 2\sin\left(2\pi r\right)} + \mathcal{O}(\epsilon^2).$$

Then we have

$$\lim_{N\to\infty} -p_\alpha(0,0,0) = 0 \implies 16\sin(2\pi r) - 5\sin(4\pi r) - 12\pi r = \mathcal{O}(\epsilon^2). \tag{3.21}$$

Since the domain of r is $\left[0, \frac{1}{2}\right]$, we seek to determine how many distinct values of r within this domain satisfy equation (3.21). The following lemma establishes that there exists only one such r for $0 < r < \frac{1}{2}$ where the equation holds.

Lemma 27. *Let $f(r) = 16\sin(2\pi r) - 5\sin(4\pi r) - 12\pi r$. $f(r)$ has a unique root on $\left(0, \frac{1}{2}\right)$.*

Proof. The first and second derivatives of $f(r)$ are

$$f'(r) = 32\pi\cos(2\pi r) - 20\pi\cos(4\pi r) - 12\pi$$

and

$$f''(r) = -64\pi^2\sin(2\pi r) + 80\pi^2\sin(4\pi r).$$

We first focus on $0 < r < \frac{1}{4}$. Note that on $\left(0, \frac{1}{8}\right]$, $f''(r) > 0$ and also since $f'(0) = 0$, we know that $f'(r) > 0$ on $\left(0, \frac{1}{8}\right]$ and thus $f(r)$ is monotonically increasing on this domain. Then on $\left(\frac{1}{8}, \frac{1}{4}\right]$, $f''\left(\frac{1}{8}\right) > 0$, $f''\left(\frac{1}{4}\right) < 0$ and $f''(r)$ is monotonically decreasing, so there exists $r' \in \left(\frac{1}{8}, \frac{1}{4}\right)$ such that $f''(r') = 0$, and $f''(r) > 0$ for $r \in \left(\frac{1}{8}, r'\right)$, $f''(r) < 0$ for $r' \in \left(r', \frac{1}{4}\right)$. So $f'(r)$ increases monotonically on $\left(\frac{1}{8}, r'\right)$ and then decreases monotonically on $\left(r', \frac{1}{4}\right)$. Since $f'\left(\frac{1}{8}\right) > 0$ and $f'\left(\frac{1}{4}\right) > 0$, $f'(r) > 0$ on $\left(\frac{1}{8}, \frac{1}{4}\right]$, which means $f(r)$ is monotonically increasing. Hence, $f(r)$is monotonically increasing on $\left(0, \frac{1}{4}\right)$ and since $f(0) = 0$, so there is no root on $\left(0, \frac{1}{4}\right)$.

We then focus on $\frac{1}{4} \leq r < \frac{1}{2}$. Note that $f''(r) < 0$ on this domain, so $f'(r)$ is monotonically decreasing. Since $f'\left(\frac{1}{4}\right) > 0, f'\left(\frac{1}{2}\right) < 0$ and $f\left(\frac{1}{4}\right) > 0, f\left(\frac{1}{2}\right) < 0$, $f(r)$ has a unique root on $\left(0, \frac{1}{2}\right)$.

In conclusion, $f(r)$ has no root on $\left(0, \frac{1}{4}\right)$ and a unique root on $\left[\frac{1}{4}, \frac{1}{2}\right)$, so $f(r)$ has a unique root on $\left(0, \frac{1}{2}\right)$. $\square$

Lemma 27 tells that as $N \to \infty$, when r increases from zero, the switch of branching direction happens only once. Using Maple, we can calculate that the solution to $16\sin(2\pi r) - 5\sin(4\pi r) - 12\pi r = 0$ for $0 < r < \frac{1}{2}$ is $r \approx 0.3932$. So ignoring the ϵ effect, as $N \to \infty$, we expect that the bifurcation criticality switches from supercritical to subcritical at around $r \approx 0.3932$.

We thereby obtain the results for Theorem 6 (ii).

3.3 Connecting Original System with the Rescaled System

To show that the emergent patterned states from the homogeneous solution branch are connected with the branches of patterns in Figure 2.2, we verify by numerical simulations.

For a selected pair of (N, m), we run numerical continuation with the following steps in MATLAB to verify that the branches are connected:

(1) Set $d \ll 1$, an initial $\mu^{(0)}$ and an integer $k \in \{1, 2, \ldots, N\}$ denoting the number of nodes to be set with nonzero values for the initial guess. Then use $(a, \ldots, a, 0, 0, \ldots, 0, 0, a, \ldots, a, a)$, a vector of length N with k elements taking on value $a = \sqrt{1 + \sqrt{1 - \mu^{(0)}}}$ and $N - k$ elements taking on 0, as the initial

guess to convert to a near-by solution, $U^{(0)}$, to $d(\Delta_m U)_n + f(u_n, \mu^{(0)}) = 0$ using `fsolve`.

(2) Use $(U^{(0)}, \mu^{(0)})$ as the starting solution and use numerical continuation to continue the solution branch of the full system in terms of μ. Stop until the solution in (U, μ) gets close to the lower-left region, i.e., u_n and μ both become close to 0. Denote the end solution as $(U^{(1)}, \mu^{(1)})$ where $U^{(1)} = \left(u_1^{(1)}, u_2^{(1)}, \ldots, u_N^{(1)}\right)$.

(3) Let $\lambda^{(0)} = \frac{\mu^{(1)}}{d}$ and $V^{(0)} = \left(\frac{u_1^{(1)}}{\sqrt{d}}, \frac{u_2^{(1)}}{\sqrt{d}}, \ldots, \frac{u_N^{(1)}}{\sqrt{d}}\right)$. Use $(V^{(0)}, \lambda^{(0)})$ as the initial solution and continue the solution branch in the rescaled system for the lower-left region in terms of λ. To check the goodness of the initial solution, compute the residual vector $\mathbf{r}_n = (\Delta_m V^{(0)})_n - \lambda^{(0)} v_n^{(0)} + 2\left(v_n^{(0)}\right)^3 - d\left(v_n^{(0)}\right)^5$ for $1 \leq n \leq N$.

Figures 3.14 and 3.15 illustrate an example when continuing on a system with $(N, m) = (16, 3)$. The initial parameters are $d = 0.01$, $\mu^{(0)} = 0.5$ and $k = 15$.

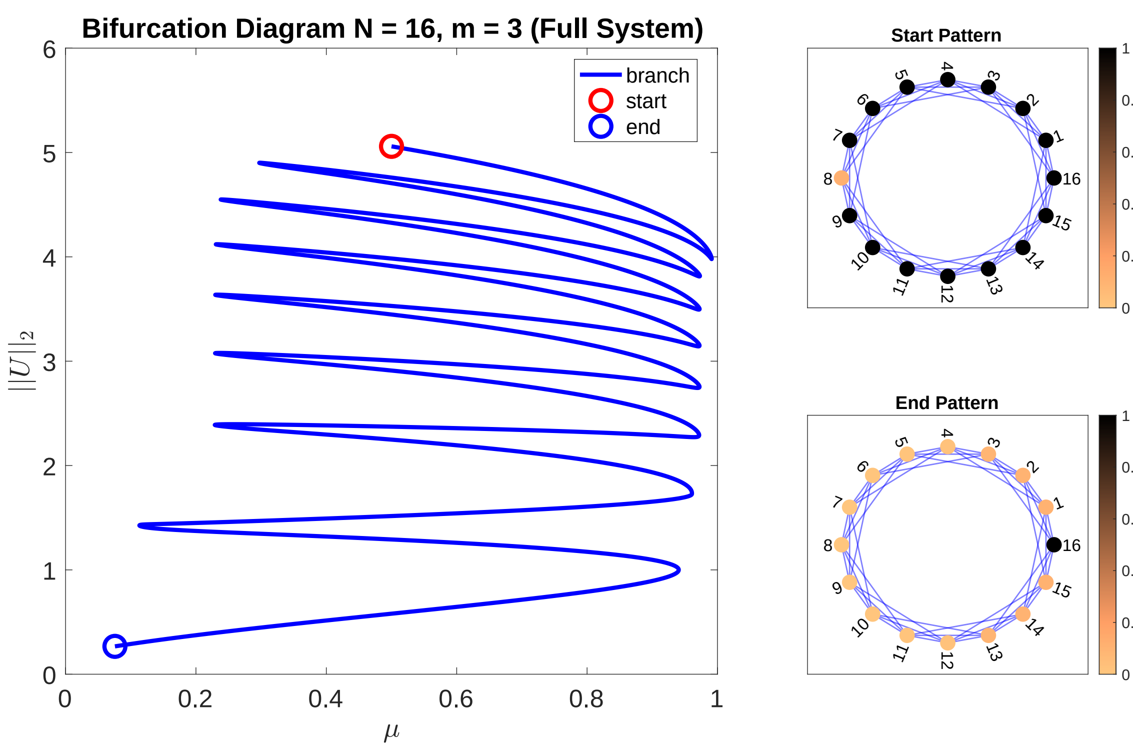

Figure 3.14: Numerical continuation on the original full system for $N = 16, m = 3$ until near the lower-left region where (u_n, μ, d) is close to $(0, 0, 0)$. The start and end solution patterns are illustrated in the right panel with normalized node values.

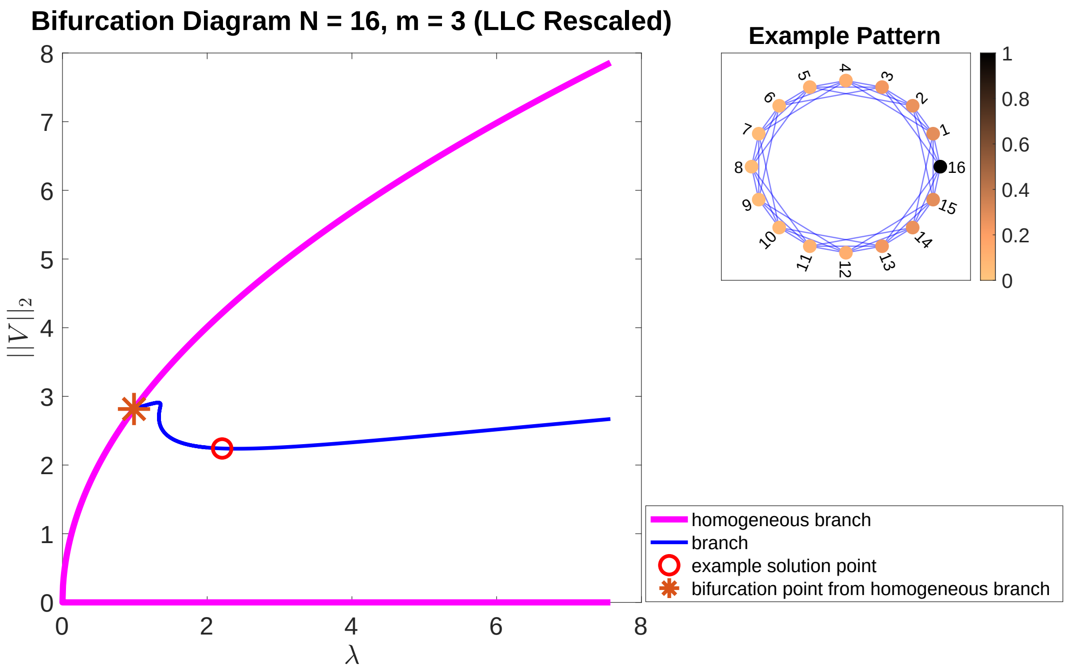

Figure 3.15: Numerical continuation on the rescaled system at the lower-left region where (u_n, μ, d) is near $(0,0,0)$, starting at solution taken from the full system. The L^2-norm of the residual vector at the initial solution is `7.4143e-07`. Detailed explanations are similar to those in Figure 3.8.

Note that when computing the homogeneous solutions and the predicted bifurcation points in Figure 3.15, we explicitly include all the higher-order terms. Specifically, to find the homogeneous solutions, we consider the rescaled system with all terms fully expressed $\mathbb{F}(V,\lambda,d)_n = (\Delta_m V)_n - \lambda v_n + 2v_n^3 - dv_n^5$, and so the homogeneous solution v_* satisfies $-\lambda v_n + 2v_n^3 - dv_n^5 = 0$. Solving for v_n yields that homogeneous solution $v_*(\lambda, d) = v_-(\lambda, d)\mathbb{e}$ where $v_-(\lambda, d) = \sqrt{\frac{1-\sqrt{1-d\lambda}}{d}}$.

Then to explicitly solve for the bifurcation points, we consider the Jacobian $\mathbb{L}(V,\lambda,d) = \Delta_m + (-\lambda + 6v_n^2 - 5dv_n^4)\, I_N$. Recall that the eigenvalues of Δ_m are

$$\lambda_j = 2\left(-m + \sum_{p=1}^{m} \cos\left(\frac{2\pi jp}{N}\right)\right) \text{ for } j = 0, 1, 2, \ldots, \left\lfloor \frac{N}{2} \right\rfloor.$$

corresponding to the discrete Fourier ansatz

$$v_{k,j} = e^{i\omega_j k}, \quad \text{where } \omega_j = \frac{2\pi j}{N}, \quad k = 1, \ldots, N, \quad j = 0, 1, \ldots, \left\lfloor \frac{N}{2} \right\rfloor.$$

So we can compute the eigenvalues to $\mathbb{L}(v_*(\lambda, d), \lambda, d)$ along the homogeneous branch $v_*(\lambda, d)$, which are $\lambda_j - \lambda + 6v_-(\lambda, d) - 5dv_-(\lambda, d)^2$. Setting the eigenvalue to 0 and solving for λ then give us the associated λ values at the bifurcation points, indexed by j:

$$\lambda^{(j)}(d) = \frac{-\lambda_j d + 2 - 2\sqrt{d\lambda_j + 1}}{4d}.$$

where $j = 0, 1, 2, \ldots, \left\lfloor \frac{N}{2} \right\rfloor$.

The asterisk marked on Figure 3.15 corresponds to the bifurcation point along homogeneous solutions, $\left(v_*(\lambda^{(1)}(d), d), \lambda^{(1)}(d), d\right)$, with index $j = 1$.

4 Bifurcation Analysis for the Upper-Right Corner

In this section, we follow the similar ideas as in Section 3 and present analysis of the bifurcation at the upper-right corner of the original system when (u_n, μ, d) is near $(1, 1, 0)$. Specifically, this section illustrate proofs for Theorems 7 and 8 as well as Lemma 19.

4.1 Bifurcation from Homogeneous Solutions

Our original ring system is

$$\dot{u}_n = d(\Delta_m U)_n + f(u_n, \mu), \quad 1 \le n \le N, \quad U = (u_1, u_2 \ldots, u_N) \in \mathbb{R}^N$$

where

$$(\Delta_m U)_n = \begin{cases} -(2m+1)u_n + \sum_{j=-m}^{m} u_{n+j}, & 1 \le m < \lfloor \frac{N}{2} \rfloor \\ -Nu_n + \sum_{j=1}^{N} u_j, & m = \lfloor \frac{N}{2} \rfloor. \end{cases}$$

In the region of upper-right corner when (u_n, μ, d) is near $(1, 1, 0)$, the nonlinearity

$$f(u_n, \mu) = f(1 + \check{u}_n, 1 - \check{\mu}) = \check{\mu} - \check{u}_n^2 + \mathcal{O}(\check{\mu}\check{u}_n + \check{u}_n^3).$$

Denote $\mathscr{F}(\check{U}, \check{\mu}, d) = d(\Delta_m \check{U})_n + \check{\mu} - \check{u}_n^2 + \mathcal{O}(\check{\mu}\check{u}_n + \check{u}_n^3)$.

We now prove for Theorem 7 (i). To do this, we analyze the rescaled system for the upper-right region. Note that after the calculations for the verification of the genericity conditions we present later, Theorem 7 (ii) can be naturally obtained based on Theorem 9, similar to the discussion in the previous Section 3.1.

Rescaled Systems

In this parameter regime where (u_n, μ, d) is near $(1, 1, 0)$, we use the scaling $\check{u}_n = \epsilon v_n, \check{\mu} = \epsilon^2 \lambda, d = \epsilon$ and let $V = (v_1, v_2 \ldots, v_N) \in \mathbb{R}^N$,

$$\mathbb{F}(V, \lambda) := \dot{v}_n = \epsilon(\Delta_m(\mathbb{e} + \epsilon V))_n + \epsilon^2 \lambda - \epsilon^2 v_n^2 + \mathcal{O}(\epsilon^3).$$

To find stationary solutions, we solve

$$\mathbb{F}(V,\lambda)=0 \quad \Rightarrow \quad (\Delta_m V)_n+\lambda-v_n^2+\mathcal{O}(\epsilon)=0 \tag{3.22}$$

since $\Delta_m \mathbb{e}=0$.

The spatially homogeneous equilibria v_n are approximately $\pm\sqrt{\lambda}+\mathcal{O}(\epsilon)$, corresponding to solutions $u_\pm(\mu)$ in u_n for $n=1,\ldots,N$. We define $v_\pm(\lambda)=\pm\sqrt{\lambda}+\mathcal{O}(\epsilon)$.

Similar to the discussion in Section 3.1, when simulating numerically, we can set $\epsilon=0$ and solve $(\Delta_m V)_n+\lambda-v_n^2=0$ for V while continuing in the parameter λ. As for the initial step, we pick a sufficiently large λ, put in the corresponding initial guess of the solution in V as $(\sqrt{\lambda},\sqrt{\lambda},\ldots,\sqrt{\lambda},-\sqrt{\lambda})$, and then converge the initial guess to a real solution close-by using `fsolve` in MATLAB.

Bifurcation Points along Homogeneous Solutions Branch

We then want to find all bifurcating points along the homogeneous solution branch near the upper-right region. Define the Jacobian of $\mathbb{F}(V,\lambda)$ with respect to V at homogeneous branch solutions as

$$\mathbb{L}(\lambda)\coloneqq D_V\mathbb{F}\left(V(\lambda),\lambda\right)=\Delta_m+(-2v_n+\mathcal{O}(\epsilon))I_N$$

where I_N is the identity matrix.

Plugging in the homogeneous solution $v_\pm(\lambda)\mathbb{e}$, we have

$$\mathbb{L}(\lambda)=\Delta_m\mp\left(2\sqrt{\lambda}+\mathcal{O}(\epsilon)\right)I_N.$$

Recall that eigenvalues of Δ_m are

$$\lambda_j = 2\left(-m + \sum_{p=1}^{m} \cos\left(\frac{2\pi jp}{N}\right)\right) \text{ for } j = 0, 1, 2, \ldots, \left\lfloor \frac{N}{2} \right\rfloor$$

with the corresponding eigenvectors defined as

$$v_{k,j} = e^{i\omega_j k}, \quad \text{where } \omega_j = \frac{2\pi j}{N}, \quad k = 1, \ldots, N, \quad j = 0, 1, \ldots, \left\lfloor \frac{N}{2} \right\rfloor$$

Hence, to find the λ value when the eigenvalue of the Jacobian along the homogeneous solutions is zero, we should solve for

$$\lambda_j \mp 2\sqrt{\lambda} + \mathcal{O}(\epsilon) = 0.$$

Notice that $\lambda_j \leq 0$ with $\lambda_j = 0$ only when $j = 0$, so we choose the "+" sign, which corresponds to homogeneous solutions $v_n^*(\lambda) = -\sqrt{\lambda} + \mathcal{O}(\epsilon)$. Then solving for λ gives us

$$\lambda^{(j)} = \frac{1}{4}\lambda_j^2 + \mathcal{O}(\epsilon) = \left(-m + \sum_{p=1}^{m} \cos\left(\frac{2\pi jp}{N}\right)\right)^2 + \mathcal{O}(\epsilon).$$

We again focus on the case corresponding to $j = 1$, which aligns with the numerical simulation. Recall that if the null space of $\mathbb{L}(\lambda_*)$ is 2-dimensional, then it is spanned by bases:

$$X = \left(\cos\left(\frac{2\pi}{N}\right), \cos\left(2 \cdot \frac{2\pi}{N}\right), \ldots, \cos\left(N \cdot \frac{2\pi}{N}\right)\right)$$
$$Y = \left(\sin\left(\frac{2\pi}{N}\right), \sin\left(2 \cdot \frac{2\pi}{N}\right), \ldots, \sin\left(N \cdot \frac{2\pi}{N}\right)\right)$$

We denote the corresponding bifurcating point from the homogeneous branch solution as (λ_*, v_*) where

$$\lambda_* = \bar{\lambda} + \mathcal{O}(\epsilon) \quad \text{with} \quad \bar{\lambda} = \left(m - \sum_{p=1}^{m} \cos\left(\frac{2\pi p}{N}\right)\right)^2$$
$$\text{and} \quad v_* = \left(-\sqrt{\bar{\lambda}} + \mathcal{O}(\epsilon)\right) \mathbb{e}.$$

4.2 Verification of Genericity Hypotheses

We assume the null space of $\mathbb{L}(\lambda_*)$ is 2-dimensional. We then apply the bifurcation results of the dihedral group to understand the bifurcations and their branching directions from the homogeneous solutions.

Here, we present proofs for Theorem 8. Our proof strategies follow a similar approach as presented in Section 3.2, relying on the results of Theorem 9. As before, we will obtain the conditions $p_\alpha(0,0,0) \neq 0$ and $p_\delta(0,0,0) \neq 0$ that are required by the theorem in the process. Therefore, the branching results presented in the theorem will automatically follow by the end.

Proof of Theorem 8 (i)

In presenting proofs for Theorem 8 (i), as before, we first derive results for Lemma 19. Recall from Section 3.2 that the spectral projection onto the center manifold of the system $\mathcal{F}(V,\eta) = \mathbb{F}(V,\lambda)$ with $\eta = \lambda - \lambda_*$ is

$$P^c\mathcal{F}\left(v_* + aX + h(a,\eta), \eta\right) = -p(a^2, a^{N-1}, \eta)a - q(a^2, a^{N-1}, \eta)a^{N-1} \tag{3.23}$$

where $a \in \mathbb{R}$, $h : E^c \times (-\eta_0, \eta_0) \to E^h$ with $h(0,0) = h_a(0,0) = 0$ and $h(a,\eta) = \mathcal{O}\left(|a|^2 + |\eta|\right)$. $P^c h(a,\eta) = 0$ for all a, η. This yields Lemma 19.

Then, our goal is to compute $-p_\eta(0,0,0)$ and $-p_\alpha(0,0,0)$ so that we can use the results from Theorem 9. In the following computations, we restrict to $N \geq 5$.

Lemma 28. *For $N \geq 5$, it follows from equation (3.23) that $-p_\eta(0,0,0) = \frac{1}{\sqrt{\lambda}} + \mathcal{O}(\epsilon)$.*

Proof. The proof follows the same approach as Lemma 25. Recall that

$$-p_\eta(0,0,0) = P^c\left(\mathcal{F}_{VV}(v_*,0)[X, h_\eta(0,0)] + \mathcal{F}_{V\eta}(v_*,0)\right).$$

So we need to compute $h_\eta(0,0)$ in order to compute $-p_\eta(0,0,0)$. Note that $\mathcal{F}(V,\eta) = \mathbb{F}(V,\lambda_* + \eta) = 0$ when $V = v^*(\eta) = \left(-\sqrt{\lambda+\eta} + \mathcal{O}(\epsilon)\right)\mathbb{e}$ and $v_* = v^*(0) = \left(-\sqrt{\lambda} + \mathcal{O}(\epsilon)\right)\mathbb{e}$. Following the same argument as before, we have

$$h_\eta(0,0) = \left(-\frac{1}{2\sqrt{\lambda}} + \mathcal{O}(\epsilon)\right)\mathbb{e}.$$

We then compute $P^c\mathcal{F}_{VV}(v_*,0)[X, h_\eta(0,0)]$. Since $\mathcal{F}_{VV}$ has no dependency on η, we may consider function $\mathcal{F}_j : \mathbb{R}^N \to \mathbb{R}$ where $\mathcal{F}_j(V) = -v_j^2 + \mathcal{O}(\epsilon)$. For $A, B \in \mathbb{R}^N$, we can calculate that

$$D_V\mathcal{F}_j(V)A = -2v_jA_j + \mathcal{O}(\epsilon)$$

and

$$D_V^2\mathcal{F}_j(V)[A,B] = -2A_jB_j + \mathcal{O}(\epsilon). \tag{3.24}$$

Using this information, we can compute

$$\begin{aligned}\mathcal{F}_{VV}(v_*,0)[X, h_\eta(0,0)] &= \left(-2X_j\left(-\frac{1}{2\sqrt{\lambda}} + \mathcal{O}(\epsilon)\right)\mathbb{e}_j\right)_{j=1,\ldots,N} \\ &= \frac{1}{\sqrt{\lambda}}X + \mathcal{O}(\epsilon).\end{aligned}$$

So

$$P^c\mathcal{F}_{VV}(v_*,0)[X,h_\eta(0,0)] = P^c\left(\frac{1}{\sqrt{\bar{\lambda}}}X + \mathcal{O}(\epsilon)\right) = \frac{1}{\sqrt{\bar{\lambda}}} + \mathcal{O}(\epsilon).$$

Note that $P^c\mathcal{F}_{V\eta}(v_*,0) = 0$. Therefore,

$$-p_\eta(0,0,0) = P^c\left(\mathcal{F}_{VV}(v_*,0)[X,h_\eta(0,0)] + \mathcal{F}_{V\eta}(v_*,0)\right) = \frac{1}{\sqrt{\bar{\lambda}}} + \mathcal{O}(\epsilon).$$

□

Lemma 29. *For $N \geq 5$, it follows from equation (3.23) that*

$$-p_\alpha(0,0,0) = -\frac{1}{2\sqrt{\bar{\lambda}}} - \frac{1}{2\lambda_2 + 4\sqrt{\bar{\lambda}}} + \mathcal{O}(\epsilon)$$

where

$$2\sqrt{\bar{\lambda}} = 2m + 1 - \frac{\sin\left(\frac{(2m+1)\pi}{N}\right)}{\sin\left(\frac{\pi}{N}\right)}$$

and

$$2\lambda_2 + 4\sqrt{\bar{\lambda}} = \frac{-2\sin\left(\frac{2\pi(m+1)}{N}\right) + 2\sin\left(\frac{\pi(4m+2)}{N}\right) - 2\sin\left(\frac{2\pi m}{N}\right)}{\sin\left(\frac{2\pi}{N}\right)}.$$

Proof. The proof follows the same approach as Lemma 26. Recall that

$$-p_\alpha(0,0,0) = \frac{1}{6}P^c D_a^3\mathcal{F}(v_* + aX + h(a,0),0)|_{a=0}$$

where

$$\begin{aligned} D_a^3\mathcal{F}(v_* + aX + h(a,0),0)|_{a=0} =& \mathcal{F}_{VVV}(v_*,0)[X + h_a(0,0)]^3 \\ &+ 2\mathcal{F}_{VV}(v_*,0)[X + h_a(0,0), h_{aa}(0,0)] \\ &+ \mathcal{F}_{VV}(v_*,0)[X + h_a(0,0), h_{aa}(0,0)] \\ &+ \mathcal{F}_V(v_*,0)h_{aaa}(0,0). \end{aligned}$$

Since $h_a(0,0) = 0$ and $P^c h_{aaa}(0,0) = 0$,

$$
\begin{aligned}
& P^c \left(D_a^3 \mathcal{F}(v_* + aX + h(a,0), 0)|_{a=0} \right) \\
= \quad & P^c \mathcal{F}_{VVV}(v_*, 0)[X]^3 + 3P^c \mathcal{F}_{VV}(v_*, 0)[X, h_{aa}(0,0)] \\
= \quad & \left(3 \left\langle X, \left(-2X_j D_a^2 h_j(0,0) + \mathcal{O}(\epsilon) \right)_{j=1,\ldots,N} \right\rangle + \mathcal{O}(\epsilon) \right) \frac{1}{|X|^2} \\
= \quad & \left(-6 \sum_{j=1}^{N} X_j^2 D_a^2 h_j(0,0) \right) \frac{1}{|X|^2} + \mathcal{O}(\epsilon)
\end{aligned}
$$

using $P^c = \langle X, \cdot \rangle \frac{1}{|X|^2}$ and equation (3.24). It follows that

$$
-p_\alpha(0,0,0) = \left(-\sum_{j=1}^{N} X_j^2 D_a^2 h_j(0,0) \right) \frac{1}{|X|^2} + \mathcal{O}(\epsilon). \tag{3.25}
$$

So to compute $-p_\alpha(0,0,0)$, we need to first find out $h_{aa}(0,0)$. To simplify the notation, let $H \coloneqq h_{aa}(0,0)$. In the proof of Lemma 26, we have derived the following relation

$$
P^h \mathcal{F}_V(v_*, 0) H = -P^h \mathcal{F}_{VV}(v_*, 0)[X]^2. \tag{3.26}
$$

Note

$$
\begin{aligned}
\mathcal{F}_V(v_*, 0) &= \Delta_m - 2v_* I_N + \mathcal{O}(\epsilon) \\
&= \Delta_m - 2\left(-\sqrt{\lambda} \right) I_N + \mathcal{O}(\epsilon) \\
&= \Delta_m + 2\sqrt{\lambda} I_N + \mathcal{O}(\epsilon)
\end{aligned}
$$

where $\sqrt{\lambda} = m - \sum_{p=1}^{m} \cos\left(\frac{2\pi p}{N} \right)$, and so we have

$$
P^h \mathcal{F}_V(v_*, 0) H = \Delta_m H + 2\sqrt{\lambda} H + \mathcal{O}(\epsilon). \tag{3.27}
$$

Then according to equation (3.24),

$$\mathcal{F}_{VV}(v_*,0)[X]^2 = \left(-2X_j^2\right)_{j=1,\ldots,N} + \mathcal{O}(\epsilon).$$

where $X_j = \cos\left(\frac{2\pi j}{N}\right)$ for $j = 1,\ldots,N$. Further simplification by the trigonometric identity gives

$$\left(-2X_j^2\right)_{j=1,\ldots,N} = -\mathbb{e} - X^{(2)}$$

where

$$X^{(2)} = \left(\cos\left(\frac{4\pi j}{N}\right)\right)_{j=1,\ldots,N}$$

is the eigenvector of Δ_m with the eigenvalue

$$\lambda_2 = 2\left(-m + \sum_{p=1}^{m}\cos\left(\frac{4\pi p}{N}\right)\right).$$

Because P^h commutes with F_{VV} and neither $\mathbb{e}$ nor $X^{(2)}$ is in $\operatorname{span}(X,Y)$, we have

$$P^h\mathcal{F}_{VV}(v_*,0)[X]^2 = -\mathbb{e} - X^{(2)} + \mathcal{O}(\epsilon). \tag{3.28}$$

Plugging equations (3.27) and (3.28) into equation (3.26) yields

$$\Delta_m H + 2\sqrt{\lambda}H + \mathcal{O}(\epsilon) = \mathbb{e} + X^{(2)} + \mathcal{O}(\epsilon). \tag{3.29}$$

We consider $H = c_0\mathbb{e} + c_2X^{(2)}$ for some $c_0, c_2 \in \mathbb{R}$ and plug this into equation (3.29):

$$2\sqrt{\lambda}c_0\mathbb{e} + \left(\lambda_2 + 2\sqrt{\lambda}\right)c_2X^{(2)} = \mathbb{e} + X^{(2)}. \tag{3.30}$$

Solving (3.30) for c_0 and c_2, we can find that

$$h_{aa}(0,0) = H = \frac{1}{2\sqrt{\lambda}}\mathbb{e} + \frac{1}{\lambda_2 + 2\sqrt{\lambda}}X^{(2)}.$$

Plugging $h_{aa}(0,0)$ back into equation (3.25), we yield

$$-p_\alpha(0,0,0) = \left(-\sum_{j=1}^{N} X_j^2 \left(\frac{1}{2\sqrt{\bar\lambda}}\mathbb{e}_j + \frac{1}{\lambda_2 + 2\sqrt{\bar\lambda}} X_j^{(2)}\right)\right)\frac{1}{|X|^2} + \mathcal{O}(\epsilon). \tag{3.31}$$

We utilize the following identities

$$\begin{aligned}
\sum_{j=1}^{N} X_j^2 &= \sum_{j=1}^{N}\cos^2\left(\frac{2\pi j}{N}\right) = \frac{N}{2},\\
\sum_{j=1}^{N} X_j^2 X_j^{(2)} &= \sum_{j=1}^{N}\cos^2\left(\frac{2\pi j}{N}\right)\cos\left(\frac{4\pi j}{N}\right) = \frac{N}{4},\\
\frac{1}{|X|^2} &= \frac{1}{\sum_{j=1}^{N}\cos^2\left(\frac{2\pi j}{N}\right)} = \frac{2}{N},
\end{aligned}$$

so equation (3.31) can be simplified as

$$-p_\alpha(0,0,0) = -\frac{1}{2\sqrt{\bar\lambda}} - \frac{1}{2\lambda_2 + 4\bar\lambda} + \mathcal{O}(\epsilon)$$

where

$$\begin{aligned}
2\sqrt{\bar\lambda} &= 2\left(m - \sum_{k=1}^{m}\cos\left(\frac{2\pi k}{N}\right)\right)\\
&= 2m + 1 - \frac{\sin\left(\frac{(2m+1)\pi}{N}\right)}{2\sin\left(\frac{\pi}{N}\right)}\\
\text{and}\quad 2\lambda_2 + 4\bar\lambda &= 4\left(-m + \sum_{k=1}^{m}\cos\left(\frac{4\pi k}{N}\right)\right) + 4\left(m - \sum_{k=1}^{m}\cos\left(\frac{2\pi k}{N}\right)\right)\\
&= \frac{-2\sin\left(\frac{2\pi(m+1)}{N}\right) + 2\sin\left(\frac{\pi(4m+2)}{N}\right) - 2\sin\left(\frac{2\pi m}{N}\right)}{\sin\left(\frac{2\pi}{N}\right)}.
\end{aligned}$$

□

Hence, using Lemma 28 and Lemma 29, we derive the results presented in Theorem 6 (i) by applying Theorem 9. Similar to the previous Section 3.2, the branching directions from the homogeneous solutions at the upper-right corner fall into the cases depicted in Figure 3.12 for odd N and Figure 3.13 for even N.

We again observe that the branching direction depends on the sign of $-p_\alpha(0,0,0)$. As before, we set $\epsilon = 0$ and explicitly compute for $N = 16, 17, 18, 19$ with $1 \leq m \leq \left\lfloor \frac{N-1}{2} \right\rfloor - 1$. The predictions again show that as m increases, the bifurcation switches from supercritical to subcritical, which is the same as discussed in Section 3.2. Here, we have again checked numerically and confirmed that the numerical observations align with the analytical predictions. Specifically, we find that the lowest value of m for which $-p_\alpha(0,0,0)$ becomes positive for each N is $(N,m) = (17,7), (18,7), (19,8)$, and for $N = 16$, we find that $-p_\alpha(0,0,0) < 0$ for any $m = 1, \ldots, 6$.

Criticality in Limiting Case $N \to \infty$

Assuming that the null space of $\mathbb{L}\left(\lambda_*\right)$ is 2-dimensional, we now present proofs for Theorem 8 (ii). According to Equation (3.11) in Theorem 9, the branching equation in terms of x corresponding to $z = x + iy$ is

$$\eta = -\frac{p_\alpha(0,0,0)}{p_\eta(0,0,0)} x^2 + \cdots \,. \tag{3.32}$$

Let $r = \frac{m}{N}$ and $h = \frac{1}{N}$. We then plug the expressions for $p_\eta(0,0,0)$ and $p_\alpha(0,0,0)$ presented in Lemma 28 and 29 respectively into $\frac{p_\alpha(0,0,0)}{p_\eta(0,0,0)}$, and Taylor expand with respect to $h = 0$:

$$-\frac{p_\alpha(0,0,0)}{p_\eta(0,0,0)} = \frac{2\pi r - 3\sin(2\pi r) + \sin(4\pi r)}{-4\sin(2\pi r) + 2\sin(4\pi r)} + \mathcal{O}(h). \tag{3.33}$$

Finding when the criticality changes in the limiting case $N \to \infty$ is equivalent to finding the root in r for

$$\mathcal{C}(r) = \frac{2\pi r - 3\sin(2\pi r) + \sin(4\pi r)}{-4\sin(2\pi r) + 2\sin(4\pi r)}$$

where $r \in (0, \frac{1}{2})$. Further notice that $-4\sin(2\pi r) + 2\sin(4\pi r) < 0$ for all $r \in (0, \frac{1}{2})$. Hence, it suffices to find the root of $f(r) = 2\pi r - 3\sin(2\pi r) + \sin(4\pi r)$ on $r \in (0, \frac{1}{2})$. Before solving for such root, we first prove that there is a unique root within the domain, and so then we know the criticality of bifurcation changes only once when $N \to \infty$. We show this by the following lemma.

Lemma 30. *Let $f(r) = 2\pi r - 3\sin(2\pi r) + \sin(4\pi r)$. $f(r)$ has a unique root on $\left(0, \frac{1}{2}\right)$.*

Proof. The proof follows the same strategies as Lemma 27. Note that the first and second derivatives of $f(r)$ are

$$f'(r) = 2\pi - 6\pi\cos(2\pi r) + 4\pi\cos(4\pi r)$$

and

$$f''(r) = 12\pi^2\sin(2\pi r) - 16\pi^2\sin(4\pi r).$$

We first focus on $0 < r < \frac{1}{4}$. Note that on $\left(0, \frac{1}{8}\right]$, $f''(r) < 0$ and also since $f'(0) = 0$, we know that $f'(r) < 0$ on $\left(0, \frac{1}{8}\right]$ and thus $f(r)$ is monotonically decreasing on this domain. Then on $\left(\frac{1}{8}, \frac{1}{4}\right]$, $f''\left(\frac{1}{8}\right) < 0$, $f''\left(\frac{1}{4}\right) > 0$ and $f''(r)$ is monotonically increasing, so there exists $r' \in \left(\frac{1}{8}, \frac{1}{4}\right)$ such that $f''(r') = 0$, and $f''(r) < 0$ for $r \in \left(\frac{1}{8}, r'\right)$, $f''(r) > 0$ for $r' \in \left(r', \frac{1}{4}\right)$. So $f'(r)$ decreases monotonically on $\left(\frac{1}{8}, r'\right)$ and then increases monotonically on $\left(r', \frac{1}{4}\right)$. Since $f'\left(\frac{1}{8}\right) < 0$ and $f'\left(\frac{1}{4}\right) < 0$, $f'(r) < 0$ on $\left(\frac{1}{8}, \frac{1}{4}\right]$, which means $f(r)$ is monotonically decreasing. Hence, $f(r)$is monotonically decreasing on $\left(0, \frac{1}{4}\right)$ and since $f(0) = 0$, so there is no root on $\left(0, \frac{1}{4}\right)$.

We then focus on $\frac{1}{4} \leq r < \frac{1}{2}$. Note that $f''(r) > 0$ on this domain, so $f'(r)$ is monotonically increasing. Since $f'\left(\frac{1}{4}\right) < 0, f'\left(\frac{1}{2}\right) > 0$ and $f\left(\frac{1}{4}\right) < 0, f\left(\frac{1}{2}\right) > 0$, $f(r)$ has a unique root on $\left(0, \frac{1}{2}\right)$.

In conclusion, $f(r)$ has no root on $\left(0, \frac{1}{4}\right)$ and a unique root on $\left[\frac{1}{4}, \frac{1}{2}\right)$, so $f(r)$ has a unique root on $\left(0, \frac{1}{2}\right)$. $\square$

Lemma 30 tells that as $N \to \infty$, when r increases from zero, the switch of branching direction happens only once. Using Maple, we can calculate that the solution to $2\pi r - 3\sin(2\pi r) + \sin(4\pi r) = 0$ for $0 < r < \frac{1}{2}$ is $r \approx 0.4077$. So ignoring the ϵ effect, as $N \to \infty$, we expect that the bifurcation criticality switches from supercritical to subcritical at around $r \approx 0.4077$.

We hence obtain the results for Theorem 8 (ii).

4.3 Connecting Original System with the Rescaled System

We now numerically verify that the emergent patterned states from the homogeneous solution branch in the upper-right region are connected to the snaking branches of patterns illustrated in Figure 2.2. The workflow is similar to that described in Section 3.3, albeit with different computational details.

For a selected pair of (N, m), we run numerical continuation with the following steps in MATLAB to verify the connection of the branches:

(1) Set $d \ll 1$, an initial $\mu^{(0)}$ and an integer $k \in \{1, 2, \ldots, N\}$ denoting the num-

ber of nodes to be set with nonzero values for the initial guess. Then use $(a, \ldots, a, 0, 0, \ldots, 0, 0, a, \ldots, a, a)$, a vector of length N with k elements taking on value $a = \sqrt{1 + \sqrt{1 - \mu^{(0)}}}$ and $N - k$ elements taking on 0, as the initial guess to convert to a near-by solution, $U^{(0)}$, to $d(\Delta_m U)_n + f(u_n, \mu^{(0)}) = 0$ using `fsolve`.

(2) Use $(U^{(0)}, \mu^{(0)})$ as the starting solution and use numerical continuation to continue the solution branch of the full system in terms of μ. Stop until the solution in (U, μ) gets close to the upper-right region, i.e., u_n and μ both become close to 1. Denote the end solution as $(U^{(1)}, \mu^{(1)})$ where $U^{(1)} = \left(u_1^{(1)}, u_2^{(1)}, \ldots, u_N^{(1)}\right)$.

(3) Let $\lambda^{(0)} = \frac{1-\mu^{(1)}}{d^2}$ and $V^{(0)} = \left(\frac{u_1^{(1)}-1}{\sqrt{d}}, \frac{u_2^{(1)}-1}{\sqrt{d}}, \ldots, \frac{u_N^{(1)}-1}{\sqrt{d}}\right)$. Use $(V^{(0)}, \lambda^{(0)})$ as the initial solution and continue the solution branch in the rescaled system for the upper-right region in terms of λ. To check the goodness of the initial solution, compute the residual vector

$$\mathbf{r}_n = \lambda^{(0)} d + d(\Delta_m V^{(0)})_n - 4\left(v_n^{(0)}\right)^2 d + \lambda^{(0)} v_n^{(0)} d^2 - 8\left(v_n^{(0)}\right)^3 d^2 - 5\left(v_n^{(0)}\right)^4 d^3 - \left(v_n^{(0)}\right)^5 d^4$$

for $1 \le n \le N$.

Figures 3.16 and 3.17 illustrate an example when continuing on a system with $(N, m) = (16, 4)$. The initial parameters are $d = 0.05$, $\mu^{(0)} = 0.4$ and $k = 1$.

When computing the homogeneous solutions and the predicted bifurcation points in Figure 3.17, we explicitly include all the higher-order terms. Specifically, to find the homogeneous solutions, we consider the rescaled system with all terms fully expressed

$$\mathbb{F}(V, \lambda, d)_n = \lambda d + d(\Delta_m V)_n - 4v_n^2 d + \lambda v_n d^2 - 8v_n^3 d^2 - 5v_n^4 d^3 - v_n^5 d^4,$$

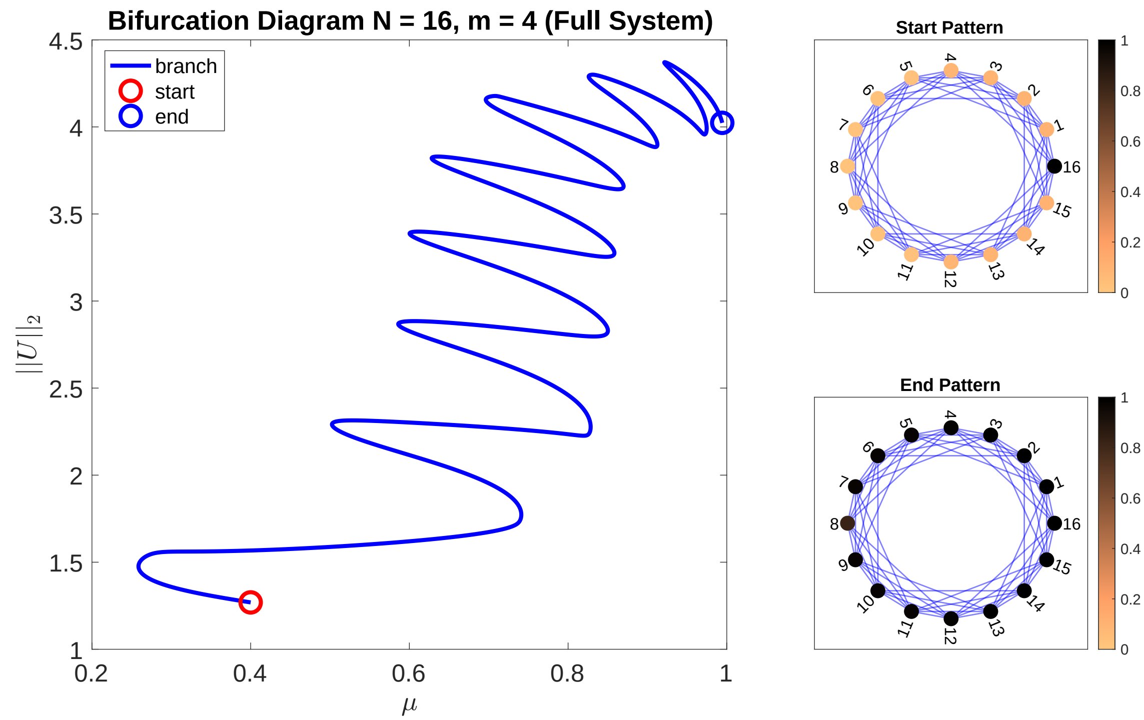

Figure 3.16: Numerical continuation on the original full system for $N = 16, m = 4$ until near the upper-right region where (u_n, μ, d) is close to $(1, 1, 0)$. The start and end solution patterns are illustrated in the right panel with normalized node values.

and so the homogeneous solution v_* satisfies

$$\lambda - 4v_n^2 + \lambda v_n d - 8v_n^3 d - 5v_n^4 d^2 - v_n^5 d^3 = 0.$$

Solving for v_n yields that homogeneous solution $v_*(\lambda, d) = v_-(\lambda, d)\mathbb{e}$ where

$$v_-(\lambda, d) = \frac{-1 + \sqrt{1 - d\sqrt{\lambda}}}{d}.$$

Then to explicitly solve for the bifurcation points, we consider the Jacobian

$$\mathbb{L}(V, \lambda, d) = d\Delta_m + \left(-8v_n d + \lambda d^2 - 24v_n^2 d^2 - 20v_n^3 d^3 - 5v_n^4 d^4\right) I_N.$$

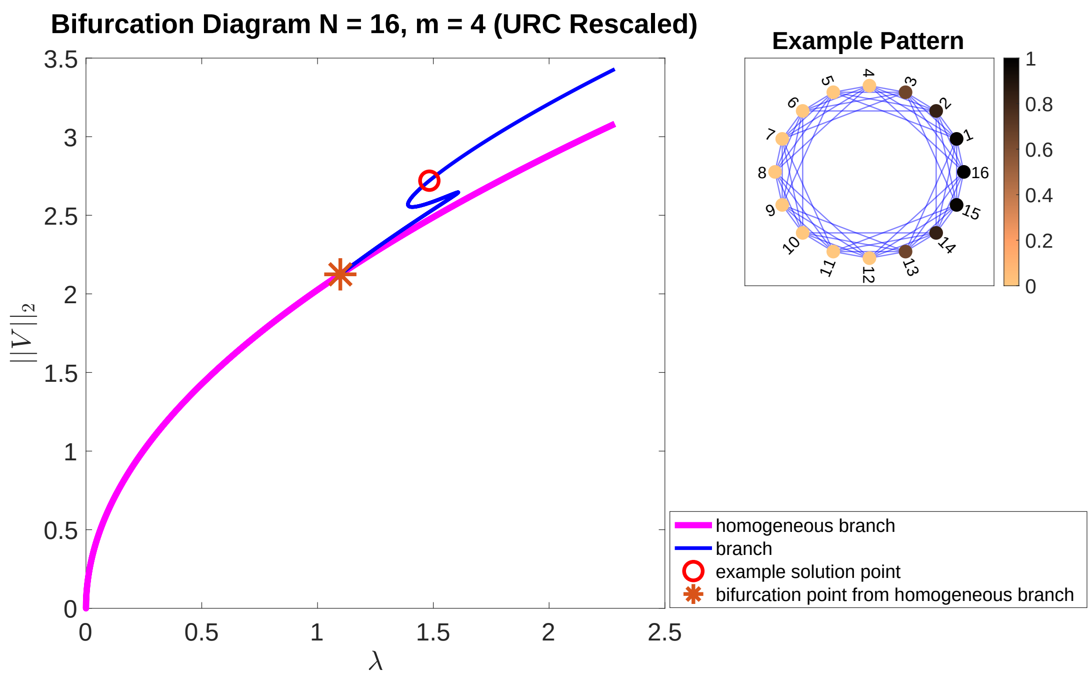

Figure 3.17: Numerical continuation on the rescaled system at the upper-right region where (u_n, μ, d) is near $(1, 1, 0)$, starting at solution taken from the full system. The L^2-norm of the residual vector at the initial solution is `7.3035e-09`. Detailed explanations are similar to those in Figure 3.8.

Recall that the eigenvalues of Δ_m are

$$\lambda_j = 2\left(-m + \sum_{p=1}^{m} \cos\left(\frac{2\pi jp}{N}\right)\right) \text{ for } j = 0, 1, 2, \ldots, \left\lfloor \frac{N}{2} \right\rfloor.$$

corresponding to the discrete Fourier ansatz

$$v_{k,j} = e^{i\omega_j k}, \quad \text{where } \omega_j = \frac{2\pi j}{N}, \quad k = 1, \ldots, N, \quad j = 0, 1, \ldots, \left\lfloor \frac{N}{2} \right\rfloor.$$

So we can compute the eigenvalues to $\mathbb{L}(v_*(\lambda, d), \lambda, d)$ along the homogeneous branch $v_*(\lambda, d)$, which are $d\lambda_j - 8dv_-(\lambda, d) + \lambda d^2 - 24d^2 v_-(\lambda, d)^2 - 20d^3 v_-(\lambda, d)^3 - 5d^4 v_-(\lambda, d)^4$. Setting the eigenvalue to 0 and solving for λ then give us the associated λ values at the bifurcation points, indexed by j:

$$\lambda^{(j)}(d) = \frac{2 + d\lambda_j - 2\sqrt{d\lambda_j + 1}}{4d^2}.$$

where $j = 0, 1, 2, \ldots, \left\lfloor \frac{N}{2} \right\rfloor$.

The asterisk marked on Figure 3.17 corresponds to the bifurcation point along homogeneous solutions, $\big(v_*(\lambda^{(1)}(d), d), \lambda^{(1)}(d), d\big)$, with index $j = 1$.

5 Code

We here present the MATLAB code for `isotypic.m`, as mentioned in Section 2.2. For a given N, representing the number of nodes, the code computes the projection of the linear representation of the Laplace operator in the ring lattice system onto the irreducible representations of the dihedral group D_N, using equation (3.9). It then computes the dimension of the projection space by calculating the trace of the projection matrix. Ultimately, the function returns a vector that records the dimension of the projection onto each of the irreducible representations. By comparing the dimensions of the projections with the dimensions of the irreducible representations, we find that no irreducible representation appears more than once for N up to 120.

```
function ndim = isotypic(n)

ndim = [];

if rem(n,2)==0
```

```
% n is even
v = zeros(1,n);
v(n) = 1;
A = circulant(v); % rotation forward e.g.
   1->2,2->3...
R = zeros(n); % reflection
R(n,n) = 1; R(n/2,n/2) = 1; % when even, last and
   middle nodes are fixed
for l = 1:n/2-1
        R(l,n-l) = 1;
        R(n-l,l) = 1;
end

% one-dimensional representations
ni = 1;

Pi = zeros(n);
for j=0:(n-1)
        Pi = Pi + A^j + A^j*R;
end
Pi = ni/(2*n)*Pi;
ndim = [ndim, trace(Pi)];

Pi = zeros(n);
for j=0:(n-1)
        Pi = Pi + A^j - A^j*R;
end
Pi = ni/(2*n)*Pi;
ndim = [ndim, trace(Pi)];
```

```
        Pi = zeros(n);
        for j=0:(n-1)
                Pi = Pi + (-1)^j*(A^j + A^j*R);
        end
        Pi = ni/(2*n)*Pi;
        ndim = [ndim, trace(Pi)];

        Pi = zeros(n);
        for j=0:(n-1)
                Pi = Pi + (-1)^j*(A^j - A^j*R);
        end
        Pi = ni/(2*n)*Pi;
        ndim = [ndim, trace(Pi)];

        % two-dimensional representations
        ni = 2;
        for k=1:(n-2)/2
                Pi = zeros(n);
                for j=0:(n-1)
                        char = 2*cos(2*pi*j*k/n);
                        Pi = Pi + A^j*char;
                end
                Pi = ni/(2*n)*Pi;
                ndim = [ndim, trace(Pi)];
        end
else
        % n is odd
        v = zeros(1,n);
```

```
v(n) = 1;
A = circulant(v); % rotation forward e.g.
    1->2,2->3...
R = zeros(n); % reflection
R(n,n) = 1; % when odd, last node is fixed
for l = 1:(n-1)/2
        R(l,n-l) = 1;
        R(n-l,l) = 1;
end

% one-dimensional representations
ni = 1;

Pi = zeros(n);
for j=0:(n-1)
        Pi = Pi + A^j + A^j*R;
end
Pi = ni/(2*n)*Pi;
ndim = [ndim, trace(Pi)];

Pi = zeros(n);
for j=0:(n-1)
        Pi = Pi + A^j - A^j*R;
end
Pi = ni/(2*n)*Pi;
ndim = [ndim, trace(Pi)];

% two-dimensional representations
ni = 2;
```

```
        for k=1:(n-1)/2
                Pi = zeros(n);
                for j=0:(n-1)
                        char = 2*cos(2*pi*j*k/n);
                        Pi = Pi + A^j*char;
                end
                Pi = ni/(2*n)*Pi;
                ndim = [ndim, trace(Pi)];
        end
end

ndim = round(ndim);

if sum(ndim)~=n
        disp('dimensions do not match')
end
```

Chapter Four

Robustness of Community Structure under Edge Addition

This chapter is based on work presented in Tian and Moriano (2023).

1 Introduction

Many complex systems, such as critical infrastructures, biological networks and social groups, exhibit network structures consisting of nodes and edges that capture their connectivity Amaral and Ottino (2004). Extracting different features from these networks is useful to better understand their structure and function Newman (2003), Girvan and Newman (2002). Among different properties of networks, many real networked systems demonstrate community structures, or clusters, which are groups of nodes that have higher probability of sharing links with other nodes within the same group than with nodes in different groups. These communities typically represent essential functional or behavioral units in the networks Girvan and Newman (2002), Fortunato (2010), Fortunato and Hric (2016). Therefore, it is important to understand the conditions under which they persist. Community *robustness* describes how much network perturbation a community structure can tolerate while still being able to recover its original structure Fortunato (2010), Karrer et al. (2008). The community robustness problem is of practical interest because we want to understand how well the components in networks can sustain their basic functionalities when facing errors or attacks (Barabási and Pósfai, 2016, Chapter 8). Usually, network perturbations are used to model either random failures or deliberate attacks in real networked systems Schaeffer et al. (2021).

Studying the robustness of communities in networks confronts two main challenges. First, although community structure in networks can provide insights into the organization of nodes based on their connectivity, there is no universal definition of community. This makes the detection of communities itself an ill-posed problem, and hence, in practice, discovering community structure often depends on the methods and application Fortunato and Hric (2016). Second, community robustness involves network perturbations, and there are various ways a network can be modified. Studies so far have focused on edge rewiring and node or edge removal as the network perturbation schemes for studying a system's ability to sustain basic functionality when some components fail Karrer et al. (2008), Wang and Liu (2019), Albert et al. (2000), Amancio et al. (2015), Wang et al. (2017), Carissimo et al. (2018), Mozafari and Khansari (2019).

However, real networked systems, such as communication, citation, or social networks, often increase connectivity over time, so it is important to consider the scenario of an increasing number of edges Leskovec et al. (2005). Added edges can also simulate errors or attacks Albert et al. (2000), Holme et al. (2002), Borgatti et al. (2006). For example, when simulating errors, added edges can simulate false-positive edges (i.e., edges that are present in data erroneously but do not actually represent the real relations). This is one type of measurement error commonly found, such as in online community, communication, and collaboration network data Wang et al. (2012). Similarly, added edges can also simulate deliberate attacks intended to destroy the established community structure to quickly disrupt the functionality of the system as in the case of a Distributed Denial of Service attack Zargar et al. (2013), Osanaiye et al. (2016). Therefore, there is a need to understand the effect of network densification on community robustness.

Here, we conduct a systematic study to understand the impact of edge addition on the robustness of communities. We focus on both the synthetic Lancichinetti-Fortunato-Radicchi (LFR) benchmark graphs Lancichinetti and Fortunato (2009b) and empirical networks to investigate the limits of the robustness of the initial community structure as the network is perturbed through edge addition. We study two scenarios of edge addition, namely random and targeted addition. Random addition selects from the set of all nonexistent edges, and this process is analogous to a random error in the system Wang et al. (2012), Borgatti et al. (2006). Targeted addition selects only from the nonexistent, cross-community edges, which we propose to use to simulate attacks. We compute the effects on community robustness by using Normalized Mutual Information (NMI) Fred and Jain (2003), which is a community similarity measure often used in network community analysis, and by using element-centric clustering similarity Gates et al. (2019) to control for biases when comparing clusters. We specifically select four community detection algorithms commonly used in community detection benchmarking studies Lancichinetti and Fortunato (2009a), Emmons et al. (2016): Infomap, Label Propagation, Leiden, and Louvain. We also demonstrate and compare community robustness results by using the same set of community detection algorithms on empirical email network data, in which the edge density increases over time.

Our results suggest that the chosen clustering algorithm strongly affects community robustness under edge addition. Specifically, in both synthetic and empirical networks, we observe that for different types of community detection algorithms, the similarity measures between communities in the original and the perturbed networks decay with distinct rates while more and more edges are being added. Additionally, in synthetic experiments on LFR benchmark graphs, we observe that with a smaller mixing parameter, which means that initial communities are more loosely connected to each other, the communities tend to be more robust. Synthetic experimental results also align with the expectation that targeted edge addition tends to destroy the original community structure more rapidly compared with random addition, so communities are less robust with targeted addition. In experiments using empirical data, we observe that the choice of community similarity metrics, NMI or element-centric clustering similarity in particular, also affects the results on community robustness. This stems from the fact that, on certain occasions, different similarity metrics can produce varying measures for the same pair of community structures, indicating different levels of resemblance between them.

2 Methods

2.1 LFR benchmark

The LFR benchmark graphs Lancichinetti et al. (2008), Lancichinetti and Fortunato (2009b) are commonly used in network community studies to create graphs with ground-truth partitions. The advantage of using an LFR benchmark is that the degree and the community size both follow power-law distributions, which more closely resemble the properties observed in many real-world networks Lancichinetti et al. (2008), Newman (2003), Palla et al. (2005), Clauset et al. (2004), Guimerà et al. (2003). The exponents of degree distributions are controlled by parameter α, and the exponents of community size distributions are controlled by parameter β. We take the typical values of the exponents observed in real networks, i.e., $\alpha = -2$ and $\beta = -1$ Lancichinetti et al. (2008). Other parameters required for generating LFR benchmark graphs include the average degree $\langle k \rangle$, maximum degree $maxk$, minimum community size $minc$, maximum community size $maxc$, and the mixing parameter μ, which represents the fraction of nodes that each node shares edges with across different communities. The lower the μ, the higher the ratio between the number of internal and external connections. This leads to higher modularity, which is a quality function commonly used to express the strength of communities in studies of communities Fortunato (2010). Thus, the smaller the μ, the stronger the partition.

Although we use LFR benchmark graphs for the synthetic experiments, our method is generally applicable to any type of benchmark graph that provides ground-truth community labels, such as the Girvan-Newman benchmark Girvan and Newman (2002) and the stochastic block model Holland et al. (1983). We generate the LFR benchmark graphs by using the publicly available implementation Fortunato (2021) of the algorithm described in Lancichinetti and Fortunato (2009b). We conduct experiments on 1000 nodes and then on 10 000 nodes to study the effect of perturbations at different scales. We also examine the effect of the strength of the initial community by varying the mixing parameter, μ. The specific parameter values used for generating the LFR benchmark graphs are listed in Table 4.1.

Table 4.1: Synthetic experiment parameters.

Parameter	**Description**	**Value**
N	Number of nodes	$1000, 10\,000$
$maxk$	Max degree for LFR	$0.1N$
$\langle k \rangle$	Average degree for LFR	25
$minc$	Min community size for LFR	50
$maxc$	Max community size for LFR	$0.1N$
α	Degree distribution exponent for LFR	-2
β	Community size distribution exponent for LFR	-1
μ	Mixing parameter for LFR	$0.01, 0.1, 0.2, 0.3, 0.4, 0.5$
h	Times of initial number of edges added up to	10
s	Number of steps to add edges	50
r	Number of realizations per step	50

2.2 Community detection

Community detection is the task of assigning nodes in a network into clusters based on topological similarity Fortunato (2010). Nodes within the same community are more densely connected compared with the ones across distinct communities. Various community detection algorithms have been developed to find clusters in networks. These algorithms are based on different methodologies to achieve their optimal clustering solutions. In this work, we use four algorithms based on three popular methods of community detection: information-theoretic-based algorithm Infomap Rosvall and Bergstrom (2008), message-passing-based algorithm Label Propagation Raghavan et al. (2007), and modularity-based algorithms Leiden (partly based on smart local move algorithm and improved from Louvain) Traag et al. (2019) and Louvain Blondel et al. (2008). These chosen algorithms have low enough computational complexity Yang et al. (2016), Traag et al. (2019) to accomplish our experiments in reasonable run time. For Infomap, Label Propagation, and Louvain, we use the publicly available package Fortunato (2021) implemented by Lancichinetti and Fortunato (2012). The package for Leiden is publicly available on GitHub Traag (2020) and described in the original paper Traag et al. (2019). We use the undirected and unweighted implementations for all four algorithms to ensure consistency with the LFR benchmark graphs we generate. Rigorous analysis of these four clustering algorithms is presented in previous work Emmons et al. (2016).

The community detection algorithm is an essential component for studying communities because, although the benchmark graphs have ground-truth labels of the communities, few empirical networks have ground-truth partitions. Moreover, the temporal evolution of the networks makes it more difficult to obtain ground-truth clustering information at all times. Notably, although graph embeddings have become popular for downstream tasks, they have not been developed thoroughly enough to efficiently achieve good graph clustering results; their hyper-parameter tuning is cumbersome when attempting good performance Tandon et al. (2021). By comparison, traditional community detection algorithms require no parameter tuning but can provide relatively good clustering results in a reasonable run time. For these reasons, we use the four well-developed community detection algorithms for our experiments.

2.3 Community similarity

To measure similarity between communities, we use NMI Fred and Jain (2003) and element-centric clustering similarity Gates et al. (2019) as the metrics. Without loss of generality, suppose that C_1 and C_2 are partitions on the same set of N nodes. The NMI score of the two partitions is defined as

$$NMI(C_1, C_2) = \frac{-2\sum_{i=1}^{|C_1|}\sum_{j=1}^{|C_2|}\mathbb{P}(i,j)\log\left(\frac{\mathbb{P}(i,j)}{\mathbb{P}_1(i)\mathbb{P}_2(j)}\right)}{\sum_{i=1}^{|C_1|}\mathbb{P}_1(i)\log\mathbb{P}_1(i) + \sum_{j=1}^{|C_2|}\mathbb{P}_2(j)\log\mathbb{P}_2(j)}, \tag{4.1}$$

where $\mathbb{P}_1(i) = \frac{|C_{1i}|}{N}$, $\mathbb{P}_2(j) = \frac{|C_{2j}|}{N}$, and $\mathbb{P}(i,j) = \frac{|C_{1i} \cap C_{2j}|}{N}$ for $C_{1i} \in C_1$, $C_{2j} \in C_2$ as the clusters of partition C_1 and C_2, respectively. We use the scikit-learn implementation of NMI Pedregosa et al. (2011) in our experiments.

In addition to NMI, we also compute the similarity between communities by using element-centric clustering similarity, which better copes with issues such as bias in randomized membership, bias in skewed cluster sizes, and the problem of matching Gates et al. (2019). Although NMI tends to favor more clusters, element-centric clustering similarity overcomes such bias in the number of clusters. We report the experimental results computed in this metric using the CluSim package Gates and Ahn (2019) along with the default parameter. Both NMI and element-centric clustering similarity range from 0 to 1, where a higher value means more similarity between partitions.

2.4 Experimental procedure

We experiment on several computer-generated networks and empirical temporal networks to examine the robustness of their community structures. The empirical networks are real-world data, and we have no control over their intrinsic network properties. The ground-truth communities and the interpretability of the clusterings found by detection algorithms on these data are often unclear Peel et al. (2017), so in the studies on clusterings in networks, synthetic networks often serve as handy examples for tests. Here, we illustrate the details of the experimental procedures for synthetic and empirical networks. The tests on synthetic and empirical networks are designed differently because the synthetic network is stationary without natural perturbations, whereas the empirical data does not have ground-truth community labels and requires further cleaning to work as comparable examples. Our code is publicly available at: http://github.com/Moyi-Tian/CommunityRobustness.

2.4.1 Experiments on synthetic networks

Suppose the initial network is $G = (V, E)$, where $V = \{1, 2, \ldots, N\}$ is the set of N nodes, and $E = \{e_{ij} : i, j \in V\}$ is the set of M edges. Let E^c be the set of edges in the complement graph of G. The benchmark graph provides each node a community label denoted by c_i for $i \in V$. The graph partition is then $C = \bigcup_{k \in \bigcup_{i\in V}\{c_i\}} \left\{ \bigcup_{j \in V} \{j : c_j = k\} \right\}$. We also define a set for nonexistent edges across different communities denoted by $E^c_{inter} = \{e_{ij} \in E^c : c_i \neq c_j, i, j \in V\}$. To start, we choose a community detection algorithm and specify parameters h, s, and $r \in \mathbb{Z}_+$, where h is how many times the initial number of edges is added up, s is the number of steps to add edges, and r is the number of realizations per step. The parameters we use for the synthetic experiments are listed in Table 4.1.

We illustrate the effects of edge addition on community structures through two different network perturbations: random addition and targeted addition. Let $t \in \{0, 1, 2, \ldots, s\}$. For the random addition approach, we select $E_\nu \subseteq E^c$ uniformly at random. For targeted addition, we choose $E_\nu \subseteq E^c_{inter}$ uniformly at random, where $|E_\nu| = \left\lfloor \frac{hM}{s} \right\rfloor t$. Notably, the random addition is analogous to the case in which random errors or random additional connections appear. Conversely, targeted addition simulates the case in which much of the information about the community structure is known, and there is an intention to break the current partitions through increasing connectivity. In each of these edge-addition configurations, we create a new graph, $G' = (V, E')$, such that $E' = E \cup E_\nu$.

We then apply the specific community detection algorithm on G' to yield an associated graph partition, C'. We repeat the previous steps for r-independent times at each t: specifically r realizations at every single step t over the total s steps. Suppose the chosen community similarity metric is $\mathcal{S}$. We then calculate the metric score $\mathcal{S}_k(C, C'_k)$ for each realization, k, where C'_k is the associated graph partition, and report the average $\mathcal{S}_{avg} = \frac{1}{r}\sum_{k=1}^{r} \mathcal{S}_k(C, C'_k)$.

2.4.2 Experiments on empirical temporal networks

Temporal email networks are natural candidates for empirical experiments and are comparable to the synthetic experiments. The email conversations between users in these networks naturally emerge at their sent time, which can be directly considered as additional edges over time steps.

Unlike the benchmark graphs, empirical networks do not have ground-truth community labels, so we must first identify a reliable community partition on the initial graph before the start of network perturbation. In doing so, we apply the fast consensus algorithm Tandon et al. (2019), which is based on the idea of consensus clustering Lancichinetti and Fortunato (2012). Because established community detection algorithms produce nondeterministic partitions, consensus clustering was proposed for more stable and accurate results after iterations among multiple clustering results given a prespecified clustering method. There are two parameters we must specify as inputs for the fast consensus algorithm: the number of partitions, np, and the clustering method. The default value for np in the fast consensus algorithm is set to be 20, which is also the value used for tests demonstrated in the original paper Tandon et al. (2019). We also found that $np = 20$ balances performance and run time. This choice of the value is specified in Table 4.2. For the clustering method, we choose it to be consistent with the one used for community detection in the later perturbed networks.

In addition, there are other issues that must be addressed before testing on email networks with time stamps associated with edge emergence.

First, the problem is finding appropriate empirical network examples on which we can perform experiments comparable to the synthetic case. Specifically, the empirical network should have a temporally growing number of edges on a fixed set of nodes, and the growth within the recorded time frame should be on the comparable scale as the synthetic experiment, where we add edges up to $10\times$. The problem is that temporal email networks always expand in the number of edges *and* in the number of nodes. If we look at the graph on the set of all users who appear within the given time frame, then we usually find that only a tiny fraction of edges, or sometimes none, are added until the end of the recorded time. This is because there are always new users joining the networks, occasionally even at the very end. For some networks, there is also a co-occurring issue that many users are not very active and do not contribute many new communications (i.e., edges) over time. This is why, rather than using the entire network datasets as obtained, we instead first identify appropriate subnetworks extracted from the original email data and then use them as examples for our empirical experiments. There are different ways to select subnetworks from the original ones. When the entire network is small enough, choosing subnetworks based on an exhaustive search may be possible. However, due to the size of our original empirical datasets, checking all possible combinations of nodes and the growth in density of their induced subnetworks will be computationally expensive. Therefore, our approach is to search over a family of subnetworks induced by the first n nodes showing up in time with n swept from 1 to N where N is the total number of users present in the full dataset. We then look at the growth in density for each of these subnetworks and select an appropriate one as the example to use. More details of our subnetwork selection and the corresponding network properties are described in Section 3.2.

Second, email networks usually have multiedges emerging in time because several emails can be sent between the same pair of users, but the synthetic networks we test on have no multiedges. Here, we align our empirical experiment with the synthetic case by preprocessing the network data so that there are no repeating edges. We do so by removing the edges that arrived later and already showed up once at a previous time from the edge list. In this way, we consider an edge to represent an existing relationship between users, thereby omitting the number of conversations that occurred.

Third, we must also identify which network should be treated as the initial network. The empirical networks always start with zero edges, but it is not meaningful to use the null graph because then no communities will ever exist at the initial time. Also, the community detection algorithms take in only the edge lists and so only the nodes incident to the edges present in the list are assigned with community labels. So, to use the algorithms, we must ensure all nodes appear in the edge lists. Therefore, in our empirical experiment, we choose the initial network by picking the first one without any isolated nodes when growing the network in time. This is achieved by adding edges one at a time according to their associated time stamp and checking at which time every node is at least incident to one edge.

In our empirical experiments, we use np for fast consensus, and we also have parameters s and r. Here s refers to the number of steps with respect to time, and r is the number of realizations per step. Table 4.2 lists the parameter values for the empirical experiments.

Table 4.2: Empirical experiment parameters.

Parameter	**Description**	**Value**
np	Number of partitions (fast consensus)	20
s	Number of steps	50
r	Number of realizations per step	10

As previously mentioned, we preprocess and identify suitable empirical networks for our experiment. The experimental procedure is as follows. Suppose that we have a precleaned empirical network dataset (without multiedge) with $V = \{1, 2, \ldots, N\}$ to be the set of nodes and M to be the number of edges. Recall that edges appear in time one by one, so there are M associated time stamps. At time stamp $i \in \{1, 2, \ldots, M\}$, we denote the emergent edge pointing from node $v_s(i)$ to node $v_t(i)$ by $e_{v_s(i),v_t(i)}$, where $v_s(i), v_t(i) \in V$. Using these notations, the dataset can be presented as an edge list $\{e_{v_s(1),v_t(1)}, e_{v_s(2),v_t(2)}, \ldots, e_{v_s(i),v_t(i)}, \ldots, e_{v_s(M),v_t(M)}\}$. Then we grow the network until the time stamp $t_0 = \min\left\{t_s : \bigcup_{1\le i\le t_s} \{v_s(i), v_t(i)\} = V, 1 \le t_s \le M\right\}$, which is the first time when there are no isolated nodes. The initial network is chosen to be $G_0 = (V, E_0)$, where $E_0 = \{e_{v_s(i),v_t(i)} : 1 \le i \le t_0\}$. Before each experiment, we specify a clustering method and parameters, $np, s, r \in \mathbb{Z}_+$ (s is upper bounded by $M - t_0$, and our preprocessing should provide an appropriate dataset that $M \gg t_0$). We first apply fast consensus on G_0 using np as the hyperparameter for the number of partitions and the chosen method for the clustering algorithm. The consensus algorithm yields np initial partitions $C_{0,w}$ for $1 \leq w \leq np$. Then we simulate on the evolved networks over time. Specifically, for $1 \leq p \leq s$, let $t_p = t_0 + \left\lfloor \frac{M-t_0}{s} \right\rfloor p$. The new graph $G_p = (V, E_p)$ at time step p is constructed such that $E_p = \{e_{v_s(i),v_t(i)} : 1 \leq i \leq t_p\}$. Use the chosen clustering method to find partitions of G_p for r times independently and denote the corresponding clustering results as $C_{p,q}$ for $1 \leq q \leq r$. For each $1 \leq p \leq s$, we report the average community similarity metric score: $\mathcal{S}_{avg,p} = \frac{1}{np \cdot r} \sum_{w=1}^{np} \sum_{q=1}^{r} \mathcal{S}(C_{0,w}, C_{p,q})$.

3 Results and Discussion

This section describes the computational results from the synthetic experiments on LFR benchmark graphs and the empirical experiments on subnetworks obtained from temporal email networks.

Note that while more edges are added to the initial network, it is likely that the community structure evolves over perturbation. However, our focus is not on tracking changes in the community structure itself but on understanding the limits of the robustness of the initial community structure under edge-addition perturbation.

3.1 Synthetic networks

We test on LFR benchmark graphs with 1000 and 10 000 nodes and report the results calculated with the NMI metric. The results for the same series of experiments using the element-centric clustering similarity metric are presented in Section 5.1. We also include the associated plots of standard deviation for all synthetic experiments in Section 5.3.

Figures 4.1 and 4.2 show how the four different community detection algorithms—Infomap, Label Propagation, Leiden, and Louvain—perform when the LFR benchmarks with 1000 and 10 000 nodes are perturbed under uniformly random edge addition. Recall that in this setting, the edges added at each step are selected uniformly at random from all the nonexistent edges in the initial network, while multiedges are prohibited. This is analogous to random errors in real-world networks.

LFR benchmark graphs with lower μ values (i.e., stronger initial partitions) have higher NMI values compared with the ones with higher μ after $10\times$ the original number of edges are added. Note that adding edges is essentially a process of balancing the fraction of intercommunity edges with that of intracommunity edges. Hence, this observation aligns with our intuition because when a community partition is stronger, it requires more edges to be added until the established community structure becomes less clear, meaning that the community structure is more robust.

The modularity-based algorithms, Louvain and Leiden, have relatively higher NMI scores vs Infomap and Label Propagation. For example, if we look at the $\mu = 0.3$ curves in Figure 4.1, then Louvain and Leiden need about $6.3\times$ the original number of edges to be added until the similarity scores drop 50%, whereas Infomap and Label Propagation only need about $1.1\times$ and $0.9\times$, respectively. This indicates

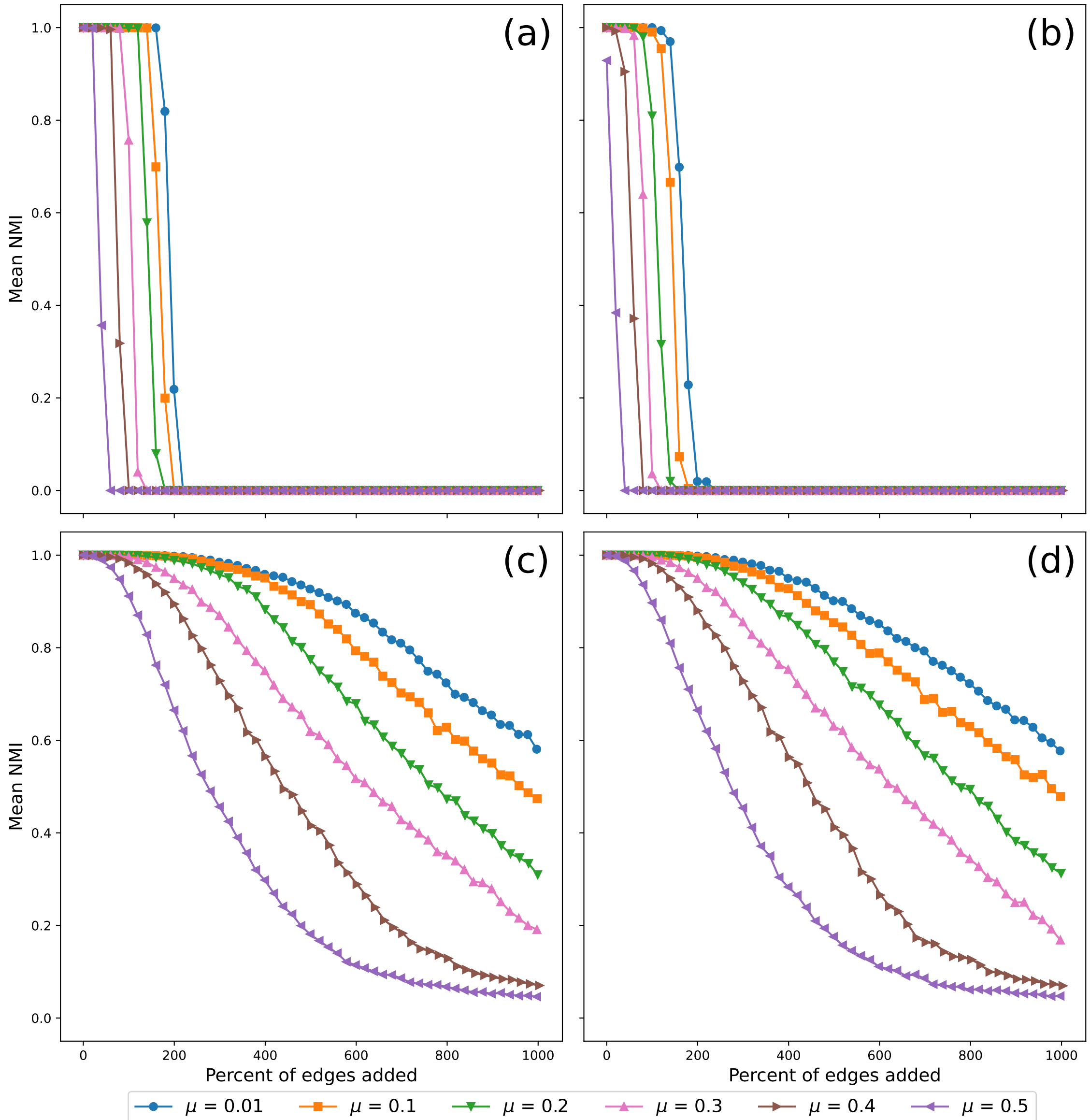

Figure 4.1: Mean NMI over the percentage of edges added uniformly at random on LFR benchmark graphs with 1000 nodes. Communities detected by (a) Infomap, (b) Label Propagation, (c) Leiden, and (d) Louvain. Average degree is 25. Edges are added up to 10× the original number over 50 independent steps and are selected without producing multiedges. For each algorithm, we average NMI between the ground-truth partition and new partitions of the perturbed network over 50 independent runs at each step. The maximum amount of edges we add is about 25% of all nonexistent edges.

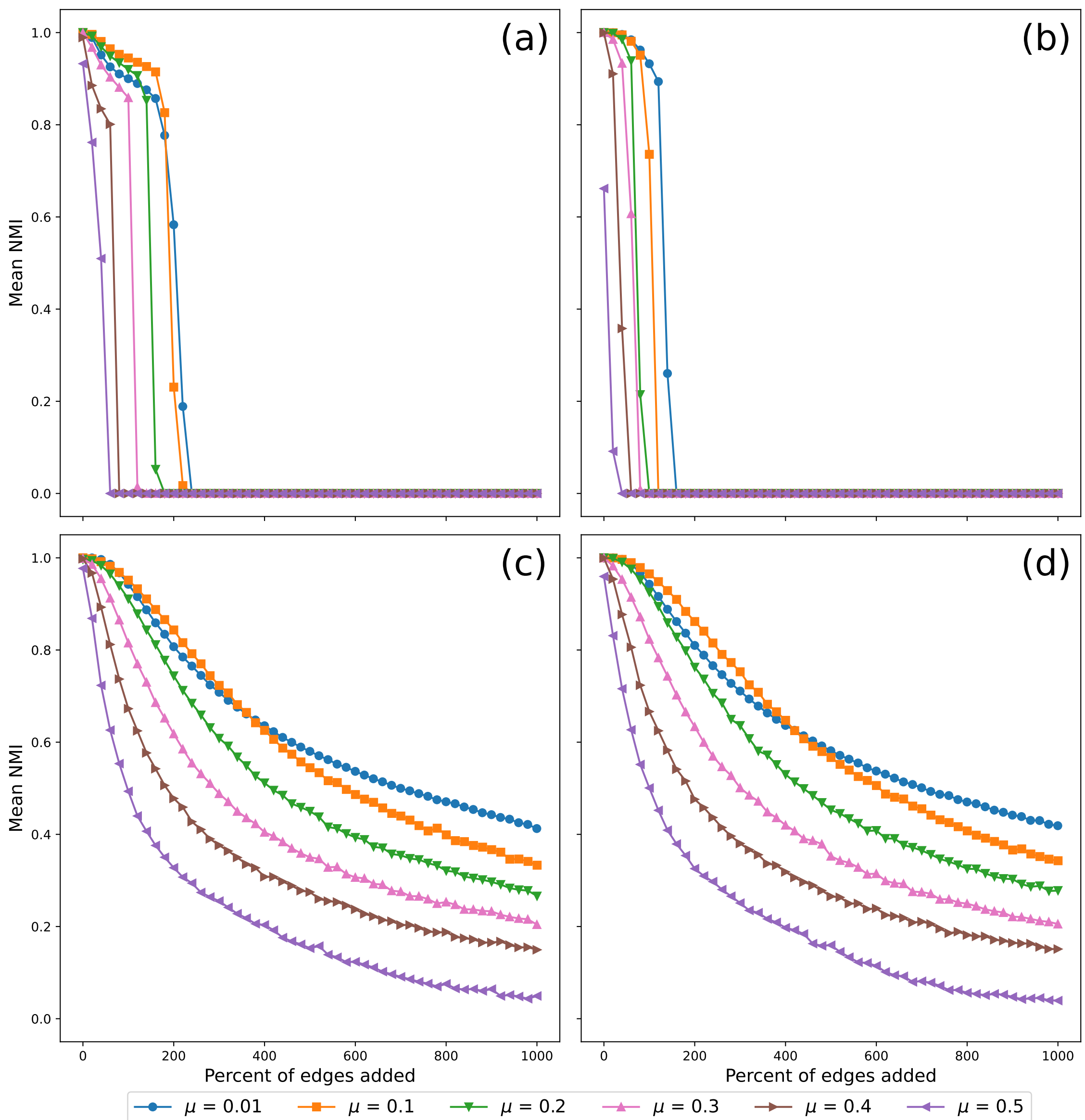

Figure 4.2: Mean NMI over the percentage of edges added uniformly at random on LFR benchmark graphs with 10 000 nodes. Communities detected by (a) Infomap, (b) Label Propagation, (c) Leiden, and (d) Louvain. Same parameter values are used as with the 1000-node case. The maximum amount of edges we add is about 2.5% of all nonexistent edges.

that Louvain and Leiden are better at detecting community structures that are similar to those initial ones in the LFR benchmark graphs after a large number of edges is added. The exact reasons are unclear, but a plausible explanation is that the algorithms have different behaviors due to their assumptions and methodologies when performed on graphs with different intrinsic network properties. Specifically, we observe that our method of appending edges shifts the degree distribution from the initial power-law distribution to a distribution closer to the binomial.

In our experiments, Infomap and Label Propagation end up only finding one giant community for the entire network after about 1× or 2× the original number of edges are added. According to the original Infomap paper Rosvall and Bergstrom (2008), this flow-based method excels at identifying movement patterns, whereas the modularity-based method is better at detecting structure in networks with pairwise relations but not many flows. The rapid drop in NMI for Infomap could result from our perturbation methods focusing on adding connections between nodes because this focus more directly alters the topological structure of the graph rather than representing any flow of patterns. For Label Propagation Raghavan et al. (2007), the authors explicitly state that their method only detects a single community for the giant connected component in those homogeneous networks without community structures, such as the Erdős-Rényi model. A reason for the rapid drop in NMI for Label Propagation could be that as we fix the number of nodes and keep adding edges selected uniformly at random among the nonexistent edges (with restriction to the cross-community ones for the targeted case), the perturbed graph gradually becomes more and more homogeneous, which gets closer to the structure of an Erdős-Rényi random graph while growing in its density.

Figures 4.3 and 4.4 demonstrate the results on LFR benchmark graphs under targeted edge addition for 1000 nodes and 10 000 nodes, respectively, which means that we restrict the new edges to be across distinct communities in the initial networks. Because the appended edges are forced to connect different communities, the targeted addition should be able to destroy the original community structure quicker than random addition, which is similar to the purpose of attacks on real networks. As expected, the targeted edge addition has relatively lower NMI values for all four algorithms vs the previous results with random edge addition. For example, if we again look at the $\mu = 0.3$ curves with 1000 nodes in Figure 4.3 but for targeted addition, Louvain and Leiden need to add about $2.7\times$ (vs $6.3\times$ for random addition), whereas Infomap and Label Propagation need to add about $0.9\times$ and $0.7\times$ (vs $1.1\times$ and $0.9\times$ for random addition) the original number of edges, respectively, to drop the similarity scores below 0.5. In targeted addition, we also observe that networks with stronger initial community structures tend to be more robust, and this is the same trend we see in random addition. Moreover, we again observe that Louvain and Leiden are better at detecting clusters similar to the originals.

Notably, in experiments with larger networks, specifically in Figure 4.2, the curves for $\mu = 0.01$ and $\mu = 0.1$ with Louvain and Leiden cross each other when about $4\times$ of the original number of edges is added. Also, in Figure 4.4, the curves with Louvain and Leiden for $\mu = 0.01$ and $\mu = 0.1$ are almost superimposed on each other. Recall that, as we previously discuss in Section 2.3, there are limitations with the NMI metric. For this reason, we also compute results with the element-centric clustering similarity, for which there is a clear separation between curves. We show these results in Figs. 4.12 and 4.14 in Section 5.1.

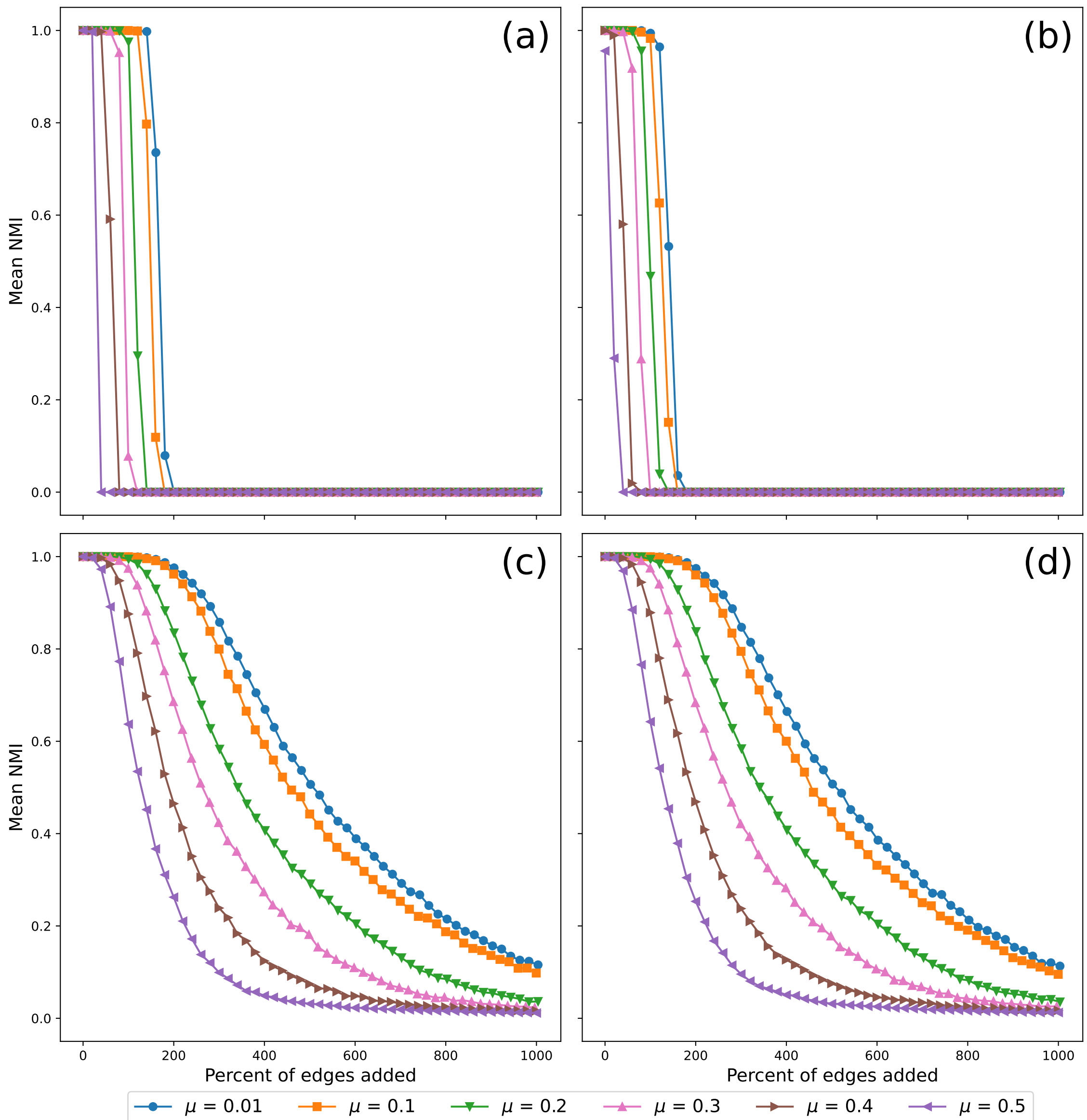

Figure 4.3: Mean NMI over the percentage of edges added that are selected uniformly at random across different communities on LFR benchmark graphs with 1000 nodes. Communities detected by (a) Infomap, (b) Label Propagation, (c) Leiden, and (d) Louvain. Same parameter values are used as in previous experiments. The maximum numbers of edges we add are between 26% and 28% of all nonexistent cross-community edges for all μ.

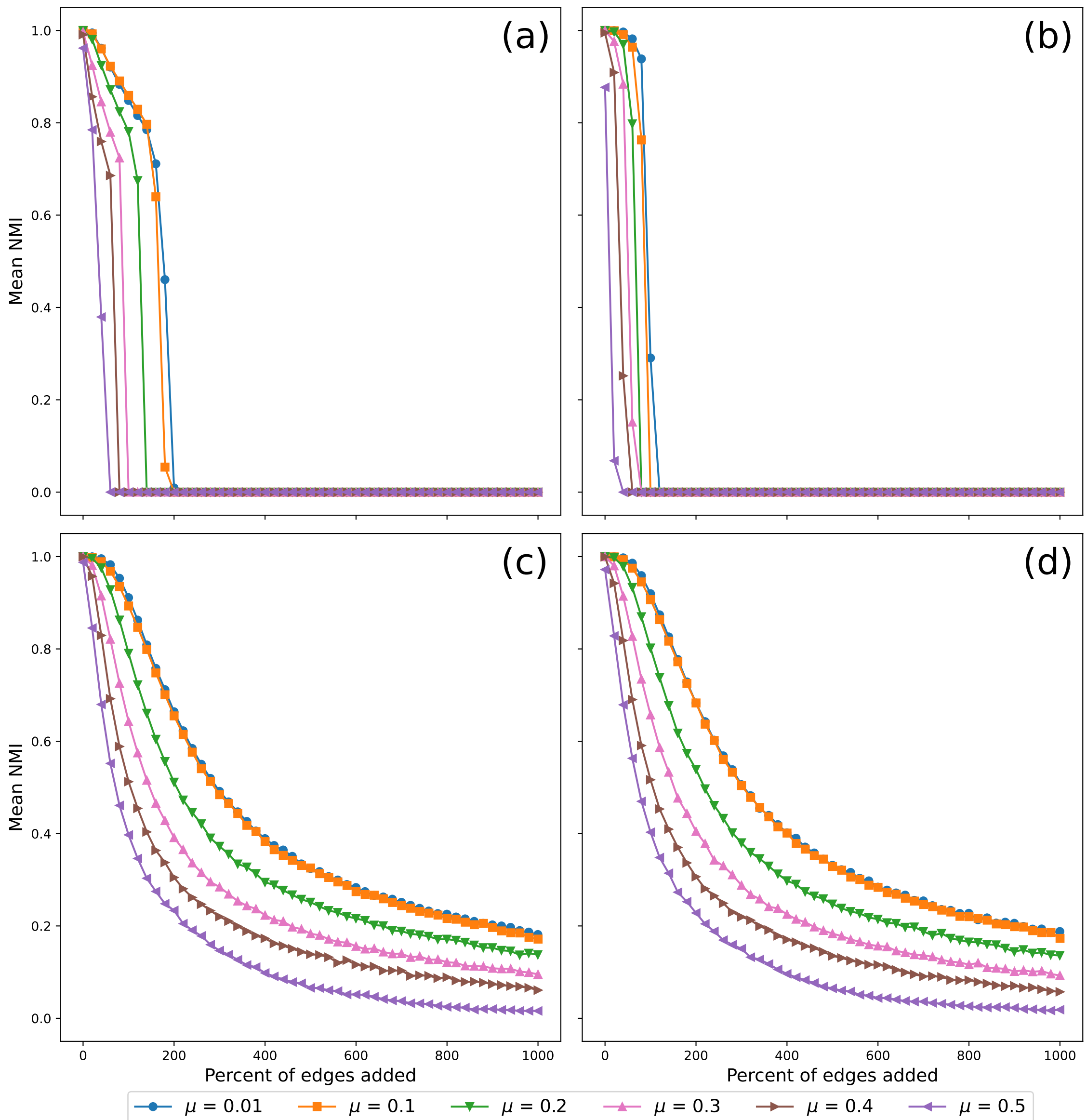

Figure 4.4: Mean NMI over the percentage of edges added that are selected uniformly at random across different communities on LFR benchmark graphs with 10 000 nodes. Communities detected by (a) Infomap, (b) Label Propagation, (c) Leiden, and (d) Louvain. Same parameter values are used as in previous experiments. The maximum numbers of edges we add are in the range from 2.4% and 2.7% of all nonexistent cross-community edges for all μ.

3.2 Empirical networks

For the empirical experiments, we use three empirical email networks with time stamps provided for all edges and test on their subnetworks. The specific procedure for these experiments is described in Section 2.4.2. The first network is the ia-radoslaw-email network Rossi and Ahmed (2015). The entire dataset is email network activity over the course of 6 months among 167 employee email addresses at a mid-sized manufacturing company. The second network is the Enron network as part of the Koblenz Network Collection Kunegis (2013). The original network consists of more than 80 000 users and 1 million emails between Enron employees from 1999 to 2003. The last network is the email-Eu-core-temporal network Leskovec (2017) generated from email data among 986 members of a large European research institution between 2003 and 2005.

To select appropriate subnetworks, we look at all subnetworks induced by subsets of nodes $\{1, 2, \ldots, n\}$ for every $1 \leq n \leq N$ in the entire graph $G = (V, E)$, where $|V| = N$, and the nodes' ids are assigned according to their first appearance in time. We then extract the subnetwork that has a significant increase in density in time, so the demonstration can be comparable to the synthetic results for how many multiples of edges are added by the end. The number of nodes represented in the following network examples refers to the subnetworks on the email users who show up first in time. Specifically, the ia-radoslaw-email subnetwork has the first 74 nodes in time with their corresponding 1457 edges, the Enron subnetwork is obtained by first trimming down to a 1999–2002 time frame and then selecting the first 120 nodes in time with their associated 1603 edges, and the email-Eu-core-temporal subnetwork is the first 282 nodes with 4544 edges.

Figures 4.5–4.7 show the mean NMI over the percentage of added edges in the subnetworks of the ia-radoslaw-email, Enron, and email-Eu-core-temporal networks, respectively. The corresponding results for standard deviation are included in Figs. 4.25–4.27 in Section 5.4.

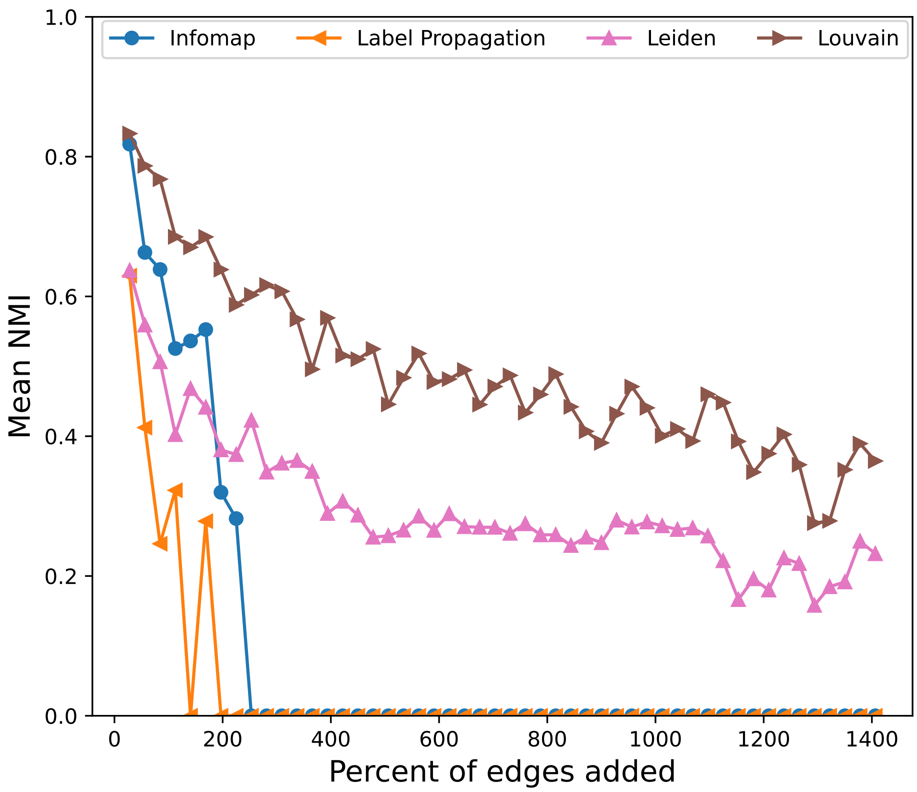

Figure 4.5: Mean NMI over the percentage of edges added for the ia-radoslaw-email subnetwork with 74 nodes. We use fast consensus to obtain 20 initial community partitions. Edges are added over 50 steps following time stamps from the dataset. The average NMI is computed over all pairs of the initial consensus partitions and the partitions from 10 independent realizations at each time step.

Notably, empirical networks are more complex to analyze because they lack ground-truth community structure, the degree distribution might not belong to a certain family of distributions, and the set of edges added in time may be governed by different unknown factors that we cannot control.

In considering the effect of edge-addition rules in the empirical compared with

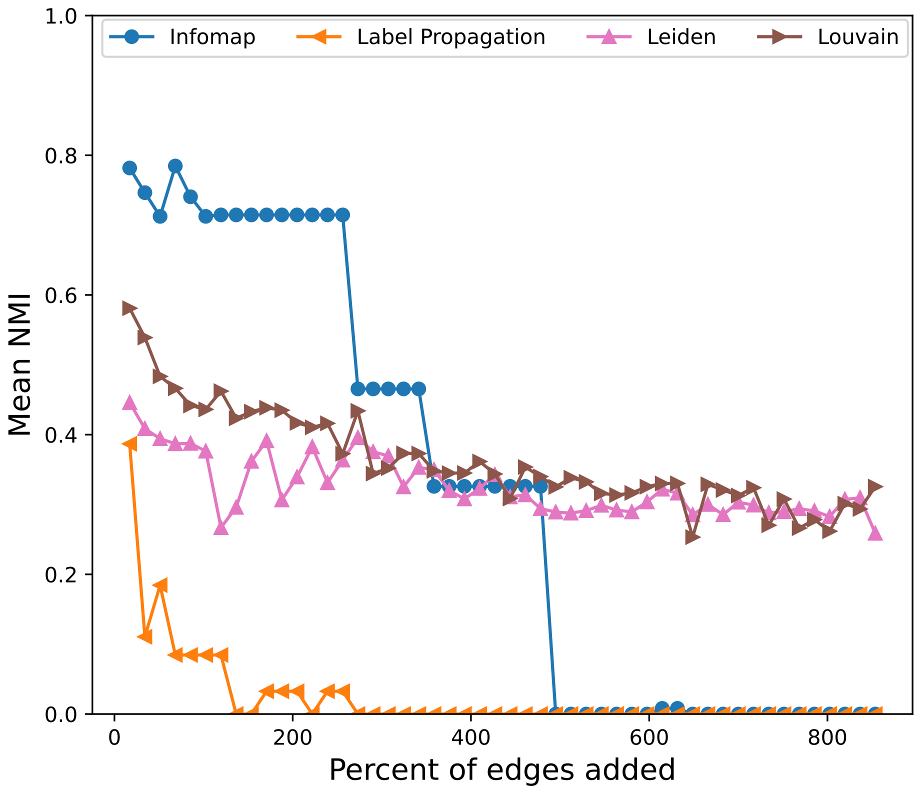

Figure 4.6: Mean NMI over the percentage of edges added for the Enron subnetwork with 120 nodes.

the synthetic cases, we look at the ratio of intercommunity edges among all added edges over time for each empirical network. For ia-radoslaw-email, Enron, and email-Eu-core-temporal subnetworks, the intercommunity ratios are $94\%, 90\%$, and 59%, respectively. Note that the LFR benchmark graphs are sparse and so there is a lower fraction of intracommunity edges available to be added. Specifically, for the LFR benchmark on 1000 nodes, the number of intracommunity nonexistent edges is only about twice the original number of edges but the number of intercommunity nonexistent edges can go to about $37\times$. This means that for our random addition on LFR benchmark with 1000 nodes, the fraction of intercommunity edges added is around 95%, and due to the limited number of intracommunity edges, it is impossible

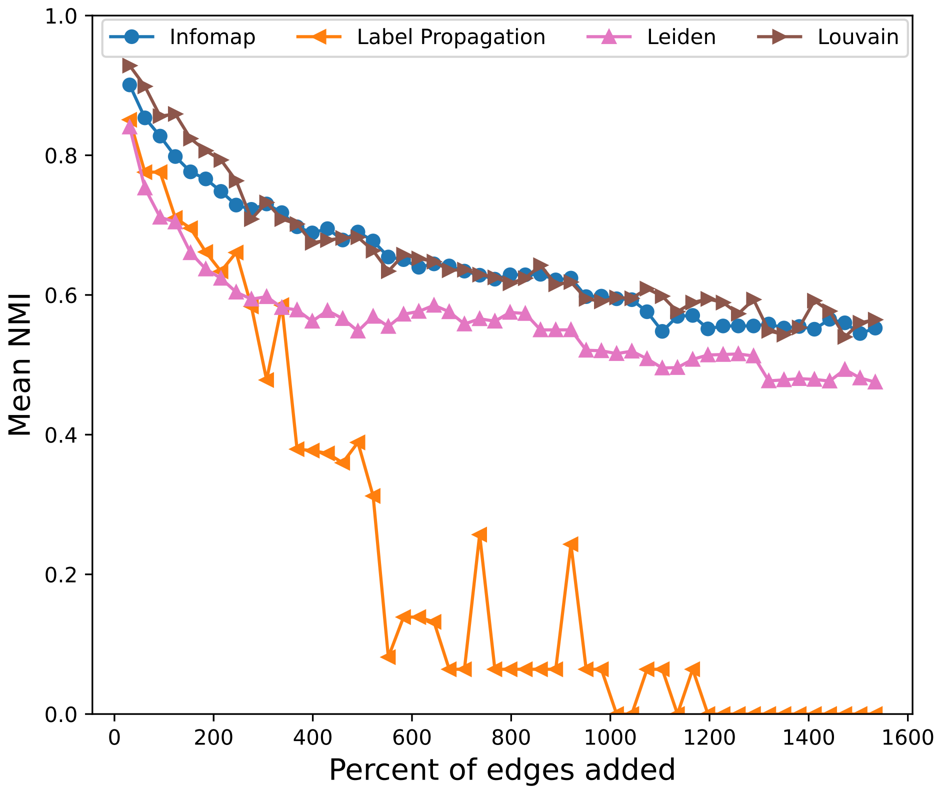

Figure 4.7: Mean NMI over the percentage of edges added for the email-Eu-core-temporal subnetwork with 282 nodes.

to have intracommunity edges taken more than 20% of the 10× additional edges. The ia-radoslaw-email subnetwork has the ratio of added intercommunity edges most comparable with our previous synthetic experiments on 1000 nodes. To draw a direct comparison between the empirical and the synthetic cases, we experiment on synthetic networks where the ratio of added intercommunity edges is controlled to match the one in ia-radoslaw-email subnetwork, namely 94%. The results show similar behaviors as the previous synthetic ones and we include them in Section 5.2.

In addition, we acknowledge that the chosen subnetworks described here are not as large as the synthetic benchmark graphs: The benchmark graphs have thousands of nodes, whereas the empirical network examples only have hundreds.

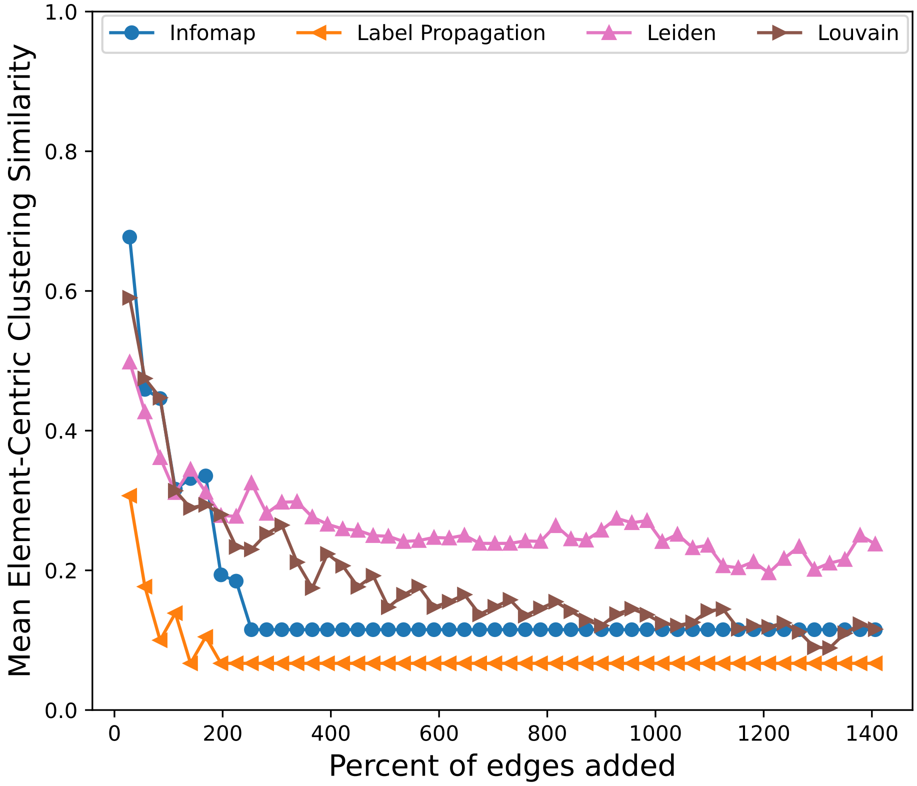

Figure 4.8: Mean element-centric clustering similarity over the percentage of edges added for the ia-radoslaw-email subnetwork.

Among these results in NMI, the experiments on the ia-radoslaw-email and Enron subnetworks reveal similar behaviors as the synthetic networks (i.e., Leiden and Louvain appear to detect more sustainable community structure than Infomap or Label Propagation as more edges are added). However, in the experiments on the email-Eu-core-temporal subnetwork, Infomap has performance similar to Leiden and Louvain, whereas Label Propagation has the lowest NMI score almost throughout all time steps. Although there may be intertwining reasons for these results, one shared phenomenon we observe for all subnetworks is that with Infomap or Label Propagation, the mean NMI drops to almost 0, whenever the detection algorithm begins to detect only one community in the perturbed networks.

While community detection algorithms have different performance, we also observe effects from using different community similarity metrics. Specifically, we repeat the same sets of experiments but replace the NMI metric with the element-centric clustering similarity. Figures 4.8–4.10 illustrate these results. The corresponding standard deviations are provided in Figs. 4.28–4.30 in Section 5.4. Using this different metric, we find that Infomap, Leiden, and Louvain do not show consistent advantages over each other, but Label Propagation, although not necessarily dropping to 0 by the end of time, always has the lowest metric value.

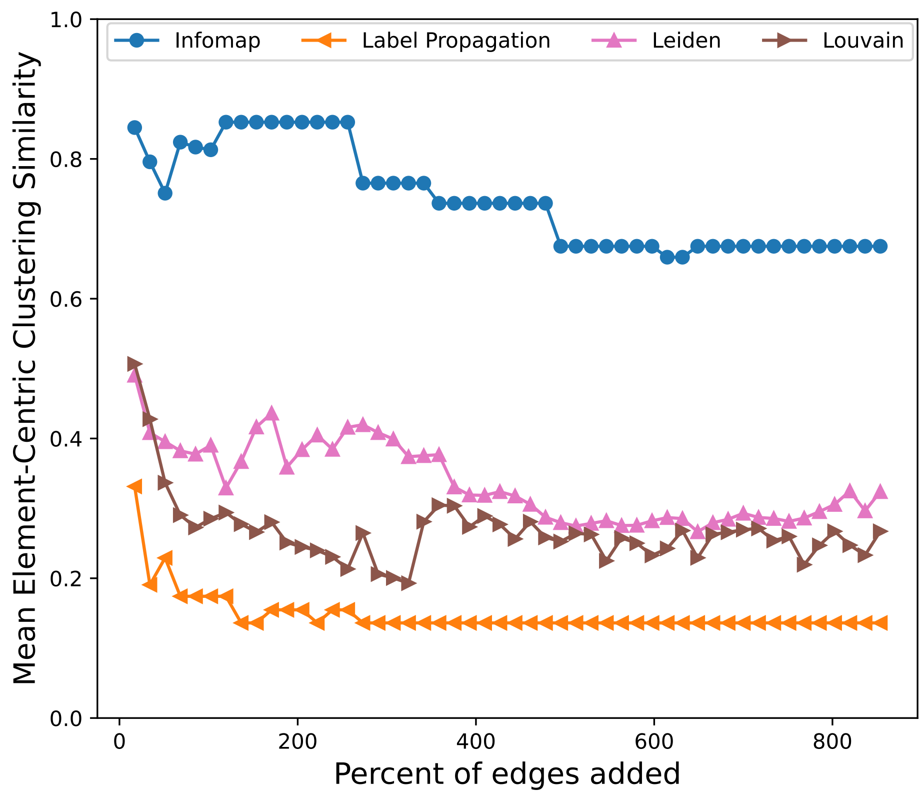

Figure 4.9: Mean element-centric clustering similarity over the percentage of edges added for the Enron subnetwork.

One noticeable difference in these element-centric clustering similarity results from the NMI results is the curve for Infomap in the Enron subnetwork. In the NMI

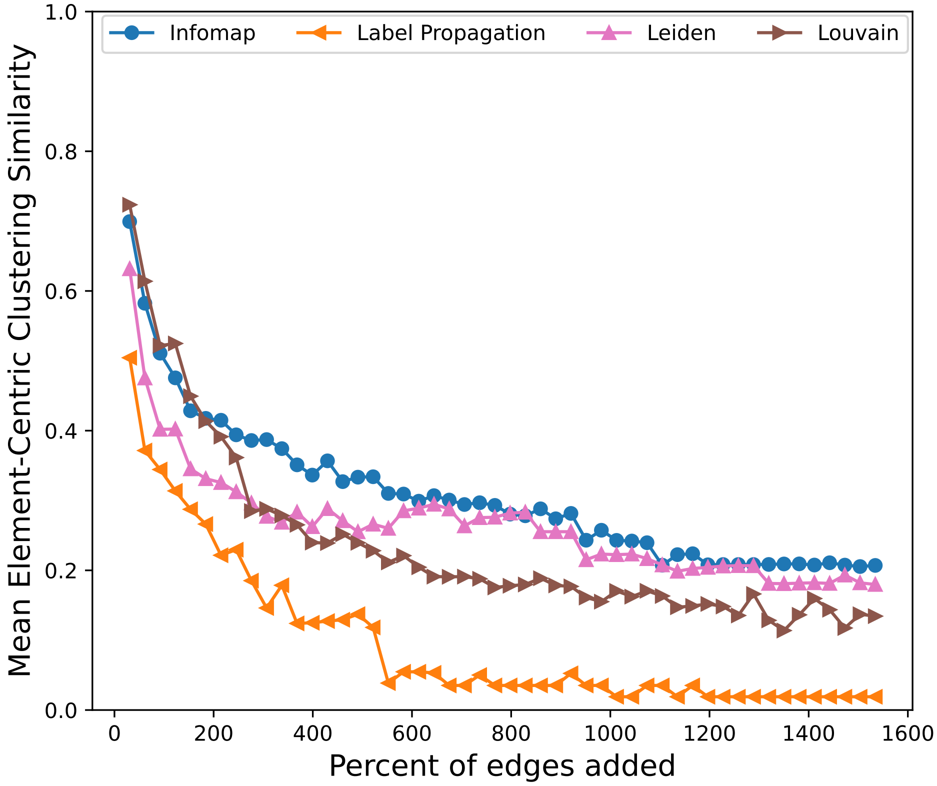

Figure 4.10: Mean element-centric clustering similarity over the percentage of edges added for the email-Eu-core-temporal subnetwork.

plot (Figure 4.6), the value eventually drops to 0, which shows that the community structure detected by Infomap is not as robust as that by Leiden or Louvain in terms of NMI. However, in the element-centric clustering similarity metric, the clustering similarity value is the highest for Infomap throughout time among the four algorithms, and this suggests that the community structure found by Infomap is the most robust in our experiments according to this alternative metric. To determine what is happening, we look at the mean number of communities detected by the four algorithms at each step and find that it drops from higher numbers to 1 for both Infomap and Label Propagation but maintains around 5 or 6 for Leiden and Louvain by the end of time. Note that the NMI always outputs 0 whenever one of the two partitions being compared has only one community due to the formulation of this metric, so we suspect that this property might have hindered NMI from capturing some similarities between the communities in the initial and the highly perturbed networks, especially after the number of detected communities drops to 1.

Nonetheless, when networks are perturbed under edge addition, and the density is increased by a significant amount, different community detection algorithms start to show clear discrepancies in whether they can find a community structure similar to the initial one. Hence, the chosen community detection algorithm plays an important role in detecting robust community structures over time.

4 Conclusion

We design synthetic and empirical experiments to test the robustness of community structure under the perturbation of edge addition by using different community detection algorithms. Overall, we found that community robustness strongly depends on the community detection algorithm selected. In the synthetic experiments, we use LFR benchmark graphs and control the mixing parameter, μ. To mimic how edges may be added in different scenarios in real networks and to illustrate the difference in the outputs, we add random edges in two different ways. Both ways select additional edges from nonexistent edges. One is a completely uniformly random selection, which is analogous to random errors, and the other is a targeted selection from edges across different communities, which is analogous to attacks in real-world networks.

We demonstrate results for six different mixing parameter values and the two different edge-addition methods described above. The clustering similarity scores computed in NMI indicate that networks with lower mixing parameters (i.e. stronger partitions) have more robust community structures under the perturbation of edge addition. Our targeted edge-addition method can more efficiently alter the initial communities compared with the random addition. As expected, the NMI values drop faster in the targeted case among all chosen community detection algorithms.

In these synthetic experiments, modularity-based algorithms, Leiden and Louvain, show better performance in detecting more similar communities to the initial ones vs Infomap and Label Propagation, which cannot detect any community structure when graphs become too dense. In other words, Leiden and Louvain excel at finding more robust communities in networks that can withstand more severe network perturbations. We also observe effects caused by community similarity metrics, NMI and element-centric clustering similarity specifically, but the takeaways in the two metrics are not significantly different in the qualitative sense. The overall impacts of the initial partition strength, the edge-addition method, and the selected community detection algorithm are similar with either metric.

We acknowledge that empirical temporal networks introduce more complexity, and we see different community similarity metrics demonstrate significantly different results when determining whether the detected communities are similar to the initial ones (i.e., whether the community detection algorithm can find a robust community structure). In the empirical experiments, we again find that community detection algorithms play an important role in the robustness of communities. Specifically, for all three empirical subnetworks tested, we observe that Label Propagation performs the worst among the four algorithms in detecting robust communities over time using either NMI or element-centric clustering similarity.

When considering future research directions, we note that the different metrics and community detection algorithms show different outcomes on the empirical temporal networks. To understand more about their effects on the community robustness performance, we need many more network examples in which edge densities expand over time. Adequate network candidates with properties in different families—including scales, densities, degree distributions, and edge-addition rules—are needed for comparison tests in order to distinguish the effects from each individual aspect. Another direction for future research is to explore different types of generative models for benchmarking and include community detection algorithms based on other methods for comparison.

5 Additional Results

5.1 Synthetic Results Using Element-Centric Clustering Similarity Metric

Figures 4.11 and 4.12 show the results of using the element-centric clustering similarity metric for the LFR benchmark graphs with 1000 nodes and 10 000 nodes, respectively, with added edges selected uniformly at random from all nonexistent edges while multiedges are prohibited. Notably, the parameter values are chosen the same as in experiments that use NMI, and the experimental procedure follows Section 2.4.1. Figures 4.13 and 4.14 show the LFR benchmark graphs with 1000 nodes and 10 000 nodes, respectively, with additional edges selected uniformly at random but restricted to ones that cross different communities.

Results in element-centric clustering similarity agree with the observations from results in NMI. Networks with stronger initial partitions, specifically those with lower

μ values, are relatively more robust in the community structure. Targeted edge addition can more quickly destroy the original community structure. Also, community robustness is highly dependent on the chosen community detection algorithms. In particular, Leiden and Louvain can detect communities similar to the initial ground truth as the graphs increase the number of edges significantly.

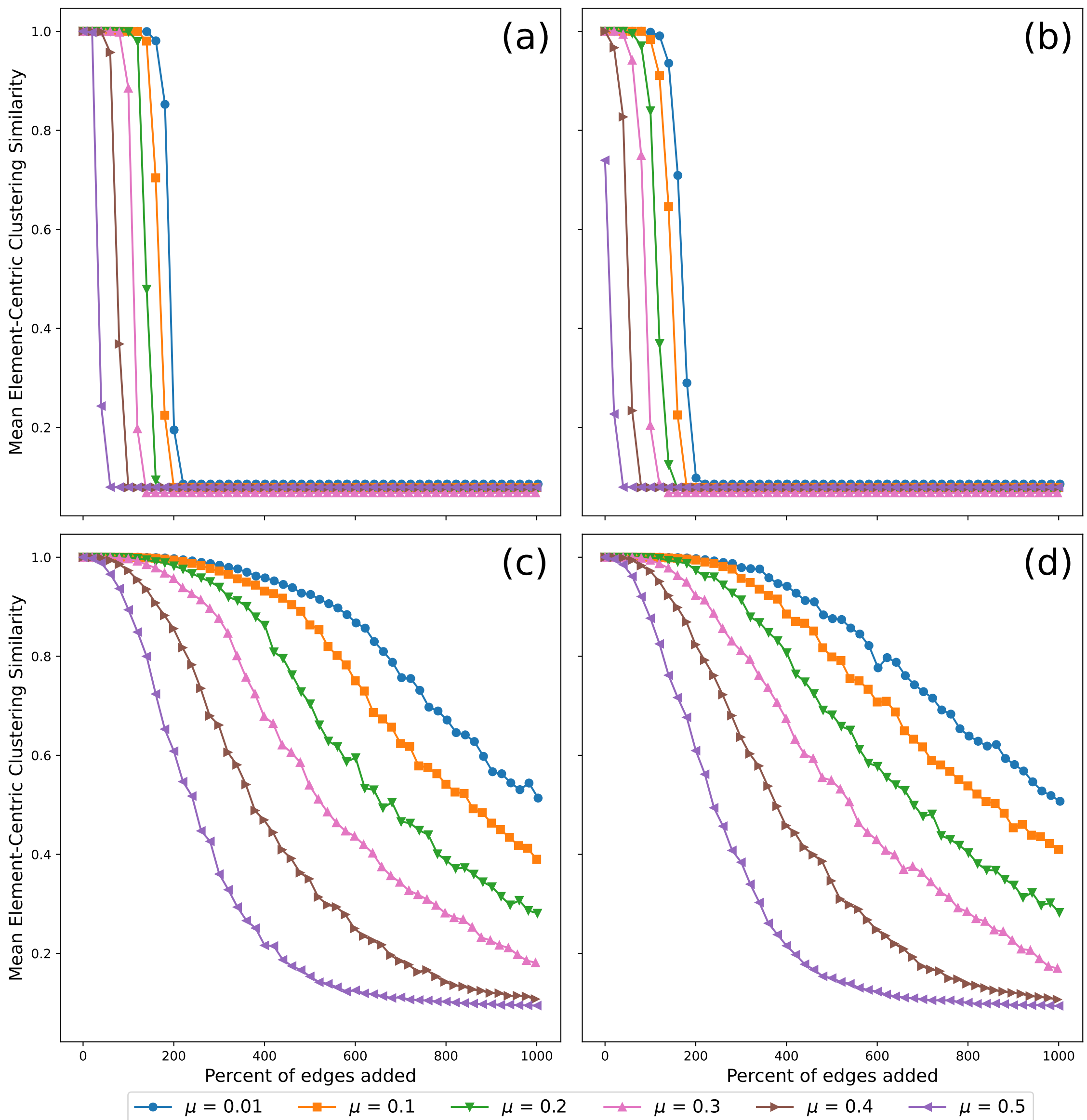

Figure 4.11: Mean element-centric clustering similarity over the percentage of edges added uniformly at random on LFR benchmark graphs with 1000 nodes. Communities detected by (a) Infomap, (b) Label Propagation, (c) Leiden, and (d) Louvain.

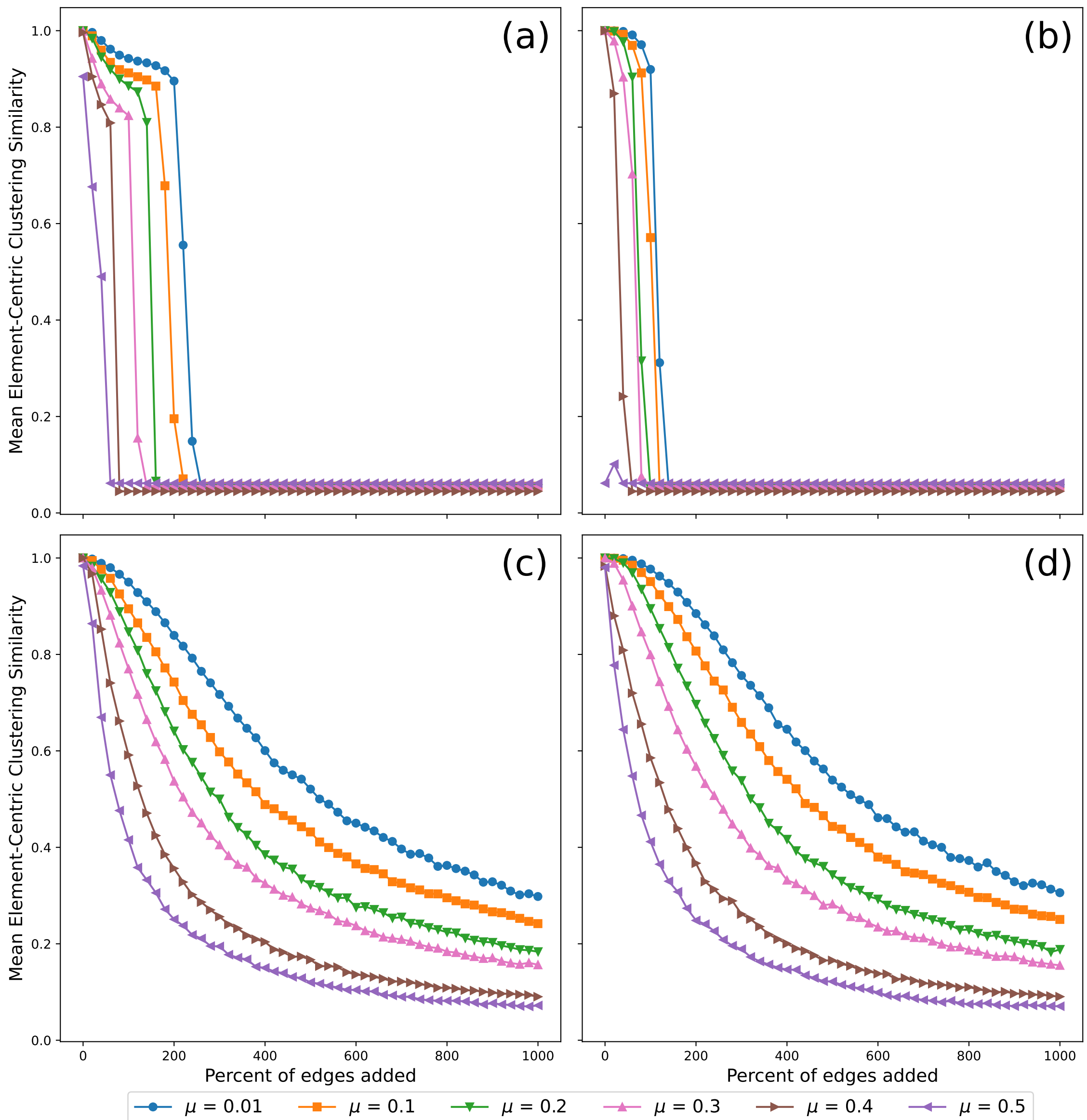

Figure 4.12: Mean element-centric clustering similarity over the percentage of edges added uniformly at random on LFR benchmark graphs with 10 000 nodes. Communities detected by (a) Infomap, (b) Label Propagation, (c) Leiden, and (d) Louvain.

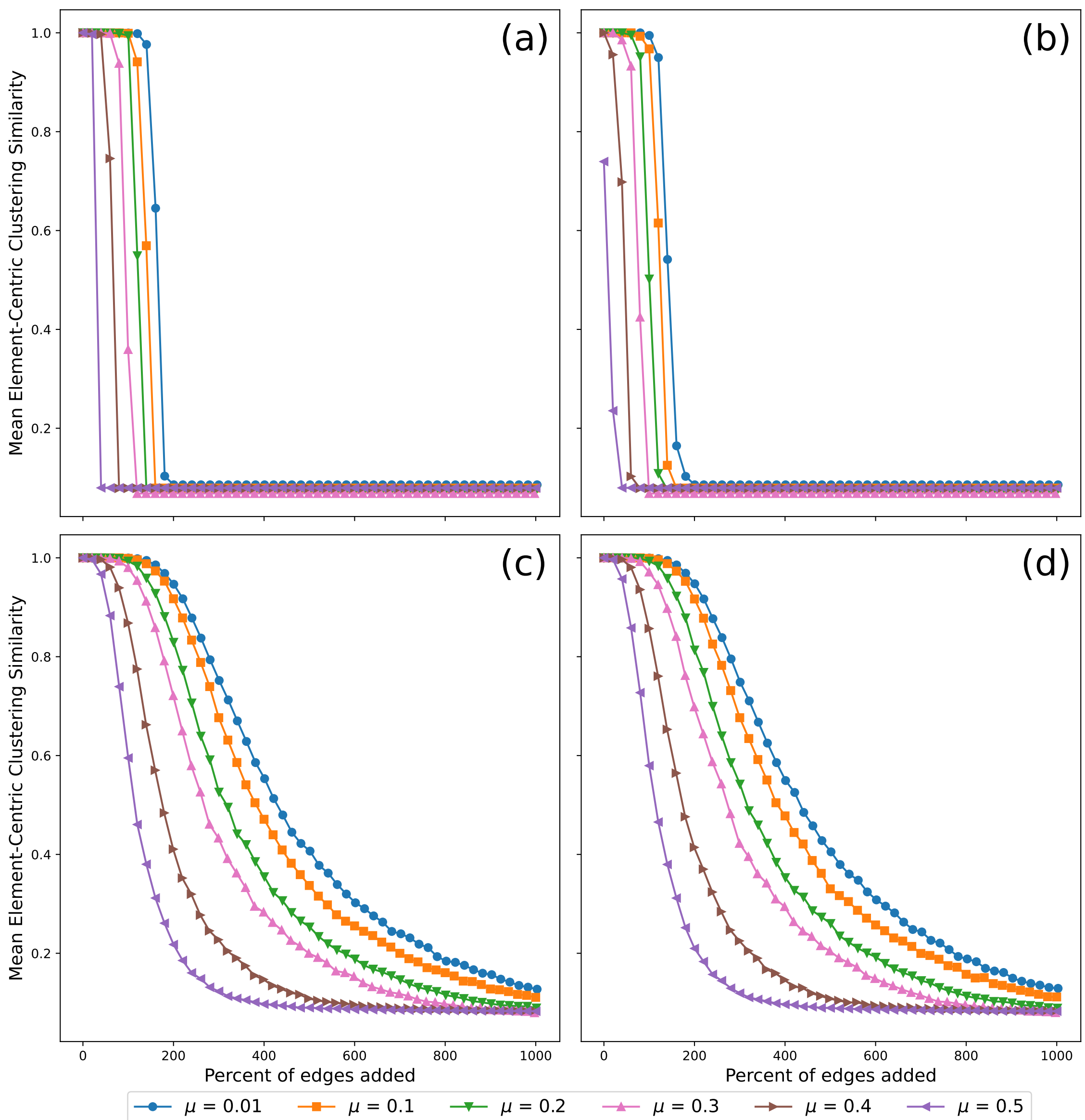

Figure 4.13: Mean element-centric clustering similarity over the percentage of edges added that are selected uniformly at random across different communities on LFR benchmark graphs with 1000 nodes. Communities detected by (a) Infomap, (b) Label Propagation, (c) Leiden, and (d) Louvain.

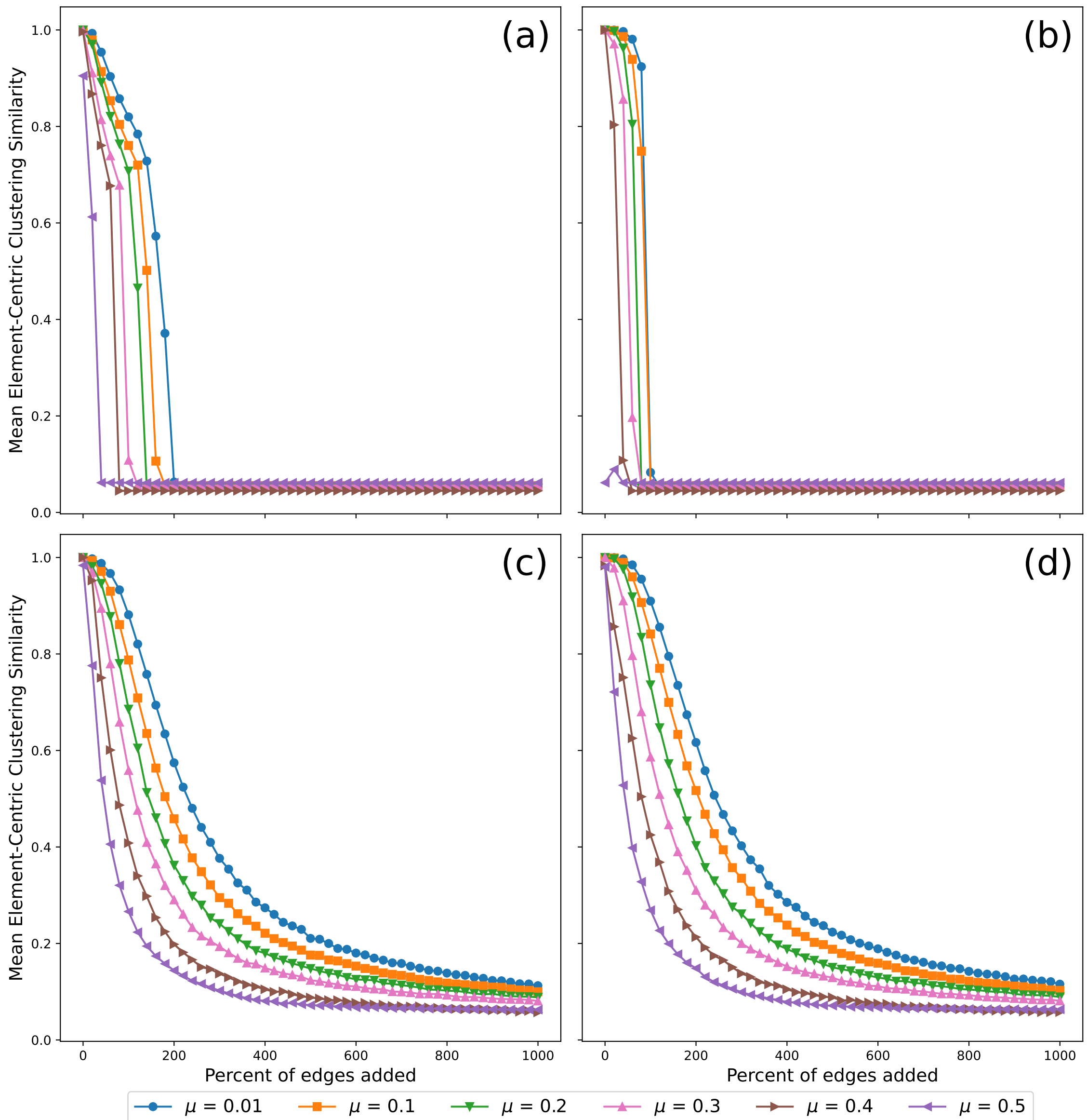

Figure 4.14: Mean element-centric clustering similarity over the percentage of edges added that are selected uniformly at random across different communities on LFR benchmark graphs with 10 000 nodes. Communities detected by (a) Infomap, (b) Label Propagation, (c) Leiden, and (d) Louvain.

5.2 Synthetic Results Matching Ratio of Intercommunity Edges in Empirical Experiments

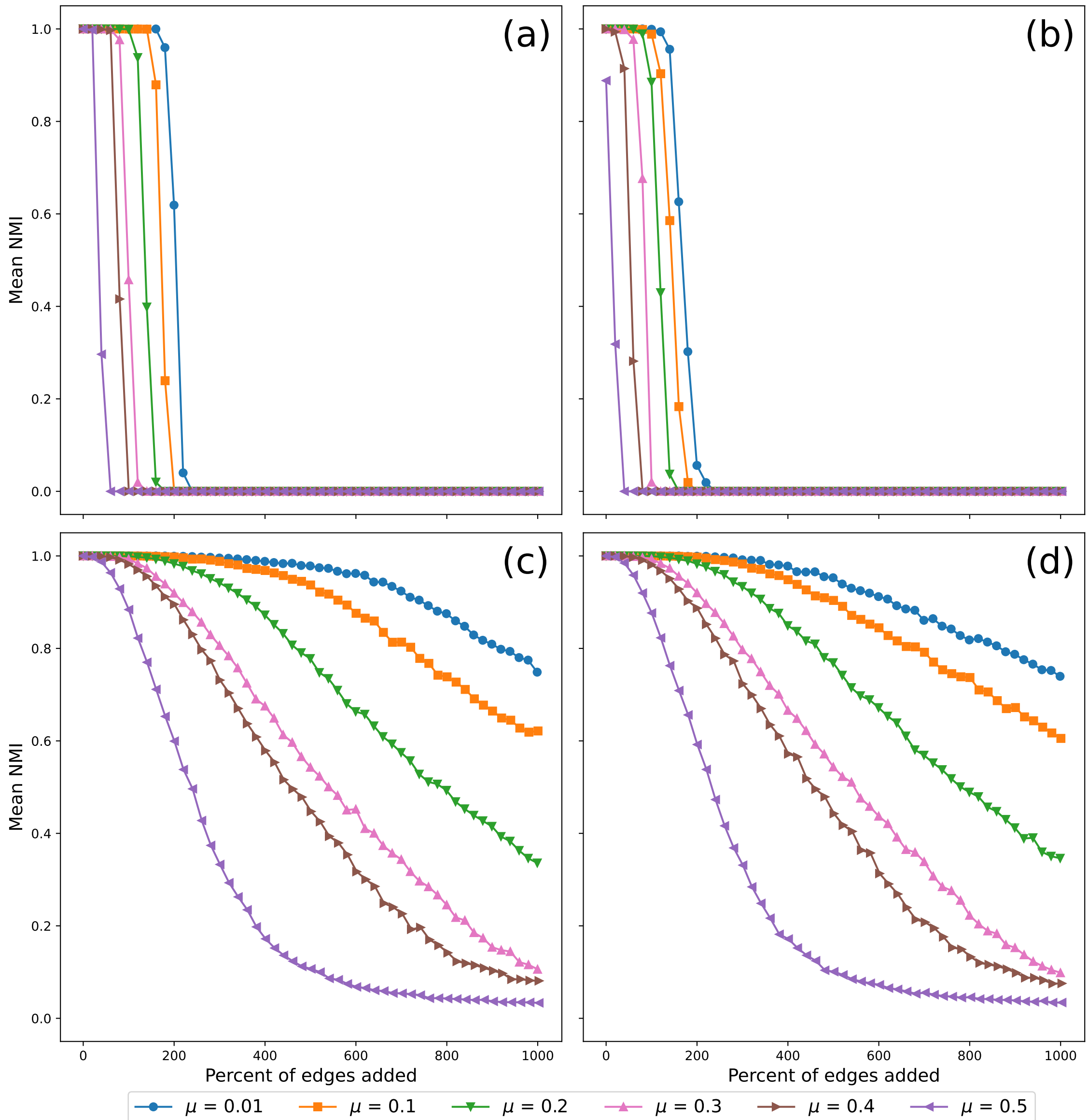

Figure 4.15: Mean NMI over the percentage of edges added on LFR benchmark graphs with 1000 nodes. The ratio of intercommunity edges added is 94%, which matches the one in the ia-radoslaw-email subnetwork. Communities detected by (a) Infomap, (b) Label Propagation, (c) Leiden, and (d) Louvain.

Figures 4.15 and 4.16 show mean community similarity metrics, NMI and element-centric clustering similarity respectively, over percentage of edges added

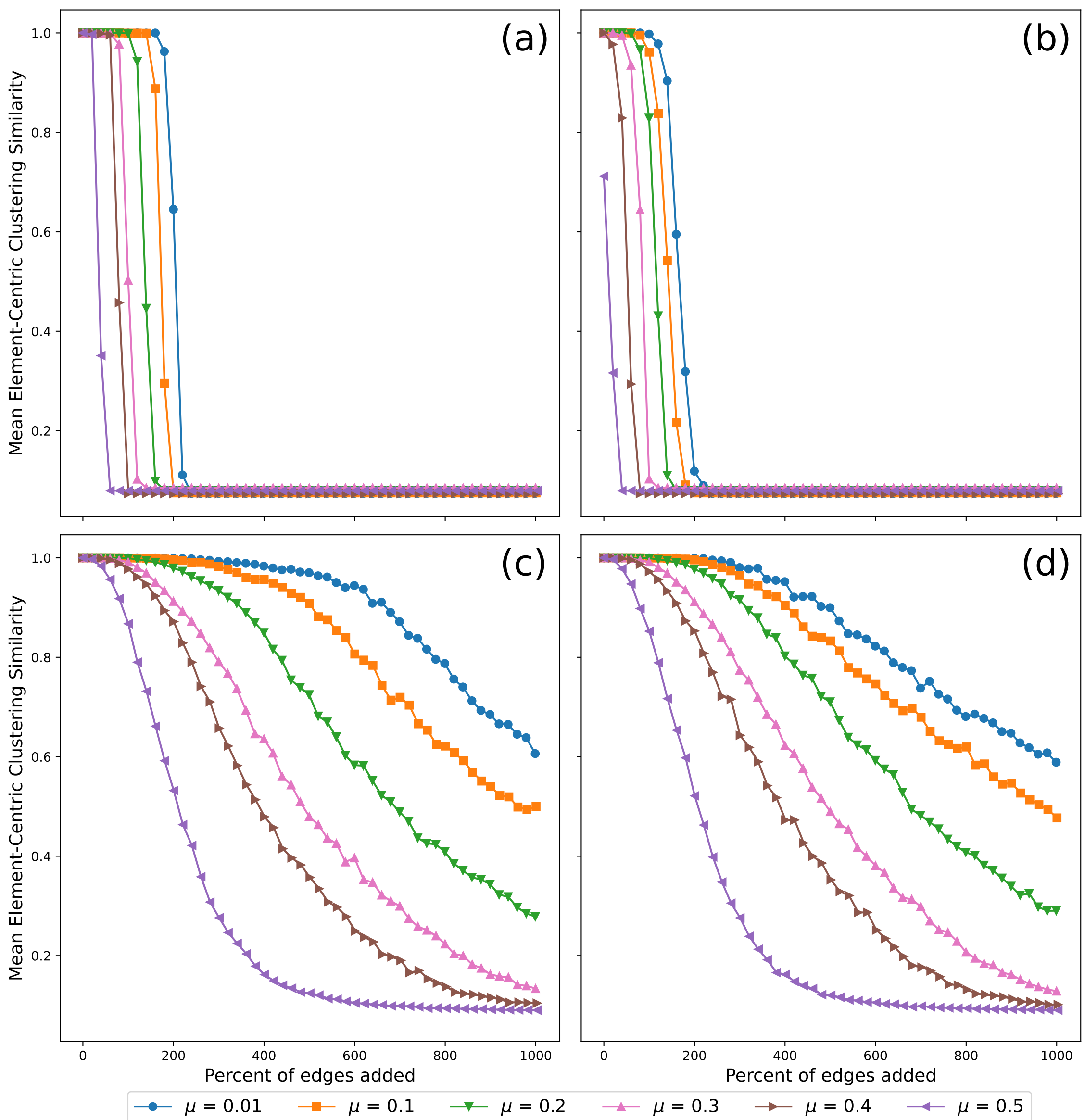

Figure 4.16: Mean element-centric clustering similarity over the percentage of edges added on LFR benchmark graphs with 1000 nodes. The ratio of intercommunity edges added is 94%. Communities detected by (a) Infomap, (b) Label Propagation, (c) Leiden, and (d) Louvain.

on LFR benchmark graphs with 1000 nodes. Here, at each step, we force 94% of the added edges to be randomly selected from the pool of intercommunity nonexistent edges. This ratio matches the proportion we found for the intercommunity edges added of the total additional edges in the ia-radoslaw-email subnetwork. Specifically, since we have four community detection methods and each of them has $np = 20$ initial communities found by the fast consensus algorithm, we have 80 corresponding ratios and then we take the mean as the estimate.

These results show similar behaviors as those observed in the synthetic experiments: A lower mixing parameter, μ, tends to have a more robust community structure, and among the four community detection algorithms, Leiden and Louvain can detect communities more similar to the initial ground truth.

5.3 Standard Deviation for Synthetic Results

Figures 4.17 – 4.24 show the standard deviation of NMI and element-centric clustering similarity metric for the synthetic results. Note that the overall changes in the standard deviation are generally restricted to a region with negligible scale compared with the mean. However, the only exception is for Infomap (a) and Label Propagation (b) where we observe a spike for almost every curve within the region when less than $2\times$ the original number of edges are added. Further investigation of the mean and the distributions reveals that these locations with large standard deviations correspond to the steps where the rapid drops in the means happen. Specifically, values of the community similarity metric at these steps are split into two families with comparable size – one with 0s and the other with values very close to 1. Recall that at each step, there are 50 independent realizations, meaning 50 different perturbed graphs, so we suspect this is the uncertainty from the edge-addition stochastic process.

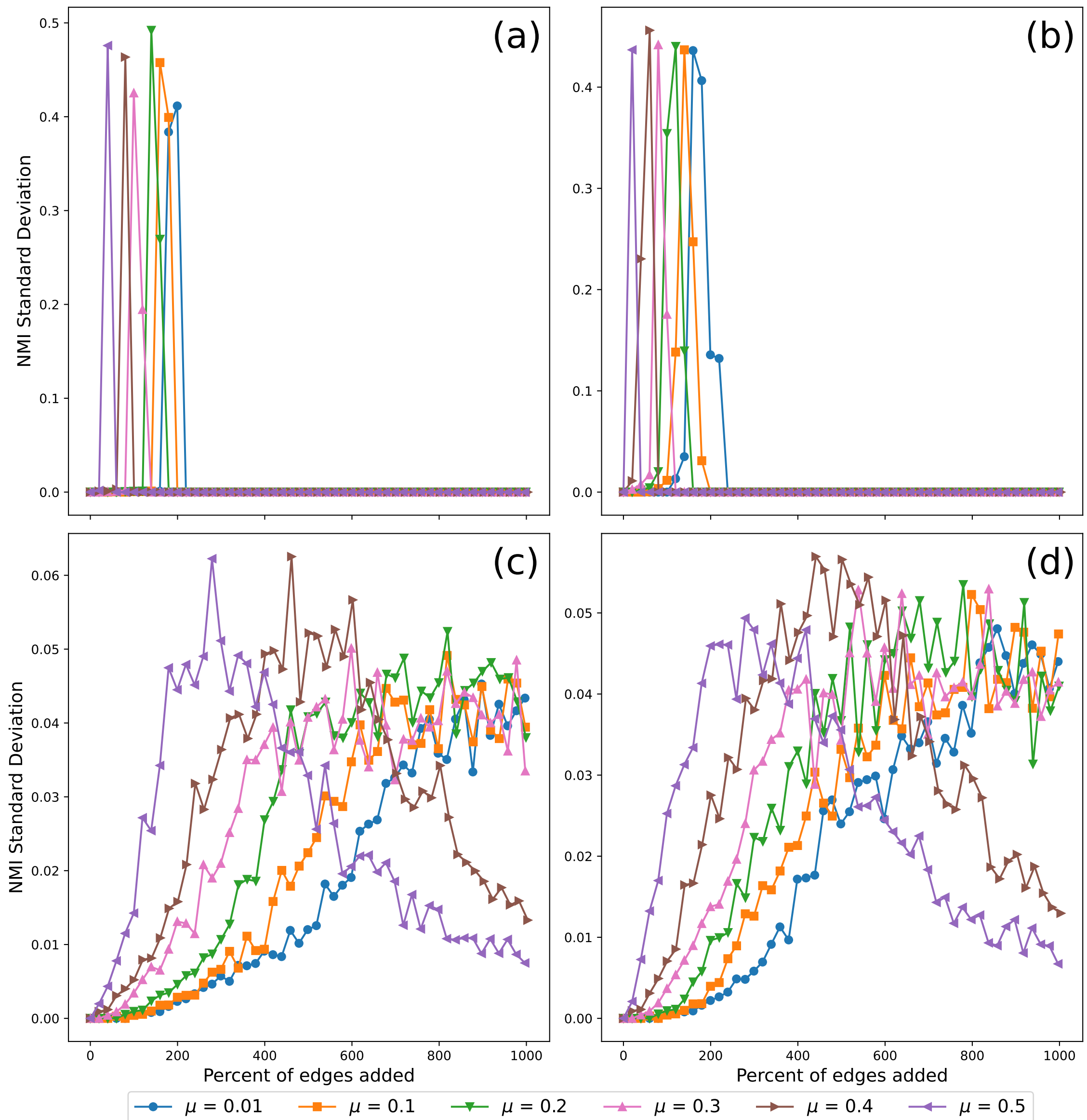

Figure 4.17: Standard deviation of NMI over the percentage of edges added uniformly at random on LFR benchmark graphs with 1000 nodes. Communities detected by (a) Infomap, (b) Label Propagation, (c) Leiden, and (d) Louvain.

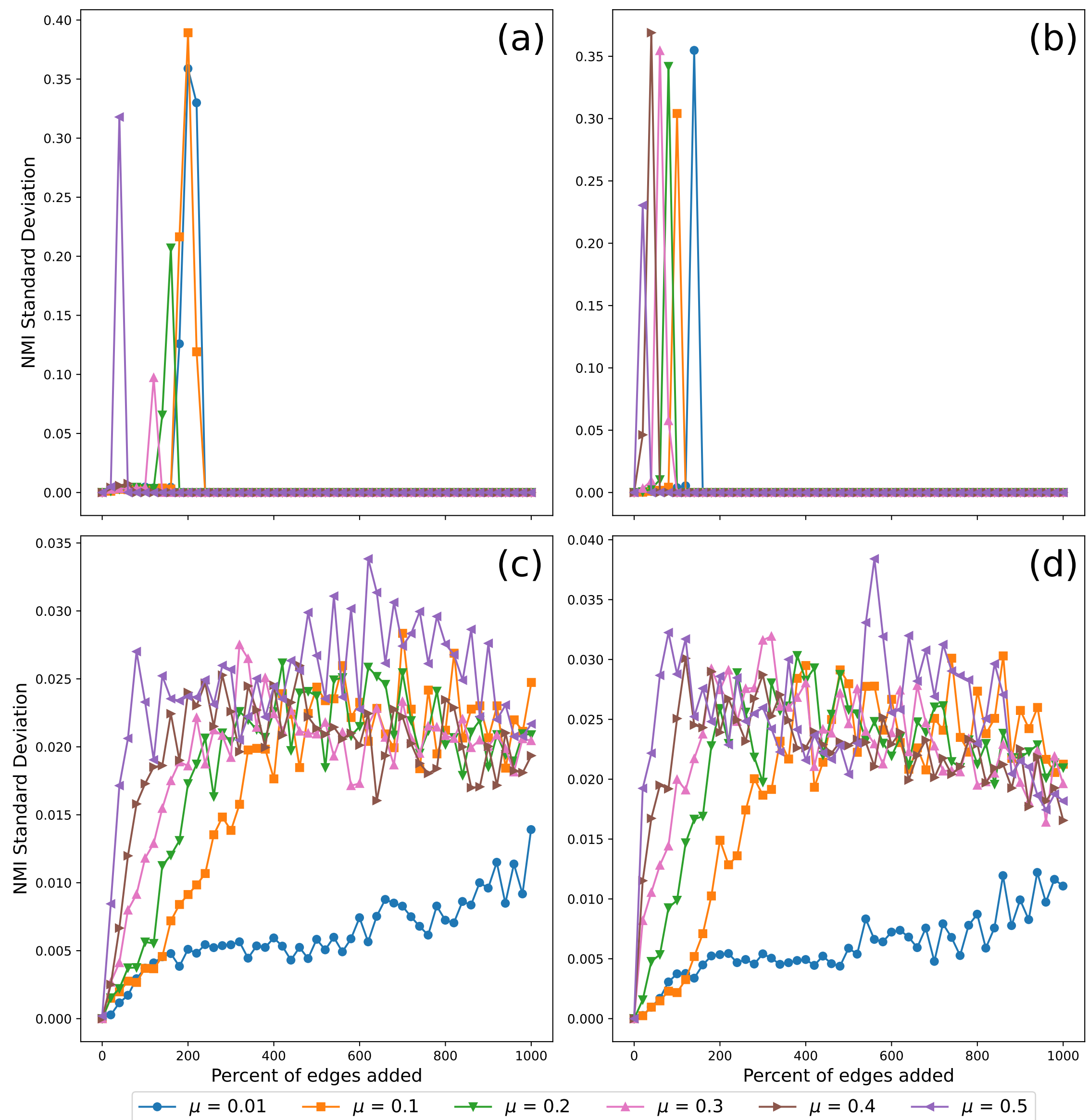

Figure 4.18: Standard deviation of NMI over the percentage of edges added uniformly at random on LFR benchmark graphs with 10 000 nodes. Communities detected by (a) Infomap, (b) Label Propagation, (c) Leiden, and (d) Louvain.

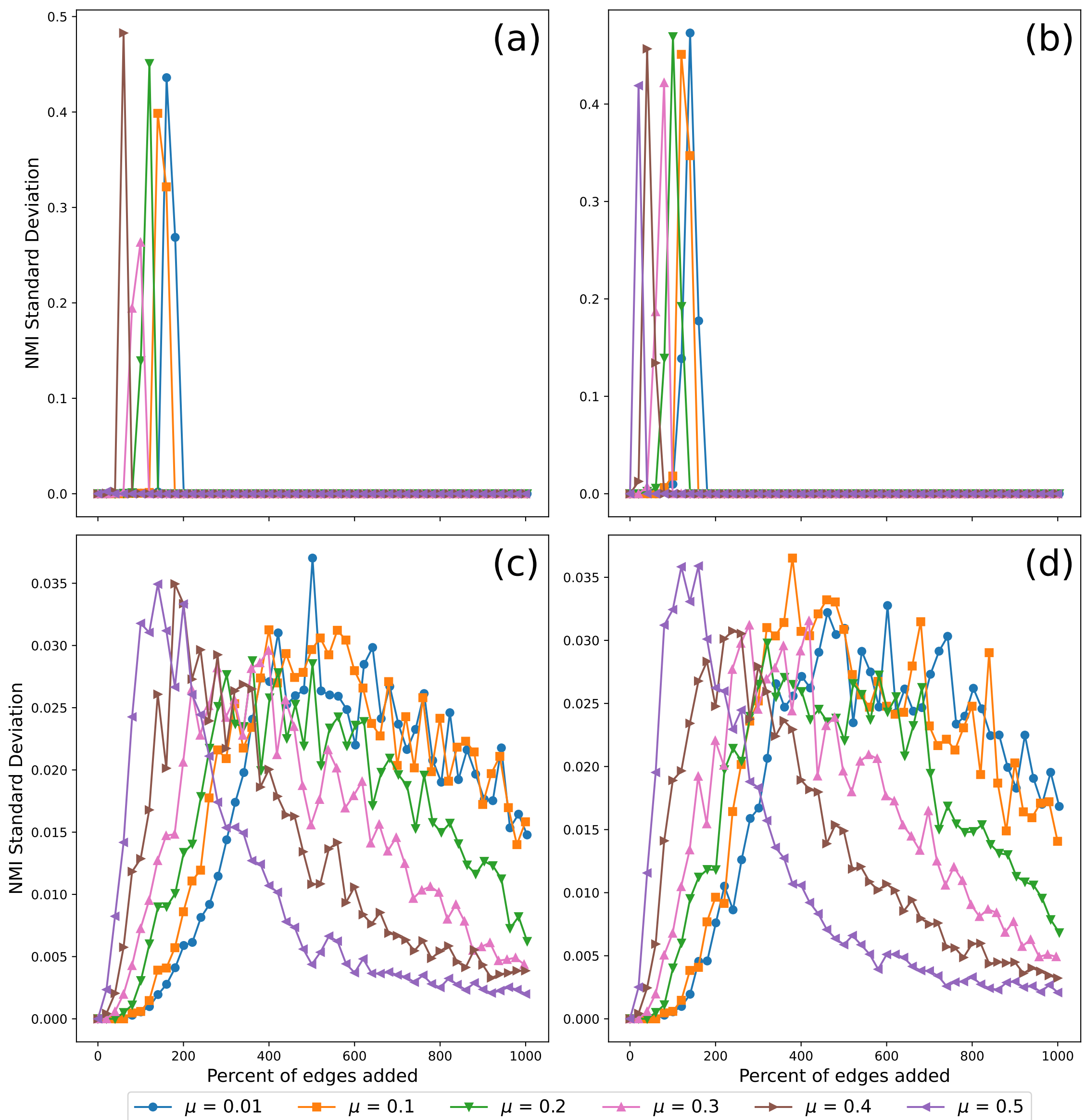

Figure 4.19: Standard deviation of NMI over the percentage of edges added that are selected uniformly at random across different communities on LFR benchmark graphs with 1000 nodes. Communities detected by (a) Infomap, (b) Label Propagation, (c) Leiden, and (d) Louvain.

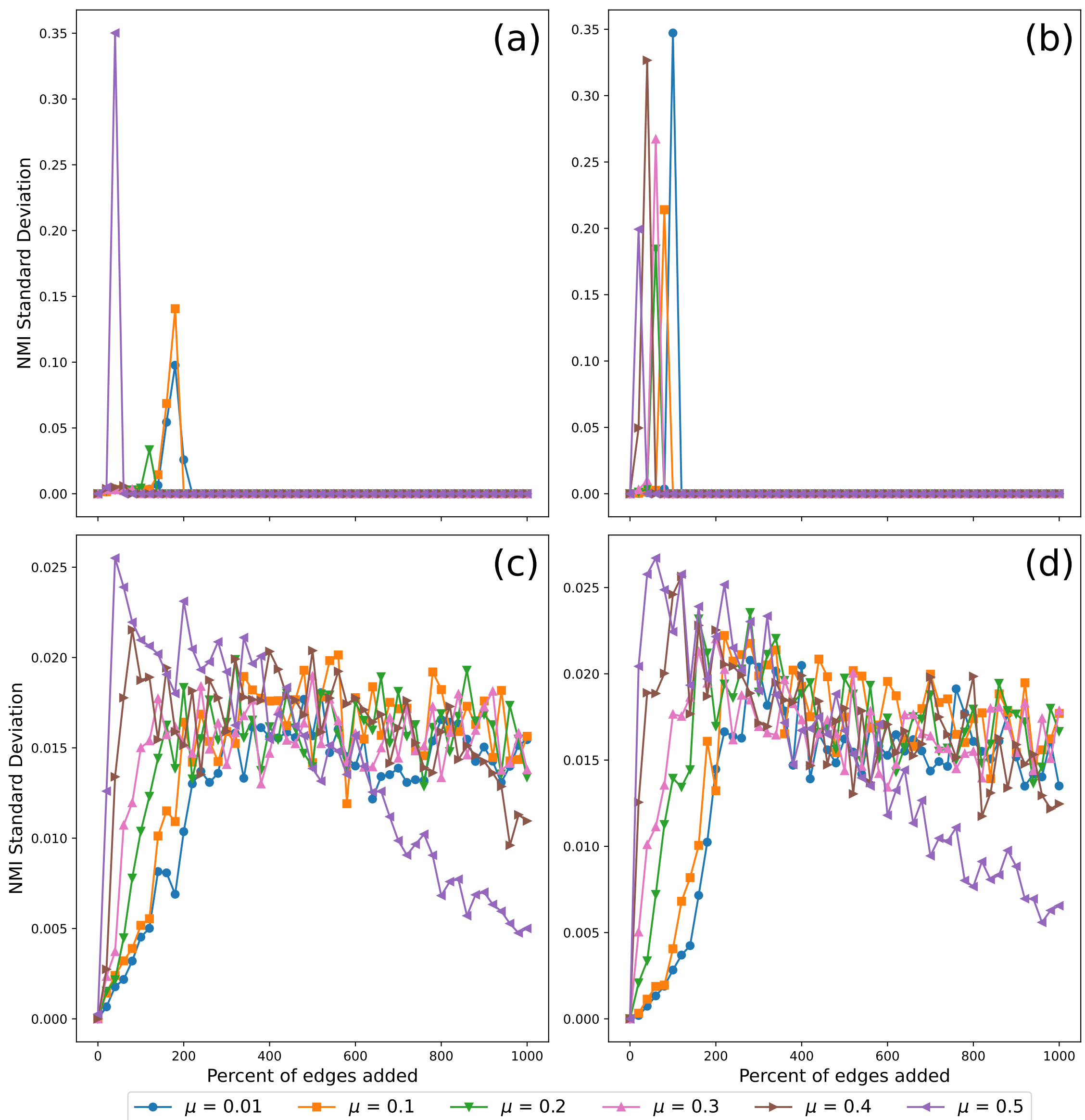

Figure 4.20: Standard deviation of NMI over the percentage of edges added that are selected uniformly at random across different communities on LFR benchmark graphs with 10 000 nodes. Communities detected by (a) Infomap, (b) Label Propagation, (c) Leiden, and (d) Louvain.

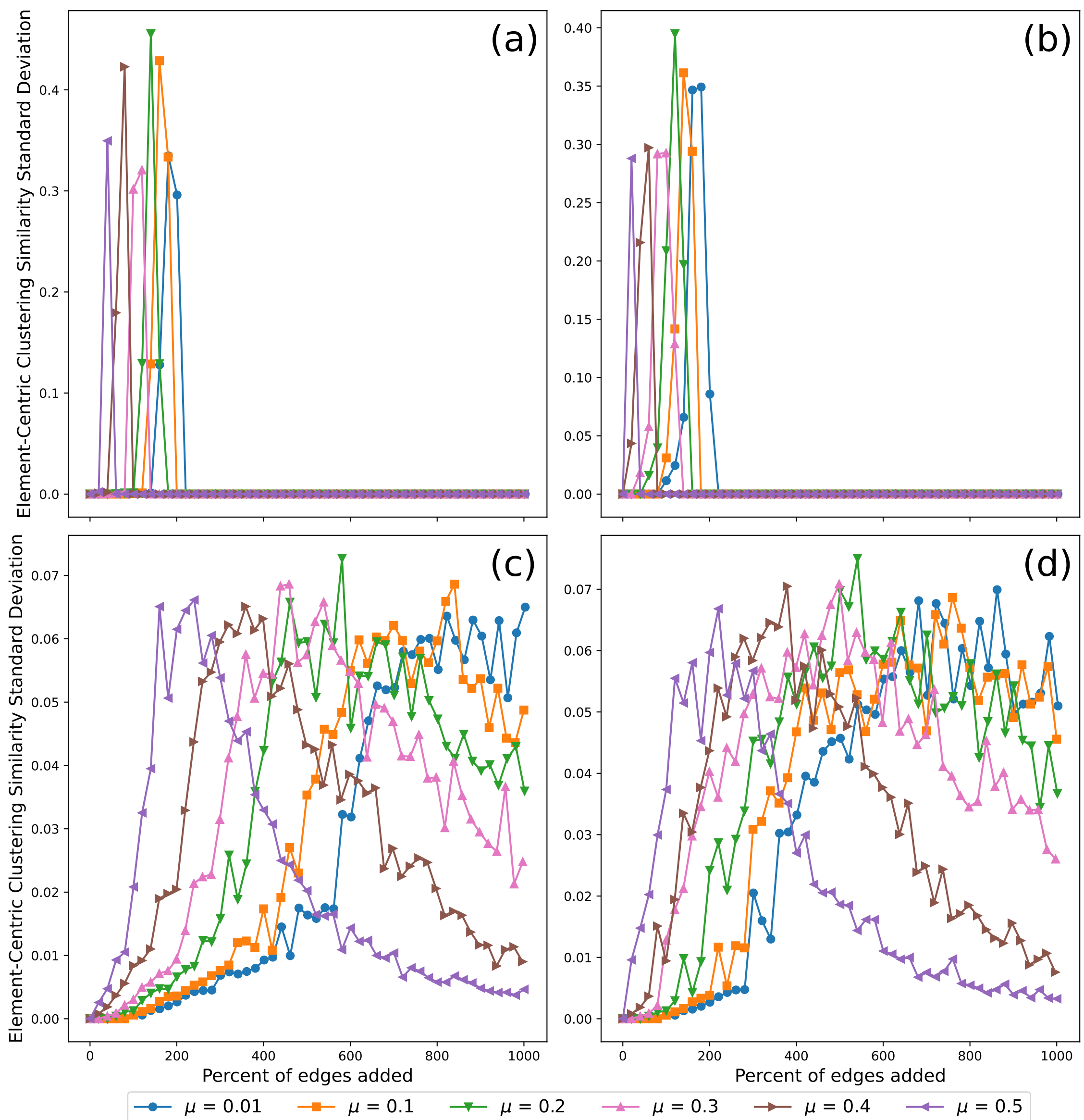

Figure 4.21: Standard deviation of element-centric clustering similarity over the percentage of edges added uniformly at random on LFR benchmark graphs with 1000 nodes. Communities detected by (a) Infomap, (b) Label Propagation, (c) Leiden, and (d) Louvain.

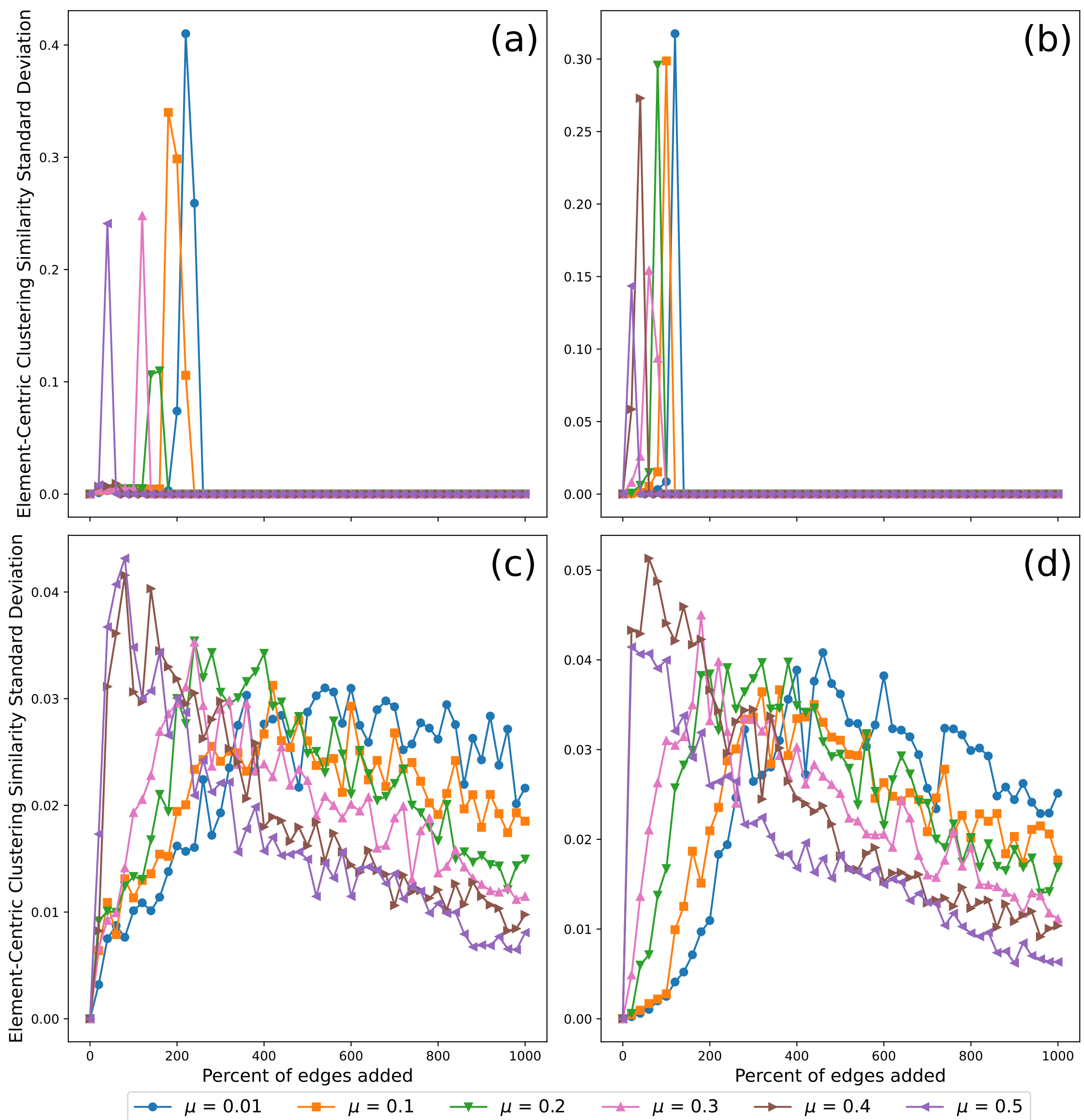

Figure 4.22: Standard deviation of element-centric clustering similarity over the percentage of edges added uniformly at random on LFR benchmark graphs with 10 000 nodes. Communities detected by (a) Infomap, (b) Label Propagation, (c) Leiden, and (d) Louvain.

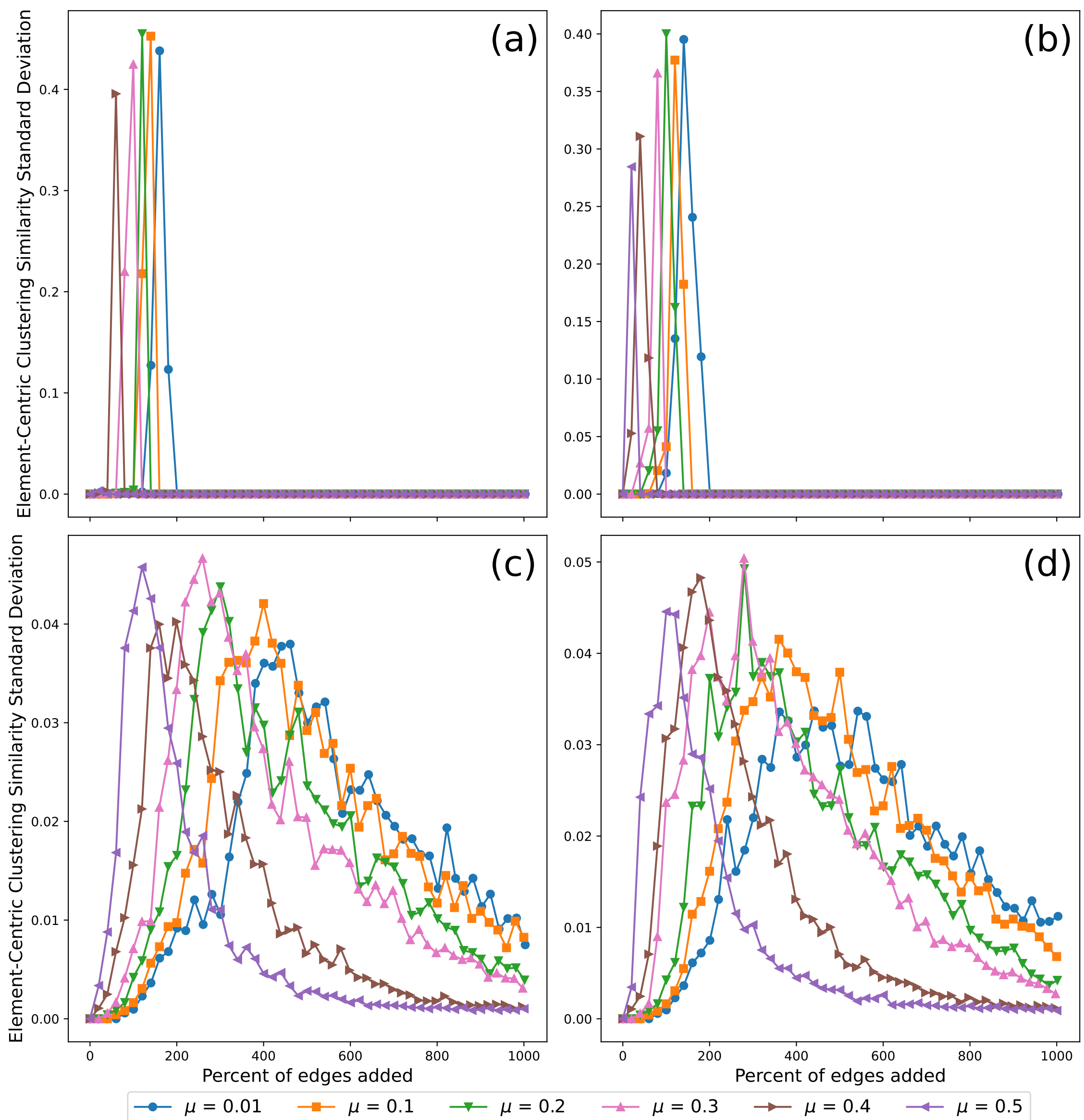

Figure 4.23: Standard deviation of element-centric clustering similarity over the percentage of edges added that are selected uniformly at random across different communities on LFR benchmark graphs with 1000 nodes. Communities detected by (a) Infomap, (b) Label Propagation, (c) Leiden, and (d) Louvain.

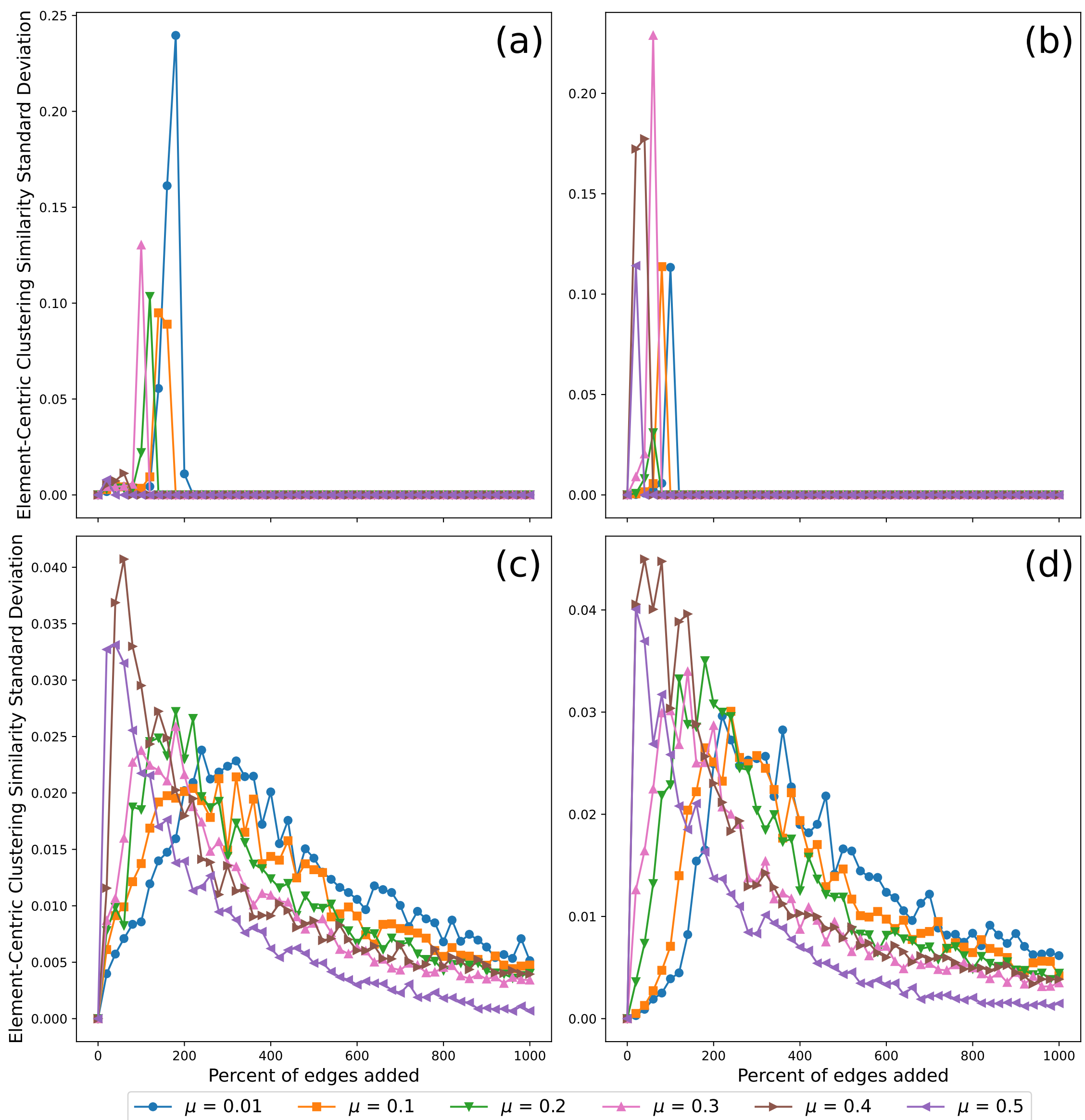

Figure 4.24: Standard deviation of element-centric clustering similarity over the percentage of edges added that are selected uniformly at random across different communities on LFR benchmark graphs with 10 000 nodes. Communities detected by (a) Infomap, (b) Label Propagation, (c) Leiden, and (d) Louvain.

5.4 Standard Deviation for Empirical Results

Figures 4.25 – 4.30 show the standard deviation of NMI and element-centric clustering similarity metric for the empirical results. Note that the changes in standard deviation over steps are always restricted to a small region and the values are kept in scales that are negligible compared to the mean.

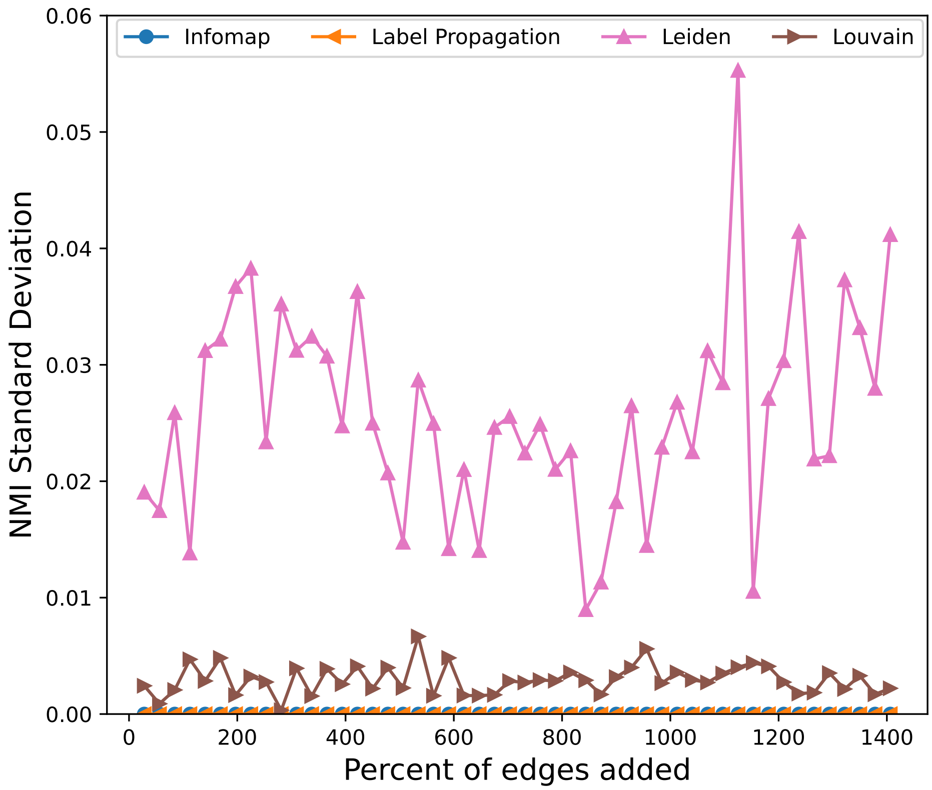

Figure 4.25: Standard deviation of NMI over the percentage of edges added for the ia-radoslaw-email subnetwork.

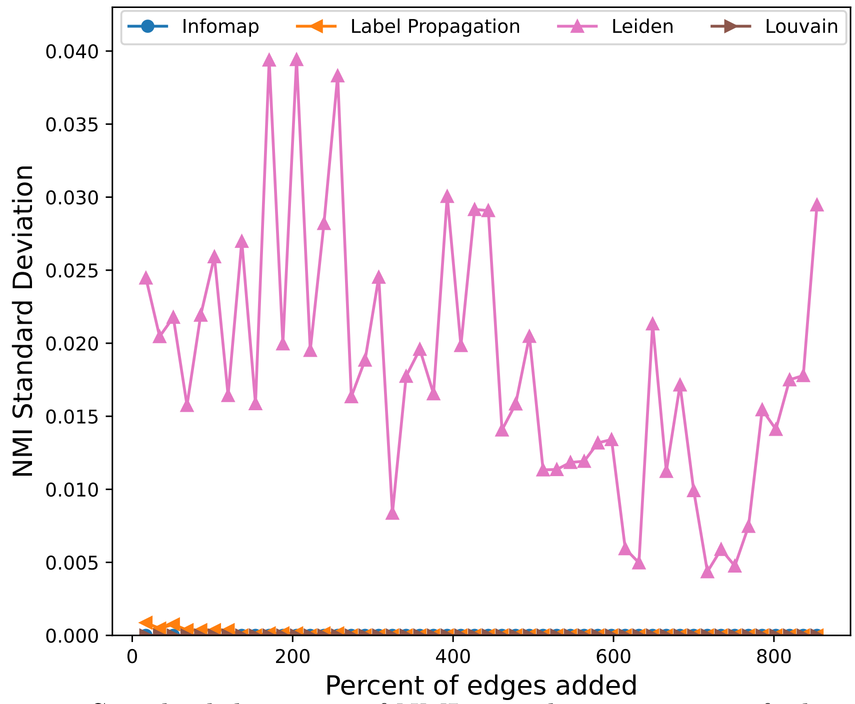

Figure 4.26: Standard deviation of NMI over the percentage of edges added for the Enron subnetwork.

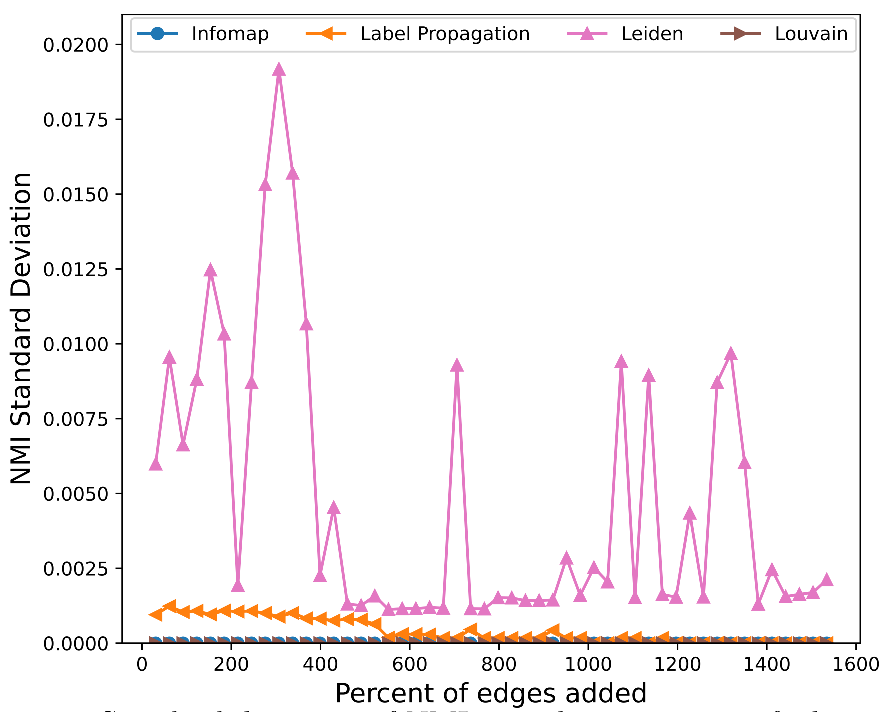

Figure 4.27: Standard deviation of NMI over the percentage of edges added for the email-Eu-core-temporal subnetwork.

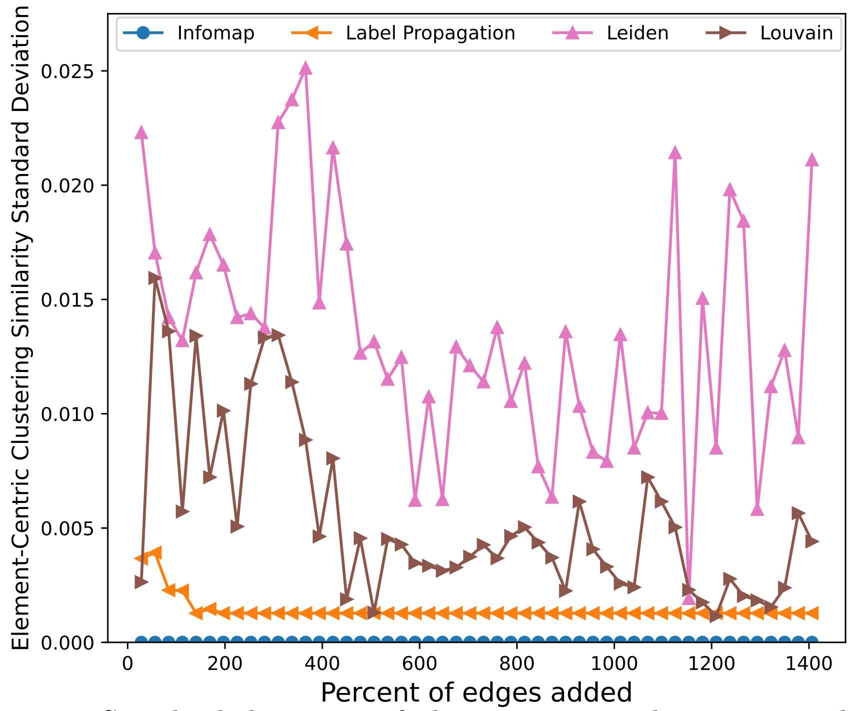

Figure 4.28: Standard deviation of element-centric clustering similarity over the percentage of edges added for the ia-radoslaw-email subnetwork.

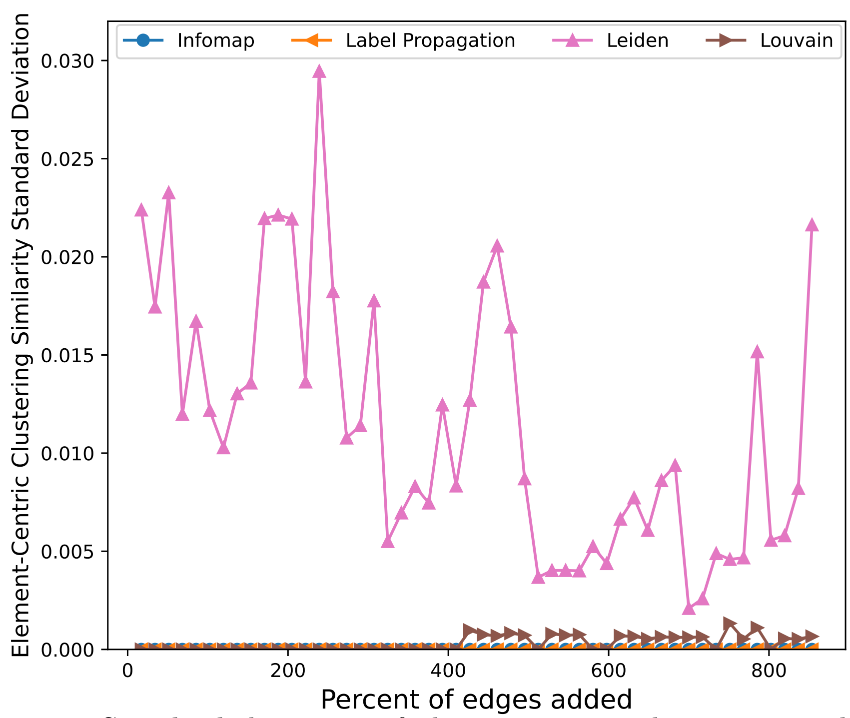

Figure 4.29: Standard deviation of element-centric clustering similarity over the percentage of edges added for the Enron subnetwork.

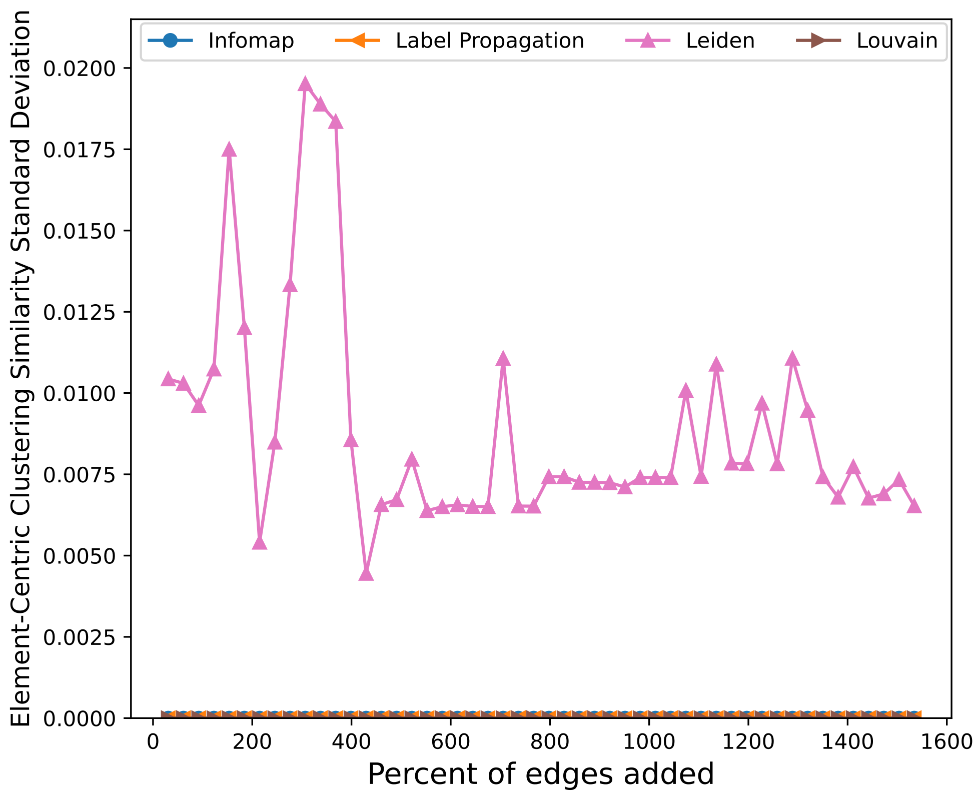

Figure 4.30: Standard deviation of element-centric clustering similarity over the percentage of edges added for the email-Eu-core-temporal subnetwork.

Chapter Five

Conclusion

1 Summary of Contributions

In this thesis, we have explored patterns in network dynamics from two distinct perspectives. The first project analyzes the bifurcation of patterns as stationary solutions in ring dynamical systems, while the second project focuses on patterns identified as communities in data and examines their robustness through various computational experiments.

Although analyzing patterns from the perspectives of purely mathematical models and purely data-driven approaches differ significantly, they both provide valuable insights into the important characteristics of network dynamical systems. When addressing real-world problems, we often require both model-driven and data-driven analyses, which complement each other effectively. Despite the differences in problem setups, objectives, and methodologies, the findings from both projects emphasize the significant impact of network structure on systems dynamics, whether it pertains to the analytical solutions of stationary patterns or the community patterns identified from data. Below, we briefly outline the contributions of these projects.

1.1 Bifurcation of Localized Patterns on Rings

While many social and physical systems naturally manifest as dynamical systems on networks, the impact of graph structures on pattern formation in such systems is less understood. We undertake an initial investigation of this problem by focusing on the study of patterned solutions in bistable reaction-diffusion systems on symmetrically coupled ring graphs with varying interaction lengths. Specifically, we analyze the bifurcation of localized solutions to the system and find that the graph structure, which is represented in terms of the coupling degree in our work, significantly influences how the solution branches are connected in the bifurcation diagram.

In Chapter 2, we analyzed the bifurcation of localized patterns in ring dynamical systems with sparse coupling, corresponding to cases of nearest-neighbor and next-nearest-neighbor couplings, as well as all-to-all coupling. We find that with sparse coupling, the localized solution patterns are connected through a snaking curve, where the number of folds increases with the number of nodes in the graph. In contrast, with all-to-all coupling, the solutions form a closed curve in the bifurcation diagram, consistently exhibiting six folds. For all-to-all coupling, we also find that solution branches bifurcate from the homogeneous solutions near the system's configuration space's two opposite extremities. Moreover, we have explored two specific graph structures with almost-all-to-all coupling, which applies when the system has an even number of nodes and the coupling nearly forms a complete graph, except that no node is connected to the one at the farthest distance. We find that the bifurcation diagram forms a snaking curve in such cases with almost-all-to-all coupling as well. However, due to the underlying symmetry, the patterns do not connect in the regular way as they do with sparse coupling.

In Chapter 3, we addressed the unresolved questions from Chapter 2 by examining the solution branches at the extremities of the system's configuration space in more general cases, beyond just all-to-all coupling. Using equivariant bifurcation theory, we find that the patterned solution branch bifurcates from the homogeneous solutions, and the criticality of the bifurcation is determined by the degree of coupling for any given number of nodes. Furthermore, we have delved into the limiting scenario when the number of nodes in the system approaches infinity and outlined the approaches for analytically computing the predicted ratio of the coupling degree to the number of nodes at which we expect a transition in the bifurcation criticality.

1.2 Community Robustness under Edge Addition

In Chapter 4, we designed computational methods to study the robustness of community structures, as identified by community detection methods, under edge-addition perturbations to networks. Our studies include experiments on both synthetic and empirical network data. With synthetic networks, we have complete control over the strength of the initial community structures and the edge-addition strategies, allowing us to isolate and examine the impacts of these different factors. We also explored the effects of different community detection algorithms and community similarity metrics, presenting comparative results from both synthetic and empirical experiments. Furthermore, we demonstrated how synthetic data could facilitate the analysis of empirical results by comparing empirical experiments to their synthetic counterparts through an edge-addition parameter. Overall, our findings suggest that community robustness is strongly influenced by the choice of community detection method, underscoring the importance of selecting an appropriate algorithm for studies on community structures and their robustness in networks.

2 Future Directions

The analytical and computational methodologies presented in this thesis illustrate different approaches to studying patterns. In this section, we outline several future directions inspired by these projects.

2.1 Bifurcation of Localized Patterns on Rings

In Chapters 2 and 3, we presented analyses aimed at understanding how interaction length influences the bifurcation of localized solution patterns in reaction-diffusion systems on symmetrically coupled ring graphs. Several open questions remain unexplored. One such question pertains to extending our analysis to more general coupling regimes. Specifically, although we have numerically observed snaking bifurcations beyond the sparse coupling case, we have yet to provide proofs for these scenarios. Furthermore, our understanding of the almost-all-to-all coupling case is incomplete, particularly regarding how to study it in a more general way beyond specific graph realizations. An essential step toward this goal involves understanding the impact from the Laplace operator. In Chapter 3, we briefly discussed one potential approach, which is to analyze the Laplacian by leveraging the irreducible representation of the dihedral group.

Moreover, in Chapter 3, we have shown numerically that the branch of patterned solutions, which bifurcates from the homogeneous branch at the extremities of the system's configuration space, connects with the snaking curve of solutions. However, this fact has not yet been proven. Also, in the numerical continuation of the localized solution branch in Chapter 3, we observed that when we continue through the bifurcation point on the homogeneous branch, the numerical computation switches to other branches, but only to certain ones. It is not yet clear why and in what way the switching of solution branches occurs during computation.

Another level of extension of our analysis is to look at other types of graph structures and investigate how patterns may connect differently in the corresponding configuration space. For instance, a potential modification to the ring system could involve making the couplings asymmetric. Another natural extension is to examine the influence of connecting multiple simple graphs and explore the existence of solution patterns when the graph structure becomes more complex.

2.2 Community Robustness under Edge Addition

In Chapter 4, we presented computational results from three relatively small empirical temporal networks and provided preliminary analysis and explanations for the observed experimental behaviors. With a more extensive collection of empirical data, we could further investigate the effects of various factors, including scale, density, degree distributions, and edge-addition rules, on community robustness. The synthetic methods could be adapted to control these properties more closely, making them more comparable to empirical data and aiding in analysis.

While empirical studies can always benefit from incorporating a broader range of algorithms and metrics, a more profound direction would involve a generic analysis of how and why the underlying mathematical properties, whether in the objectives or the metrics, contribute to the observed variations in community robustness. Such an approach could provide deeper insights into interpreting these behaviors.

2.3 Patterns in Network Dynamics

In Chapters 2 and 3, we explored analytical approaches for studying the bifurcation of patterned solutions in reaction-diffusion systems on rings. In Chapter 4, we conducted a computational study on the robustness of community patterns, identified in network data, under edge additions. These two distinct projects serve as examples to demonstrate that the study of patterns in network dynamics encompasses a wide range of problems, objectives, and strategies. However, it is important to note that these varying model-driven and data-driven perspectives are not isolated from each other. In fact, they often contribute to the development of one another, collectively offering a more comprehensive understanding of patterns in systems with graph structures.

To further illustrate this point, we discuss an open problem that could benefit from integrating techniques from both projects, thereby setting a direction for future research. The discovery of communities in temporal networks presents a significant challenge, as highlighted by Cazabet and Rossetti (2019). The main difficulty lies in interpreting the identified communities and understanding the variety of changes in community structure that result from alterations in the networks. These changes often involve latent dynamics, making it challenging to evaluate how accurately the detected communities represent the true underlying structure. A combined model-driven and data-driven approach could provide a way to tackle this issue by relating the community pattern to the steady-state solution of the underlying dynamical systems.

For example, if we know the model governing the dynamics of network structure and node interaction, then analytical and numerical techniques can assist in making more accurate predictions about network evolution and in tracking the temporal community patterns by finding the corresponding stationary solutions to the system. This is known as a forward problem. Conversely, by using data from empirical observations, we can learn the form of the dynamics and infer their parameters, thereby validating and enhancing the model to better represent the real-world system of interest. This is considered an inverse problem. Bridging these forward and inverse problems can lead to a more precise and deeper understanding of the patterns in network dynamics within real-world complex systems.

Chapter Six

Bibliography

Bibliography

R. Albert, H. Jeong, and A.-L. Barabási. Error and attack tolerance of complex networks. *Nature*, 406(6794):378–382, 2000. doi: 10.1038/35019019. URL https://doi.org/10.1038/35019019.

D. R. Amancio, O. N. Oliveira, and L. da F Costa. Robustness of community structure to node removal. *J. Stat. Mech.: Theory Exp.*, 2015(3):P03003, mar 2015. doi: 10.1088/1742-5468/2015/03/P03003. URL https://dx.doi.org/10.1088/1742-5468/2015/03/P03003.

L. A. N. Amaral and J. M. Ottino. Complex networks. *Eur. Phys. J. B*, 38(2): 147–162, 2004. doi: 10.1140/epjb/e2004-00110-5. URL https://doi.org/10.1140/epjb/e2004-00110-5.

D. Avitabile, D. J. B. Lloyd, J. Burke, E. Knobloch, and B. Sandstede. To snake or not to snake in the planar Swift–Hohenberg equation. *SIAM J. Appl. Dynam. Syst.*, 9:704–733, 2010. doi: 10.1137/100782747.

A.-L. Barabási and M. Pósfai. *Network science*. Cambridge University Press, Cambridge, 2016. ISBN 9781107076266 1107076269. URL http://barabasi.com/networksciencebook/.

M. Beck, J. Knobloch, D. J. B. Lloyd, B. Sandstede, and T. Wagenknecht. Snakes, ladders, and isolas of localised patterns. *SIAM J. Math. Anal.*, 41:936–972, 2009. doi: 10.1137/080713306.

V. D. Blondel, J.-L. Guillaume, R. Lambiotte, and E. Lefebvre. Fast unfolding of communities in large networks. *J. Stat. Mech.: Theory Exp.*, 2008(10):P10008, oct 2008. doi: 10.1088/1742-5468/2008/10/p10008. URL https://doi.org/10.1088/1742-5468/2008/10/p10008.

S. P. Borgatti, K. M. Carley, and D. Krackhardt. On the robustness of centrality measures under conditions of imperfect data. *Soc. Netw.*, 28(2):124–136, 2006. ISSN 0378-8733. doi: https://doi.org/10.1016/j.socnet.2005.05.001. URL https://www.sciencedirect.com/science/article/pii/S0378873305000353.

J. J. Bramburger. Isolas of multi-pulse solutions to lattice dynamical systems. *Proc. Roy. Soc. Edinburgh A*, pages 1–36, 2020. doi: 10.1017/prm.2020.44.

J. J. Bramburger and B. Sandstede. Spatially localized structures in lattice dynamical systems. *J. Nonlinear Sci.*, 30(2):603–644, 2020a. ISSN 0938-8974. doi: 10.1007/s00332-019-09584-x. URL https://doi.org/10.1007/s00332-019-09584-x.

J. J. Bramburger and B. Sandstede. Localized patterns in planar bistable weakly coupled lattice systems. *Nonlinearity*, 33(7):3500–3525, 2020b. ISSN 0951-7715. doi: 10.1088/1361-6544/ab7d1e. URL https://doi.org/10.1088/1361-6544/ab7d1e.

P. C. Bressloff. *Stochastic gene expression and regulatory networks*, pages 233–355. Springer International Publishing, Cham, 2021. ISBN 978-3-030-72515-0. doi: 10.1007/978-3-030-72515-0_5. URL https://doi.org/10.1007/978-3-030-72515-0_5.

J. Burke and E. Knobloch. Localized states in the generalized Swift–Hohenberg equation. *Phys. Rev. E*, 73(5):056211, 2006. ISSN 1539-3755.

J. Burke and E. Knobloch. Snakes and ladders: localized states in the Swift–Hohenberg equation. *Phys. Lett. A*, 360(6):681–688, 2007. ISSN 0375-9601.

A. Carissimo, L. Cutillo, and I. De Feis. Validation of community robustness. *Comput. Stat. Data Anal.*, 120:1–24, 2018. ISSN 0167-9473. doi: 10.1016/j.csda.2017.10.006. URL https://doi.org/10.1016/j.csda.2017.10.006.

R. Cazabet and G. Rossetti. *Challenges in community discovery on temporal networks*, pages 181–197. Springer International Publishing, Cham, 2019. ISBN 978-3-030-23495-9. doi: 10.1007/978-3-030-23495-9_10. URL https://doi.org/10.1007/978-3-030-23495-9_10.

S. J. Chapman and G. Kozyreff. Exponential asymptotics of localised patterns and snaking bifurcation diagrams. *Physica D*, 238(3):319–354, 2009. ISSN 0167-2789. doi: 10.1016/j.physd.2008.10.005. URL http://dx.doi.org/10.1016/j.physd.2008.10.005.

C. Chong and D. E. Pelinovsky. Variational approximations of bifurcations of asymmetric solitons in cubic-quintic nonlinear Schrödinger lattices. *Discrete Contin. Dyn. Syst. Ser. S*, 4(5):1019–1031, 2011. ISSN 1937-1632. doi: 10.3934/dcdss.2011.4.1019. URL https://doi.org/10.3934/dcdss.2011.4.1019.

C. Chong, R. Carretero-González, B. A. Malomed, and P. G. Kevrekidis. Multistable solitons in higher-dimensional cubic-quintic nonlinear Schrödinger lattices. *Physica D*, 238(2):126–136, 2009. ISSN 0167-2789. doi: 10.1016/j.physd.2008.10.002. URL https://doi.org/10.1016/j.physd.2008.10.002.

A. Clauset, M. E. J. Newman, and C. Moore. Finding community structure in very large networks. *Phys. Rev. E*, 70:066111, Dec 2004. doi: 10.1103/PhysRevE.70.066111. URL https://link.aps.org/doi/10.1103/PhysRevE.70.066111.

P. Coullet, C. Riera, and C. Tresser. Stable Static localized structures in one dimension. *Phys. Rev. Lett.*, 84(14):3069–3072, 3 April 2000.

J. H. P. Dawes. The emergence of a coherent structure for coherent structures: localized states in nonlinear systems. *Philos. Trans. R. Soc. Lond. Ser. A*, 368 (1924):3519–3534, 2010. ISSN 1364-503X. doi: 10.1098/rsta.2010.0057. URL https://doi.org/10.1098/rsta.2010.0057.

A. P. S. Dias and A. Rodrigues. Secondary bifurcations in systems with all-to-all coupling. II. *Dyn. Syst.*, 21(4):439–463, 2006. ISSN 1468-9367. doi: 10.1080/14689360600759689. URL https://doi.org/10.1080/14689360600759689.

T. Elmhirst. S_N-equivariant symmetry-breaking bifurcations. *Internat. J. Bifur. Chaos Appl. Sci. Engrg.*, 14(3):1017–1036, 2004. ISSN 0218-1274. doi: 10.1142/S0218127404009697. URL https://doi.org/10.1142/S0218127404009697.

S. Emmons, S. Kobourov, M. Gallant, and K. Börner. Analysis of network clustering algorithms and cluster quality metrics at scale. *PLOS ONE*, 11(7):1–18, 07 2016. doi: 10.1371/journal.pone.0159161. URL https://doi.org/10.1371/journal.pone.0159161.

W. J. Firth, L. Columbo, and T. Maggipinto. On homoclinic snaking in optical systems. *Chaos*, 17:037115, 2007.

S. Fortunato. Community detection in graphs. *Phys. Rep.*, 486(3):75–174, 2010. ISSN 0370-1573. doi: https://doi.org/10.1016/j.physrep.2009.11.002. URL https://www.sciencedirect.com/science/article/pii/S0370157309002841.

S. Fortunato. Santo Fortunato's website: resources, October 2021. URL https://www.santofortunato.net/resources. Last Accessed: January 11, 2023.

S. Fortunato and D. Hric. Community detection in networks: a user guide. *Phys. Rep.*, 659:1–44, Nov. 2016. ISSN 0370-1573. doi: 10.1016/j.physrep.2016.09.002.

A. L. N. Fred and A. K. Jain. Robust data clustering. *2003 Proc. IEEE Comput. Soc. Conf. Comput. Vis. Pattern Recognit.*, 2:II–II, 2003.

A. J. Gates and Y.-Y. Ahn. CluSim: a python package for calculating clustering similarity. *J. Open Source Softw.*, 4(35):1264, 2019. doi: 10.21105/joss.01264. URL https://doi.org/10.21105/joss.01264.

A. J. Gates, I. B. Wood, W. P. Hetrick, and Y.-Y. Ahn. Element-centric clustering comparison unifies overlaps and hierarchy. *Sci. Rep.*, 9(1):8574, 2019. doi: 10.1038/s41598-019-44892-y. URL https://doi.org/10.1038/s41598-019-44892-y.

M. Girvan and M. E. J. Newman. Community structure in social and biological networks. *Proc. Natl. Acad. Sci. U.S.A.*, 99(12):7821–7826, 2002. doi: 10.1073/pnas.122653799. URL https://www.pnas.org/doi/abs/10.1073/pnas.122653799.

R. J. Glauber. Time-dependent statistics of the Ising model. *J. Math. Phys.*, 4(2):294–307, 1963. doi: 10.1063/1.1703954.

M. Golubitsky and I. Stewart. Symmetry methods in mathematical biology. *São Paulo J. Math. Sci.*, 9(1):1–36, 2015. ISSN 1982-6907. doi: 10.1007/s40863-015-0001-9. URL https://doi.org/10.1007/s40863-015-0001-9.

M. Golubitsky, I. Stewart, and D. G. Schaeffer. *Singularities and groups in bifurcation theory. Vol. II*, volume 69 of *Applied Mathematical Sciences*. Springer-Verlag, New York, 1988. ISBN 0-387-96652-8. doi: 10.1007/978-1-4612-4574-2. URL https://doi.org/10.1007/978-1-4612-4574-2.

D. Gomila, A. J. Scroggie, and W. J. Firth. Bifurcation structure of dissipative solitons. *Physica D*, 227(1):70–77, 2007. ISSN 0167-2789.

M. D. Groves, D. J. B. Lloyd, and A. Stylianou. Pattern formation on the free surface of a ferrofluid: spatial dynamics and homoclinic bifurcation. *Physica D*, 350:1–12, 2017. ISSN 0167-2789. doi: 10.1016/j.physd.2017.03.004. URL https://doi.org/10.1016/j.physd.2017.03.004.

R. Guimerà, L. Danon, A. Díaz-Guilera, F. Giralt, and A. Arenas. Self-similar community structure in a network of human interactions. *Phys. Rev. E*, 68:065103(R), Dec 2003. doi: 10.1103/PhysRevE.68.065103. URL https://link.aps.org/doi/10.1103/PhysRevE.68.065103.

P. W. Holland, K. B. Laskey, and S. Leinhardt. Stochastic blockmodels: first steps. *Soc. Netw.*, 5(2):109–137, 1983. ISSN 0378-8733. doi: https://doi.org/10.1016/0378-8733(83)90021-7. URL https://www.sciencedirect.com/science/article/pii/0378873383900217.

P. Holme, B. J. Kim, C. N. Yoon, and S. K. Han. Attack vulnerability of complex networks. *Phys. Rev. E*, 65:056109, May 2002. doi: 10.1103/PhysRevE.65.056109. URL https://link.aps.org/doi/10.1103/PhysRevE.65.056109.

R. Hoyle. *Pattern formation: an introduction to methods*. Cambridge University Press, 2006.

B. Karrer, E. Levina, and M. E. J. Newman. Robustness of community structure in networks. *Phys. Rev. E*, 77:046119, Apr 2008. doi: 10.1103/PhysRevE.77.046119. URL https://link.aps.org/doi/10.1103/PhysRevE.77.046119.

M. J. Keeling and K. T. D. Eames. Networks and epidemic models. *J. R. Soc. Interface*, 2(4):295–307, Sep 2005. ISSN 1742-5689 (Print); 1742-5662 (Electronic); 1742-5662 (Linking). doi: 10.1098/rsif.2005.0051.

E. Knobloch. Spatial localization in dissipative systems. *Annual Rev. Condensed Matter Phys.*, 6:325–359, March 2015.

G. Kozyreff and S. J. Chapman. Asymptotics of large bound states of localized structures. *Phys. Rev. Lett.*, 97(4):044502, July 2006.

C. Kuehn. *Multiple time scale dynamics*, volume 191 of *Applied Mathematical Sciences*. Springer, Cham, 2015. ISBN 978-3-319-12315-8; 978-3-319-12316-5. doi: 10.1007/978-3-319-12316-5. URL https://doi.org/10.1007/978-3-319-12316-5.

J. Kunegis. Enron, May 2013. URL http://konect.cc/networks/enron. Last Accessed: July 13, 2022.

R. Kusdiantara and H. Susanto. Homoclinic snaking in the discrete Swift-Hohenberg equation. *Phys. Rev. E*, 96(6):062214, 2017. ISSN 2470-0045. doi: 10.1103/physreve.96.062214.

R. Kusdiantara and H. Susanto. Snakes in square, honeycomb and triangular lattices. *Nonlinearity*, 32(12):5170–5190, 2019. ISSN 0951-7715. doi: 10.1088/1361-6544/ab46e8.

A. Lancichinetti and S. Fortunato. Community detection algorithms: a comparative analysis. *Phys. Rev. E*, 80:056117, Nov 2009a. doi: 10.1103/PhysRevE.80.056117. URL https://link.aps.org/doi/10.1103/PhysRevE.80.056117.

A. Lancichinetti and S. Fortunato. Benchmarks for testing community detection algorithms on directed and weighted graphs with overlapping communities. *Phys. Rev. E*, 80:016118, Jul 2009b. doi: 10.1103/PhysRevE.80.016118. URL https://link.aps.org/doi/10.1103/PhysRevE.80.016118.

A. Lancichinetti and S. Fortunato. Consensus clustering in complex networks. *Sci. Rep.*, 2(1):336, 2012. doi: 10.1038/srep00336. URL https://doi.org/10.1038/srep00336.

A. Lancichinetti, S. Fortunato, and F. Radicchi. Benchmark graphs for testing community detection algorithms. *Phys. Rev. E*, 78:046110, Oct 2008. doi: 10.1103/PhysRevE.78.046110. URL https://link.aps.org/doi/10.1103/PhysRevE.78.046110.

J. Leskovec. SNAP datasets. Stanford large network dataset collection: email-Eu-core temporal network, February 2017. URL http://snap.stanford.edu/data/email-Eu-core-temporal.html. Last Accessed: June 15, 2022.

J. Leskovec, J. M. Kleinberg, and C. Faloutsos. Graphs over time: densification laws, shrinking diameters and possible explanations. In *Proceedings of the Eleventh ACM SIGKDD International Conference on Knowledge Discovery in Data Mining*, pages 177–187, New York, 2005. KDD '05, ACM.

D. J. B. Lloyd, B. Sandstede, D. Avitabile, and A. R. Champneys. Localized hexagon patterns of the planar Swift–Hohenberg equation. *SIAM J. Appl. Dynam. Syst.*, 7:1049–1100, 2008. doi: 10.1137/070707622.

D. J. B. Lloyd, C. Gollwitzer, I. Rehberg, and R. Richter. Homoclinic snaking near the surface instability of a polarisable fluid. *J. Fluid Mech.*, 783:283–305, 2015. ISSN 0022-1120. doi: 10.1017/jfm.2015.565.

N. McCullen and T. Wagenknecht. Pattern formation on networks: from localised activity to turing patterns. *Scientific Reports*, 6(1):27397, 2016. doi: 10.1038/srep27397. URL https://doi.org/10.1038/srep27397.

E. Meron. From patterns to function in living systems: dryland ecosystems as a case study. *Annual Rev. Condensed Matter Phys.*, 9:79 – 103, 2018. doi: 10.1146/annurev-conmatphys-033117-053959.

M. Mozafari and M. Khansari. Improving the robustness of scale-free networks by maintaining community structure. *J. Complex Netw.*, 7(6):838–864, 2019. ISSN 2051-1310. doi: 10.1093/comnet/cnz009. URL https://doi.org/10.1093/comnet/cnz009.

M. E. J. Newman. The structure and function of complex networks. *SIAM Rev.*, 45 (2):167–256, 2003. doi: 10.1137/S003614450342480. URL https://doi.org/10.1137/S003614450342480.

H. Noorazar, K. R. Vixie, A. Talebanpour, and Y. Hu. From classical to modern opinion dynamics. *Int. J. Mod. Phys. C*, 31(07):2050101, 2020. doi: 10.1142/S0129183120501016. URL https://doi.org/10.1142/S0129183120501016.

O. Osanaiye, K.-K. R. Choo, and M. Dlodlo. Distributed denial of service (DDoS) resilience in cloud: review and conceptual cloud DDoS mitigation framework. *J. Netw. Comput. Appl.*, 67:147–165, 2016. ISSN 1084-8045. doi: https://doi.org/10.1016/j.jnca.2016.01.001. URL https://www.sciencedirect.com/science/article/pii/S1084804516000023.

G. Palla, I. Derényi, I. Farkas, and T. Vicsek. Uncovering the overlapping community structure of complex networks in nature and society. *Nature*, 435(7043):814–818, 2005. doi: 10.1038/nature03607. URL https://doi.org/10.1038/nature03607.

A. Papangelo, A. Grolet, L. Salles, N. Hoffmann, and M. Ciavarella. Snaking bifurcations in a self-excited oscillator chain with cyclic symmetry. *Comm. Nonlinear Sci. Numer. Simul.*, 44:108–119, 2017. ISSN 1007-5704. doi: https://doi.org/10.1016/j.cnsns.2016.08.004. URL https://www.sciencedirect.com/science/article/pii/S1007570416302738.

F. Pedregosa, G. Varoquaux, A. Gramfort, V. Michel, B. Thirion, O. Grisel, M. Blondel, P. Prettenhofer, R. Weiss, V. Dubourg, J. Vanderplas, A. Passos, D. Cournapeau, M. Brucher, M. Perrot, and E. Duchesnay. Scikit-learn: machine learning in Python. *J. Mach. Learn. Res.*, 12:2825–2830, 2011.

L. Peel, D. B. Larremore, and A. Clauset. The ground truth about metadata and community detection in networks. *Sci. Adv.*, 3(5), May 2017. doi: 10.1126/sciadv.1602548. URL https://www.science.org/doi/abs/10.1126/sciadv.1602548.

L. M. Pismen. *Patterns and interfaces in dissipative dynamics revised and extended, now also covering patterns of active matter.* Springer Series in Synergetics. Springer International Publishing, Cham, 2nd ed. 2023. edition, 2023. ISBN 3-031-29579-X. doi: 10.1007/978-3-031-29579-9.

Y. Pomeau. Front motion, metastability, and subcritical bifurcations in hydrodynamics. *Physica D*, 23(1-3):3–11, Dec 1986.

U. N. Raghavan, R. Albert, and S. Kumara. Near linear time algorithm to detect community structures in large-scale networks. *Phys. Rev. E*, 76:036106, Sep 2007. doi: 10.1103/PhysRevE.76.036106. URL https://link.aps.org/doi/10.1103/PhysRevE.76.036106.

R. Richer and I. Barashenkov. Two-dimensional solitons on the surface of magnetic fluids. *Phys. Rev. Lett.*, 94(18):184503, 2005.

Richter, Reinhard. Mag(net)ic liquid mountains. *Europhys. News*, 42(3):17–19, 2011. doi: 10.1051/epn/2011301. URL https://doi.org/10.1051/epn/2011301.

R. A. Rossi and N. K. Ahmed. The network data repository with interactive graph analytics and visualization: IA-RADOSLAW-EMAIL, March 2015. URL https://networkrepository.com/ia-radoslaw-email.php. Last Accessed: June 14, 2022.

M. Rosvall and C. T. Bergstrom. Maps of random walks on complex networks reveal community structure. *Proc. Natl. Acad. Sci. U.S.A.*, 105(4):1118–1123, 2008. doi: 10.1073/pnas.0706851105. URL https://www.pnas.org/doi/abs/10.1073/pnas.0706851105.

S. E. Schaeffer, V. Valdés, J. Figols, I. Bachmann, F. Morales, J. Bustos-Jiménez, and E. Estrada. Characterization of robustness and resilience in graphs: a mini-review. *J. Complex Netw.*, 9(2):cnab018, 2021. doi: 10.1093/comnet/cnab018.

J.-P. Serre. *Linear representations of finite groups.*, volume 42 of *Graduate texts in mathematics*. Springer, 1977. ISBN 978-3-540-90190-7.

E. Sheffer, H. Yizhaq, E. Gilad, M. Shachak, and E. Meron. Why do plants in resource-deprived environments form rings? *Ecol. Complex.*, 4(4):192–200, 2007. ISSN 1476-945X. doi: https://doi.org/10.1016/j.ecocom.2007.06.008. URL https://www.sciencedirect.com/science/article/pii/S1476945X07000669.

M. SHORT, M. Dorsogna, V. Pasour, G. Tita, P. Brantingham, A. Bertozzi, and L. CHAYES. A statistical model of criminal behavior. *Math. Models Methods Appl. Sci.*, 18, 08 2008. doi: 10.1142/S0218202508003029.

I. Stewart, T. Elmhirst, and J. Cohen. Symmetry-breaking as an origin of species. In *Bifurcation, symmetry and patterns (Porto, 2000)*, Trends Math., pages 3–54. Birkhäuser, Basel, 2003.

A. Tandon, A. Albeshri, V. Thayananthan, W. Alhalabi, and S. Fortunato. Fast consensus clustering in complex networks. *Phys. Rev. E*, 99:042301, Apr 2019. doi: 10.1103/PhysRevE.99.042301. URL https://link.aps.org/doi/10.1103/PhysRevE.99.042301.

A. Tandon, A. Albeshri, V. Thayananthan, W. Alhalabi, F. Radicchi, and S. Fortunato. Community detection in networks using graph embeddings. *Phys. Rev. E*, 103:022316, Feb 2021. doi: 10.1103/PhysRevE.103.022316. URL https://link.aps.org/doi/10.1103/PhysRevE.103.022316.

C. Taylor and J. H. Dawes. Snaking and isolas of localised states in bistable discrete lattices. *Phys. Lett. A*, 375(1):14–22, 2010. ISSN 0375-9601. doi: https://doi.org/10.1016/j.physleta.2010.10.010. URL https://www.sciencedirect.com/science/article/pii/S0375960110013460.

M. Tian and P. Moriano. Robustness of community structure under edge addition. *Phys. Rev. E*, 108:054302, Nov 2023. doi: 10.1103/PhysRevE.108.054302. URL https://link.aps.org/doi/10.1103/PhysRevE.108.054302.

M. Tian, J. J. Bramburger, and B. Sandstede. Snaking bifurcations of localized patterns on ring lattices. *IMA J. Appl. Math.*, 86(5):1112–1140, 06 2021. ISSN 0272-4960. doi: 10.1093/imamat/hxab023. URL https://doi.org/10.1093/imamat/hxab023.

V. A. Traag. GitHub repository: networkanalysis, December 2020. URL https://github.com/CWTSLeiden/networkanalysis. Last Accessed: January 11, 2023.

V. A. Traag, L. Waltman, and N. J. van Eck. From Louvain to Leiden: guaranteeing well-connected communities. *Sci. Rep.*, 9(1):5233, 2019. doi: 10.1038/s41598-019-41695-z. URL https://doi.org/10.1038/s41598-019-41695-z.

D. J. Wang, X. Shi, D. A. McFarland, and J. Leskovec. Measurement error in network data: a re-classification. *Soc. Netw.*, 34:396–409, 2012.

S. Wang and J. Liu. Constructing robust community structure against edge-based attacks. *IEEE Syst. J.*, 13(1):582–592, 2019. doi: 10.1109/JSYST.2018.2835642.

S. Wang, J. Liu, and X. Wang. Mitigation of attacks and errors on community structure in complex networks. *J. Stat. Mech.: Theory Exp.*, 2017(4):043405, apr 2017. doi: 10.1088/1742-5468/aa6581. URL https://dx.doi.org/10.1088/1742-5468/aa6581.

P. D. Woods and A. R. Champneys. Heteroclinic tangles and homoclinic snaking in the unfolding of a degenerate reversible Hamiltonian–Hopf bifurcation. *Physica D*, 129(3-4):147–170, 1999. ISSN 0167-2789.

Z. Yang, R. Algesheimer, and C. J. Tessone. A comparative analysis of community detection algorithms on artificial networks. *Sci. Rep.*, 6(1):30750, 2016. doi: 10.1038/srep30750. URL https://doi.org/10.1038/srep30750.

A. Yulin and A. Champneys. Snake-to-isola transition and moving solitons via symmetry-breaking in discrete optical cavities. *Discrete Contin. Dyn. Syst. Ser. S*, 4(5):1341–1357, 2011. ISSN 1937-1632. doi: 10.3934/dcdss.2011.4.1341. URL https://doi.org/10.3934/dcdss.2011.4.1341.

A. V. Yulin and A. R. Champneys. Discrete snaking: multiple cavity solitons in saturable media. *SIAM J. Appl. Dynam. Syst.*, 9(2):391–431, 2010. doi: 10.1137/080734297. URL https://doi.org/10.1137/080734297.

S. T. Zargar, J. Joshi, and D. Tipper. A survey of defense mechanisms against distributed denial of service (DDoS) flooding attacks. *IEEE Commun. Surv. Tutor.*, 15(4):2046–2069, 2013. doi: 10.1109/SURV.2013.031413.00127.